Synthesis of nano-carbon structures with functionalized metal oxides and their sensing applications

THESIS SUBMITTED FOR THE AWARD OF THE DEGREE OF

Doctor of Philosophy

in

Applied Physics

by

Utkarsh Kumar
M.Sc.
Enrollment No. 696/12

Under the Supervision of

Prof. Bal Chandra Yadav

DEPARTMENT OF APPLIED PHYSICS

SCHOOL FOR PHYSICAL SCIENCES

BABASAHEB BHIMRAO AMBEDKAR UNIVERSITY,

LUCKNOW-226025, U.P., INDIA

December 2019

DECLARATION

I declare that the thesis entitled **"Synthesis of nano-carbon structures with functionalized metal oxides and their sensing applications"** has been prepared by me under the supervision of Prof. Bal Chandra Yadav, Department of Applied Physics, School for Physical Sciences, Babasaheb Bhimrao Ambedkar University, Lucknow. No part of this thesis has formed the basis for the award of any degree, diploma or fellowship previously. Further, I declare that the material embodied in the present work is based on original research work and the indebtedness to others has been duly acknowledged at relevant places. This is also declared that the thesis is essentially free from all kind of plagiarism.

(Utkarsh Kumar)

Department of Applied Physics, School for Physical Sciences,

Babasaheb Bhimrao Ambedkar University, Vidya Vihar,

Raebareli Road, Lucknow-226025, U.P., India

Date:

Place: Lucknow

Dedicated to my family and friends

BABASAHEB BHIMRAO AMBEDKAR UNIVERSITY
LUCKNOW
प्रज्ञा शील करुणा
ESTABLISHED 1996

बाबा साहेब भीमराव अम्बेडकर विश्वविद्यालय

)केंद्रीय विश्वविद्यालय(

विद्या विहार, रायबरेली रोड, लखनऊ – 226025

Babasaheb Bhimrao Ambedkar University

(A Central University)

Vidya Vihar, Raebareli Road, Lucknow – 226025

CERTIFICATE

This is to certify that the thesis titled **"Synthesis of nano-carbon structures with functionalized metal oxides and their sensing applications"** submitted by Mr. Utkarsh Kumar is an original research work and has not been previously submitted in part or full for the award of any other degree or diploma to this or any other university or institutions.

This thesis submitted to the Babasaheb Bhimrao Ambedkar University, Lucknow satisfies all the requirements as stipulated in the *Doctor of Philosophy (Ph.D.) regulations-1999 as amended in 2010* and it fit for submission and evaluation for the award of Doctor of Philosophy of the University.

Prof. B. C. Yadav
(Supervisor)

Prof. B. C. Yadav
(Head of the Department)

Date:

Place: Lucknow

ACKNOWLEDGEMENT

It is my firm belief that any major research work to result in a positive outcome including a worthy thesis requires the culmination of several factors such as a meaningful subject which can motivate a determined researcher to take up the challenge, a learned and sincere guide in the form of friend, relative and colleague who selflessly encourage and help the researcher throughout the research. I had the honour and privilege to have **Prof. Bal Chandra Yadav** as an excellent guide and Head, Department of Applied Physics, School for Physical Sciences, Babasaheb Bhimrao Ambedkar University. I take this opportunity to place on record my heartfelt and sincere gratitude and deep indebtedness to him without whose guidance this work could not have been meaningfully concluded.

I am extremely thankful to my teachers **Prof. Devesh Kumar, Dr. Ramesh Chandra**, **Dr. Anil K. Yadav**, **Dr. Khem B. Thapa** & **Dr. Devendra Singh** for their valuable suggestions and encouragements which have been a great asset to me during the entire course of study. I owe my deep gratitude towards them for their constant motivation and moral support. I feel myself blessed to have such teachers. I am very thankful to **Dr. Ravikat Tripathi** Kothari Fellow and senior member of and senior member of my Research Lab for his valuable suggestions and experimental knowledge. **Dr. Samiksha Sikarwar**, Resource Person, Department of Physics is gratefully acknowledged for her support and suggestion in writing my thesis. Also, I staff members at Babasaheb Bhimrao Ambedkar University especially **Dr. Mukesh Kumar,** STA USIC and **Mr. Mukesh Tyagi, Mr. Satrughan Lal** (DAP).

I gratefully acknowledge to **University Grant Commission, Govt. of India** for financial support in the **Rajeev Gandhi National Fellowship (RGNF)** grant no. **F1-17.1/2017-18/RGNF-2017-18-SC-UTT-41083**.

I am very thankful to my senior**, Dr. Ravindra Kumar, Dr. Rakesh Sonker, Dr. Monika Singh, Dr. Saroj Radheysham, Dr. Raj Kamal Shastri** and **Dr. Surya Goutam** for their continuous moral support and encouragement. I would like to thanks **Ms. Priyanka Chaudhary, Mr. Kuldeep Kumar, Er. Ekta Singh, Mr. Shakti Singh,**

Ms. Banani Kar, Ms. Nikita Singh, Ms. Shivani Chaudhary, Mr. Deeptarko Roy, Mr Narindra Kumar, Mr. Krishna Pal, Er. Naveen Chaurasia, Er. Swati Singh, Mr. Sudheer, **Mr. Arpit Verma, Mr Ajeet Singh** and **Mr. Nirbhay Singh** and other lab members for a joyful and healthy environment around me to work and to be with me throughout the work.

I wish to express my reverence and sense of deep gratitude to **Prof. V V Ravikanth Kumar**, Head, Department of Physics, Pondicherry University for providing the characterization facilities. Also, I wish to express my reverence and sense of thankfulness to **Mr. Toton Haldar**, Senior Researcher, of same Department for doing the important characterization of my samples. I am also very thankful to **Ms. Laxmi Kumari**, **Mr. Amrendra Gautam** from University of Lucknow and **Mr. Jagjeevan Ram** from university of Delhi for research assistance.

Finally, I would like to pay my highest regards to my parents **Mr. Shri Ram** and **Smt. Radhika Devi**, , my elder sister **Mrs. Pushpanjali** and **Mrs. Shweta** and my elder brother **Mr. Abhishek Kumar** for understanding my dreams and always being there in part of up and down phases of life. I also want to acknowledge my cute nephew **Tejus** and my niece **Divisha** and **Trisha** for being a part of my life. Finally, I am also thankful to my close friends of Malkoti Ashram **Mr. Ratindra Gautam, Mr. Ravi Singh, Mr. Saty Prakash Bharti, Mr. Vimal Raj, Er. Narendra Singh** & **Mr. Shasi Sekhar Sonu Sharma** for being a part of this journey. I am thankful to all those helping hands that directly and indirectly encouraged me and helped me to complete my research work.

My final words of thanks will be for Bharat Ratna Dr. Bhimrao Ambedkar and almighty God, for their constant support and companionship through all turmoil of my life.

Utkarsh Kumar

(Ph.D. Scholar)

LIST OF PUBLICATIONS

Part of the thesis published and communicated in the refereed journals:

- **U. Kumar**, B. C. Yadav. **Development of humidity sensor using modified curved MWCNT based thin film with DFT calculations**, Sensors and Actuators B Chemical, 288 399-407 (2019).
- **U. Kumar**, B. C. Yadav. **Synthesis of carbon nanotubes by direct liquid injection chemical vapor deposition method and its relevance for developing an ultra-sensitive room temperature based CO_2 sensor**, Journal of Taiwan Institute of Chemical Engineering 96 652-663 (2019).
- **U. Kumar**, S. Sikarwar, R. K. Sonker, B. C. Yadav **Carbon Nanotube: Synthesis and Application in Solar Cell,** Journal of Inorganic and Organometallic Polymers and Materials 26 (6), 1231-1242 (2016).
- R. K. Sonker, M. Singh, **U. Kumar**, B. C. Yadav, **MWCNT doped ZnO nanocomposite thin film as LPG sensing** Journal of Inorganic and Organometallic Polymers and Materials 26 (6), 1434-1440 (2016).
- **U. Kumar,** B. C. Yadav, **State of Art: An Approach to the Synthesis of Pure and Doped Graphene.** Advanced Science, Engineering and Medicine, 10 638-643 (2018).
- **U. Kumar,** Ravikant Tripathi, B. C. Yadav, V. V. Tyagi, **Ultralow turn-on field emitter based on multiwalled carbon nanotubes grown by direct liquid injection chemical vapour deposition method with theoretical calculations**. Sensor and Actuator A Physical. **(Communicated)**
- **U. Kumar,** B. C. Yadav, K. Kumar, T. Haldar, V. V. R. Kumar, **Development of MWCNT/TiO_2 nanocomposite thin films for the detection of LPG and humidity at room temperature with theoretical calculations.** Sensors and actuators B Chemical **(Communicated)**
- **U. Kumar,** B. C. Yadav, C. K. Dixit, Pramod Yadawa, Synthesis of MWCNT/PPY nanocomposite using oxidation polymerization method and its employment in sensing such as CO_2 and humidity. Sensors and actuators B Chemical **(Communicated)**

Work not included in Thesis

- S. Singh, **U. Kumar,** K. Kumar, R. Tripathi, B. C. Yadav, K. Singh **Development of scattering based glucose sensor using hydrothermally synthesized cuprous oxide nanoparticles**. Results in Physics 15 102772 (2019)
- E. Singh, **U. Kumar**, R. Srivastava, B. C. Yadav**. Catalytic growth of CNT on different substrates and its application as Optoelectronic Humidity Sensor**. Carbon Letter. (2019) **DOI** https://doi.org/10.1007/s42823-019-00090-4
- A. Gautam, **U. Kumar,** B. C. Yadav, C. R. Gautam, **Synthesis and structural analysis of graphene-reinforced h-BN solids for LPG sensing applications.** Material Research Express (2019) **DOI** https://doi.org/10.1088/2053-1591/ab5c6c
- K. Kumar, **U. Kumar**, M. Singh, B. C. Yadav, **Synthesis and characterizations of chemically reduced exohedral functionalized Graphene Oxide with iron nanoparticles and its application for the detection of the humidity**. Journal of Materials Science: Materials in Electronics. 30 (14) 13013–13023 (2019)
- J. Ram, R. G. Singh, F. Singh, V. Kumar, V. Chauhan, R. Gupta, **U. Kumar**, B. C. Yadav, R. Kumar **Development of WO_3-PEDOT:PSS hybrid nanocomposites based devices for liquefied petroleum gas (LPG) sensor.** Journal of Materials Science: Materials in Electronics. 30 (14) 13593–13603 (2019)
- E Singh, **U. Kumar,** R Srivastava, B. C. Yadav **Carbon Nanotubes Based Thin Films as Opto-Electronic Moisture Sensor** Advanced Science, Engineering and Medicine, 10 638-643 (2018)
- T. Haldar, **U. Kumar,** B. C. Yadav. V. V. R. Kumar, **Tunable negative permittivity of Bi_2O_3-SiO_2@MWCNT glass-nanocomposites at Radio frequency region.** Composite Part B. **(Communicated)**
- K. Kumar, **U. Kumar**, A. Singh, B. C. Yadav. **The beauty inhabited inside the modified Graphene for the moisture detection at different frequencies.** Carbon Letters **(Communicated)**
- M. Singh, B. C. Yadav, **U. Kumar**, A. Ranjan, M. Kaur, R. Srivastava. **Fabrication of nanostructured lead-free bismuth sodium titanate thin film**

and its liquefied petroleum gas sensing. Sensors and actuator A Physical **DOI** DOI: 10.1016/j.sna.2019.111765 (2019).

- J. Ram, R. G. Singh, V. Kumar, F. Singh, V. Chauhan, R. Gupta, **U. Kumar**, B. C. Yadav, R. Kumar **Ion beam induced modifications in WO_3-PEDOT: PSS hybrid nanocomposite thin films for LPG detection at room temperature** Optical Material **(Communicated)**

Papers presented in International Conference/Proceedings

- **U. Kumar,** B. C. Yadav, Synthesis of MWCNT/TiO_2 using DLICVD method and its application as LPG sensors, "**POLY-CHAR 2019**" 19^{th} -24^{th} April 2019, **Tribhuwan University, Kathmandu Nepal.**
- **U. Kumar,** B. C. Yadav, Synthesis and functionalization of MWCNT and its application as CO_2 sensor, "**International Conference on Renewable Energy for Sustainable Environment: Challenges and Remedies"** 20^{th}-21^{st} March **2017, SMVDU, Katra, Jammu & Kashmir.**
- **U. Kumar,** B. C. Yadav, Synthesis of carbon nanotubes and its application as gas sensor, **International Conference on Nanoscience and Nanotechnology (ICNN,** September 22-24 **2017).**
- **U. Kumar,** B. C. Yadav, Synthesis of carbon nanotube using chemical vapor deposition technique, **International Conference on "Plasma Science, Technology and Application",** 20-21 January **2016, Amity University, Lucknow.**
- **U. Kumar,** B. C. Yadav, **Poster presentation** at the **International Conference on "Environmental System and Sustainable Development" CTBC, Shirur and SPPU,** 15-16 January**, 2016, Pune.**
- **Workshop on Nano Science and Life (under the auspices of UGC Networking Programme) 26^{th} February – 2^{nd} March, 2015, BHU, Varanasi.**
- **U. Kumar,** B. C. Yadav, Synthesis of carbon nanotube and its application as solar cell **3^{rd} International Conference on Nanostructured Materials and Nanocomposites (ICNM 2015)** 12-14 December 2015**, HCST Mathura.**

Papers presented in National Conference/Proceedings

- **U. Kumar,** B. C. Yadav, Chemical vapor deposition an approach for synthesis of nanomaterials, National Seminar on **सूक्ष्म पदार्थ एवं सम्बद्ध चेतन ऊर्जा,** 01 – 03rd February, 2019, BBAU, Lucknow.
- **U. Kumar,** B. C. Yadav, Synthesis of CNT and its application as humidity sensor with DFT calculations, Indian Science Congress (ISC 106)
- **U. Kumar,** B. C. Yadav, Synthesis of MWCNT and its application as field emission devices, **National Seminar on Nano Science and Nano Biotechnology,** 25th – 26th February**, 2017, DAVC, Kanpur.**
- **U. Kumar,** B. C. Yadav, Synthesis and doping of Graphene**, National Conference Recent Advance and Innovative Material Science (RAIMS 2017, February 22-24).**
- **U. Kumar,** B. C. Yadav, Synthesis of carbon nanotube and its application as toxic gas detection, **3rd Lucknow Science Congress and National conference on 'Science for Society: An Interdisciplinary Approach'** organized by **B.B.A.U.** Lucknow during October 31st – November 2nd **2015**.

ABSTRACT

In human history, technology and the gathering of scientific information seems to have progressed in a more or less exponential, self-enhancing manner. This has certainly been true after the enlightenment when in the world, the gain in scientific knowledge and technology mastery that has been enabled by it has spurred on the development of the natural sciences when itself is helping to create new technologies to better exploit our resources and create new opportunities. From the early days of cross-ocean ship travel, through the industrial revolution in the part of the 18^{th} century to the internet age, the frequency of technological revolution has increased and will likely increase further through the 21^{st} century, global resources permitting. Today, we stand at the beginning of what looks like a scientific and technological revolution: the age of nanotechnology. This holds the promise of enabling us to manipulate material at the nanometer scale, resulting in tools and technologies never dreamt of in earlier centuries, from the nanomaterial-based sensor, solar cells to high-performance nanocomposites, Nanotechnology opens up new frontiers for innovation in electronics medicine and material, etc.

A leading thread in the unfolding story of nanotechnology is carbon nanostructures, the discovery and research of which has significantly contributed to shape the route that science at the nanoscale has taken. These carbon nanostructures include fullerenes, carbon nanotube and graphene. All of these nanostructures are composed entirely of sp^2 hybridized carbon atom forming different structures, from tubular carbon sheet: carbon nanotube to soccer ball type structure: fullerenes. The physical and chemical properties of these materials vary with their atomic structure. From the earliest theoretical investigation in the electrical, chemical and physical property of graphene and carbon nanotube, it becomes very clear that the graphene and carbon nanotube have some unusual properties such as very high electrical conductivity with highly thermally stable atomic structure. Now from last two decades, a more and more extraordinary properties of graphene and carbon nanotubes have come in the light, for example, the high charge carrier mobility of graphene and carbon nanotubes, exceptional mechanical properties, such as Young's modulus higher than 1Tpa for CNTs

and similar values for graphene and fullerene. With the discovery of more and more of their exotic properties the incentive for further research and the promise for practical applications of these materials become even greater.

The evolution of the research into carbon nanostructures has also shown a self-enhancing character, in part due to the highly interconnected character of this field of research and the fact that experts and research groups in the fieldwork on various nanostructures simultaneously. The discovery of fullerenes in 1985 paved the way and provided the context for the discovery of carbon nanotubes and later the discovery of graphene.

There are seven chapters in the Thesis and a brief outline of its contents is as follows:

Chapter 1: This chapter contains the basic introduction of different types of carbon nanostructures. The detail information of the synthesis of carbon nanomaterial with the advantage of chemical vapor deposition method over other synthesis methods. Further, the chapter provides the application of carbon nanotubes in various fields like humidity sensing, gas sensing, photo sensing and field emission devices.

Chapter 2: This chapter includes the synthesis of MWCNT at different temperatures and studies the effect of temperature on field emission property along with the photosensing property. The synthesized material was then investigated using SEM, XRD and UV-visible absorption technique. The dilute solution of the material was analyzed using TEM and particle size analyzer. Field emission current for both the samples were calculated. The emission of photocurrent at room temperature through thin film was also calculated. Sensitivity along with response and recovery time were investigated. The experiment was repeated from time to time to check the repeatability, response and recovery times. The material synthesis at different temperature was employed in a field emission device to observe the field emission capability of the material. Experimental data were verified by theoretical data using DFT calculations.

Chapter 3: In this chapter, the synthesis and development of humidity sensor using modified curved MWCNT based thin film with DFT calculation have been reported. The MWCNTs was then investigated using SEM, XRD, UV-visible absorption techniques,

FTIR, Raman and particle size analyzer. The MWCNT based thin film was employed as a humidity sensor to observe the humidity sensing potential of the film. Sensitivity along with response and recovery time was calculated. Experimental data were verified by the theoretical data using DFT calculations.

Chapter 4: This chapter describes the CO_2 sensing capability of MWCNT based sensor. f-MWCNT was synthesized using DLICVD technique HNO_3 and H_2SO_4 was used as functionalizing materials. The f-MWCNT was then investigated using SEM, XRD, FTIR and Raman spectrophotometer. The average pore size of the film was calculated by using BET. The maximum sensor response of the sensor was found as 2.1 at 5000 ppm.

Chapter 5: In this chapter, synthesis of modified MWCNT with PPY has been reported. Thin film of the synthesized material was prepared on various substrate and it was investigated by using SEM, TEM, XRD, UV-visible spectroscopy and Particle size analyzer. Optimized thin film was employed as room temperature CO_2 sensor to observe the CO_2 sensing potential. Sensor response along with response and recovery time was calculated. Sensor response was found improved 4 times with the previous reported data chapter 4. Experimental data were verified by theoretical data using DFT calculations.

Chapter 6: This chapter includes two parts Part A and part B. Part A reports the effect of LPG on the resistance of MWCNT/ZnO based thin film at room temperature. The film was then investigated using SEM, TEM, FTIR and UV-visible spectroscopy. The average particle size of the material was calculated by using particle size analyzer. The highest sensor response was found as 60 at 2 vol%. Part B reports the synthesis of MWCNT/TiO_2 composite film by DLICVD technique. The prepared film was characterized using various techniques SEM, TEM, FTIR, UV etc and further it was employed as LPG sensor. The sensitivity and sensor response of the sensor were found improved over the sensor fabricated with MWCNT/ZnO.

Chapter 7: This chapter summarized the entire work of the Thesis with concluding remarks and future scope of MWCNT and its nanocomposite in various fields for gas, humidity and photo sensing.

PREFACE

Over the past few decades, humidity and gas have acquired much importance. Humidity refers to the water in gaseous form, therefore, obeys gas laws. Humidity is one of the fundamental biotic factors that decide the habitat of a particular plant or animal. Humidity monitoring is important for weather forecasts, also as it is not only itself a climate variable but also interacts with other climate variables sturdily. At high humidity if the surrounding is warmer than the body temperature, the condition of hyperthermia, fatigue and loss of concentration may occur; whereas some respiratory disorders may be tracked through humidity concentration in breath.

Due to day by day increase in air pollution and the global warming, there is a great deal of interest for developing a gas sensor for checking air pollution, detecting harmful gases, monitoring other agro based products, home safety and hand held breath analyser etc. Lot of research work has been done on miniaturization of gas sensor which is economically cheap with high sensitivity, good sensor response and least response time and recovery time. There are various n-types and p-types metal oxide semiconductors gas sensor like ZnO, TiO_2, NiO, SnO_2, CuO, In_2O_3, Fe_2O_3 etc available in the market for the detection of harmful gases. However, after literature survey, I found that there is very less work done on design and development of a LPG and CO_2 sensors operable at room temperature (300 K). The main goal of the present investigation is to design and fabricate a LPG sensor which would be robust, more sensitive with reduced response time, economically cheap and easy to fabricate than previously reported sensors. For this purpose, we have focused on synthesis of carbon nanomaterials which possess twin behaviour having a high surface area with tubular structure and enhanced sensing features for the detection of LPG and CO_2 at room temperature. MWCNT, Modified MWCNT, Polymer functionalized MWCNT and metal oxide doped MWCNT were prepared by various chemical method and MWCNT was synthesized by DLICVD technique. Further, the structural, morphological and optical properties of the nanomaterials were optimized and LPG, CO_2, humidity and photo sensing applications were carried out.

The present thesis is divided into seven chapters. Chapter 1 contains the introductory part of synthesis of carbon nanomaterials and application in various fields. It

also focuses on the detailed description of synthesis of carbon nanotube and its sensing applications. A detailed investigation including synthesis, characterization and application as field emitter and photo sensor on multiwall carbon nanotube is depicted in Chapter 2. In Chapter 3, the synthesis, characterization and humidity sensing property of modified MWCNT are reported. Chapter 4 describes the fabrication of f-MWCNT thin film using ethanol as carbon precursor and its application as CO_2 sensor at room temperature. Chapter 5 reports the synthesis of MWCNT/PPY nanocomposite using oxidation polymerization method and its application as CO_2 and humidity sensor at room temperature. Chapter 6 reports the effect of LPG on the resistance of MWCNT/ZnO based thin film at room temperature. It also reports the enhanced sensitivity and sensor response of the sensor by doping of MWCNT with TiO_2. A summery of study of synthesis, characterization with gas, photo and humidity sensing properties of MWCNT, f-MWCNT and their nanocomposites have been reported in Chapter 7. This chapter also gives the guidelines for further scope of research work in the field of field emission gas and humidity sensing.

LIST OF ABBREVIATIONS

S. No.	Name Compound	Full Name
1.	MWCNT	Multiwall Carbon Nanotube
2.	SWCNT	Single Walled Carbon Nanotube
3.	DLICVD	Direct Liquid Injection Chemical Vapor Deposition
4.	f-MWCNT	Functionalized Multiwall Carbon Nanotube
5.	NMP	N-Methyl Pyrrolidone
6.	LPG	Liquid Petroleum Gas
7.	LEL	Lower Explosive Limit
8.	PPY	Poly Pyrrol
9.	NPs	Nanoparticles
10.	XRD	X-Ray Diffraction
11.	SEM	Scanning Electron Microscope
12.	FE-SEM	Field Emission-Scanning Electron Microscope
13.	UV-vis	Ultra Violet-Visible spectroscopy
14.	TEM	Transmission Electron Microscope
15.	AFM	Atomic Force Microscope
16.	FTIR	Fourier Transformation Infrared Spectroscopy
17.	EDX	Electron Dispersive X-ray
18.	EPMA	Electron Probe Micro Analyzer

19.	BET	Brunauer-Emmett-Teller
20.	BJH	Barrett-Joyner-Halenda
21.	DFT	Density Functional Theory

LIST OF TABLES

LIST OF FIGURES

APPENDIX: EXPERIMENTAL METHODS AND CHARACTERIZATION TECHNIQUES

LIST OF APPENDICES

TABLE OF CONTENTS

CHAPTER 1

INTRODUCTION AND AIM OF PRESENT RESEARCH WORK

This chapter contains the basic introduction of different type of carbon nanostructures and their roles in different type of sensing application have also been discussed. This chapter also provides detail information of the synthesis of carbon nanomaterial and the advantage of chemical vapor deposition method over other synthesis methods. The chapter provides the application of carbon nanotubes in various fields like humidity sensing, gas sensing, photo sensing and field emission devices. The chapter also introduces the detailed information about the ongoing research on carbon nanomaterials in the field of sensors.

CHAPTER 1

Introduction and aim of present research work

1. Introduction

In human history, technology and the gathering of scientific information seems to have progressed in a more or less exponential and self-enhancing manner. This is certainly been true after the enlightenment when in the world, the gain in scientific knowledge and technology mastery that has been enabled by it has spurred on the development of the natural sciences. This itself helping to create new technologies to better exploit our resources and create new opportunities. From the early days of cross-ocean ship travel, through the industrial revolution in the part of the 18^{th} century to the internet age, the frequency of technological revolution has increased and will likely increase further through the 21^{st} century. Today, we stand at the beginning of what looks like a scientific and technological revolution: the age of nanotechnology. This holds the promise of enabling us to manipulate material at the nanometer scale, resulting in tools and technologies never dreamt of in earlier centuries, from the nanomaterial-based sensor, solar cells to high-performance nanocomposites, nanotechnology opens up new frontiers for innovation in electronics, medicine and material etc.

A leading thread in the unfolding story of nanotechnology is carbon nanostructures, the discovery and research of which has significantly contributed to shape the route that science at the nanoscale have taken. These carbon nanostructures include fullerenes, carbon nanotube and graphene. All of these nanostructures are composed entirely of sp^2 hybridized carbon atom forming different structures, from tubular carbon sheet: carbon nanotube to soccer ball type structure: fullerenes. The physical and chemical properties of these materials vary with their atomic structure. From the earliest theoretical investigation in the electrical, chemical and physical property of graphene and carbon nanotube, it becomes very clear that the graphene and carbon nanotube have some unusual properties such as very high electrical conductivity with highly thermally stable atomic structure. Now from last two decades, a more and more extraordinary property of graphene and carbon nanotubes have come in the light,

for example, the high charge carrier mobility of graphene and carbon nanotubes, exceptional mechanical properties, such as Young's modulus higher than 1 TPa for CNTs and similar values for graphene and fullerene. With the discovery of more and more of their exotic properties the incentive for further research and the promise of practical applications of these materials become even greater.

The evolution of the research into carbon nanostructures has also shown a self-enhancing character, in part due to the highly interconnected character of this field of research and the fact that experts and research groups in the fieldwork on various nanostructures simultaneously. The discovery of fullerenes in 1985 paved the way and provided the context for the discovery of carbon nanotubes and later the discovery of graphene.

1.2 Motivation

The challenges of nanotechnology and carbon nanostructure research, in particular, can be addressed on two fronts, one of them is the preparation of carbon nanostructure, the other the investigation of their sensing application in various fields. In order to explore and harness the rich physics of carbon nanotubes, the new method is required to tailor their properties and current methods of sample investigation need to be adapted. This thesis is a contribution to the advancement of both of these goals, through the following studies:

- Exploring the cheapest method for synthesis of pure carbon nanotube using the chemical vapor deposition method.
- Introducing a sample preparation technique that solves the sample solubility issues and detection of humidity/Gas/Photo sensor at room temperature.
- Investigating the physical and chemical properties of carbon nanotubes with a different type of interaction using the computational methods.

In the introductory chapters, the properties of graphene, carbon nanotube and functionalized carbon nanotubes will be presented along with the relevant experimental investigation methods. Further the challenges faced in the investigation of the above three topics will be explored and the answered.

1.3 Carbon nanomaterials

Carbon in the form of coal has been the driving force of the industrial revolution. Today, carbon nanostructures are a significant part of another technological and scientific revolution. Fibrous carbon materials are already part of everyday life in the form of carbon reinforced composites. During the 1960s and 1970s carbon fibers have started out on the road to becoming an important industrial material and today they have found uses from sports equipment to vehicle parts, anywhere where low weight and high strength is required. Carbon nanotube and graphene promise even greater benefits if their extraordinary properties could be harnessed.

In the following sections, an introduction to the physical properties of carbon nanotube and graphene will be given. Since the electronic properties of carbon nanotubes can be derived from that of graphene, therefore, the properties of graphene will be discussed first.

1.3.1 Graphene

Graphene is a two-dimensional (2D) layer of the ordered sheet of sp^2 hybridized carbon in which carbons are extended in a honeycomb network with outstanding allotropes as shown in Fig. 1.1. It can be rolled into a single sheet to form carbon nanotubes and can also be wrapped to form fullerenes. Highly ordered graphene have extraordinary thermal, mechanical and electrical properties. The theoretical investigation of single-layered graphene first and foremost yielded access to a large amount of interesting physics. Initial studies include the observation of graphene ambipolar field effect [1], the quantum Hall effect at room temperature [2-7], measurement of extremely high carrier mobility [8-10] and even the first ever detection of single-molecule adsorption events [11-12]. These possibilities are implemented as applications of graphene into many other devices like thermally & electrically conductive reinforced composite, sensors, a transparent electrode and flexible display and solar cell using CNTs [13] and fullerenes [14, 15]. In past top-down approaches were used to produce high-quality samples but the method is neither high output nor high-yielding. So, there are number of approaches to form single sheet as they are connected by Van der Wall forces.

In present, people use Bottom-up approach to grow graphene directly on organic precursors and attempt to catalyzed growth in situ on the substrate. Both approaches have their drawback as in chemically derived graphene the modification such as complete exfoliation in solution is required to enhance the device performance [16, 17].

Graphene is a zero band gap semiconductor with extraordinary properties at room temperature. Use of the graphene in single electron transistor must contain some band gap, so the doping of graphene may be done by different types of chemical process and it behaves as an n-type or p-type semiconductor.

1.3.1.1 Band structure of Graphene

As predicted by the Wallace in 1947 [18], Graphene has a unique band structure and has a special 2D arrangement of atoms with two sp^2 hybridized carbon atom in one unit cell as shown in Fig. 1.2. The sp^2 carbon atom provides two orbitals; π and π^* to form valence band and conduction band respectively. These two bands are only allowed to touch at six points, called as Dirac points. Because of orthogonal condition, π and π^* do not overlap each other and they make the graphene a zero band gap semiconductor. At Fermi level, the Dirac-cone band structure has linear energy-momentum dispersion which is essentially important for the electron transport. Such a linear dispersion indicates that electron in graphene exhibits zero rest mass, which is equivalent to massless fermions in the relativistic Dirac equation [19].

1.3.2 Carbon nanotube

With the discovery of pure carbon structures, different from graphite and diamond, a new and fast-developing area in nanomaterial science began. In particular, tube-like structures were first reported by Iijima in 1991 [20]. The diameter of these carbon nanotubes is in the nanometer range, but their length can be in the micrometer range. Meanwhile, their mechanical properties have been studied by theoretical predictions and experimental measurements. Due to their structure and form, they tolerate extreme distortion without fracture. They also show elastic bending, twisting, buckling, and other reversible deformations. The bending stiffness is in the range of 0.4 TPa to 4

TPa. Furthermore, a local tension of hundreds of giga-pascals can be reached before the fracture occurs. Due to these properties, carbon nanotubes can be used to reinforce polymer composites. Here, they possess the potential for large increase in strength and stiffness in comparison to conventional carbon-fiber-reinforced polymer composites. Thus, nanotube-polymer composites have gained considerable interest in the materials research community.

As we know that the arrangement of graphene sheet folded in cylindrical form gives results in the shape of carbon nanotube which is much stronger and there are two possible high symmetric structures of carbon nanotubes known as zig-zag and armchair. In practice, it is believed that most of the carbon atoms does not have a highly symmetric form but few have it which is called as chiral structure. The honeycomb-shaped hexagonals are arranged helically around the tube axis.

The best way to define nanotechnology is "The design, characterization, production, and application of structures, devices, and systems by controlled manipulation of size and shape at the nanometer scale (atomic, molecular, and macromolecular scale) that produces structures, devices, and systems with at least one novel/superior characteristic or property".

1.3.2.1 Carbon nanotube structure and their properties

Graphene consists of different possible arrangement to form nanotube shown in Fig. 1.3 and it is given by the equation 1.1:

$$C = n\overrightarrow{a_1} + m\overrightarrow{a_2} \ldots\ldots\ldots\ldots\ldots (1.1)$$

Where a_1 & a_2 are unit cell based vectors, n & m are integers as found in the crystal lattice. Hence, if n≥m it forms armchair and if m=0 then it forms zigzag nanotube and the diameter of a nanotube is given by equation 1.2.

$$d = 0.246(n^2 + m^2 + nm)^{1/2} \ldots (1.2)$$

1.3.2.2 The Brillouin zone of nanotubes

The simplest model to construct the nanotube's Brillouin zone is the zone-folding method. This method takes into account only the confinement effect and neglects the contribution of curvature. The aforementioned rolling-up process is equal to the introduction of a periodic boundary condition along the circumference. The hexagonal Brillouin zone of graphene is shown in Fig. 1.4.

Deriving the nanotube from the graphene sheet has two main consequences; (i) the size of the first Brillouin zone in the direction related to the tube axis is determined by the translational period 't' as given in equation 1.3.

$$k_{\parallel} = 2\pi/t \ldots\ldots\ldots\ldots (1.3)$$

Due to the nearly infinite size of the nanotube in this direction, the wave vector is continuous.

(ii) The wave vector is quantized in the direction related to the circumference ($k\perp$) as a result of the periodic boundary condition is given by equation 1.4

$$\mathbf{k} \cdot \mathbf{c} = 2\pi l,\ k_{\perp} = \frac{2\pi}{c} l = \frac{2}{d} l \ldots\ldots\ldots\ldots\ldots\ldots (1.4)$$

where l has integer values : $l = -q/2 + 1, \ldots, -1, 0, 1, \ldots, q/2$, where q is the number of graphene unit cells in the nanotube unit cell and given by equation 1.5

$$q = 2 (n^2 + nm + m^2)/NR \ldots\ldots\ldots\ldots (1.5)$$

where N is the greatest common divisor of (n, m), and R = 3 if (n – m)/3N is an integer, and R = 1 otherwise. Thus the zone-folding method reduces the two-dimensional Brillouin zone of graphene to q equidistantly separated parallel lines. These lines are parallel to the direction related to the nanotube axis, and their lengths are determined by the translational period.

1.3.2.3 Metallic and semiconducting nanotubes

The allowed k-points in the Brillouin zone are confined to parallel lines in the zone folding approximation. The idea of the model is that the band structure of the nanotube is given by the graphene electronic energies along the allowed lines as shown in Fig. 1.5. The length and orientation of these lines are determined by the (n, m) pair of

integers. Although this approximation is rather crude, it provides us with many useful details about the electrical properties of nanotubes.

The most interesting property of nanotubes is that they can be metallic or semiconducting merely due to the way the carbon atoms are arranged on their surface. In the zone-folding picture, this essentially different behavior depends on whether any of the allowed *k*-lines cross the K-point. The allowed lines fulfill the condition. Their properties are governed by the (n, m) indices through the chiral vector **c**. The coordinate of the K-point is $(1/3k_1, -1/3k_2)$. The condition for a nanotube to be metallic is given by equation 1.6, 1.7, 1.8,

$$k.c = 2\pi l = 1/3(k_1-k_2)\,(na_1+ma_2) \quad \ldots\ldots\ldots (1.6)$$

$$l = 2\pi/3(n-m) \quad \ldots\ldots\ldots\ldots\ldots\ldots\ldots\ldots\ldots\ldots (1.7)$$

$$3l = (n-m) \quad \ldots\ldots\ldots\ldots\ldots\ldots\ldots\ldots\ldots\ldots\ldots\ldots (1.8)$$

This means that one-third of the nanotubes are metallic in an ensemble which contains all possible chiralities. Representation of the electronic structure through the density of states (DOS) is very common because it is equally understandable for scientists coming from either a physics or chemistry background.

The band structure and the possible energy levels of a single-walled carbon nanotube is depicted in this way, the analogy to chemical energy level diagrams is obvious. The vertical axis is the energy of the electronic states and the horizontal axis on the DOS figures on the right is the number of allowed states having that energy.

The band structure of metallic nanotube in which the crossing bands at the Fermi level results in an infinite density of states and metallic behavior. The other non-crossing bands cause Van Hove singularities. The band structure of semiconducting nanotube in which there are no allowed states at the Fermi energy, the tube behaves as a semiconductor. Van Hove singularities appear at the band minima and maxima as a result of the 1D electronic system.

At the flat maxima and minima in the band structure, many *k* values correspond to the same energy and the number of allowed states shows an abrupt increase; these spikes are called Van Hove singularities and are analogous to discrete molecular energy levels. This structure is the consequence of quantum confinement of the electrons within the graphene sheet in the radial direction. At the same time, there is a continuous

background in almost the whole energy range, corresponding to the electronic states on the surface of even one single nanotube, which behaves like a solid. This continuous background is finite at the Fermi level for metallic tubes, where the bands cross, but the number of states is less due to the steeper dispersion. For semiconducting tubes, there are no allowed states at the Fermi level and the highest occupied and lowest unoccupied states are those of the first Van Hove singularities. The distance between these two levels depends inversely on the diameter.

1.4 Synthesis of carbon nanomaterial

1.4.1 Synthesis of Carbon nanotube

Carbon nanotubes are produced by three main techniques; arc discharge, laser ablation and chemical vapor deposition. Growth of CNTs by arc discharge and laser involve the addition of carbon dimers (C_2) to the CNT edges. Sometime CNTs are also prepared by flame synthesis using camphor or mesh-like structure [14]. In the arc discharge process, the atmosphere of inert gas or some carbon-containing gas is created by an arc discharge between two carbon electrodes [21] with or without the catalyst. In the laser ablation technique, a high power laser beam impinges on a volume of carbon-containing feedstock gas. Laser ablation produces a small number of clean nanotubes [22], whereas the arc discharge method generally produces large quantities of impure CNTs. CVD results in MWCNTs or poor quality SWCNTs. The SWCNTs produced with CVD have a large diameter range.

1.4.1.1 Different Mechanism of Synthesis

1.4.1.1.1 Growth Mechanism

Nanotubes are formed by a gas phase process which starts with evaporated gas from the source of carbon; gases will be evaporated from a surface due to heating by laser pulses or through heating by arcs or solar radioactive fluxes. Each technique has a common aspect and they have numerous proposed mechanism for the formation of SWCNT. Such process consists of three steps; firstly the formation of a precursor consisting of some metal nanoparticles that provide the nucleation point at high

temperatures then dissociation of gas takes place. Later the carbon atoms are deposited on the nucleation point and the growth will start in two ways: in root growth, the catalyst will be placed at the bottom of the tubes and in tip growth, the catalyst will at the top of the tubes (Fig. 1.6).

1.4.1.1.2 Reaction Mechanism

Carbon nanotubes are also formed by reactions, in which the hydrocarbon molecules are decomposed on free Ni, Co metal surface, producing carbon atom with the simultaneous evolution of molecular hydrogen. Growth of carbon nanotubes and nano-fibers are based on decomposition on supported Ni crystal by magnetometric using methane. This is due to the reason that high electrons as carriers are generated at a high temperature which creates nucleation point for the growth of nanotube. Carbon atoms are decomposed from methane gas and deposited on the surface of Ni particle dissolved into bulk and form sub-stoichiometric nickel carbide at the early stage. This carbide phase then decomposes into metallic nickel particle and outside graphite layers which encapsulate the host nickel particles. The metal particle is then squeezed out by a strong pressure buildup due to the formation of the graphite layer at the internal surface of the graphite envelope. This is possible because of the liquid-like behavior of the metal due to melting point depression from the dissolution of carbon atoms that remained in the bulk; the fresh surface of the squeezed out Ni particle will further decompose the methane and continues the growth of carbon nanotube.

1.4.1.2 Different Synthesis Techniques

1.4.1.2.1 Arc-Discharge

In this method, under the inert atmosphere, carbon vapor is created by an arc discharge between two carbon electrodes [21] with or without the catalyst. The arc discharge method initially used for producing C_{60} fullerenes [22], is the most common and easiest way to produce carbon nanotubes. However, these techniques produce a mixture of components and require to extract the nanotubes from the soot and the catalytic metals present in the basic product.

This method produces nanotubes through arc-vaporization by two carbon rods [23] placed end to end with distance at approximately 1 mm and the chamber is usually filled with the inert gas (helium/argon) at low pressure (between 50 and 700 bar). In recent investigations, it is found that production of carbon nanotubes in liquid nitrogen, deionized water and NaCl solution is also possible. A direct current of 50–100 Å driven by ~20 V creates a high-temperature discharge of 2000–3000 ℃ between the two electrodes. The discharge vaporizes from one carbon rod and deposited on the other rod. The yield of nanotubes depends on the uniformity of the plasma arc and the temperature of the deposit form on the carbon electrode. Synthesis of CNTs by the discharge method using different conditions is presented in Table 1.

Table 1 describes how the nanotubes were formed by changing the surroundings of the arc discharge chamber and material used in the electrode. For high yield and purity of CNTs, fullerenes etc. Y/N_2 and CaC_2 were used under a helium atmosphere. Carbon onions, MWCNT and SWCNTs were prepared by using the deionized water in liquid arc discharge method. The nanotubes obtained during this process are usually short in range with the diameter for ranging from 0.6 to 1.4 nm for single-walled and 10–14 nm diameter multi-walled nanotubes. These tubes can be single walled tubes or multiple walled nanotubes, depending on whether the catalyst is placed in a rod or not. This method is relatively easy to implement and has a yield of ~30 %. The nanotubes produced in such process having high impurity and large defects, in comparison with another method; and lengths of the tubes are somewhat random. Both the single-walled nanotubes and multi-walled nanotubes created by this method are to be decided by the synthesis process followed by the doping of Ni/Co in anode which yields the SWCNT and the use of pure graphite rod without any doping yields the MWCNT (Fig. 1.7).

1.4.1.2.2 Laser Ablation

Standard laser ablation process occurs in a tubular furnace in which a block of graphite mixed with the catalytic metals such as Ni, Co, Pt etc. is heated from 700 to 1500 K. The graphite block is then targeted with a high energy laser and argon (Ar) gas is pumped in the direction of laser. As laser ablates the target, carbon nanotubes are formed and carried by the gas flow into a cooled copper collector.

The mechanism for the formation of the nanotube is same as the arc discharge in which the laser will penetrate the target material and the vapor of carbon is created inside the chamber which will grow on the cooled copper collector by growth mechanism. This process may not be easily implemented, but the high heating furnace is required for yield up to 70 %.

Table 2 describes the production of nanotubes by using different types of lasers with varied target materials and atmosphere. Power and intensity of laser source cause the phenomenon of ablation which gives CNTs of different diameters and lengths.

1.4.1.2.3 Chemical Vapor Deposition

A typical CVD process involves a substrate, which is exposed to one or more volatile precursors, placed in the quartz tube and heated to the desired growth temperature. Carbon carrying gas is flowing through the quartz tube with a predetermined flow rate and temperature. After the growth mechanism, the furnace is slowly cooled down and the wafer is inspected for the nanotube growth.

Table 3 describes the synthesis of CNTs by using different substrates in CVD chamber by the variation of temperature and carbon containing gases in which the lowest growth is found at 650℃ using CO_2, but in this case, the gas released is very toxic. To avoid the formation of toxic gases, methane gas is used for this synthesis which easily gets hydrolyzed. These techniques were first used for the silicon substrate to grow single-walled nanotubes [61]. The CVD process [54, 60, 62, 63] has also gained the popularity for pure SWCNT growth (Fig. 1.9).

1.4.1.3 Precursor

Carbon-containing compounds have been used as precursors and the most common ones are: carbon monoxide (CO) [58, 62, 63], methane (CH_4) [64], ethylene (C_2H_4) [60], acetylene (C_2H_2) [65], benzene (C_6H_6) [57], toluene (C_7H_8), ethanol (C_2H_5OH) [56], and methanol (CH_3OH). Each gas decomposes at different temperatures, cause to grow nanotubes. Sometimes the rate of dissociation will be controlled by the pressure of the gases such as CO, which will dissociate more at high pressure and causes

to increase the yield of nanotubes. The flow rate causes the growth of nanotubes; sometimes larger nanotube will be formed at slow flow rate in comparison to higher flow rate. Sometimes a carbon precursor also produces unwanted nanotubes by premixed gas in the cylinder, therefore, for producing well aligned or well-controlled nanotubes, a gas filter or sometimes cleaning gas is used in the CVD chamber.

1.4.1.4 Functionalization of CNTs

CNTs have inert surface property, but they are generally insoluble in the solvent because of strong Vander Wall interaction that tightly holds them together forming bundles. For many other applications, the solubility will increase by some modification called functionalization. The functionalization method will be categorized into two following major groups:

1.4.1.4.1 Inside Functionalization (Endohedral)

In this, nanoparticles of different materials are filled inside the nanotubes for functionalization, which can be achieved by spontaneous penetration of exploiting the situation where nanotubes are filled with colloidal suspensions. This process followed by the capillary action of the tubes; or by wet chemistry, when the nanotubes are filled with some compounds, they will react at a particular temperature and pressure after several circumstances resulting the nanoparticle trapped inside the nanotube [66, 67].

1.4.1.4.2 Outside Functionalization (Exohedral)

This group can also be subdivided into three subgroups based on the mechanism of attachment in which the different groups or compounds are attached to the sidewall of the nanotubes:

(i) Covalent functionalization in which the functionalization group is attached either on the defect side or at the end of the nano tubes [68, 69].

(ii) Covalent functionalization through ‘‘sidewall functionalization’’ [70, 71].

(iii) Non-covalent exohedral functionalization in which the nanotubes are wrapped inside the polymer [72, 73].

Table 4 describes the different methods of functionalizing the nanotubes and their applications in a different field with various advantages and disadvantages. The sidewall functionalization with cyclo and nucleophilic addition radical reactions is the best for solar cells.

1.5 Application as sensor

The sensor is a device that produces a measurable output as a function of provided input. They are useful for in-situ measurements such as in the industrial process, scientific applications, daily necessity, homes, offices, etc. They act as critical components in all measurement and controlled applications, responsible for converting any physical phenomenon such that temperature, pressure etc. into a measurable quantity through data acquisition (DAQ) system. It does not perform itself but acts as a part of the larger assembled system that may incorporate many other devices such as a transducer, detectors, data recorders, signal conditioners, signal processors, memory devices, actuators, etc.

Rapid growth in microelectronics and advancement in technology made machine more autonomous and intelligent day by day. It provoked a demand for artificial sensing organs which perform independently [75-76]. Thus people developed devices according to their requirement and now sensors are ubiquitously used in our daily lifestyle. 3S factor plays an important role in remarking a sensor as a good sensor and these three factors are sensitivity, selectivity and stability. Sensors can be classified into three types:

1- **Physical sensor**- A physical sensor is based on the measurement factor where no chemical reaction occurs. Measurement can be in the form of absorbance, temperature, mass, refractive index, conductivity, etc. Temperature sensor, Pressure sensor etc. are well known physical sensors [77-79].
2- **Chemical sensor** – A chemical sensor is a sensor in which analyte participate to perform a chemical reaction and give an analytic signal corresponding to the input. Various gas sensors and humidity sensors are well known chemical sensors [80-81].

3- **Biosensor**- Sensor that is used in biological applications is termed as biosensors. Immuno sensor, Microbial potentiometric sensor, etc. are the example of biosensors [82-83].

1.5.1 Chemical Sensor

Chemical sensors are a special variety of gas sensors, to detect and analyze which substance is present and in what concentration in our environment. With our senses, we can not only see, hear and feel but also smell and taste. Consequently, a chemical sensor is also known as artificial noses or artificial tongues. A chemical sensor interacts with the sample and transforms its chemical information to the analyst to produce analytically useful signals. The chemical information may be due to the chemical reaction of the analyte or due to physical measuring parameters of the system [84-86]. Many scientists gave their different definition for a chemical sensor according to their observations. It just concluded that the chemical sensor is an interface between the chemical world and the electronic. Or it is just the primary link of the measuring chain.

Chemical sensors consist of two important units a receptor part and a transducers part [87-89]. Sometimes few sensors are provided with separator also. Receptor part of a sensor is a chemical interface; there is an occurrence of chemical interaction of the analyte with a surface of the sample producing a change in its physical/ chemical parameters. The chemical information provided by the analyst is transformed into a desirable form of energy which is further measured by the transducer. The transducer part is a device which converts one form of energy to another accordingly [90-91].

1.5.2 Gas Sensor

The gas sensor is the sub class of the chemical sensor. In 1927, Oliver W. Johnson introduced an explosive gas indicator of a portable gas cylinder which was considered as the first commercial portable sensor which was not lesser than a miracle those days. This led to the beginning of fabrication of the sensor and its commercialization all over the world [92]. After that researcher developed various types of gas sensors such as electrochemical sensors, catalytic combustion sensors, calorimetric gas sensor, capacitive gas sensor, optical gas sensor, infrared sensors, and acoustic wave-based sensors, metal oxide based gas sensor etc. These sensors are applicable in various fields such as

chemical engineering, research and development, architecture, medical, pharmaceutical, agriculture, etc [93-94].

1.5.2.1 Classification of Gas Sensors

There are six types of gas sensors depending upon their transduction principle. They are as follows:

1. Electrochemical Gas Sensor
2. Acoustic Gas Sensor
3. Metal Oxide Gas Sensor
4. Colorimetric Gas Sensor
5. Capacitive Gas Sensor
6. Optical Gas Sensor

An electrochemical gas sensor consists of two major parts; first is electrolyte/ gel used and another one is anode and cathode based. The anode is responsible for all the oxidation process while the cathode is responsible for the reduction process. Due to this phenomenon current is created and positive and negative ions are developed. Positive ions flow towards the cathode rod and the negative ions flow towards the anode rod. The output is directly proportional to the concentration or partial pressure of the gaseous species. Nowadays in the electrochemical gas sensor, the liquid electrolyte is replaced by solid-state electrolyte but the whole working is the same [97-98].

The acoustic gas sensors are based on sound effects. These types of sensor consist of a piezoelectric substrate containing inter-digital electrodes. When RF voltage of particular frequency is given then the mechanical waves are produced in the piezoelectric substrate. These Rayleigh surfaces then propagate and type of acoustic waves are generated and its frequency is determined. The mechanical energy is converted into electrical RF voltage [99].

The metal oxide gas sensor is also called chemo-resistor gas sensor. Semiconductors are found to be very sensitive to the very low concentration of gas. This type of sensor requires stain gauze, thick film, thin film, etc. The capacitive gas sensor is used to detect a change in the capacitive behavior of the film by volatile analytes which

are proportional to the concentration of target analyte. The capacitive gas sensor gives the output signal by converting the capacitance of the film in the form of voltage.

The calorimetric gas sensor is used to detect the combustible gas present in the surrounding. Its principle is based on the change in temperature in the presence of gas. Generally, any substance burns at its ignition temperature, similarly the combustible gas also burns at their ignition temperature but the gas begins to ignite in presence of certain catalytic material even at very low temperature. This type of sensor is also called a catalytic sensor.

This sensor consisting of an optical fiber with palladium and titanium coating and was used for detecting hydrogen gas. The optical gas sensor gives higher sensitivity, stability, and selectivity than the non-optical gas sensor. Photons play an essential role in the optical gas sensor. They have residual mass with no charge so neither charge nor mass-based detection is done through it. This type of sensor is based on absorption and emission scattering of a gas species. An optical gas sensor consists of a light emitting element, optical fiber, a gas sensing element, a photodetector, and a filter for picking up fluorescence or phosphorescence phenomenon.

1.5.2.2 Applications of Gas Sensor

There are many applications of the gas sensor. Some of them are given below:

1. The gas sensor is used in process control industries.
2. They are used for fire detection to avoid any miss-happening.
3. They are used for environmental monitoring.
4. They are used in mines for the detection of harmful gases.
5. They are used as a breath sensor for detection of alcohol.
6. They are used for grading of agro-based in the coffee industry or tea industry.
7. They are used as boiler sensor
8. They are used in Atomic reactors.
9. They are used at home for safety purpose.

1.5.3 Humidity sensor

Humidity measurement can be done in diverse ways based on the measurement technique used. The most commonly used terms are — Absolute Humidity (AH) and Relative Humidity (RH). Absolute humidity can be measured by two modes: Parts Per Million (ppm) by weight or volume and Dew/Frost Point. Absolute Humidity (vapor density) is defined as the ratio of the mass of water vapor in the air to the volume of air. Its unit is grams per cubic meter or grains per cubic foot (1 grain = 1/7000 pound lb.) and expressed as Eqn. 1.9

Absolute Humidity (AH) = $\frac{m}{v}$…. (1.9)

where m is the mass of water vapor and V is the volume of air.

The relative humidity is defined as the ratio of the amount of moisture content in the air to the maximum (saturated) moisture level that the air can hold at the same temperature and pressure. The RH measurement is stated as percentage and obtained by the following expression given in Eqn. 1.10:

Relative Humidity (%RH) = $\frac{Q_1}{Q_2}$..... (1.10)

where Q_1 is the amount of water vapor present in a given volume of air at a given temperature and Q_2 is the amount of water vapor required to saturate the same volume of air at the same temperature.

RH being temperature dependent quantity hence called the relative measurement. Also, it can be expressed in terms of partial pressure as the ratio of the actual partial pressure of moisture content in the air (P_a) to the saturated pressure of moist air (P_s) at the same temperature (both in Bar or KPa), given in Eqn. 1.11:

Relative Humidity (%RH) = $\frac{P_a}{P_s} \times 100\%$ ..... (1.11)

Also, RH can be defined as the ratio of absolute humidity (AH) to saturation humidity (SH) as shown in Eqn. 1.12:

Relative Humidity (%RH) = $\frac{AH}{SH} \times 100\%$..... (1.12)

Parts Per Million by volume (PPMv) is defined as the volume of water vapor content per volume of dry gas, and Parts Per Million by weight (PPMw) is obtained by multiplying PPMv by the molar weight of water per molar weight of that gas or air. Dew point is defined as the temperature (above 0°C) at which the water vapor content of the gas begins to condense into liquid form, and Frost point is the temperature (below 0°C) at which the water vapor in a gas solidifies into ice. D/F point parameters are functions of the pressure of the gas, but independent of temperature and are amongst the absolute humidity measurements. In other words, the dew point is the temperature at which the saturation water vapor pressure is equal to the partial pressure of the water vapor (in an air atmosphere). The difference between the ambient temperature and the dew point temperature is a measure of the ambient relative humidity [100-111].

The most commonly used sensors are those that measure the variation in capacitance of a dielectric material [112] or the variation in resistance [113-114] of a conductive material as a function of RH. The principal sensor groups for humidity sensing thus include many resistive ceramics [115-118], organic polymers [119, 120] and resistive polyelectrolytes [121]. Although polymer sensors [117, 118, 119, 120] are of simple structure and low cost, however, they can measure only a limited range of moisture content and show hysteresis and drift at high humidity and they are relatively sensitive to chemical interference and dust deposition. Electrolytic sensors [121] require a constant flow rate for measurement. Also, the cell in which measurements are to be carried out requires regular-regeneration. This cell may be easily damaged by accidental water immersion. Infrared spectroscopy can also be used to measure RH. In infrared hygrometer [122, 123] absorption due to water vapor takes place at 2.6 μm and the split beam is used to compare sample cell and reference. Some other methods for humidity measurement are based on the surface acoustic wave (SAW) [124-127] and on microwave attenuation.

Also, there are certain parameters which decide the efficiency of a particular sensor at a particular place. These parameters depend upon the type of sensing element.

Some material that is efficient for a particular place may not be as good for some other place. The parameters of the humidity sensing are defined as below:

Sensitivity: It is the ratio of the change in the output signal (Impedance, capacitance, resitance, optical power etc.) to that of the input signal (%RH).

Accuracy: It is the conformity to a standardized reference signal.

Response time: It is the time required to reach 10% of the final sensor output after stepwise increasing the humidity.

Recovery time: It is the time required to reach 10% of the final sensor output after stepwise decreasing the humidity.

Drift: It is the change of the sensor output signal with time at a constant input signal.

Repeatability: It is the distribution of sensor outputs after when performing consecutive readings under similar conditions.

Reproducibility: It is the distribution of sensor outputs when measuring the same under different conditions.

Hysteresis: It is the difference in the output signal when measured for an up-trace and down-trace of the input signal.

Temperature dependence: It is the variation of sensor output with the temperature at constant humidity.

1.5.3.1 Types of Humidity Sensors

Humidity sensors are classified in the following groups:

- Electrical sensors
- Mechanical sensors
- Optical sensors
- Integrated sensors

The first group consists of sensors based on capacitive or impedance-type and measures the variation in capacitance or resistance of a dielectric material or conductive material respectively as a function of RH. The second group i.e. mechanical sensors consist of sensors based on strain-effects and mass-loading effects. The third and the most important group i.e. optical sensors, the variation of the optical signal in terms of transmission, reflection and quenching of electromagnetic waves is considered. The last group contains miscellaneous integrated humidity sensors that contain on-chip passive or electronic components for linearization, calibration, transmission etc. [128].

1.5.3.2 Applications of Humidity Sensors

Humidity sensors have revealed noteworthy significance in a broad range of applications [129]. Some of them are shown in Fig.1.15. Various techniques of humidity sensing have been employed to perform humidity measurements depending upon the need and type of application some of the important applications are as follows:

- Building and Construction
- Food Processing
- Agriculture
- Medical and health monitoring
- Fuel

1.5.4 Photosensor

Photosensors are the devices which to be used for converting light into electricity. A photodetector has a p-n junction that generates electron-hole pair when the photon emits on that device. There are so many modern techniques for the conversion of photons into electricity that affects our daily life. Photosensor is the main component or we can say the heart of any photodetector. On the basis of their mechanism the photodetectors are classified in the following:

Photoelectric effect: The photons generate free electron from the material by transitions from the conduction band. This effect is also used in so many devices such as:

- **Gaseous ionization detectors:** These are used in the experiment of particle physics to detect photons and particles with sufficient energy to ionize gas atom or molecules. Electron and ions generated by ionization cause current flow which can be measured.
- **Photomultipliers:** They contain a photocathode which emits electrons when photon are incident and these electrons are then amplified by a chain of dynodes.
- **Phototubes:** In such tubes, the current generated by the electrons of the cathode is directly proportional to light intensity.
- **Microchannel photodetector:** These are a type of silicon-based multiplier.

Thermal effect: The photon cause electrons to transition to midgap states then decay back to the lower band, introducing phonon generation and thus heat. Such effects are used in number of applications as given below:

- **Bolometer:** A bolometer is used to measure the power of incident electromagnetic radiation via heating a material with a temperature dependent electrical resistance. A microbolometer is a specific type of bolometer used as a detector in a thermal camera.
- **Cryogenic detector:** They are very sensitive to measure the energy of single X-ray, visible and infrared photons.
- **Pyroelectric detector:** They detect photons through the heat they generate and subsequent voltage generated in pyroelectric materials.
- **Thermopiles detector:** They detect electromagnetic radiation through heat, then generating a voltage in the thermocouple.

Polarization: Photons induce a change in the polarization states of suitable materials, which may lead to change in the index of refraction and other polarization effect and their applications are given as below:

- **Data storage:** The photorefractive effect is used in holographic data storage.
- **Linear polarization detector:** Polarization sensitive photodetectors use optically anisotropic materials to detect photons of a desired linear polarization.

Photochemical: Photons induce a chemical change in material and they are used in different applications as given below:

- **Photoreceptor cell:** The photoreceptor cell in the retina detect light through a rhodopsin photon-induced chemical cascade.
- **Photographic plate:** Such detector is used in photographic plate, in which silver halide molecule is split into an atom of metallic silver and a halogen atom. The photographic developer causes the adjacent molecule to split similarly.

There are certain parameters which decide the efficiency of a particular sensor at a particular place. These parameters depend upon the type of sensing element. Some materials that are efficient for a particular place may not be as good for some other place. The parameters of the photo sensing are defined as below:

- **Spectral response:** The response of the photodetector as a function of photon frequency.
- **Quantum efficiency:** The number of the carriers generated per photon.
- **Responsivity:** The output current divided by total light power falling upon the photodetector.
- **Noise equivalent power:** The amount of light power needed to generate a signal comparable in size to the noise of the device.
- **Detectivity:** The square root of the detector area divided by the noise equivalent power.
- **Gain:** The output current of a photodetector divided by the current produced by the photon incident on the detector.
- **Dark current:** The current flowing through a photodetector even in the absence of light.
- **Response time:** The time needed for a photodetector to go from 10% to 90% of the final output.
- **Noise spectrum:** The intrinsic noise voltage or current as a function of frequency. This can be represented in the form of noise spectral density.

The carbon nanomaterials such as graphene and carbon nanotube have been exhibiting the strong rectifying behavior and high photoresponsivity. Graphene couples with silicon quantum dots on the top of Si to form a photodetector. There are also some devices fabricated by using carbon nanotube which behaves as a photodetector. The main reason for showing the photosensitive property is the high conductivity and another is the tubular structure of the nanotubes which enhances surface conductivity for the generation of more photocurrent.

1.6 Application as Device

The carbon nanomaterial has extraordinary gas sensing, humidity sensing and photo sensing property, Due to these reason, they are widely used in device febrication.

1.6.1 Field Emission Device

We are living in an era of the energy crisis. Energy generation is an expensive process and if we save the generated energy, this can help in energy harvesting. Increasing demand for electronic devices having the display and cold emitters is using significant amounts of generating energy. Carbon-based field emitters are extensively investigated for better field emission devices [130-133]. Carbon nanotubes (CNTs) [134] have extraordinary physical, chemical, structural and mechanical properties. They are ideal quantum systems for exploring the one-dimensional physics and applications in a nanoscale device. The growth of CNTs is done by using so many different approaches like arc discharge, Laser ablation and chemical vapor deposition, but the chemical vapor deposition method is the best for synthesizing carbon nanotubes having high purity and high yield. CNTs have attracted worldwide attention because of having one-dimensional growth, high aspect ratio, and unique structural property, so they are also used in many electronic devices [132]. A variety of catalysts such as Au, Ag, PT, Fe, Mn, Mo and Mg are used for the growth of CNTs but the best growth is found by using transition metal catalysts like Fe, Co, Ni and the advantages of such catalysts are that they can easily be filtered from the nanotubes by the distillation process [134]. The excellent electrical conductivity and high optical transparency of carbon nanotubes based thin films prove their suitability to be used in electronic applications over the thin film fabricated by using

metal oxides and other nanomaterials having a low electrical conductivity and optical transparency [135, 136]. Also, due to such extraordinary and attractive properties of CNTs, they are used in a large number of devices and also replace the indium tin oxide (ITO) glass.

1.6.2 Solar Cell

In the present world, most of the energy is produced by fossil fuel, but they also produce very dangerous and hazardous gases like carbon monoxide, which pollutes the environment every second. Therefore for producing clean energy, we use solar energy which is eco-friendly and does not disturb the economic balance. For utilizing more and more solar energy, solar cells may be fabricated which converts solar energy into the electrical energy and this electrical energy may be stored in batteries through charging. Operation of a solar cell depends on the following factors:

- Absorption of light to create electron-hole pairs.
- Diffusion of charge carriers.
- Separation of electron and hole.
- Collection of charge carriers.

1.6.2.1 Efficiency

The efficiency of solar cells is categorized in different classes like thermodynamic efficiency, reflectance efficiency, charge carrier separation efficiency and reflectance efficiency. The overall efficiency of solar cells is the product of all these individual efficiencies. The solar cells usually have high voltage-dependent efficiency curves, temperature coefficients and shadow angles. Due to the difficulty in measuring these parameters directly, we use the ratio of powers to measure the efficiency of the solar cell. Solar cell efficiency (P) is defined as the ratio of output power to the input power

$$P = \frac{Output\ power}{Input\ power}$$

1.6.2.2 Mechanism of Solar Cell

The working of solar cells is based on the transition of free electrons by gaining the extra energy when photons are incident at the film surface. Now, after analyzing the band structure of the solar cell, Bu Jong et al. found that cell gains energy from the photons and generates free electrons, which recombines and generates some photovoltaic current so the binding energy of the film will decrease which indicates that the maximum number of electrons are generated. Therefore, for increasing the efficiency of the solar cell, thin film based method is used in which a large amount of light is absorbed for a broader range of the solar spectrum. Theory of solar cell is may be depicted in the following steps:

(1) Photons in sunlight strike the solar panel and are absorbed by semiconducting materials, such as silicon and germanium.

(2) Electrons are excited from their current molecular/atomic orbitals. Once excited, the electron can either dissipate their energy and return to its orbital or travel through the cell until it reaches to an electrode. Current starts flowing through the material to cancel the potential and these electricity is captured. Due to the special composition of solar cells, the electrons are allowed to move only in a single direction.

(3) An array of solar cells converts solar energy into a usable amount of direct current (DC) electricity. On analyzing those solar cells, it was found that the efficiency had increased by a little amount. Therefore, for further increasing the efficiency of the solar cell, carbon nanotubes were used in these cells which acts as a p-type semiconductor and silica acts as an n-type semiconductor and thus hetro-junctions were formed between silica and SWCNT as shown in Fig. 1.8.

From Fig. 1.8, we analyze that the CNTs act as p-type semiconductor and silica-based materials act as n-type semiconductor so the transition of electrons and holes start when hetero-junction would be formed establishing a certain band-gap between them. After emerging the light on such cell, the holes gain energy and transfer electrons from silica to CNT thus generating the photovoltaic current which is stored in the battery. After analyzing SWCNT, it was found that the absorption power was increased on

replacing the SWCNT to poly chiral MWCNT. The MWCNT absorbed a broad range of frequency spectrum in comparison to all other solar cells.

1.6.2.3 Thin Film Based Solar Cell

Thin film technique reduces the amount of material required for creating solar cells and most of the thin film based solar cells are manufactured by the sandwiching the thin film between two panes of glass to make a module. Cost comparison per unit power production between fossil fuel combustion and silicon solar cells was found to yield a large difference. The main component of these cells is a thin material coating. Fabrication of these solar cells requires a very low quantity of material (compared to silicon wafers, it is only 1%). This is the main reason why this technology is cheaper to some extent. The majority of this type of cells is made from amorphous silicon that is devoid of a crystalline structure. These are much cheaper fabricators but have a very low efficiency of about 8%.

Incorporation of nanomaterials into thin-film solar cells enhances the conversion efficiency at a lower cost. Nowadays, many nanomaterials are investigated for photovoltaic applications. The following are the three benefits of using nano-structured layers in thin-film solar cells:

(a) The effective optical absorption path becomes larger than the actual film thickness because of multiple reflections.

(b) There is a reduction in recombination losses due to the shorter path followed by light-generated electrons and holes. The absorber layer thickness in traditional thin-film solar cells is l μm, while in nanostructured solar cells it can be as thin as 150 nm.

(c) The energy band gap of different layers, made of desired design value, uses nanoparticles of various sizes. This allows more design flexibility in the absorber and window layers of the solar cells. ‘Al’ and ‘W’ are used as dopants for enhancing photovoltaic properties, Al-doped titanium dioxide and electrodes increase open circuit voltage (V_{oc}), but reduce short-circuit current (I_{sc}) [137].

Table 5 depicts the efficiency of synthesis techniques with the advantages and disadvantages of different types of solar cells. It can be seen that the efficiency of solar cell increases on incorporating the carbon nanotubes inside the cell. Bu-jong et al. had fabricated new solar cell by using Carbon nanotubes (CNTs) which is twice efficient for converting sunlight into electrical power than the previous one [138].

The other carbon nanomaterials like fullerene and graphene can also be used for the fabrication of solar cell as they show the photovoltaic properties by enhancing the absorption range. R.G. Shrestha et al. [139] synthesized one-dimensional (1D) single-crystalline fullerene C_{60} nanorods by using ultrarapid interfacial formation method at room temperature. The nanorods were of ~11 nm in diameter and ~215 nm in length with the hexagonal close-packed crystal structure. The optical transitions revealed the dominance of charge transfer excitonic transitions with excellent charge transfer characteristic. In another work, L.K. Shrestha et al. [140] reported the surfactant-triggered assembly of fullerene (C_{60}) into 3D flower-like microcrystals at the liquid-liquid interface following the growth of crystals using liquid-liquid interfacial precipitation (LLIP) method by layering surfactant solution. These microcrystals have a better future scope in solar cell based optoelectronic devices (Fig. 1.9). In another work [141], he synthesized macroporous and mesoporous fullerene crystals with bimodal pore architectures using the same (LLIP) method which can be used for the fabrication of nanodevices including organic solar cells.

Graphene is different from most 3-d materials. Intrinsic graphene is known to be a zero-gap semiconductor or a semi-metal. It has very high electron mobility, almost two times than that of Si thereby making it highly conducting. As well, since it causes a direct band gap, thus can absorb more photons in a much thinner region as compared to indirect bandgap semiconductors like Si. Graphene, having special optical properties, can be applied as transparent electrodes and interconnects the two subcells in tandem solar cells. It is a carbon sheet of one atom thickness, consisting of condensed six-member rings. The carbon atoms are sp^2 bonded and form a hexagonal 2D lattice. Ideal graphene has a very high carrier mobility of the order of 10^5 $cm^2/(V–s)$ at room temperature. This exceeds the carrier mobility of Silicon by one or two orders suggesting that graphene can be used as a

replacement for Silicon in nano-electronics. Besides its exceptional electrical properties, it has very high mechanical durability. Graphene also has a tunable bandgap. 3D graphene is known as graphite. It is the thinnest material with the highest strength; it is also highly transparent & highly conducting. This makes graphene an attractive option to form transparent electrodes in solar cells.

Thin-film photovoltaic materials are better than conventional solar-cell materials (such as silicon) because they are lighter, more flexible and cheaper to fabricate; working of these cells is based on the principle in which they absorb photons from sunlight and convert them into electron-hole pairs (or excitons). To generate electric current, an electron and hole must be rapidly separated before the two particles have a chance to come back together and be reabsorbed into the material. In solar cells, the exciton must quickly travel to another layer in the device (where the charge separation will occur) for the best light-absorption efficiencies.

Single-walled carbon nanotubes (SWCNTs) are ideal for thin-film photovoltaic material, as they absorb light across a wide range of wavelengths from the visible to the near infrared and possess charge carriers (electrons or holes) that move quickly. However, most thin-film cells containing SWCNTs have so far suffered from limited current and voltage, and therefore poor power conversion efficiencies [138].

1.7 Outline of the Thesis

There are seven chapters in the Thesis and a brief outline of its contents is as follows:

Chapter 1: The Chapter 1 contains the basic introduction of different types of carbon nanostructures and their role in sensing applications. This chapter also provides the detail information for the synthesis of carbon nanomaterial and the advantage of chemical vapor deposition method over other synthesis methods. The chapter provides the application of carbon nanotubes in various fields like humidity sensing, gas sensing, photo sensing and field emission devices.

Chapter 2: This chapter includes the synthesis of MWCNT at different temperatures and studies the effect of temperature on field emission property and its photosensing property. The synthesized material was then investigated using SEM, XRD and UV-visible absorption technique. The dilute solution of the material was analyzed using TEM and Particle Size Analyzer. Field emission current of both the samples were measured. The emission of photocurrent at room temperature through thin film was also observed. Sensitivity along with response and recovery time was calculated. The experiment was repeated from time to time to check the repeatability, response and recovery times. Both the materials were employed in field emission device to observe the field emission capability of the material. Experimental data were verified by theoretical data using DFT calculations.

Chapter 3: In this chapter, the synthesis and development of humidity sensor using modified curved MWCNT based thin film with DFT calculation have been reported. The MWCNTs was then investigated using SEM, XRD, UV-visible absorption techniques, FTIR, Raman and Particle Size Analysis. The MWCNT based thin was employed as humidity sensor to observe the humidity sensing potential of the film. Sensitivity along with response and recovery time was calculated. Experimental data were verified by the theoretical data using DFT calculations.

Chapter 4: This chapter includes the functionalization of MWCNT by HNO_3 and H_2SO_4 along with the CO_2 sensing. The f-MWCNT was then investigated using SEM, XRD, FTIR and Raman analysis. The average pore size of the material was calculated by using BET. This chapter also describes the effect of CO_2 on the resistance of f-MWCNT at room temperature. The highest sensor response of the sensor was found as 2.1 at 5000 ppm.

Chapter 5: In this chapter, synthesis of modified MWCNT with PPY has been reported. The film of the material was further investigated by using SEM, TEM, XRD, UV-visible spectroscopy and Particle Size Analyzer and further employed as room temperature CO_2 sensor to observe the CO_2 sensing potential. Sensor response along with response and recovery time was calculated. Sensor response was improved by 4 times then the

previous reported data. Experimental data were verified by theoretical data using DFT calculations.

Chapter 6: This chapter reports the effect of LPG on the resistance of MWCNT/ZnO based thin film at room temperature. The film was then investigated using SEM, TEM, FTIR and UV-visible spectroscopy. The average particle size of the material was calculated by using Particle Size Analyzer. The highest sensor response was found as 60 at 2 vol%. This chapter also reports the enhanced sensitivity and sensor response of the sensor by doping of MWCNT with TiO_2.

Chapter 7: This chapter summarizes the entire work of the Thesis with concluding remarks and future scope of MWCNT and its nanocomposites in various sensor for gas, humidity and photons.

References

[1] K. S. Novoselov, A. K. Geim, S. V. Morozov, D. Jiang, Y. Zhang, S. V. Dubonos, I. V. Grigorieva, A. A. Firsov. Electric Field Effect in Atomically Thin Carbon Films. Nat. Phys., 306, (2004) 666.

[2] K. S. Novoselov, E. McCann, S. V. Morozov, V. I. Fal'ko, M. I. Katsnelson, U. Zeitler, D. Jiang, F. Schedin, A. K. Geim. Unconventional quantum Hall effect and Berry's phase of 2pi in bilayer graphene. Nat. Phys., 2, (2006) 177.

[3] Z. Jiang, Y. Zhang, Y. W. Tan, H. L. Stormer, P. Kim. Quantum Hall effect in graphene Solid State Commun., 143, (2007) 14.

[4] Z. Jiang, Y. Zhang, H. L. Stormer, P. Kim. Quantum Hall States near the Charge-Neutral Dirac Point in Graphene Phys. Rev. Lett., 99, 2007) 106802.

[5] Y. B. Zhang, Y. W. Tan, H. L. Stormer, P. Kim. Experimental observation of the quantum Hall effect and Berry's phase in graphene. Nature, 438, (2005) 201.

[6] K. S. Novoselov, Z. Jiang, Y. Zhang, S. V. Morozov, H. L. Stormer, U. Zeitler, J. C. Maan, J. C. G. S. Boebinger, P. Kim, A. K Geim. Quantum Hall Effect in Metal Oxides and Graphene. Science, 315, (2007) 1379.

[7] B. Ozyilmaz, P. Jarillo-Herrero, D. Efetov, D. A. Abanin, L. S. Levitov, P. Kim. Electronic Transport and Quantum Hall Effect in Bipolar Graphene p-n-p Junctions Phys. Rev.Lett. 99, (2007) 186804.

[8] K. S. Novoselov, A. K. Geim, S. V. Morozov, D. Jiang, M. I. Katsnelson, I. V. Grigorieva, S. V. Dubonos, A. A. Firsov. Two-dimensional gas of massless Dirac fermions in graphene. Nature, 438, (2005) 197.

[9] S. V. Morozov, K. S. Novoselov, M. I. Katsnelson, F. Schedin, D. C. Elias, J. A. Jaszczak, A. K Geim. Giant Intrinsic Carrier Mobilities in Graphene and Its Bilayer. Phys. Rev. Lett., 100, (2008) 016602.

[10] M. Han, B. Ozyilmaz, Y. Zhang, P. Jarillo-Herero. Honeycomb Carbon: A Review of Graphene. Basic Solid State Phys., 244, (2007) 4134.

[11] F. Schedin, A. K. Geim, S. V. Morozov, E. W. Hill, P. Blake, M. I. Katsnelson, K. S. Novoselov. Detection of individual gas molecules adsorbed on graphene. Nat. Mater., 6, (2007) 652.

[12] K. Novoselov, A. Geim. The Rise of Graphene Mater. Technol., 22, (2007)178.

[13] U. Kumar, S. Sikharwar, R. K. Sonkar, B. C. Yadav. Carbon nanotube: synthesis and application in solar cell. Inorg Organomet polymer 26 (6), (2016) 1231.

[14] B. C. Yadav, R. Kumar, R. Srivastava, T. Shukla. Flame Synthesis of Carbon Nanotubes using Camphor and its Characterization. Int. J. Gr. Nanotechnol 3(3), (2011) 170.

[15] B. C. Yadav, R. Kumar. Structure, properties and applications of fullerenes Int J. Nanotechnol App 2(1), (2008) 15.

[16] S. S. Han, M. Wang, K. L. Wang, R. B. Kaner. A Chemical Route to Graphene for Device Applications. Nano Lett., 7, (2007) 3394.

[17] K. Gomez-Navarro, C. Weitz, R. T. Bittner, A. M. Scolari, M. Mews, A. Burghard, M. Kern. Electronic transport properties of individual chemically reduced graphene oxide sheets. Nano Lett., 7, (2007) 3499.

[18] P. R Wallace. The Band Theory of Graphite Phys. Rev., 71, (1947) 476.

[19] L. Liao, H. Peng, Z. Liu Diels−Alder. Chemistry Makes Graphene beyond Graphene J. Am. Chem. Soc., 136, (2014) 12194−12200.

[20] S. Iijima. Helical microtubules of graphitic carbon. Nature 354 (6348), (1991) 56.

[21] M. Wilson. Nanotechnology: basic science and emerging technologies. 2002: CRC Press, New York.

[22] P.G. Collins, P. Avouris. Nanotubes for electronics. Scientific American, 283 (6) (2000) 62.

[23] C. Journet, W. K. Maser, P. Bernier, A. Loiseau, M. Lamy de la Chapelle, S. Lefrant, P. Deniard, R. Lee and J. E. Fischer. Large-scale production of single-walled carbon nanotubes by the electric-arc technique. Nature, 388 (1997) 756.

[24] H. Qiu, Z. Shi, L. Guan, L. Lou, M. Gao, S. Zhang, J. Qiu and Z. Gu. High-efficient synthesis of double-walled carbon nanotubes by arc discharge method using chloride as a promoter. Carbon, 44 (2006) 516.

[25] J. L. Hutchison, N. A. Kiselev, E. P. Krinichnaya, A. V. Krestinin, R. O. Loutfy, A. P. Morawsky, V. E. Muradyan, E. D. Obraztsova, J. Sloan, S. V.

Terekhov and D. N. Zakharov, Double-walled carbon nanotubes fabricated by a hydrogen arc discharge method. Carbon, 39 (2001) 761.

[26] Y. Saito, T. Nakahira and S. Uemura. Growth conditions of double-walled carbon nanotubes in arc discharge. J. Phys. Chem. B, 107 (2003) 931.

[27] H. Huang, H. Kajiura, S. Tsutsui, Y. Murakami, M. Ata. High-quality double-walled carbon nanotube super bundles grown in a hydrogen-free atmosphere J. Phys. Chem. B, 107 (2003) 8794.

[28] M. Cadek, R. Murphy, B. McCarthy, A. Drury, B. Lahr, R. C. Barklie, M. Panhuis, J. N. Coleman, W. J. Blau, Optimisation of the arc-discharge production of multi-walled carbon nanotubes Carbon, 40 (2002) 923.

[29] S. J. Lee, H. K. Baik, J. Yoo, J. H. Han, Large scale synthesis of carbon nanotubes by plasma rotating arc discharge technique. Diamond Rel. Mat., 11 (2002) 914.

[30] H. W. Zhu, X. S. Li, B. Jiang, C. L. Xu, Y. F. Zhu, D. H. Wu, X. H. Chen. Formation of carbon nanotubes in water by the electric-arc technique. Chem. Phys. Lett., 366 (2002) 664.

[31] H. Lange; M. Sioda, A. Huczko, Y. Q. Zhu, H. W. Kroto, D. R. M. Walton, Nanocarbon production by arc discharge in water Carbon, 41 (2003) 1617.

[32] Y. L. Hwang, K. C. Chen, F. R. Kai. Production and in-situ Metal Filling of Carbon Nanotubes in Water. Adv. Mat., 13 (2001) 830.

[33] S. D. Wang, M. H. Chang, K. M. D. Lan, Ch-Ch. Wu, J. J. Cheng, H. K. Chang. Spontaneous formation of carbon-based nanostructures by thermolysis-induced carbonization of halocarbon Carbon, 43 (2005) 1778.

[34] M. V. Antisari, R. Marazzi, R. Krsmanovic. Synthesis of multiwall carbon nanotubes by electric arc discharge in liquid environments. Carbon, 41 (2003) 2393.

[35] N. Sano, J. Nakano, T. Kanki. Synthesis of single-walled carbon nanotubes with nanohorns by arc in liquid nitrogen. Carbon, 42 (2004) 686.

[36] T. Okada, T. Kaneko, R. Hatakeyam. Conversion of toluene into carbon nanotubes using arc discharge plasmas in solution. Thin Solid Films, 515 (2007) 4262.

[37] M. Ishigami, J. Cumings, A. Zettl, S. Chen. A simple method for the continuous production of carbon nanotubesChem. Phys. Lett., 319 (2000) 457.

[38] Z. Shi, Y. Lian, F. H. Liao, X. Zhou. Z. Gu, Y. Zhang, S. Iijima, H. Li, K. T. Yue, S. L. Zhang, Large scale synthesis of single-wall carbon nanotubes by arc-discharge method J. Phys. Chem. Solid, 61 (2000) 1031.

[39] H. J. Li, L. H. Guan, Z. J. Shi, Z. N. Gu, Direct synthesis of high purity single-walled carbon nanotube fibers by arc discharge J. Phys. Chem. B, 108 (2004) 4573.

[40] M. Yao, B. Liu, Y. Zou, L. Wang, D. Li, T. Cui, G. Zou, B. Sundqvist, Synthesis of single-wall carbon nanotubes and long nanotube ribbons with Ho/Ni as catalyst by arc discharge. Carbon, 43 (2005) 2894.

[41] Y. H. Wang, S. C. Chiu, K.M. Lin, Y. Y. Li. Formation of carbon nanotubes from polyvinyl alcohol using arc-discharge method. Carbon, 42 (2004) 2535.

[42] A. Szabó, C. Perri, A. Csató, G. Giordano, D. Vuono, J.B. Nagy. Synthesis methods of carbon nanotubes and related materials. Materials, 3 (2010) 3092.

[43] H. Zhang, Y. Ding, C. Wu, Y. Chen, Y. Zhu, Y. He, Y. Zhong, The effect of laser power on the formation of carbon nanotubes prepared in CO_2 continuous wave laser ablation at room temperature Physica B, 325 (2003) 224.

[44] E. Muñoz, W. K. Maser, A. M. Benito, M. T. Martinez, G. F. Fuente de la, Y. Maniette, A. Righi, E. Anglaret, J. L. Sauvajol. Gas and pressure effects on the production of single-walled carbon nanotubes by laser ablation Carbon, 38 (2000) 1445.

[45] S. Bandow, S. Asaka, Y. A. M Rao, L. Grigorian, E. Richter, P. C. Eklund, Effect of the growth temperature on the diameter distribution and chirality of single-wall carbon nanotubes Phys. Rev. Lett., 80 (1998) 3779.

[46] W. K. Maser, E. Muñoz, M. T. Martníez, A. M. Benito, Fuente de la. Study of parameters important for the growth of single wall carbon nanotubes Opt. Mater., 17 (2001) 331.

[47] M. Yudasaka, F. Kokai, K. Takahashi, R. Yamada, N. Sensui, T. Ichihashi, S. Iijima, Formation of Single-Wall Carbon Nanotubes: Comparison of CO_2 Laser Ablation and Nd:YAG Laser Ablation. J. Phys. Chem. B, 103 (1999) 3576.

[48] H. Kataura,Y. Kumazawa, Y. Maniwa, Y. Ohtsuka, R. Sen, S. Suzuki, Y. Achiba, Diameter control of single-walled carbon nanotubes. Carbon, 38 (2000) 1691.

[49] W. K. Maser, A. M. Benito, E. Muñoz, G. M. de Val, M. T. Martınez ,A. L. Fuente. CO_2-laser evaporation of various carbonaceous feedstock materials. Nanotechnology, 12 (2001) 147.

[50] T. Azami, D. Kasuya, T. Yoshitake, Y. Kubo, M. Yudasaka, T. Ichihashi, S. Iijima. Production of small single-wall carbon nanohorns by CO_2 laser ablation of graphite in Ne-gas atmosphere Carbon, 45 (2007) 1364.

[51] M. Kusaba, Y. Tsunawaki. Production of single-wall carbon nanotubes by a XeCl excimer laser ablation Thin Solid Films, (2006) 506.

[52] G. Radhakrishnan, P. M. Adams and L. S. Bernstein. Room-temperature deposition of carbon nanomaterials by excimer laser ablation Thin Solid Films, 515 (2006) 1142.

[53] A. A. Gorbunov, R. Friedlein, O. Jost, M. S. Golden, J. Fink, W. Pompe, Gas-dynamic consideration of the laser evaporation synthesis of single-wall carbon nanotubes. Appl. Phys. A (Suppl.), 69 (1999) S593.

[54] J. Liu. Abstracts of Papers of the American Chemical Society, 227 (2004) U273.

[55] J. H. Hafner. Catalytic growth of single-wall carbon nanotubes from metal particles Chemical Physics Letters, 296 (1-2) (1998) 195.

[56] S. Maruyama. Low-temperature synthesis of high-purity single-walled carbon nanotubes from alcohol. Chemical Physics Letters, 360 (3-4) (2002) 229.

[57] L. M. Huang. Cobalt ultrathin film catalyzed ethanol chemical vapor deposition of single-walled carbon nanotubes Journal of Physical Chemistry B, 110 (23) (2006) 11103.

[58] A. M. Cassell, Large scale CVD synthesis of single-walled carbon nanotubes Journal of Physical Chemistry B, 103 (31) (1999) 6484.

[59] Z. Jin, Ultralow feeding gas flow guiding growth of large-scale horizontally aligned single-walled carbon nanotube arraysNano Letters, 7 (7) (2007) 2073.

[60] K. Hata. Electric field effect in atomically thin carbon films. Science, 306 (5700) (2004) 1362.

[61] H. J. Dai. Nanotube growth and characterization. Carbon nanotube 80 (2001) 29.

[62] K. Hata. Water-assisted highly efficient synthesis of impurity-free single-walled carbon nanotubes. Science, 306 (5700) (2004) 1362.

[63] J. Liu, Controlling the diameter of carbon nanotubes in chemical vapor deposition method by carbon feeding. J. of American Chemical Society, 227 (2004) p.U273.

[64] C. G. Lu, J. Liu, Controlling the diameter of carbon nanotubes in chemical vapor deposition method by carbon feeding. Journal of Physical Chemistry B, 110 (41) (2006) p.20254.

[65] B. Zheng. Efficient CVD growth of single-walled carbon nanotubes on surfaces using carbon monoxide precursor. Nano Lett., 2(8) (2002) 895.

[66] E. Dujardin, T. W. Ebbesen, H. Hiura, K. Tanigaki. Capillarity and wetting of carbon nanotubes Science 265, (1994) 1850.

[67] A. H. Angew. Functionalization of single-walled carbon nanotubes. Chem. Int. Ed. 41, (2002) 1853.

[68] M. Simmons, B. M. Nichols, S. E. Baker, S. Marcus, Matthew, O. M. Castellini, C. S. Lee, R. J. Hamers, M. A. Eriksson. Effect of Ozone Oxidation on Single-Walled Carbon Nanotubes. J. Phys. Chem. B 110, (2006) 7113.

[69] S. C. Lim, C. S. Jo, H. J. Jeong, Y. M. Shin, Y. H. Lee, I. A. Samayoa. Effect of oxidation on electronic and geometric properties of carbon nanotubes J. Choi, Appl. Phys. 41, (2002) 5635.

[70] M. A. Herranz, N. Martin, S. Campidelli, M. Prato, G. Brehm, D. M. Guldi, Controlover. Angew Control over electron transfer in tetrathiafulvalene-modified single-walled carbon nanotubes. Chem. Int. Ed. 45, (2006) 4478.

[71] X. Guo, J. P. Small, J. E. Klare, Y. Wang, M. S. Purewal, I.W. Tam, B. H. Hong, R. Caldwell, L. Huang, S. O. Brien, J. Yan, R. Breslow, S.J. Wind, J. Hone, P. Kim, C. Nuckolls. Covalently bridging gaps in single-walled carbon nanotubes with conducting molecules Science 311, (2006) 356.

[72] C. Klumpp, K. Kostarelos, M. Prato, A. Bianco. Functionalized carbon nanotubes as emerging nanovectors for the delivery of therapeutics Biochim. Biophys. Acta Bio memb 1758, (2006) 404.

[73] D. Tasis, N. Tagmatarchis, A. Bianco, M. Prato. Chemistry of carbon nanotubes. Chem. Rev. 106, (2006) 1105.

[74] H. J. Kim, J. H. Lee. Highly sensitive and selective gas sensors using p-type oxide semiconductors: Overview, Sens. Actuators B: Chem., 192 (2014) 607.

[75] J. Cadena, G. J. Riu, F. X. Rius. Gas sensors based on nanostructured materials. Analyst, 132 (2007) 1083.

[76] M. Schenk, A. R. Reichelt. An electron microphone as a force sensor for combined scanning probe microscopy. Ultramicroscopy, 65 (1996) 109.

[77] F. He, Q. Huang, M. Qin. A silicon directly bonded capacitive absolute pressure sensor. Sens. Actuator A: Phy., 35 (2007) 507.

[78] C. T. Huang, C. L. Shen, C. F. Tang, S. H. Chang. A wearable yarn-based piezo-resistive sensor. Sens. Actuator A: Phy., 141(2) (2008) 396.

[79] C. V. G. Reddy, S. V. Manorama, V. J. Rao, Preparation and characterization of ferrites as gas sensor materials, J. Mater. Sci. Lett. 19 (2000) 775.

[80] S. Singh, B. C. Yadav, R. Prakash, B. Bajaj, J. R. Lee. Synthesis of nanorods and mixed shaped copper ferrite and their applications as liquefied petroleum gas sensor; App. Surf. Sci., 257 (2011) 10763.

[81] C. Peng. Principle and Application of Biomedical Sensors, Higher Education Press, Beijing, China, (2000) 157.

[82] L. A. Mercante, V. P. Scagion, F. L. Migliorini, L. H. C. Mattoso, D. S. Correa Electrospinning-based (bio) sensors for food and agricultural applications: A review, Trends in Analytical Chemistry 91 (2017) 91.

[83] G. Korotcenkov, B. K. Cho. Metal oxide composites in conductometric gas sensors: Achievements and challenges, Sens. Actuators B: Chem., 244 (2017) 182.

[84] L. Gajdosik. Tin oxide Gas Sensors, Encyclopedia of Sensors, 10 (2006) 361.

[85] K. Shimanoe, M. Yuasa, T. Kida, N. Yamazoe. Semiconductor gas sensor using nano-sized oxide for high-sensitive detection of environment-related gases, in

Proceedings of the IEEE International Conference on Nanotechnology Materials and Devices (2011) 38.

[86] G. Neri. Metal Doping in semiconductor Gas Sensors, Encyclopedia of Sensors, 6 (2006) 1.

[87] T. Seiyama, A. Kato, K. Fujiishi, M. Nagatani, A new detector for gaseous components using semiconductive thin films. Anal. Chem., 34 (1962) 1502.

[88] D. E. Williams, Semiconducting oxides as gas-sensitive resistors. Sens. Actuators B: Chem., 57 (1999) 1.

[89] A. A. Tomchenko, G. P. Harmer, B. T. Marquis, J. W. Allen, Semiconducting metal oxide sensor array for the selective detection of combustion gases. Sens. Actuators B: Chem., 93 (2003) 126.

[90] N. Yamazoe, K. Shimanoe. Theory of power laws for semiconductor gas sensors. Sens. Actuators B: Chem., 128 (2002) 566.

[91] C. Massie, G. Stewart, G. M. Gregor, and J. R. Gilchrist, Design of a portable optical sensor formethane gas detection, Sens. Actuators B: Chem., 113 (2) (2006) 830.

[92] S. C. Gadkari, M. Kaur, V. R. Katti, V. B. Bhandarkar, K. P. Muthe, S. K. Gupta. Solid State Sensors for H_2, H_2S and NH_3, Encyclopedia of Sensors, 10 (2006) 21.

[93] R. Binions, H. Davies, A. Afonja, S. Dungey, D. Lewis, D. E. Williams, D.E, I.P. Parkin. Zeolitemodified discriminating gas sensors. J. Electrochem. Soc. 156 (2009) J46.

[94] R. K. Sonker, M. Singh, U. Kumar, B. C. Yadav, MWCNT doped ZnO nanocomposite thin film and it's sensing, Journal of Inorganic and Organometallic Polymers and Materials, 26 (6) (2016) 1434.

[95] T. Takada, T. Fukunaga, and T. Maekawa. New method for gas identification using a singlesemiconductor sensor, Sens. Actuators B: Chem., 66 (1–3) (2000) 22.

[96] J. F. Currie, A. Essalik, J. C. Marusic, Micromachined thin film solid state electrochemical CO_2, NO_2 and SO_2 gas sensors, Sens. Actuators B: Chem., 59, (2–3) (1999) 235.

[97] R. Sathiyamoorthi, R. Chandrasekaran, T. Mathanmohan, B. Muralidharan, T. Vasudevan, Study of electrochemical-based gas sensors for fluorine and chlorine, Sens. Actuators B: Chem., 99 (2–3) (2004) 336.

[98] I. D. Avramov, M. Rapp, A. Voigt, U. Stahl, M. Dirschka, Comparative studies on polymer coated SAW and STW resonators for chemical gas sensor applications. In Proceedings of 2000 IEE/EIA International Frequency Control Symposium and Exhibition, Kansas City, USA, 7–9, (2000) 58.

[99] W. H King, Piezoelectric Absorption Detector, Analytical Chemistry, 36 (1964) 1735.

[100] S. Kamekichi, T. Tatsumi, Wet and dry plate dew point Hygrometer, Humidity and Moisture1, Ed. by R. E. Ruskin (1965) 64.

[101] M. Yoshitake, I. Shimizu. Experimental results of the psychrometer constant, humidity and moisture 1, Ed. by R. E. Ruskin (1965) 70.

[102] R. J. Taylor. The response of psychrometer fluctuations in vapour pressure, Humidity and Moisture 1, Ed. by R. E. Ruskin (1965) 76.

[103] W. W. Robert. Psychrometer Determination of relative humidities in the air with dry-bulb temperatures exceeding 212˚F, Humidity and Moisture1, Ed. by R. E. Ruskin (1965) 105.

[104] R. G. Wylie, D. K. Davies, W. A. Caw, The basic process of the dew-point hygrometer, Humidity and Moisture 1, Ed. by R. E. Ruskin (1965) 125.

[105] A. W. Brewer, The dew-or frost-point hygrometer, Humidity and Moisture 1, Ed. by R. E. Ruskin (1965) 136.

[106] C. Y. Lee, G. B. Lee. Micro-machine based humidity sensors with integrated temperature sensors for signal drift compensation. J. Micromech. Microeng.13 (2003) 620.

[107] P. Pascal-Delannoy, B. Sorli, A. Boyer. Quartz Crystal Microbalance (QCM) used as a humidity sensor. Sens. Actuators B: Chem. 84 (2000) 285.

[108] W.H. King Jr., The piezoelectric sorption hygrometer, Humidity and Moisture 1, Ed. by R. E. Ruskin (1965) 570.

[109] M. Jose, M. Perez, C. Freyre. A poly(ethyleneterephthalate)-based humidity sensor. Sens. Actuators B: Chem. 42 (1977) 27.

[110] I. Hayakawa, Y. Iwamoto, K. Kikuta, S. Hirano. Gas sensing properties of metal organics derived Pt dispersed-TiO_2 thin film fired in NH_3. Sens. Actuators B: Chem. 67 (2000) 270.

[111] Y. Sakai, M. Matsuguchi, T. Hurukawa. Humidity sensor using cross-linked poly (chloromethyl styrene). Sens. Actuators B: Chem. 66 (2000) 135.

[112] J. Das, S. M. Hossain, S. Chakraborty, U. Gangopadhyay, H. Saha. Capacitive type Humidity Sensor based on Porous Silicon. Proceedings of the Tenth International Workshop on the Physics of Semiconductor Devices 1 (1999) 707.

[113] B. C. Yadav, A. K. Srivastava, P. Sharma. Resistance based humidity sensing properties of TiO_2. Sens. & Trans. J. 81(7) (2007)1348.

[114] W. Qu, W. Wlodarski, U. Jorg. Comparative study on micromorphology and humidity sensitive properties of thin-film and thick-film humidity sensors based on semiconducting $MnWO_4$.Sens. Actuators B: Chem. 64 (2000) 76.

[115] B. C. Yadav, R. Srivastava, C. D. Dwivedi. Synthesis of ZnO nanorods and their application as humidity sensors. Synthesis and Reactivity in Inorganic, Metal-Organic and Nano-Metal Chemistry 37 (2007) 1.

[116] B. C. Yadav, P. Sharma, A. K. Srivastava, A. K. Yadav. Synthesis of antimony doped tin oxide and it's use as an electrical humidity sensor. Sens. & Trans. J. 92 (5) (2008) 99.

[117] B. C. Yadav, P. Sharma, P. K. Khanna. Morphological and Humidity Sensing Characteristics of SnO_2-CuO, SnO_2-Fe_2O_3 and SnO_2-SbO_2 nano co-oxides. Bull.of Mater. Sci. 34 (1) (2011) 1.

[118] W. Qu, M. Jorg-Uwe, A novel thick film ceramic humidity sensor, Sens. Actuators B: Chem. 40 (1997) 175.

[119] B. C. Yadav, R. Srivastava, C. D. Dwivedi. Synthesis and characterization of ZnO-TiO2 nano-composite and its application as a humidity sensor. Philosophical Magazine 88 (2008) 7.

[120] A. K. Srivastava, B. C. Yadav. Humidity sensing properties of TiO_2-Sb_2O_5 nanocomposite. Materials Science 28(2) (2010) 493.

[121] Y. Sakai, Y. Sadaoka, Y. Matsuguchi. Humidity sensors based on polymer thin films. Sens. Actuators B: Chem. 35 (1-3) (1996) 85.

[122] B. Yang, B. Aksas, Q. Lin, M. Sitti, Compliant and low-cost Humidity Sensors using Nano-porous polymer membranes. Sens. Actuators B: Chem. 114 (2006) 254.

[123] Y. Mu-Roug, C. Ko-Shao. Humidity Sensors using polyvinyl alcohol mixed with electrolytes, Sens. Actuators B: Chem. 49 (1998) 240.

[124] F. S. Wayne, W. F. Laurence, P. J. Hans, Infrared Absorption Hygrometer, Humidity and Moisture 1, Ed. by R. E. Ruskin (1965) 465.

[125] R. C. Wood. The Infrared Hygrometer-Its application to Difficult humidity measurement Problems, Humidity and Moisture 1, Ed. by R.E. Ruskin (1965) 492.

[126] N. M. Tashtoush, J. D. N. Cheeke, N. Eddy. Surface Acoustic Wave Humidity Sensor based on a thin poly XIO film. Sens. Actuators B: Chem. 49 (1998) 218.

[127] R. H. Huang. Sensor Calibration of a SAW Resonator for absolute humidity measurements in microelectronic packages.Sens. Actuators B: Chem.25 (1-3) (1995) 686.

[128] D. W. Galipean, J. D. Stroschine, K. A. Snow, K. A. Vetelino, K. R. Hines. A study of condensation and dew point using a SAW. Sens. Actuators B: Chem. 25(1-3) (1995) 696.

[129] C. Caliendo, E. Verona, A. D'Amico, A. Furlani, G. Iucci, M.V. Russo. Surface acoustic wave humidity sensor. Sens. Actuators B: Chem. 16(1-3) (1993) 288.

[130] N. Dwivedi, S. Kumar, R. K. Tripathi, H. K. Malik, O. S. Panwar. Field emission, morphological and mechanical properties of variety of diamond-like carbon thin films. Applied Physics A 105 (2011) 417.

[131] R. K. Tripathi, O. S. Panwar, A. K. Srivastava, Ishpal, M. Kumar, S. Chockalingam. Structural, Nanomechanical, and Field Emission Properties of Amorphous Carbon Films Having Embedded Nanocrystallites Deposited by Filtered Anodic Jet Carbon Arc Technique. Journal of Nanoscience 11 (2013) 2013.

[132] N. Dwivedi, S. Kumar, R. K. Tripathi, J. D. Carey, H. K. Malik, M. K. Dalai. Structural and Electronic Characterization of Nanocrystalline Diamond-like Carbon Thin Films. ACS applied materials & interfaces 4 (2012) 5309.

[133] N. Dwivedi, S. Kumar, J. D. Carey, R. K. Tripathi, H. K. Malik, M. K. Dalai. Influence of Silver Incorporation on the Structural and Electrical Properties of Diamond-Like Carbon Thin Films. ACS Applied Materials & Interfaces 5 (2013) 2725.

[134] U. Kumar, S. Sikarwar, R. K. Sonkar, B. C. Yadav, Carbon nanotube: synthesis and application in solar cell. Journal of Inorganic Organometallic Polymers 26 (2016) 1231.

[135] A. Singh, K. Senapati, M. Kumar, T. Som, A. K. Sinha, P. K. Sahoo, Role of work function in field emission enhancement of Au island decorated vertically aligned ZnO nanotapers. Applied Surface Science 411 (2017) 117.

[136] S. Ding, Y. Zhou, M. Ye, W. Lei. Hierarchically Structured Ni3S2/Carbon Nanotube Composites as High-Performance Cathode. Vacuum 139 (2017) 33.

[137] B. C. Yadav, P. Kumar, S. Singh, R. Kothari. Development in Metal Oxide Nanomaterial-based Solar Cells. Emerg Energy Alternatives Sustainable Environ, Chapter 23, (2015) 1.

[138] B. J. Kim, S. H. Han, J. S. Park. Surf. Coat. Technol. 271, (2015) 22.

[139] L. K. Shrestha, J. P. Hill, T. Tsuruoka, K. Miyazawa, K. Ariga. Surfactant-assisted assembly of fullerene (C_{60}) nanorods and nanotubes formed at a liquid-liquid interface. Langmuir 29, (2013) 7195.

[140] L. K. Shrestha, Y. Yamauchi, J. P. Hill, K. Miyazawa, K. Ariga. Fullerene crystals with bimodal pore architectures consisting of macropores and mesopores. J. Am. Chem. Soc. 135, (2013) 586.

[141] R. G. Shrestha, L. K. Shrestha, A. H. Khan, G. S. Kumar, S. Acharya, K. Ariga. Demonstration of ultrarapid interfacial formation of 1D fullerene nanorods with photovoltaic properties Appl. Mater. Interfaces 6, (2014) 15597.

[142] X. Mathew, J. P. Enriquez, A. Romeo, A. N. Tiwari. CdTe/CdS solar cells on flexible substrates Sol. Energy 77, (2004) 831

[143] B. Marsen, H. Wilhelm, L. Steinkopf, S. Klemz, T. Untold, R. Scheer, H.-W. Schock, Effect of copper-deficiency on multi-stage co-evaporated Cu (In, Ga) S2 absorber layers and solar cells Thin solid film 519, (2011) 7224.

[144] H. Katagiri, K. Imbo, W. Shwemaw, K. Oishi, M. Yamazaki, H. Araki, A. Takeuchi. Thin. Film. Chalcogenide. Photovolt. mater. 517(7), (2009) 2455.

[145] K. Shin, J. B. Yoo, H. Park. Photoelectrochemical cell/dye-sensitized solar cell tandem water splitting systems with transparent and vertically aligned quantum dot sensitized TiO_2 nanorod arrays J. Power Sources 225, (2013) 263.

[146] E. Shi, L. Zhang, Z. Li, P. Li, Y. Shang, Y. Jia, J. Wei, K. Wang, H. Zhu, D. Wu, S. Zhang, Anyuan Cao. TiO_2-Coated Carbon Nanotube-Silicon Solar Cells with Efficiency of 15%. Nature. (2012). doi: 10.1038/srep00884

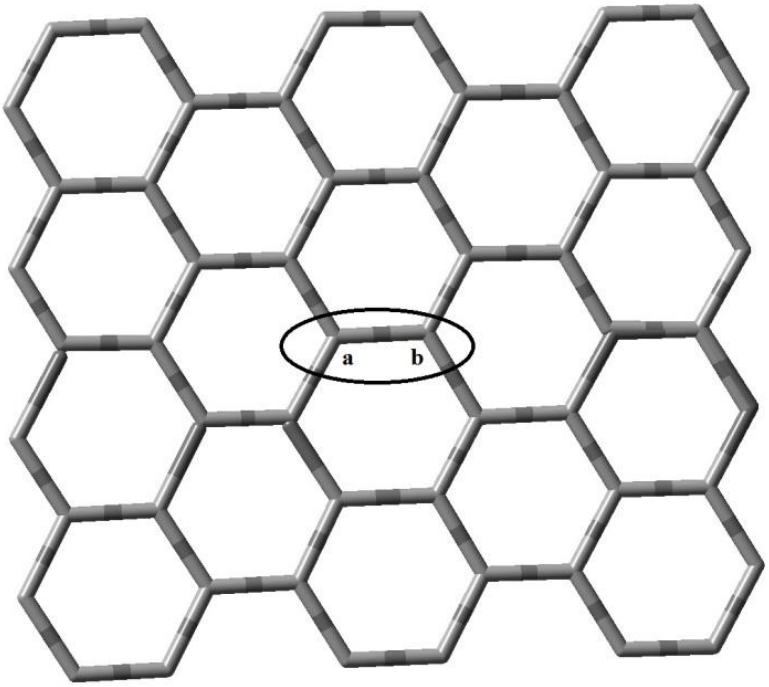

Fig. 1.1 Hexagonal honeycomb lattice of graphene with two carbon atoms (a and b) per unit cell

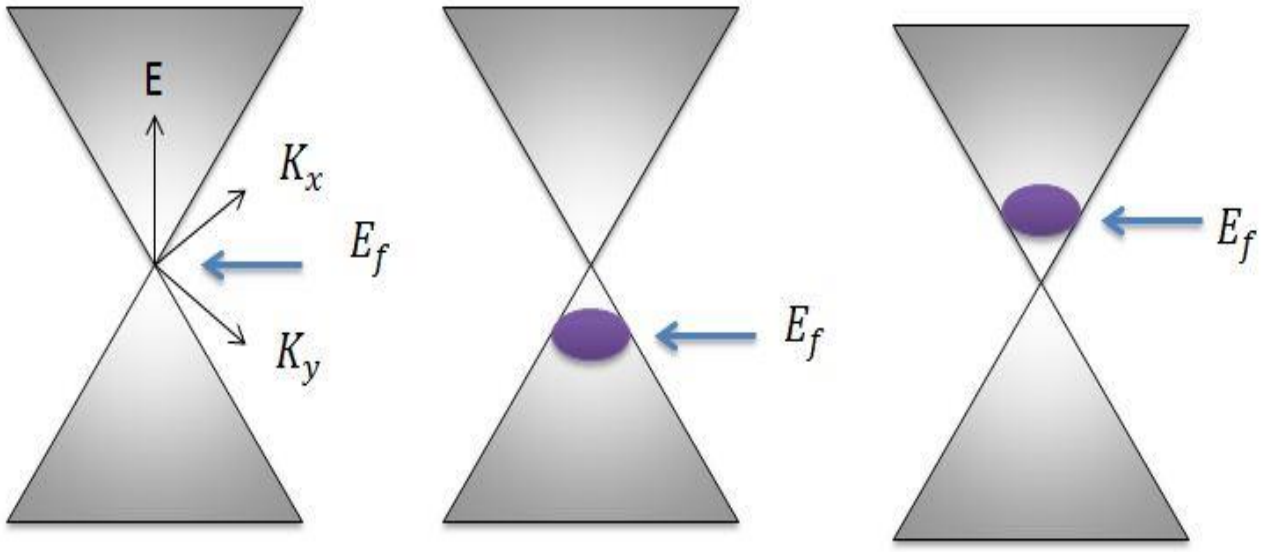

Fig. 1.2 Schematic band structure of graphene, a) band structure of pristine graphene with zero bandgap b) band structure of p-type graphene c) band structure of n-type graphene

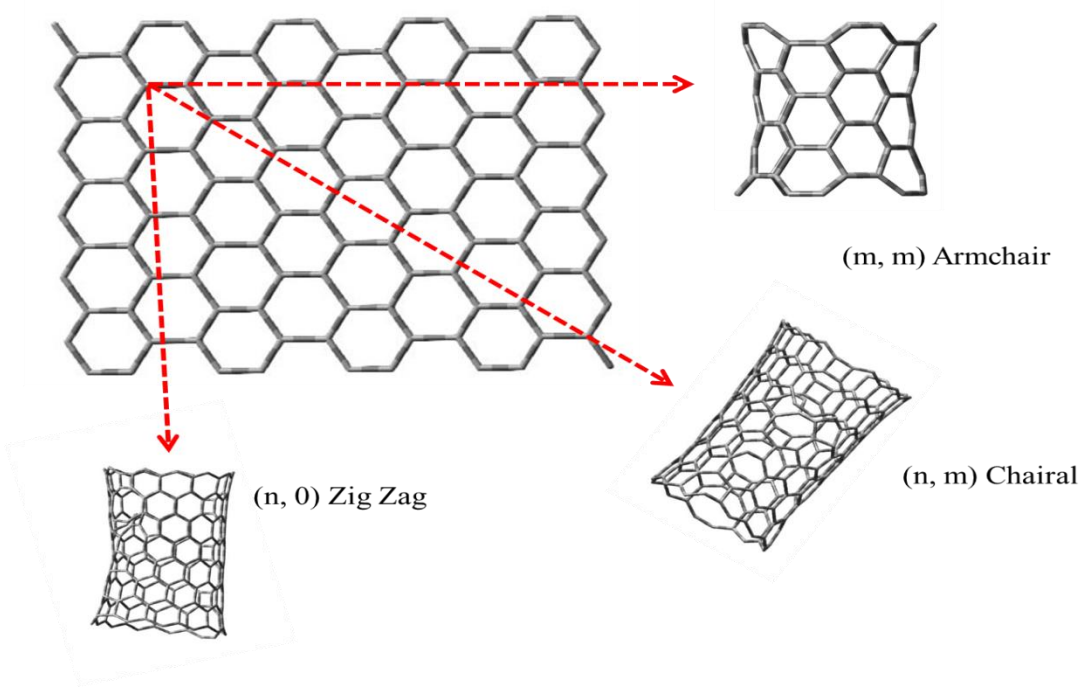

Fig. 1.3 Honeycomb structure of the graphene sheet. The chiral vector is constructed by the lattice vectors a_1, a_2 and the (n, m) indices. $c = na_1 + ma_2$. Chiral nanotubes correspond to the (n, n) armchair and (n, 0) zig-zag directions.

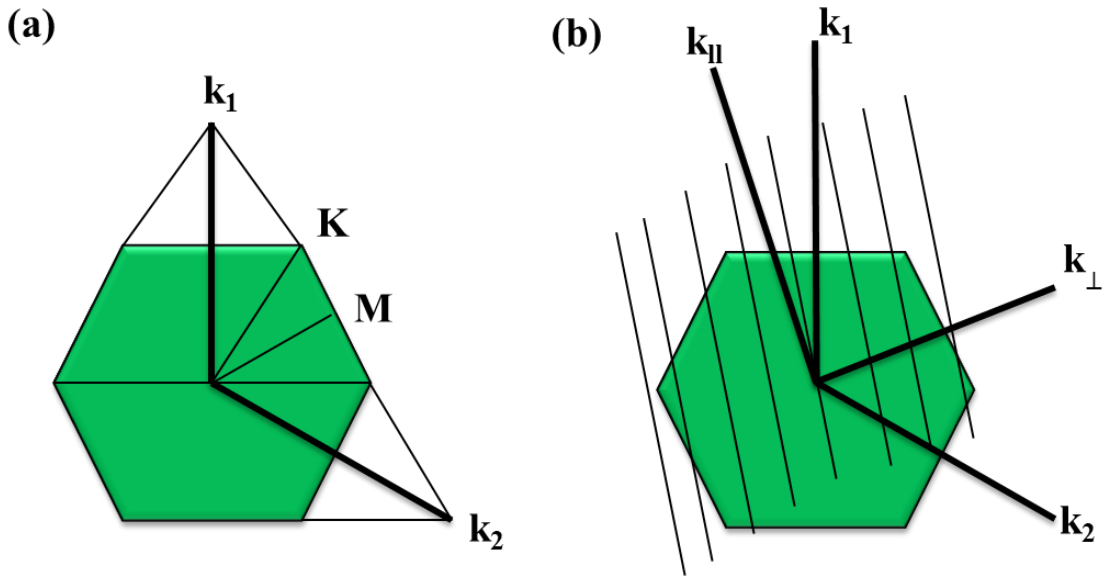

Fig. 1.4 Brillouin zone of carbon nanotubes

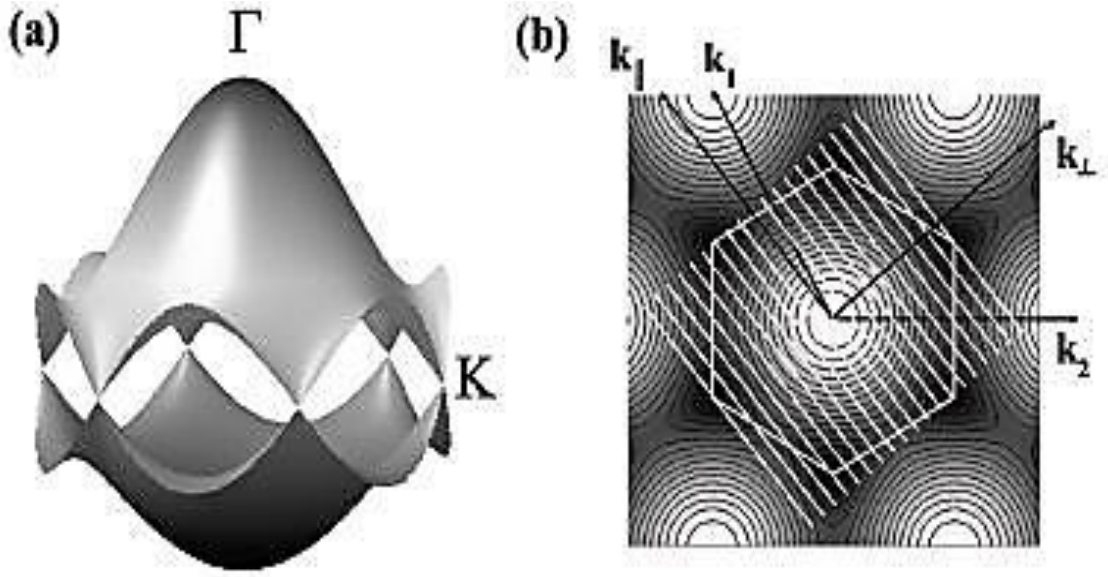

Fig. 1.5 a) Tight-binding band structure of graphene and the conduction and valence band cross at the K points. b) Contour plot of the graphene electronic band structure with the allowed lines in case of the (12, 3) chiral tube.

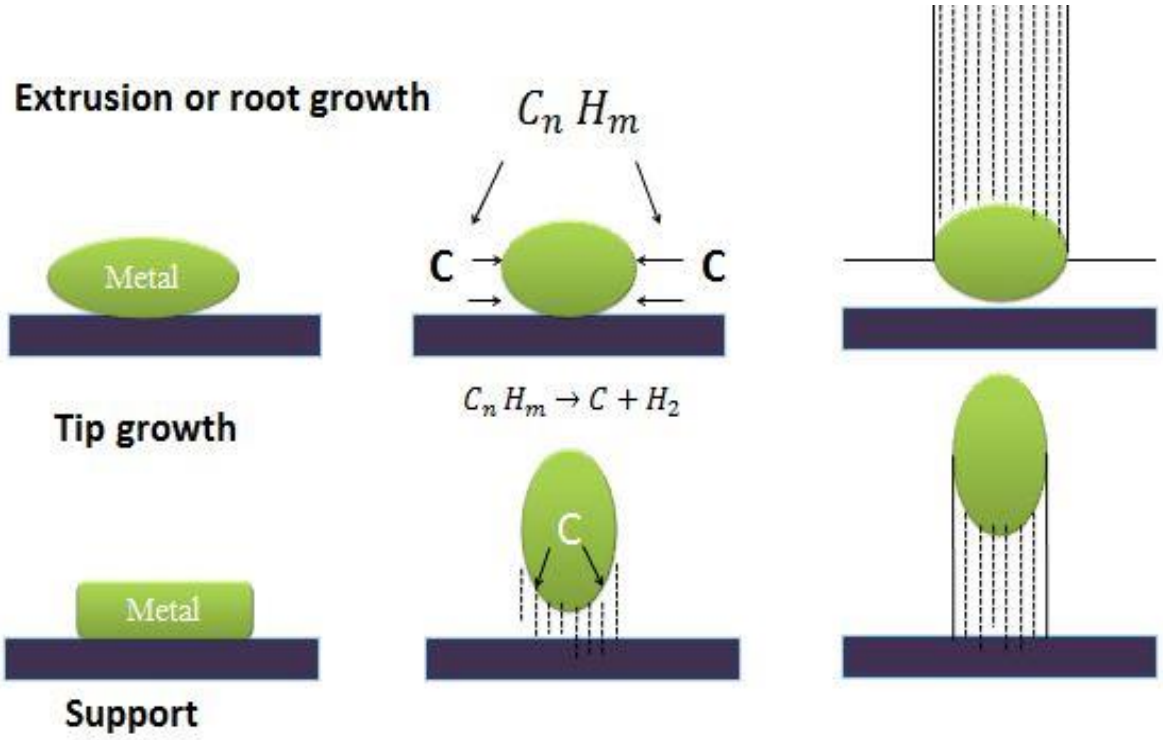

Fig. 1.6 Growth mechanism of carbon nanotubes

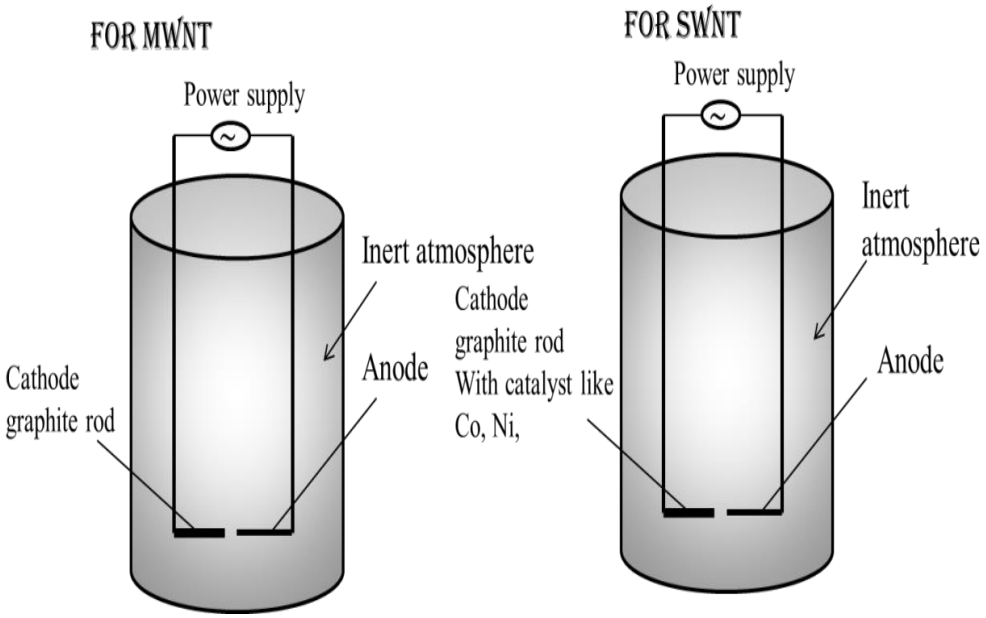

Fig. 1.7 Arc discharge method for synthesis of SWCNT and MWCNT

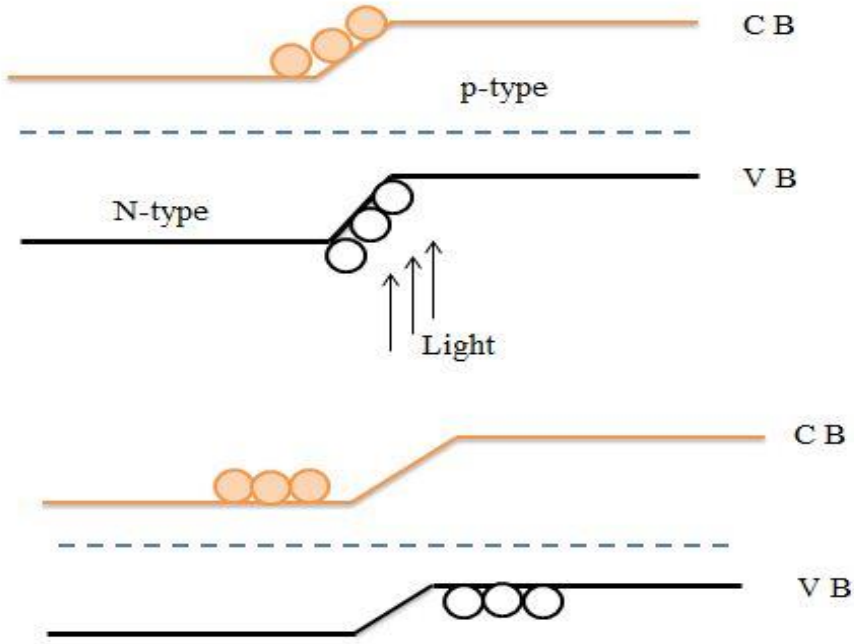

Fig. 1.8 Diagram showing the variation of band structure of CNT based solar cell

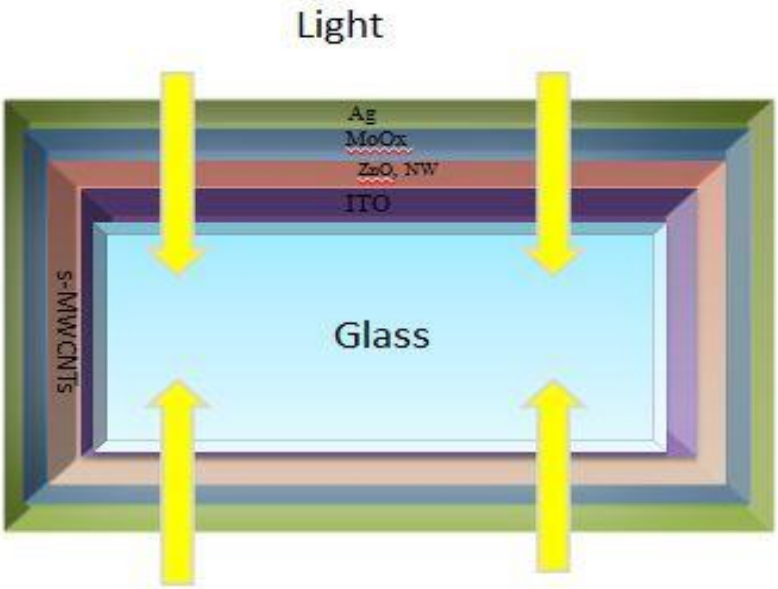

Fig. 1.9 Fabrication of solar cell using carbon nanotube

Table 1.1 Synthesis of carbon nanotubes by arc discharge method under various conditions

Types of arc discharges	Circumstances	Product	Remark	References
Normal arc discharge	KCl/FeS catalyst under the atmosphere of Ar	DWNT (double walled nanotubes)	Large and high quality, diameter 2-6nm	[24-28]
	A mixture of Catalyst using Co/Ni/Fe with a small quantity of S in the atmosphere of Ar		Large length and diameter of 4-7 nm	
	The catalyst used FeS, CoS in the atmosphere of hydrogen		Bundles of high quantity nanotubes	
	Using Graphite electrode in the atmosphere of hydrogen		Optimization process	
Plasma rotating arc discharge	Pure graphite electrodes using a hydrogen atmosphere	CNT	The large scale of production	[29]
Liquid arc discharge	Deionized water	MWNT, carbon onions, CNTs	Metal filled inside the tubes	[30-42]
	NaCl solution with electrodes in a liquid environment	MWNT, carbon nanocapsules, SWNT	Irregular morphology with a disordered shape	
	Toluene with using a different catalyst	Tube-like and spheroid nanocarbon,	Continuous production of tubes	
	Y/Ni and CaC_2 catalyst under the atmosphere of helium	SWNT, fullerenes, SWNT fibers, metallofullerenes,	High purity and high yield with the diameter of 0.9-14 nm	

		CNTs		
	Using polymers such as PVA and PVA/Fe and various Fe sources	MWNTs, sheet-like structures, spherical particles, beaded CNTs	The type of product totally depends on the catalytic composition	

Table 1.2 Synthesis of carbon nanotubes by laser ablation method at various conditions

LASER	Materials	Circumstances	References
CO_2 continuous wave	SWCNT bundles with bamboo-like structure	Laser power 400-900W At Room temperature Ar atmosphere under 200-400 torr	[43]
	SWCNT bundles	High-temperature 1100℃ with Ar and He atmosphere under 50-500 torr	[44]
CO_2 pulsed wave	SWCNTs	Laser power 12-9-6 kW with Ar and N_2 atmosphere 50-450 torr	[45- 47]
Pulsed Nd-YAG Laser	Thin SWCNT	Gas flow rate	[48]
	SWCNT bundles	Laser intensity 532nm, 1024 Using catalyst C, Ni, Co under the atmosphere of Ar Furnace temp 800-1150℃	[49]
	SWCNT	Laser intensity varies, furnace temperature 550℃ and depends on gas flow rate and pressure	[50]
XeCl excimer	SWCNT bundles, fullerenes,	Furnace temperature 1100-1350℃ using catalyst C,Co,Ni under Ar atmosphere	[51]
KrF excimer	MWCNT, nano onions	Target metals using a composite of C/Co, C/Co/Ni in the atmosphere O_2 and Ar at room temp	[52]
	Carbon nanohorns	Using pure carbon in the atmosphere of Ar, Ne, He	[53]

Table 1.3 Synthesis of Carbon nanotube by Chemical Vapor Deposition Technique

Precursor	Carrier gas	Temperature	Flow rate	Advantage	Disadvantage	References
Si/SiO_2 with some catalyst like Fe	CO with H_2 (30% - 70%)	900℃	1000 sccm for both gases	Good growth is achieved by adding hydrogen. Efficient production of long SWNT by fast heating technique	Self-deposition causes amorphous carbon deposited in the quartz tube. Hazardous nature of CO so exhausts properly. Metal impurity destroying the flow rate controller	[54, 55]
Co either in solution form or in thin film form	C_2H_5OH with Ar and H_2 gas	750℃ without H_2 860℃ with H_2	450 sccm for Ar 50 sccm for H_2	Low-temperature method for growing SWNT. Ultra-long nanotube and Multiple chiral nanotubes are found.	Sometimes impurities may be found as analyzed under Raman spectroscopy	[56, 57]
Silicon wafer with Mueller catalyst	CH_4 with H_2	940°C to 980°C	2 Sccm for CH_4 and 4 sccm for H_2	Low flow rate required for the growth mechanism. Ultra-long Nanotube will be obtained.	High temperature requires for growth mechanism	[58,59]
Si/SiO_2 with Fe catalyst	Ethylene with water vapor and Ar gas	750°C	150 sccm for ethylene and 40 sccm for Ar also cooled after growth with the	Ultra-tall vertical forest of the nanotube is to found, Water will help the self-cleaning and increases the	Defects may be created some time	[60]

			flow of Ar at 600 sccm and H_2 at 400 Sccm	lifetime		

Table 1.4 Functionalization of carbon nanotubes by various methods and its applications in different fields

Functionalization type			**Mechanism**	**Advantage**	**Disadvantage**	**Area of application**	**References**
Exohedral functionalization	Covalent functionalization	Sidewall functionalization	Cyclo and nucleophilic addition radical reactions	Production of stable functionalized CNTs Easily dispersed in a chemical solvent with a high degree of functionalization	Destruction and shortening of carbon nanotube which disintegrates the chemical and physical property	Chemical sensors LED Solar cell Transistor	[68, 69]
		Defect or end functionalization	Oxidation of carbon nanotubes e.g. carboxyl functionalization	Easily produced and simply dispersed in polar solvents	Having a small surface area with some destructed network	Chemical sensors LED Solar cell Transistor	[70, 71]
	Noncovalent functionalization		Vander wall interaction in which CNT's are wrapped with polymers	Electronic, chemical property and length of tubes will not be affected	Unstable nanotubes will found and dispersibility in covalent solution is low	CNT based polymer composite used in aerospace CNT based biomolecule composite used in biosensors	[72, 73]

Endohedral functionalization	Wet chemistry in which materials are filled inside the tube by capillary action	The structure is preserved and length is also not affected	The outer surface remains unusual	Hydrogen storage materials Drug delivery system	[66, 67]

Table 1.5 Development of solar cells by various methods

Materials	**Deposition technique**	**Theoretical/ Experimental efficiency**	**Junction**	**Advantages**	**Problems**	**References**
CdTe/CdS	Evaporation sublimation, screen printing technique	30% /16%	Controversial	Good stability High module efficiency	Toxicity of Cd Availability of Te	[142]
CuIn (G)-Se(S)	Evaporation, sputter deposition, electroplating ,spray deposition	28-30% / 20%	Homo-junction	Good stability	Multiple binary phases Cell to cell mismatch	[143]
CZTS(Se)	PVD, sputtering, spry pyrolysis, screen printing	30% / 9.6%	Direct Band gap 1.4-1.6 eV	Abundant, cheap, green material	Mixed phases Difficult to synthesis	[144]

PEC using dyed TiO_2/ TCO	PVD, sputtering, electroplating	30% / Upto 12%			Difficult to manufacture ,	[145]
CNT based	CVD, sputtering, electroplating	More then 30% / 16%	Direct band gap	Lighter, flexible, high efficient		[146]

CHAPTER 2

SYNTHESIS OF MULTIWALLED CARBON NANOTUBES (MWCNT) BY DIRECT LIQUID INJECTION CHEMICAL VAPOR DEPOSITION METHOD AND THEIR APPLICATIONS AS ULTRA-LOW TURN ON FIELD EMITTER AND PHOTOSENSOR

This chapter includes the synthesis of MWCNTs at temperatures 650 ℃ and 750 ℃ and the investigations on the field emission and photosensing property. The synthesized material was then investigated using SEM, XRD and UV-visible absorption technique. The dilute solution of the material was analyzed using TEM and Particle Size Analyzer. Field emission current of both the samples were calculated. The emission of photocurrent at room temperature through thin film was also measured. Sensitivity along with response and recovery time was calculated. The experiment was repeated from time to time to check the repeatability, response and recovery times. The material was employed in field emission device to observe the field emission capability of the material. Experimental data were verified by theoretical data using DFT calculations.

CHAPTER 2

Synthesis of Multiwalled Carbon Nanotubes (MWCNT) by Direct Liquid Injection Chemical Vapor Deposition method and their applications as ultra-low turn on Field Emitter and Photosensor

2.1. Introduction

We are living in an era of the energy crisis. Energy generation is an expensive process and if we save the generated energy this can help in energy harvesting. Increasing demand for electronic devices having a display and present cold emitters is using significant amounts of generating energy. Carbon-based field emitters are extensively investigated for better field emission devices [1-5]. Carbon nanotubes (CNTs) [6] have extraordinary physical, chemical, structural and mechanical properties. They are ideal quantum systems for exploring the one-dimensional physics and applications in a nanoscale device. The growth of CNTs [7] is done by using so many different approaches like arc discharge, laser ablation and chemical vapour deposition, but the chemical vapour deposition method is the best for synthesizing carbon nanotubes having high purity and high yield [8, 9]. CNTs have attracted worldwide attention because of having one-dimensional growth, high aspect ratio, and unique structural property, so they are also used in many electronic devices [8-11]. A variety of catalysts such as Au, Ag, Pt, Fe, Mn, Mo and Mg are used for the growth of CNTs but the best growth is found by using transition metal catalysts like Fe, Co, Ni and the advantages of such catalysts are that they can easily be filtrated from the nanotubes by the distillation process [5, 12]. The excellent electrical conductivity and high optical transparency of carbon nanotubes based

thin films prove their suitability to be used in electronic applications over the thin film fabricated by using metal oxides and other nanomaterials having a low electrical conductivity and optical transparency [13, 14]. Also, due to such extraordinary and attractive properties of CNTs, they are used in a large number of devices and also replace the indium tin oxide (ITO) glass.

The application of CNTs in field emission displays and electron microscope probes have been extensively investigated because of their low threshold voltage, high emission current, the unique structure and chemical stability. They are also used for the field effect transistor (FET) and in the probe of a single electron transistor (SET) [15]. The field emission properties of both single-walled carbon nanotube (SWCNT) and multiwalled carbon nanotubes (MWCNT) were investigated and MWCNT have high field emission property [16-25]. The MWCNT synthesized at high temperature using thermal CVD method [26-30] requires substrate and catalyst for the growth of the tube after the formation of tubes on the substrate are not easy to remove catalyst from the substrate. To overcome such problems, we used the high-temperature method in which the catalyst particles are easy to be filtered out from the tubes.

The role of photodetector is very important in modern life. Photodetectors are used in so many devices such as smartphones and digital cinematography. The photodetector which is operated in infrared (IR) spectrum are widely used in national security system applications like remote sensing, night vision and environment monitoring because they have the ability to convert optical signal to electrical signal. Today most of the commercial photodetectors are based on inorganic crystalline devices. The main advantages of such devices are their fast response and high sensitivity in the

visible region. These feature leads to a strong interest to replace the common sensor but they have two major drawbacks first is environment unfriendliness and second is they show insufficient long term stability. This exotic nature of materials can lead to issues of reliability, integration, size and cost. This compilled with the constant search for new and more complex applications which spurred a tremendous amount of interest in exploring new materials and detection modalities. The nanomaterials and nano-devices have unique optoelectronic, geometrical and structural properties that could enable photodetectors with new form factors, tunability and flexibility.

In this investigation, we have synthesized the MWCNTs by substrate free growth using cobalt as a catalyst under a controlled condition at different temperatures using direct liquid injection thermal CVD method [31-33]. The filtrations were done by the centrifugation and repeated washing process. Normally ultrahigh vacuum is required for checking the field emission properties of the nanomaterials. One another outcome of the present research work is that we have used rotary vacuum systems to investigate the field emission properties of MWCNTs, which reduces the production cost of fabricated devices based on these nanomaterials. The aim of this research was to employ these MWCNTs in the field emission devices.

The quantum dots, quantum wells, carbon nanotubes and graphene have shown unique properties and has a broad range of photodetection from the ultraviolet to the THz. In this chapter, synthesis of carbon nanotubes using DLICVD and its use as photodetector and field emitter have been presented. The CNTs are used for the fabrication of photosensor because the atomic structure of the CNT can be obtained by imagining a graphene sheet that is rolled to make a closed cylinder. This one-dimensional

nature of CNTs, leads to important differences for the optical properties as compared to graphene. The first important difference is due to the fact that each sub-band in a CNT has specific angular momentum, as a consequence, there is selection rule for optical transitions. For example, optical absorption can be maximized or suppressed depending on the direction of polarization with respect to the CNT axis. The second important difference arises because the Coulomb interaction in quasi-one-dimensional material enhances which leads to significant binding energy for excitons, that dominates the visible, near and mid-infrared optical absorption in CNTs. This has important consequences for photodetectors because large enough electric field must be present to dissociate the exciton in photoconductive devices.

2.2. Experimental technique

2.2.1 Catalyst preparation

Typically 0.5 molar solution of cobalt chloride (Merck Specialities Pvt. Ltd., >99%) was prepared by using 50 ml of ethanol (Hyman laboratory, > 99% chemical formula: C_2H_5OH) by continuous stirring at room temperature for 4 h at 450 rpm. Then PEG (polyethylene glycol 600) was added dropwise to remove the chloride from the solution and stirred again for 4 h till the complete removal of the chloride ions. NaOH solution of 5 molars was prepared and added drop wisely with continuous stirring of the solution. After the fixed interval of time, the particle size of the powder becomes stable. During this process, the colour of the solution changed from blue to green and finally, the grey colour appeared when the pH of the solution reached to 11. Later, it was placed for 24 h in a dust-free chamber. After stabilizing the nanoparticle, it was filtered out and washed to maintain pH at 7. Then the sample was dried at 100 ℃ for obtaining the

powder. For removing the magnetic property of powder, it was annealed at 500 ℃ for 4 h and later it was crushed for 5 h in a mortar with a pestle for obtaining ultrafine cobalt nanoparticles (20-40 nm). These nanoparticles of cobalt having size 20-40 nm are favourable for the nucleation and growth of MWCNT at a different temperature.

2.2.2 Carbon nanotube preparation

Carbon nanotubes were synthesized using direct liquid injection chemical vapour deposition method [7, 40] in which the catalysts placed in ceramic boat were placed inside the quartz tube of programmable vacuum based CVD for 1 h, then started heating the chamber with a continuous flow of nitrogen gas at 200 Sccm (Standard cubic centimeter) at 650 ℃ (Fig. 2.1). The temperature was maintained for 15 min, then ethanol was injected with 2 ml/min. Similarly, for another growth, the same process was applied and the temperature was increased to 750 ℃ with the use of the same catalyst that was placed inside the chamber. Maintaining the temperature at 750 ℃ the ethanol was re-injected by 2 ml/min with a continuous flow of nitrogen at 200 Sccm. The growth of CNTs was depending upon the decreasing rate, the temperature of the quartz tube so the rate of decrease in temperature was kept very slow. The reaction inside the chamber has been given by Eqn 2.1 and 2.2

$$C_2H_5OH \xrightarrow{\Delta H=200℃-250℃} C_2H_2 + H_2O\ldots.(2.1)$$

$$C_2H_2 + Co \xrightarrow{\Delta H=650℃-750℃} C_nH_n(Co)\ldots\ldots(2.2)$$

2.2.3 Mechanism for the synthesis

Carbon nanotubes were synthesized by using the growth mechanism [41] in which the catalyst particles were placed in the CVD chamber, that created nucleation points at high temperature at which the decomposed carbon carrier gas molecules were

deposited like an island [42]. In our case, both the root and tip growth have been found and shown in Fig 2.1.

2.2.4 Purification of nanotubes

The synthesized nanotube at 750℃ and 650℃ contains some part of Co catalyst inside the nanotube in both mechanisms, so purification of nanotubes was required to obtain pure and defect-free nanotubes which is analyzed by using Raman spectroscopy. For this purpose, a high acid treatment method was followed in which the nanotubes prepared by catalyst were put in the solution of nitric acid (69% pure) and stirred for 12 h. Co nanoparticles were dissolved in the nitric acid and after centrifugation and washing with deionized water the pure nanotubes were obtained. The reaction for the purification of nanotube is given by Eqn. 2.3:

$$C_nH_n(Co) + HNO_3 \rightarrow C_nH_{n\,(nanotube)} + Co(NO_3)_2 + NO + H_2O\ldots..(2.3)$$

2.2.5 Device fabrication

Field emission measurements at base pressure ~1×10^{-2} Torr using a rotary pump have been carried out in an in-house designed system using the Keithley electrometer (model 6517 B). The schematic representation of the field emission unit used in the present study is depicted in Fig. 2.2 [1, 2]. The field has been applied between two electrodes, the electrons get emitted from the cathode and move towards the anode.

2.3 Characterization techniques

The surface morphological and structural property of thin film were characterized by using Scanning Electron Microscopy (SEM) (JOEL JSEM 6490 LB) and Raman spectrophotometer (A Renishaw In Via reflex micro-Raman spectrometer using a 514.5 nm Ar^+ laser for excitation at a power of 15 mW) has been used for studying the

structural properties. The transmission electron microscope (TEM) (FEI, USA) images the sample weas recorded using a Tecnai G2-F30S Twin with an acceleration voltage of 300 keV. The average crystallite size was calculated by using the powder XRD method. The XRD of the films was carried out by X-ray diffractometer (Philips X'Pert PRO PANanalytical diffractometer using CuK_{α} (1.542 A) X-ray source in the scanned region of 10–90° with scanning step of 0.02° is used at a time of 1 s per step). The particle size has been analyzed by using Particle Size Analyzer (NZS90 using a laser of 625 nm). The optical characterization of the thin film was analyzed by UV-vis spectrometer (Evolution 302) and Infrared spectrometer (Shimadzu 8700 1992). The field emission parameters were measured by using Keithley electrometer (6517 B).

2.3.1 SEM analysis

The morphology and microscopic structure of prepared carbon nanotubes were characterized by using scanning electron microscopy (SEM) at 100 nm. Fig. 2.3 shows the SEM image of CNTs grown on Co catalyst using different temperature. On each grain, the random orientation of the tubes can be seen due to the substrate-free catalytic growth of the CNT. Micrographs were taken on the same scale and magnification also exhibits that the number of CNTs grown at 650 ℃ (Fig. 2.3 a) is lesser in number in comparison to CNTs grown at 750 ℃ (Fig. 2.3 b).

At 650 ℃ lesser molecules were decomposed to give the lesser numbers of carbon atoms and have lesser nucleation points while in the case of evaporation temperature 750 ℃, the maximum molecules were decomposed yielding the maximum number of carbon atoms aligned as CNTs in the form of clusters. As the length and density of CNT grown at 750 ℃ are higher than the CNT grown on 650 ℃, so it provides maximum

surface current and higher area for tunnelling electrons, hence these are more useful for the field emission application.

2.3.2 TEM analysis

The MWCNT synthesized by using DLICVD method has been analyzed by a Tunnelling Electron Microscope. Fig. 2.4 (a) shows the tubular structure of the nanotube along with hollow space inside the tube. Fig. 2.4 (b) shows the multiple carbon layers formed in the nanotube. The inner and outer diameter of the nanotube have been found as 14 nm and 23 nm respectively.

2.3.3 UV-vis spectroscopy

Absorbance spectra of carbon nanotubes were recorded by using an ultraviolet-visible spectrometer and plotted in Fig. 2.5. In this UV-vis spectrum, molecules absorb energy through the rotational and translational vibrations depending on the frequency of electromagnetic radiation. Excited molecules are unstable and quickly drop down again giving off the energy that they received from the electromagnetic radiation. The wavelength and intensity of the electromagnetic radiation absorbed can be recorded as a spectrum. The band gap of the nanotube using absorbance spectra has been calculated by using Eqn 2.4.

$$\alpha = \frac{K\left(h\nu - E_g\right)^{n/2}}{h\nu} \quad \ldots\ldots\ldots\ldots (2.4)$$

Where α is the absorption coefficient, K is a constant, E_g the optical band gap of CNT-based thin film and n is an integer equal to 1 for a direct band gap and 4 for an indirect band gap material. Data of energy and the absorbance plotted and shown as in situ curves of Fig. 2.5 ‘a’ & ‘b’. The band gap of nanotubes varied from 3.42 eV to 3.27

eV on varying the growth temperature of the sample from 650 ℃ to 750 ℃ because of hyperchromic effect. Also, the optical band gap of CNTs was determined by the circumferential quantum confinement and the solvent used [43]. In our case, the nanotubes were dissolved in the conducting polymer, i.e. n-methyl-pyrrolidone (NMP) and these NMP molecules react with the carbon atoms forming a helical structure around the MWCNTs [44,45]. As a result, the permittivity of the environment surrounding the MWCNTs increases with raising the energy bandgap. Also, it may be understood in terms of red-shift in optical transition energies of MWCNTs as "debundling" of MWCNTs occurred which causes a blue-shift in optical transition energy and the higher band gap was observed. The absorption peak of MWCNT appears at 249 nm which may be attributed as π to π^* transition from the density of state as previously reported by Ago et al [46]. The redshift of the sample prepared at 650 ℃ is higher than the sample prepared at 750 ℃ as shown in the Fig. 2.5 (b) confirming that the quantum confinement of nanotubes was increased on increasing the evaporation temperature. The lower bandgap of CNT prepared at 750 ℃ may be useful for the higher field emission property.

2.3.4. XRD analysis

The XRD pattern of MWCNTs powder was analyzed by XRD method using CuKα as a source and plotted in Fig. 2.6. The crystalline nature of CNTs was confirmed by XRD and peak indexing (002), (100), (101) reflects the hexagonal structure [47]. The presence of (002) peak in XRD confirms the multiwalled nature of carbon nanotubes.

The crystallite size of samples prepared at different temperature was calculated by using Debye-Sherrer formula as given in Eqn. 2.5 :

$$D = \frac{K\lambda}{\beta \mathrm{Cos}\theta} \quad \text{……..(2.5)}$$

Where D is the crystallite size, K is Debye-Sherrer constant having value 0.98, λ is the wavelength of CuKα (1.51 Å), β is the full-width half maxima (FWHM) and θ is the measured angle. The highest peak found at 26.232° for the samples prepared at temperatures 650 ℃ and 750℃ corresponds to FWHM values as 1.0576° and 0.96092° respectively. The crystallite sizes (diameters) of corresponding data were estimated as 16 nm and 14 nm respectively.

2.3.5. Particle size analysis

The particle size of CNTs was analyzed by using Nano Zeta Sizer (Nano ZS90) in which the size of the particle was measured by the Brownian movement of colloidal particles. For finding the size of the particle, firstly we prepared a dispersed solution of CNT in sulfuric acid and placed inside the chamber. The laser of wavelength 625 nm is passed through the solution and due to the Brownian motion of the particle scattering phenomenon occurred. The scattered output was received by the detector placed at 90° from the sample. The highly pure catalytic CNTs synthesized at temperatures 650 ℃ and 750 ℃ by following the same method were investigated (plotted in Fig. 2.7). The highest peaks of intensity may be seen at 185 nm and 260 nm which give major difference in CNTs prepared at different temperatures. The average length and diameter of nanotubes were calculated by using the data of particle size analyzer [40].

2.3.6 Raman analysis

Fig. 2.8 shows the Raman spectrum of CNTs synthesized at 650 ℃ and 750 ℃. The two main typical graphite bands are present in the Raman spectrum of the nanotubes: the band at 1590 cm^{-1} (G band) assigned to the in-plane vibration of the C–C bond (G band) typical of defective graphite-like materials and the band at 1310 cm^{-1} (D band)

activated by the presence of disorder in carbon systems. In this case, most of the graphitic layer converted into nanotubes. The I_D/I_G ratio of CNT synthesized at 650 ℃ is 1.58 and at 750 ℃ is 1.31 so it was found that the CNT synthesized at 750 ℃ have high yield with less defective sites and increased in graphitic nature.

2.4 Field emission analysis

Field emission is one of the most versatile characteristics of CNT based thin films. The field behaviour of both the pure CNT, samples has been investigated and analyzed in terms of Fowler-Nordheim (FN) relation of emission current density and applied field [48, 49] as given in Eqn 2.6:

$$J = A\frac{\beta^2 E^2}{\Phi}\exp\left(-\frac{B\Phi^{3/2}}{\beta E}\right) \qquad \text{……..(2.6)}$$

where A and B are the constants given by $A = \frac{e^3}{8\pi h} = 1.54\text{x}10^{-6}$ AeVV^{-2} and $B = \frac{8\pi}{3eh}(2m_e)^{\frac{1}{2}} = 6.83\ \text{x}10^9\ \text{eV}^{-3/2}\text{Vm}^{-1}$, where, e, h and m_e are the elementary positive charge, plank constant and the electron mass, respectively. Here J is the current density, Φ is the potential barrier height or the work function of the emitter material, E is applied field and β is the field enhancement factor which generally depends upon the geometry of the emitter, crystal structure, vacuum gaps and spatial distribution of electron-emitting centres. The two important parameters that need to be resolved in the existing field emission properties of CNT films are ‘threshold field’ and ‘emission current’. The threshold field is the field at which the emission begins. In order to make CNT based thin film as an efficient field emitting material, the threshold field must be low as much as possible and emission current should be high. The threshold field and the emission current of CNT films depend on the types of bonding, which can be controlled either by

synthesis condition or by growth temperature of elements. We have employed a novel CNT based tubular structure for obtaining efficient field emission. In addition, we have also recorded the field emission characteristics of pure CNT synthesized at 650 ℃ and 750 ℃. Fig. 2.9 (a) shows JE curves of CNTs evaluated from their respective I–V (current-voltage) charactristics. It is evident from the figure that on increasing the growth temperature from 650 to 750 ℃, the threshold field reduced from 0.25 μm to 0.15 μm and emission current improved from 0.1 V/μm to 0.3 V/μm, respectively. The field emission properties evaluated in the present work are comparable with other reported literature shown in Table 2.1. The high density and larger length of grown CNTs give a larger number of active sites for the field emission. The lower band gap in the range of 3.42 eV to 3.27 eV was evaluated in present CNTs which confirmed high electronegativity of these nanomaterials with low emission threshold. These results are comparable to other works [3, 4, 34-39] in which nanotubes with their high aspect ratio were proven useful for field emission at lower threshold voltages.

Fig. 2.9 (a) shows the I–V curve of the CNT cathodes made with the CNT samples prepared at 650 ℃ and 750 ℃ treated for 10 min in a vacuum chamber. The curves of Fig. 2.9 (a) show that as the voltage per unit length increases, the emission current also increases. After 0.06 V/μm, emission current decreases up to 0.17 V/μm due to tunnelling effect and becomes constant up to 0.2 V/μm. Later, the emission current increases with the increase of voltage. The Raman results also corroborate the field emission properties of these CNTs, according to which the graphitic nature boosts the electrons during emission. At the same time, defected graphite improves the emission threshold of CNTs.

This fact clearly indicates that the emission current level of nanotube was strongly depended on the field enhancement. The variation in the field enhancement factor (β) would need to be quantitatively calculated for the unambiguous study of the change in the density of emission sites caused by changes in synthesis temperature. The field enhancement factor (β) has been calculated using Eqn. 2.7.

$$\beta = \frac{Bd\emptyset^{3/2}}{\text{slope}} \ldots.(2.7)$$

where B is constant, d is the thickness of the spacer and $\emptyset = 5$ eV (work function of graphite). Here the values of β have been improved from 7708.50 to 9243.16 when the synthesis temperature increased from 650 ℃ to 750 ℃. The particle size reduction in CNTs exhibits the improvement of local field generation in the CNTs which increases the β. These results were found consistent with the observed morphological and structural changes (Fig. 2. 3(b) and (d)), but the FN curve in Fig. 2.8(b) did not follow the FN model well during the initial field emission ranges, as the field enhancement factor values for each condition had several ranges as this depending on the varied length of CNTs. So, the I-V curve following the FN equation after applied field exceed turn-on barrier can be explained.

The field emission property of CNTs indicates that they have high current levels and low emission threshold voltages [49, 50]. This is very close to the reported property of CNTs synthesized at high temperature and vacuum condition in laser ablation, microwave CVD and plasma-enhanced CVD [51-53]. Also, these CNTs have enhanced emission characteristics compared to bare metal and the silicon chip. As far as the application of CNTs in FED (Field Emission Display) is considered, synthesis and

growth of CNTs on catalyst substrates at a different temperature is demanding for the fabrication of FEDs which is a low-cost method.

2.4.1 Mechanism of Field emission

Fig. 2.10 (a) shows a possible model referring to explain the mechanism of the field emission behaviour in CNTs. As we know CNTs have a combination of sp^2 and sp^3 bonded carbon atoms. They have a very high aspect ratio and they also generate a local field in the presence of an externally applied field. In the present model, we refer the network pathway of sp^2 bonded carbon atoms and sp^3 sites in between them that gives their optimum ratio which reduces the threshold field along with improvement in emission current.

Fig. 2.10 (b) shows the emission that takes place from the metal surface is mainly determined by the strength of the magnetic field in combination with the magnitude of the work function. In general, as the electric field is increased, thermionic emission over the top of the surface barrier (work function) will occur, followed by the emission over the field reduced barrier (Schottky emission). The emission will then occur partly over the barrier (at enough high temperature) and partly through the barrier. As the temperature is lowered, emission will come from electron tunnelling through the barrier (Fowler-Nordheim tunnelling) from electron states at Fermi level.

The FN theory has been applied to explain the emission from the gated emission arrays, chemical vapour deposition (CVD) grown diamond film and carbon nanotube (CNTs). The standard FN theory is based on the assumptions that the metal has a free electron based structure and the electron in the metal obey Fermi-Dirac statistics and the description of the electron tunnelling can be described in terms of the Wentzel-Kramer-

Brillouin approximation and the barrier to emission can be represented by a triangular potential onto which a classical image potential is superimposed [54].

2.5 Application as Photosensor

To measure the photoelectric properties, visible light is vertically incident on the paper-based photosensor and corresponding photoelectric behaviour of the sensor has been recorded as shown in Fig. 2.11. The photoelectrical properties of MWCNT were investigated at different intensity and different ambient condition.

Fig. 2.12 shows the photo sensing behaviour of the photosensor at different light intensities. The curves show that the photocurrent increases on increasing light intensity. From the figure, it is clear that as time increases the photocurrent of the film increases drastically in the beginning, after that the photocurrent becomes constant. Finally, when switching off the source, the photocurrent of the film approaches to their initial value. Curve (a) shows the variation of photocurrent with time at 25 mW/cm^{-1} light intensity having low sensing response. Curves (b) and (c) show the variation in photocurrent with time at 50 mW/cm^{-1} and 75 mW/cm^{-1} respectively. Both the curves show better sensing response in comparison with the previous one but the highest sensing response has been found at 100 mW/cm^{-1} as shown by curve (d).

Figure 2.13 shows the repeatability of the photosensor at 50 mW/cm^{-1} with the variation of photon emission time and we found that the amount of photocurrent is only dependent on the photon intensity and independent of the variation of emission time. Fig 2.13 shows the variation in photocurrent for 5 sec of photoemission and Fig. 2.13 (b) shows the variation in photocurrent for 10 sec of photoemission.

Response and recovery times were calculated and minimum response and recovery were found as 20 ms and 12 ms respectively at 25 mW/cm^{-1}. The response and recovery time are measured by using exponential fitting of data using the following equations (2.8) and (2.9):

$$I_m = I_0 \exp\left(\frac{-t}{t_{res}}\right) \text{……..(2.8)}$$

$$I_m = I_0\{1 - \exp\left(\frac{-t}{t_{rec}}\right)\} \text{……..(2.9)}$$

Here I_o is the initial current of the film, t_{res} and t_{rec} are response and recovery time respectively. The response time is defined as the time required to acquire the 90% of the maximum current and recovery time is defined as the time required to achieve the initial value of current.

Fig. 2.14 (a) shows the variation in sensitivity at different illumination intensity and the maximum sensitivity (4.4 μA/sec) was found at 100 mW/cm^{-1}. Fig 2.14 (b) shows the response and recovery time of the photosensor and minimum response and recovery time have been found as 20 ms and 12 ms respectively at 25 mW/cm^{-1}.

2.6 Theoretical investigation

To explain the observed result, we have designed a theoretical model of different length of CNT using Gauss view 05 and Gaussian 09 for FED. In the thin film, the current pathway is formed only across nanotubes. The overall current at the lower threshold voltage across the thin film is the sum of current passing through the individual nanotube.

For observing the current generated through the film at a lower threshold, we choose CNT of different length and analyzed the change formed in the electron affinity, ionization potential and the HOMO-LUMO gap by increasing the length. After analyzing the change in the energy level of the CNT we multiply the energies with the number of CNTs present in the thin film. In such molecular model, the calculation was carried out by using armchair (1,1) (2,2) (3,3) and (4,4) nanotube and the calculation method as B3LYP with basis set 6-31 G. In whole calculation, the spin is taken to be single with C1 point group null charge. In this computational method, we analyzed the electron affinity, ionization potential and HOMO-LUMO gap by increasing the length of CNT.

Table 2.2 shows the change found in the energy and different theoretical parameters before and after interaction with LPG and humidity. In case of electronegativity, hardness, softness and nucleophilicity index, we first calculate Higher Occupied Molecular Orbit (HOMO) and Lower Unoccupied Molecular Orbit (LUMO) and later calculated these parameters using the formula given in Eqn 2.10-2.14:

$$\text{Ionization Potential (IP)} = -\varepsilon\text{HOMO} \quad \text{…….(2.10)}$$

$$\text{Electron Affinity (EA)} = -\varepsilon\text{LUMO} \quad \text{……(2.11)}$$

$$\text{Electronegativity } (\chi) = \frac{I+A}{2} \quad \text{……..(2.12)}$$

$$\text{Hardness } (\eta) = \frac{I-A}{2} \quad \text{……..(2.13)}$$

$$\text{Softness (s)} = \frac{1}{\eta} \quad \text{……..(2.14)}$$

Where “I” is ionization potential and “A” is electron affinity.

The nucleophilicity index was calculated by using hardness and electronegativity of the material from the Eqn. 2.15.

$$\text{Nucleophllicity index} = -\frac{\chi^2}{2\eta} \text{……..(2.15)}$$

From the Table 1.2, we observe that the electron affinity, ionization potential and the HOMO-LUMO gap decrease with increasing the length of tube, leading to the conclusion that if the length of the nanotube increases more than 100 nm, the value of electron affinity and ionization potential comes to be negative and band gap decreases to ~0 eV which is more useful for the FED. The electron affinity is related to the sp^2 hybridized carbon, which is responsible for the bending of step potential and the ionization potential is related to the sp^3 hybridized carbon which is responsible for electron tunnelling. From the above data, we conclude that for CNT having a higher length gives higher emission current which was similar to our experimental data.

2.7. Conclusion

The MWCNTs were grown at different temperatures (650 ℃ & 750 ℃). The monitoring of the evaporation temperature during the nanotube growth was used to explore the capacity of CNTs as field emitters, which results in the improved field enhancement factor (β) by 971. It was found that heat treatment affected the surface morphology of CNTs and its device structure may be used as a parameter for an FE application. Also, it is concluded that the improved FE properties are responsible for the increased generation of electron emission sites. Such type of nanotubes is also used in photosensors and the highest sensitivity of the sensor has been found as 4.4μA/sec at 100 mW/cm^{-1}. The minimum response and recovery time have been found as 20 ms and 12 ms respectively at 25 mW/cm^{-1}. The experimental result was found very analogous to the predicted theory which is unique.

References

[1] N. Dwivedi, S. Kumar, R. K. Tripathi, H. K. Malik, O. S. Panwar, Field emission, morphological and mechanical properties of variety of diamond-like carbon thin films. Applied Physics A 105 (2011) 417.

[2] R. K. Tripathi, O. S. Panwar, A. K. Srivastava, Ishpal, M. Kumar, and S. Chockalingam, Structural, Nanomechanical, and Field Emission Properties of Amorphous Carbon Films Having Embedded Nanocrystallites Deposited by Filtered Anodic Jet Carbon Arc Technique. Journal of Nanoscience 11 (2013) 2013.

[3] N. Dwivedi, S. Kumar, R. K. Tripathi, J. D. Carey, H. K. Malik, M. K. Dalai, Structural and Electronic Characterization of Nanocrystalline Diamond like Carbon Thin Films. ACS applied materials & interfaces 4 (2012) 5309.

[4] N. Dwivedi, S. Kumar, J. D. Carey, R. K. Tripathi, H. K. Malik, M. K. Dalai, Influence of Silver Incorporation on the Structural and Electrical Properties of Diamond-Like Carbon Thin Films. ACS Applied Materials & Interfaces 5 (2013) 2725.

[5] U. Kumar, S. Sikarwar, R. K. Sonkar, B. C. Yadav, Carbon nanotube: synthesis and application in solar cell. Journal of Inorganic Organometallic Polymers 26 (2016) 1231.

[6] S. Iijima, Helical microtubules of graphitic carbon Nature 354 (1991) 56.

[7] U. Kumar, B. C. Yadav, Synthesis of carbon nanotube by direct liquid injection chemical vapor deposition method and its relevance for developing an ultra-

sensitive room temperature based CO_2 sensor, J. Taiwan Inst. Chem. Eng. 96 (2019) 652.

[8] U. Kumar, B. C. Yadav, State of Art: An Approach to the Synthesis of Pure and Doped Graphene. Advanced Science, Engineering and Medicine 10 (2018) 638.

[9] R. Malik, V. K. Tomer, T. Dankwort, Y. K. Mishra, L. Kienle, Cubic mesoporous Pd–WO3 loaded graphitic carbon nitride (g-CN) nanohybrids: highly sensitive and temperature dependent VOC sensors. Journal of Materials Chemistry A 6 (2018) 10718.

[10] F. Schütt, S. Signetti, H. Krüger, S. Röder, D. Smazna, S. Kaps, S.N. Gorb, Y. K. Mishra, N. M. Pugno, R. Adelung, Hierarchical self-entangled carbon nanotube tube networks Nature communications 8 (2017) 1215.

[11] E. L. Silva, Y. K. Mishra, A. J. S. Fernandes, R. F. Silva, J. Strobel, L. Kienle, R. Adelung, F. J. Oliveira, M. L. Zheludkevich, Direct Synthesis of Electrowettable Carbon Nanowall–Diamond Hybrid Materials from Sacrificial Ceramic Templates Using HFCVD. Advanced Materials Interfaces (2017) 41700019.

[12] E. Singh, R. Srivastava, U. Kumar, A. D. Katheria, Carbon Nanotube: A Review on Introduction, Fabrication Techniques and Optical Applications. Nanoscience and Nanotechnology Research 4 (2017) 120.

[13] A. Singh, K. Senapati, M. Kumar, T. Som, A. K. Sinha, P. K. Sahoo, Role of work function in field emission enhancement of Au island decorated vertically aligned ZnO nanotapers. Applied Surface Science 411 (2017) 117.

[14] S. Ding, Y. Zhou, M. Ye, W. Lei, Hierarchically Structured Ni3S2/Carbon Nanotube Composites as High Performance Cathode. Vacuum 139 (2017) 33.

[15] Y. Y. Wang, S. Gupta, M. Liang, R. J. Nemanchin, Increased field-emission site density from regrown carbon nanotube films. Journal of Applied Physics 97 (2005) 104309.

[16] A. Muhulet, F. Miculescu, S. I. Voicu, F. Schütt, V. K. Thakur, Y. K. Mishra, Fundamentals and scopes of doped carbon nanotubes towards energy and biosensing applications. Materials Today Energy 9 (2018) 154.

[17] S. Matsunaga, Y. Suwa, S. Katagiri, Nanometer-scale discernment of field emission from tungsten surface with single carbon monoxide molecule. Applied Surface Science 666 (2017) 9.

[18] P. K. Bankara, S. Rahab, M. A. Morea, D. J. Late, C. S. Route, Enhanced field emission performance of $NiMoO_4$ nanosheets by tuning the phase. Applied Surface Science 418 (2017) 270.

[19] R. Kumar, R. K. Singh, A. K. Singh, A. R. Vaz, C. S. Routd, S. A. Moshkalev, Facile and single step synthesis of three dimensional reduced graphene oxide-$NiCoO_2$ composite using microwave for enhanced electron field emission properties. Applied Surface Science 416 (2017) 259.

[20] H. Jadhav, S. Suryawanshi, M.A. Moreb, S. Sinha, Pulsed laser deposition of tin oxide thin films for field emission studies. Applied Surface Science 419 (2017) 764.

[21] X. Wu, Y. Wang, P. Yang, The field emission properties from the pristine/B-doped graphene–C70 composite. Physics Letters A 381 (2017) 2004.

[22] M. Sveningsson, R. E. Morgan, O. Nerushev, E. E. B. Campbell, Electron field emission from multi-walled carbon nanotubes Carbon 42 (2004) 1165.

[23] J. E. Jung, Y. W. Jin, J. H.Choi, Y. J. Park, T. Y. Ko, D. S. Chung, J. W. Kim, J. E. Jang, S. N. Cha, W. K. Yi, S. H. Cho, M. J. Yoon, C. G. Lee, J. H. You, N. S. Lee, J. B. Yoo, J. M. Kim, Fabrication of triode-type field emission displays with high-density carbon-nanotube emitter arrays. Physica B 323 (2002) 71.

[24] Y. Shiratori, K. Furuichi, Y. Tsuji, H. Sugime, S. Noda, Efficient field emission from triode-type 1D arrays of carbon nanotubes. Nanotechnology 20 (2009) 475707.

[25] Y. Saito, S. Uemura, Field emission from carbon nanotubes and its application to electron sources. Carbon 38 (2000) 169.

[26] R. Atchudan A. Pandurangan, The use of bimetallic MCM-41 mesoporous catalysts for the synthesis of MWCNTs by chemical vapor deposition. J. Mol. Catal. A 355 (2012) 75.

[27] R. Atchudana A. Pandurangan, Growth of ordered multi-walled carbon nanotubes over mesoporous 3D cubic Zn/Fe-KIT-6 molecular sieves and its use in the fabrication of epoxy nanocomposites. Micropor. Mesopor. Mater. 167 (2013) 162.

[28] R. Atchudan, J. Joo, P. Arumugam, An efficient synthesis of graphenated carbon nanotubes over the tailored mesoporous molecular sieves by chemical vapor deposition. Mater. Res. Bull. 48 (2013) 2205.

[29] R. Atchudan, A. Pandurangan, K. Subramanian, Effect of reaction parameters on the growth of MWCNTs using mesoporous Sb/MCM-41 by chemical vapour deposition. Appl. Surf. Sci. 258 (2011) 1045.

[30] R. Atchudan, T. N. J. I. Edison, S. Perumal, D. R. Kumar, Y. R. Leea, Direct growth of iron oxide nanoparticles filled multi-walled carbon nanotube via chemical vapour deposition method as high-performance supercapacitors. Int. J. Hydrogen Energy 44 (2019) 2349.

[31] E. Singh, U. Kumar, R. Srivastava, B. C. Yadav, Carbon Nanotubes Based Thin Films as Opto-Electronic Moisture Sensor. Advanced Science, Engineering and Medicine 10 (2018) 790.

[32] J. E. Herrera, D. E. Resacso, Loss of single-walled carbon nanotubes selectivity by disruption of the Co–Mo interaction in the catalyst. Journal of Catalysis 221 (2004) 354.

[33] S. Maruyama, R. Kojima, Y. Miyauchi, S. Chiashi, M. Kohno, Ionization and structural determination of the major isomer of Pr@C82. Chemical Physics Letters 360 (2002) 229.

[34] Z. Lu, W. Wang, X. Ma, N. Yao, L. Zhang, B. Zhang he Field Emission Properties of Graphene Aggregates Films Deposited on Fe-Cr-Ni alloy Substrates J. Nanomater. 2010 (2010) 148596.

[35] J. Dong, B. Zeng, Y. Lan, S. Tian, Y. Shan, X. Liu, Z. Yang, H. Wang, Z. F. Ren. Field emission from few-layer graphene nanosheets produced by liquid phase exfoliation of graphite J. Nanosci. Nanotechnol. 10 (2010) 5051.

[36] A. Malesevic, R. Kemps, A. Vanhulsel, M. Pal Chowdhury, A. Volodin, C. V. Haesendonck, Field emission from vertically aligned few-layer graphene J. Appl. Phys. 104 (2008) 084301.

[37] B. R. Huang, T. C. Lin, Y. K. Yang, S. D. Tzeng, The stability of the CNT/Ni field emission cathode fabricated by the composite plating method Diamond Relat. Mater. 19 (2010) 158.

[38] Z. G. Chen, J Zou Field emitters: ultrathin BN nanosheets protruded from BN fibers, J. Mater. Chem. 21 (2011) 1191.

[39] C. Y. Liu, W. S. Li, L. W. Chu, M. Y. Lu, C. J. Tsai, L. J. Chen, Nanotechnology 22 (2011) 055603.

[40] U. Kumar, B. C. Yadav, Development of humidity sensor using modified curved MWCNT based thin film with DFT calculations, Sensors and Actuators B Chemical, 288 (2019) 399.

[41] M. Shariat, S. Hosseini, B. Shokri, E. Neyts, Plasma enhanced growth of single-walled carbon nanotubes at low temperature: A reactive molecular dynamics simulation. Carbon 65 (2013) 269.

[42] A. K. Chatterjee, M. Sharon, R. Banerjee, M. N. Spallart. CVD synthesis of carbon nanotubes using a finely dispersed cobalt catalyst and their use in double layer electrochemical capacitors. Electrochimica Acta 48 (2003) 3439.

[43] G. A. Rance, D. H. Marsha, R. J. Nicholas, A. N. Khlobystova , UV–vis absorption spectroscopy of carbon nanotubes: Relationship between the π-electron plasmon and nanotube diameter. Chemical Physics Letters 493 (2010) 19.

[44] A. Ehsani, F. Babaei, H. Mostaanzadeha, Electrochemical and Optical Investigation of Conductive Polymer and MWCNT Nanocomposite Film. J. Braz. Chem. Soc. 26 (2015) 331.

[45] T. Hasan, V. Scardaci, P. H.Tan, A. G. Rozhin, W. I. Milne, A. C. Ferrari Stabilization and “Debundling” of Single-Wall Carbon Nanotube Dispersions in N-Methyl-2-pyrrolidone (NMP) by Polyvinylpyrrolidone (PVP). J. Phys. Chem. C, 111 (2007) 12594.

[46] H. Ago, T. Kugler, F. Caselli, W. R. Salanack, M. S. Shaffer, A. H. Windle, R. H..Friend, Work Functions and Surface Functional Groups of Multiwall Carbon Nanotubes. Journal of Physical Chemistry B 103 (1999) 8116.

[47] L. Cia, B. Wei, C. Xu, J. Liang, D. Wu, S. Xie, W. Zhou, Y. Li, Z. Liu, D. Tang, Crystallization behavior of the amorphous carbon nanotubes prepared by the CVD method. Journal of Crystal Growth 233 (2001) 823.

[48] W. Andrew, The physics of carbon nanotube devices The Physics of Carbon Nanotube Devices A volume in Micro and Nano Technologies (2009) 173.

[49] S. K. Srivastava, V. D. Vankar, D. V. Sridhar Rao, V. Kumar, Enhanced field emission characteristics of nitrogen-doped carbon nanotube films grown by microwave plasma enhanced chemical vapor deposition process. Thin Solid Films 515 (2006) 1851.

[50] L. Nilsson, O. Groening, C. Emmenegger, O. Kuettel, E. Schaller, L. Schlapbach, H. Kind, J. M. Bonard, K. Kern, Scanning field emission from patterned carbon nanotube films. Applied Physics Letters 76 (2000) 2071.

[51] R. K. Sonker, M. Singh, U. Kumar, B. C. Yadav, MWCNT doped ZnO nanocomposite thin film as LPG sensing. Journal of Inorganic Organometallic Polymer 26 (2016) 1434.

[52] H. Choi, Y. J. Shin, S. Cha, I. H. Kang, W. Bahng, Enhanced field-emission capacity by density control of a CNT cathode using post-plasma treatment. Solid State Communications 171 (2013) 50.

[53] J. G. Wen, Z. P. Huang, D. Z. Wang, J. H. Chen, S. X. Yang, Z. F. Ren, J. H. Wang, L. E. Calvet, J. Chen, J. F. Klemic, M. A. Reed, Growth and

characterization of aligned carbon nanotubes from patterned nickel nanodots and uniform thin films. J. Mater. Res. 16 (2001) 3246.

[54] J. D. Carey, Engineering the next generation of large-area displays: prospects and pitfalls. The Royal Society 10 (2003) 1283.

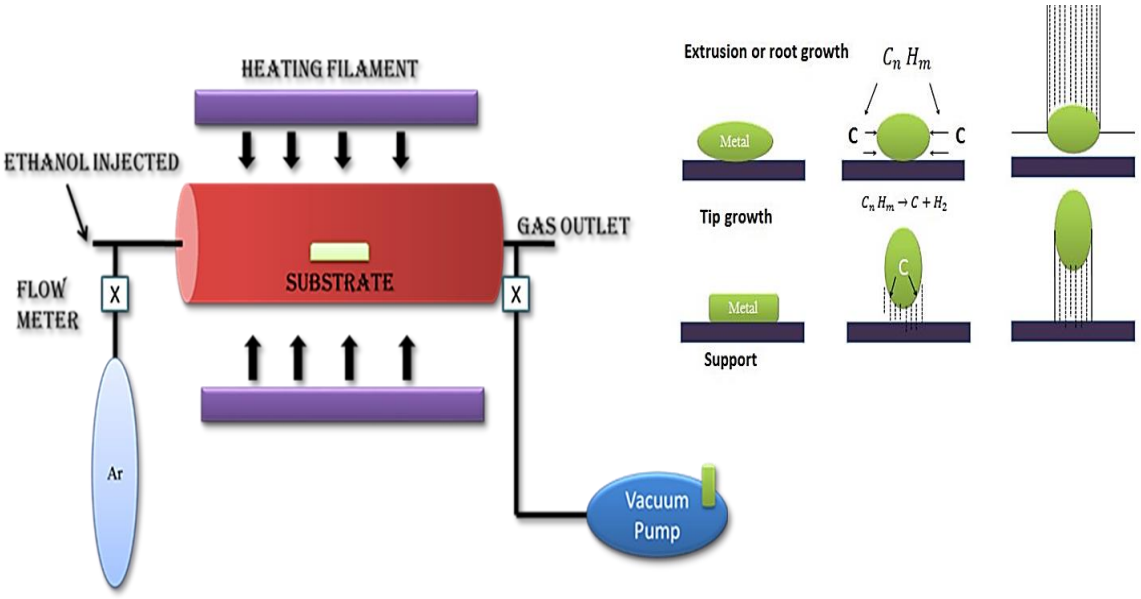

Fig. 2.1 Block diagram of the CVD chamber in DLICVD method and mechanism for the growth of CNT inside the CVD chamber

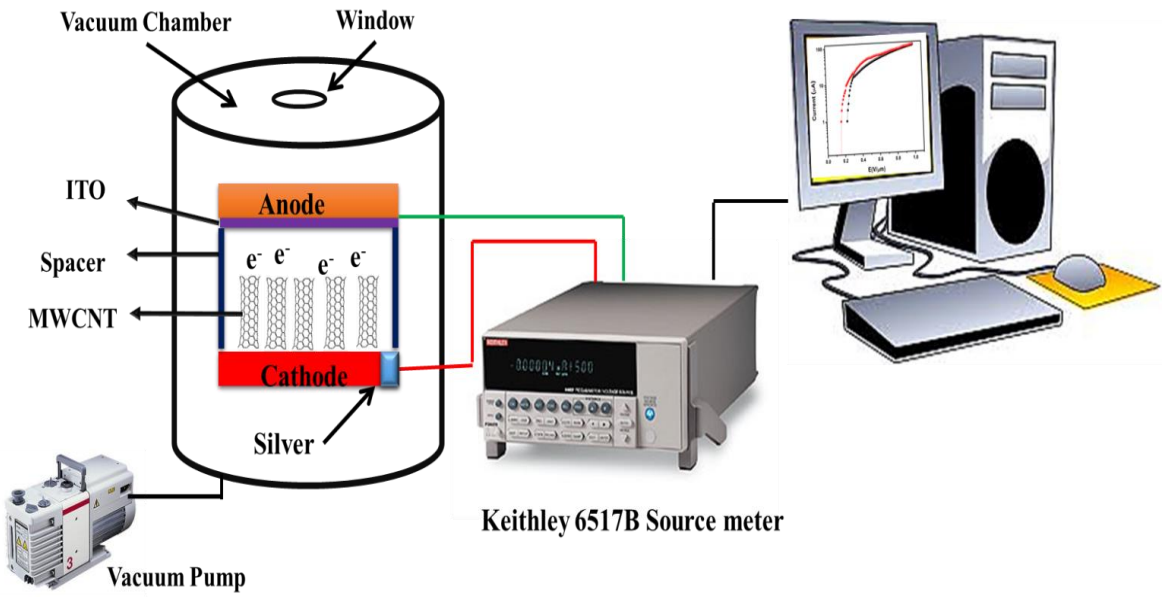

Fig. 2.2 The schematic representation of field emission set-up

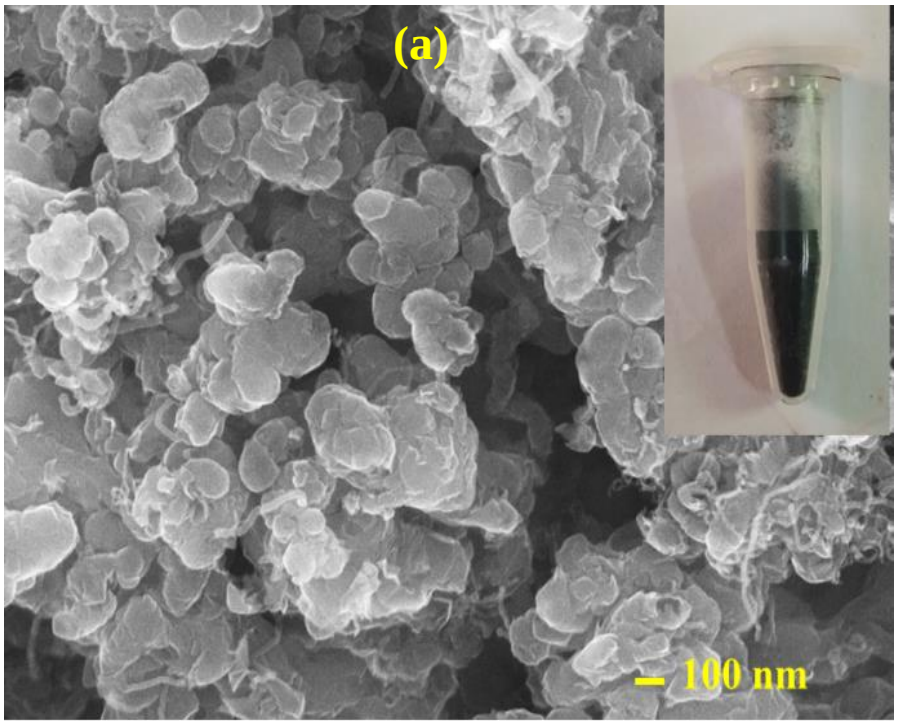
(a)
100 nm

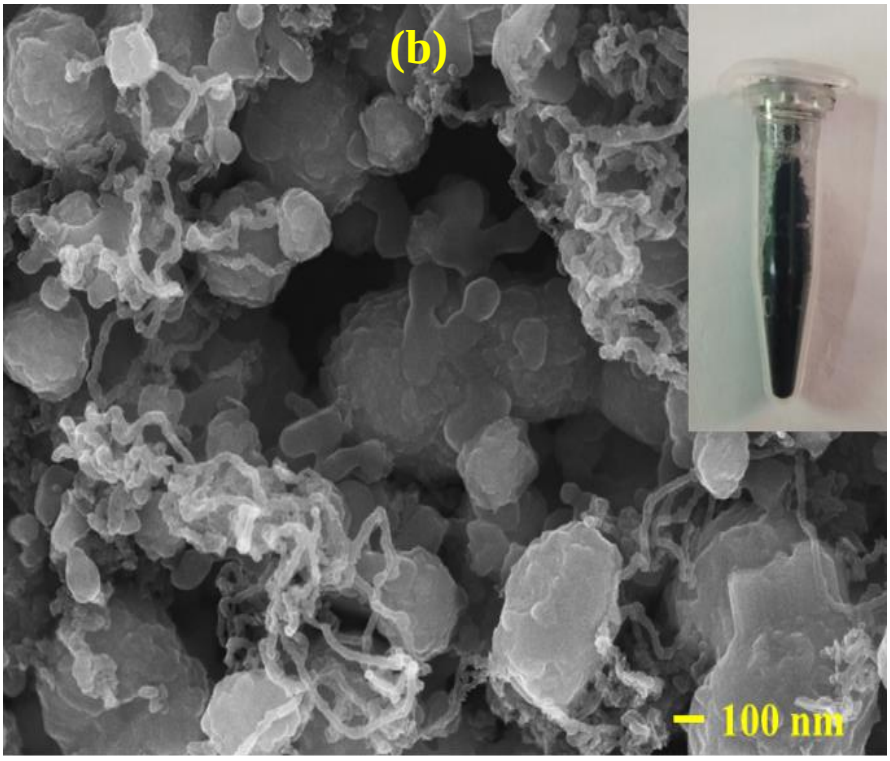
(b)
100 nm

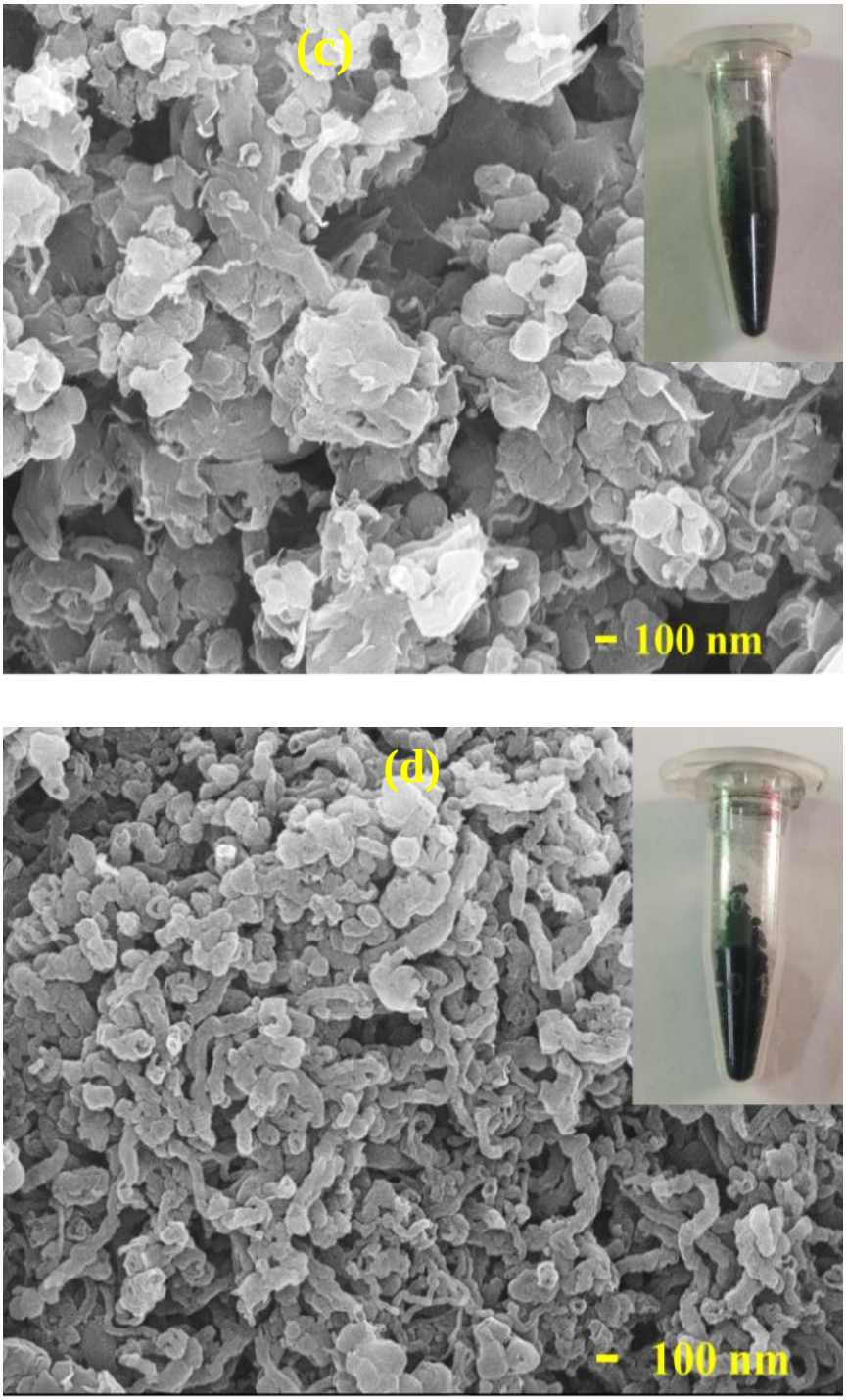

Fig 2.3. a) Growth of CNTs at 650 ℃ before purification b) After purification c) Growth of CNTs at 750 ℃ before purification d) After purification

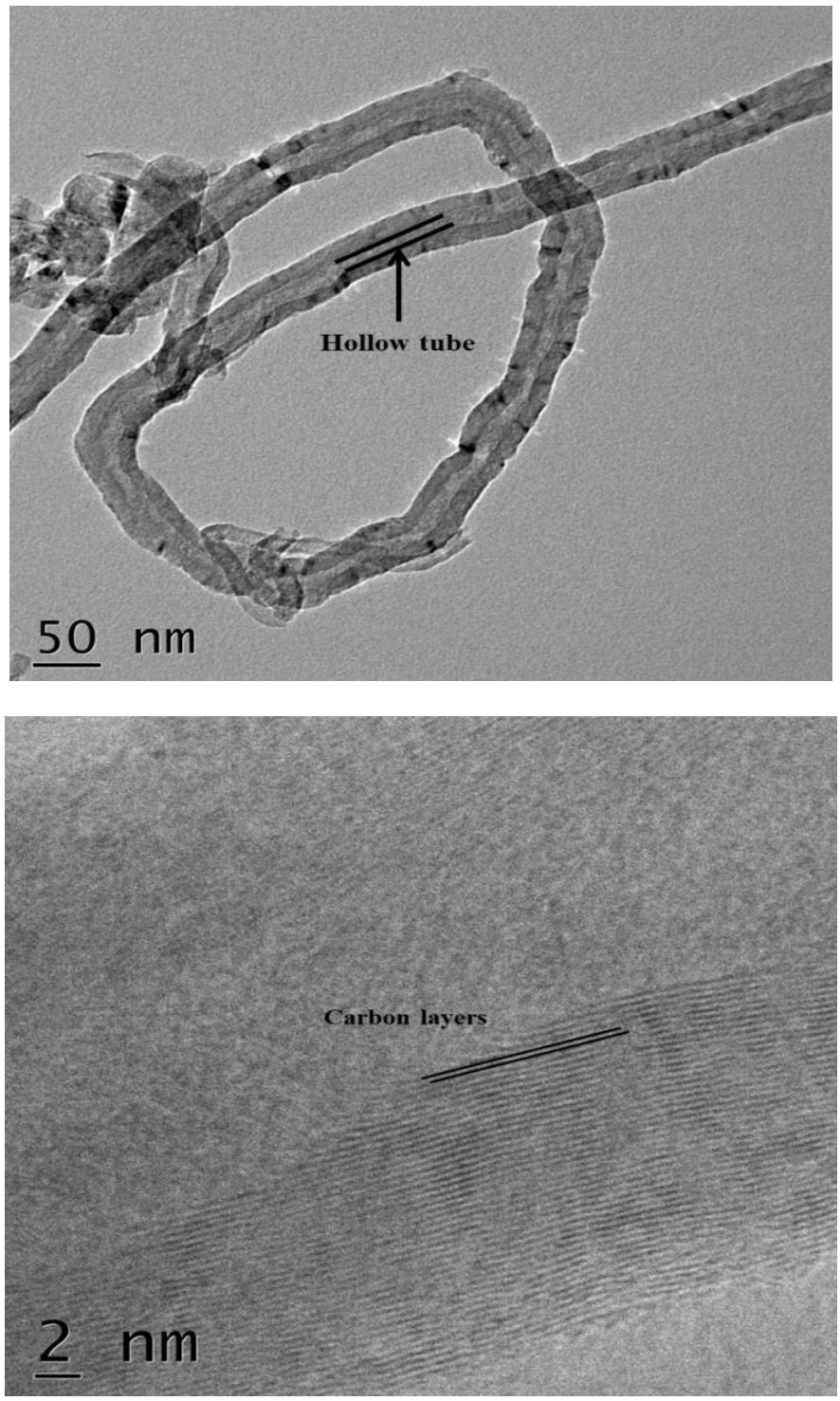

Fig. 2.4 TEM analysis of MWCNT at different scales

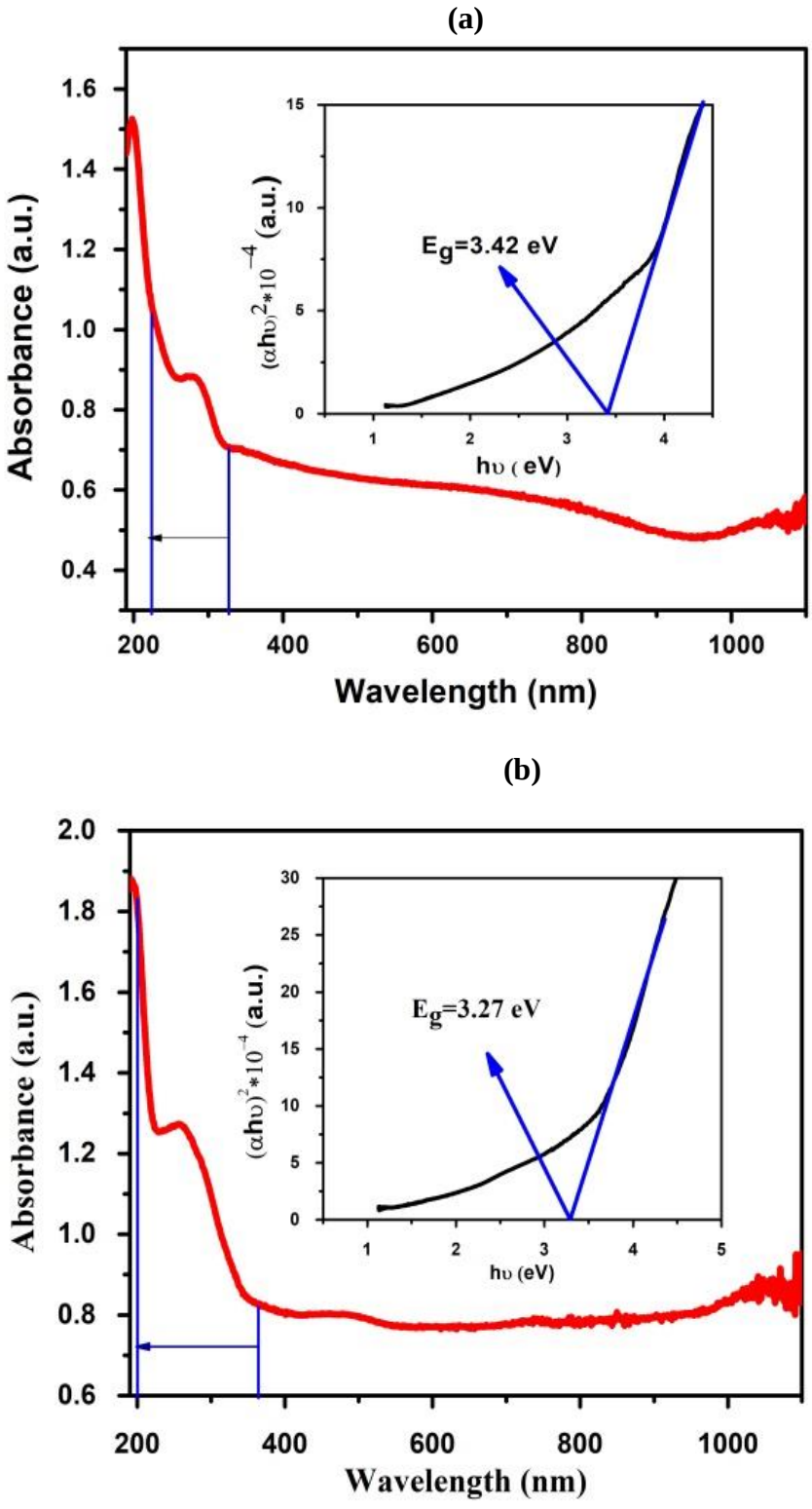

Fig 2.5 Tauc plot of CNTs at different temperatures (a) 650 ℃ (b) 750 ℃

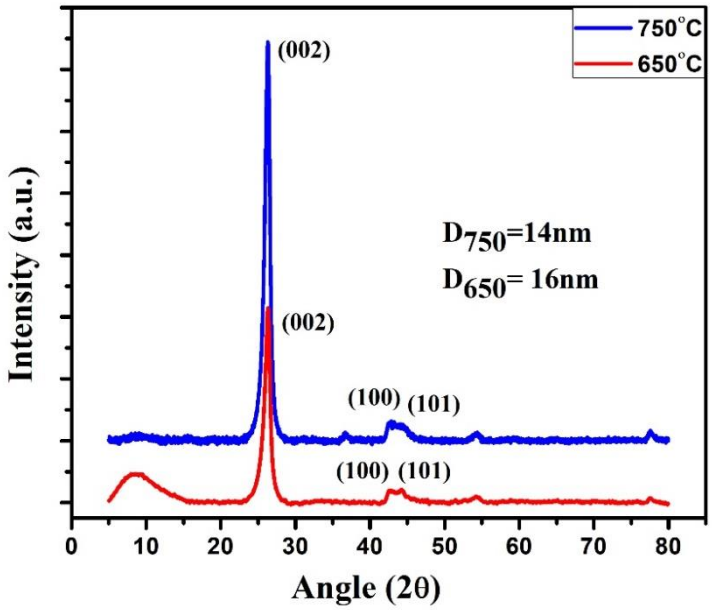

Fig. 2.6 XRD analysis of CNTs at different temperatures (a) 650 ℃ (b) 750 ℃

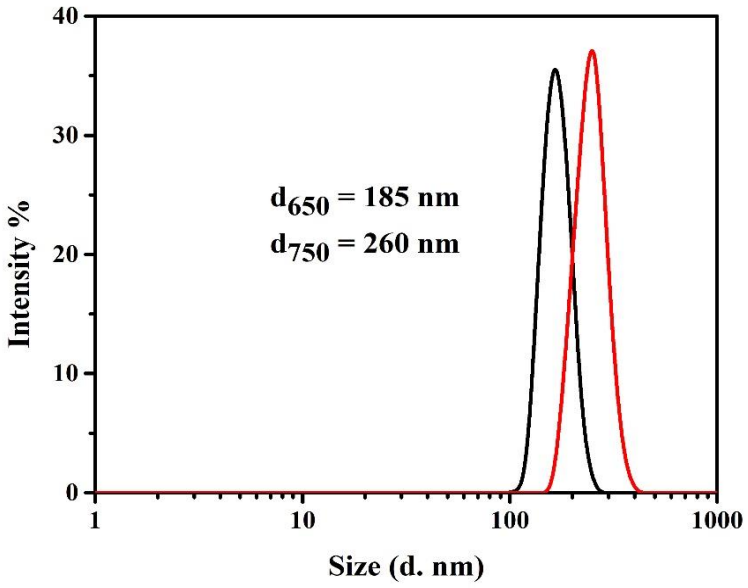

Fig. 2.7 Intensity vs particle size of CNTs synthesized at temperatures (a) 650 ℃ (b) 750 ℃

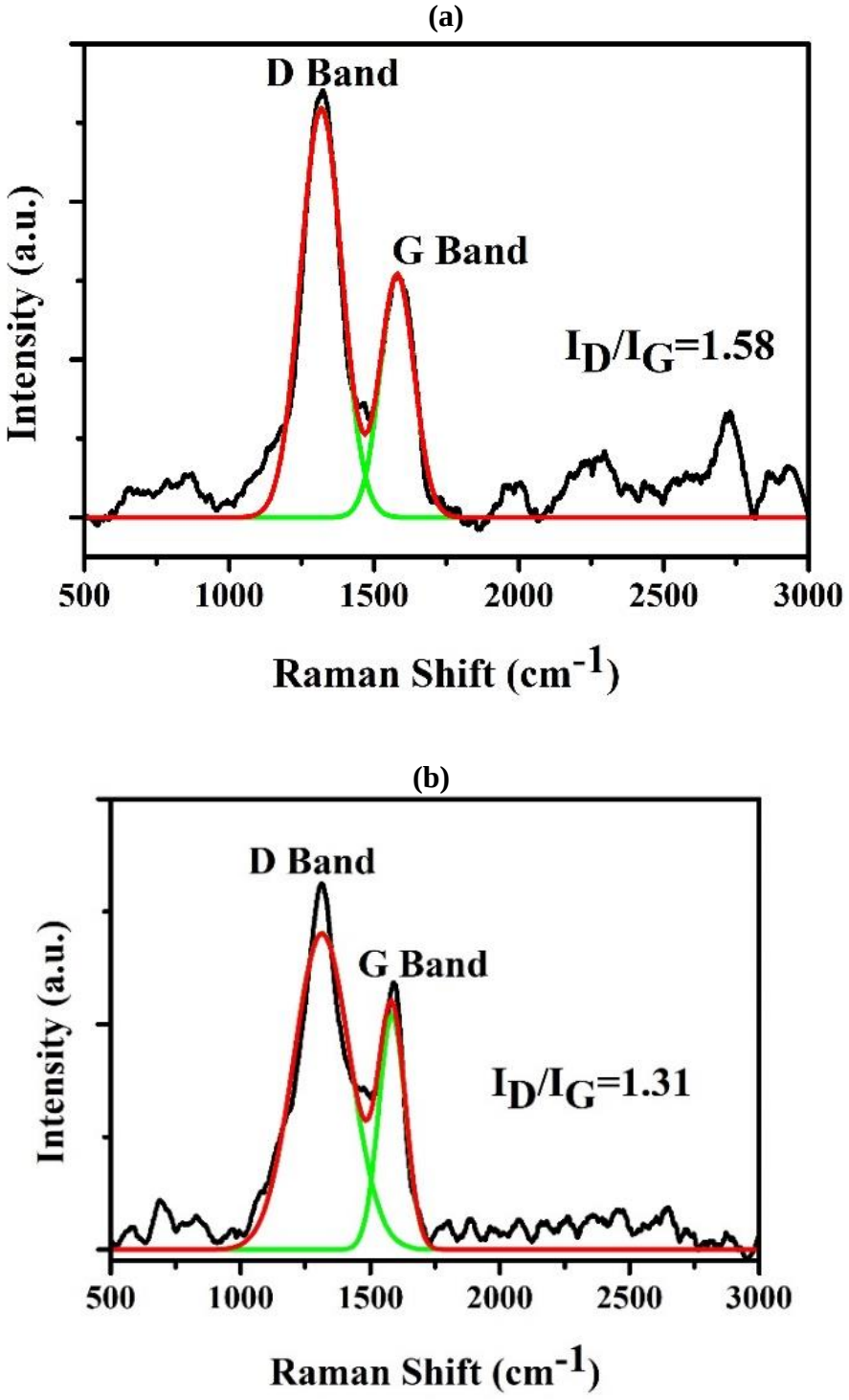

Fig. 2.8 Raman spectra of CNTs synthesized at (a) 650 ℃ (b) 750 ℃

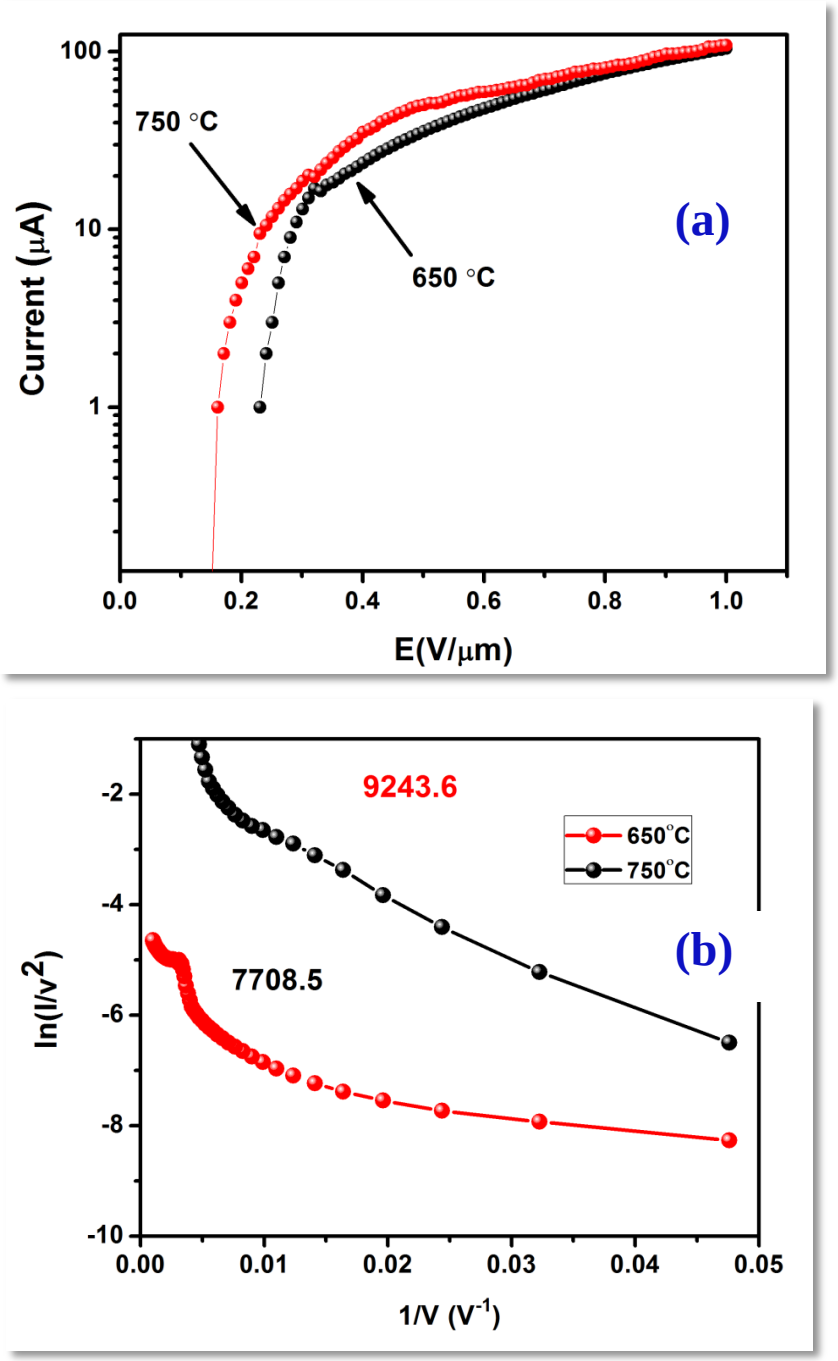

Fig. 2.9 (a) I–V curve of the CNT cathodes made by the CNT samples prepared at 650 ℃ and 750 ℃ (b) Fowler-Nordheim (FN) plots of emission data for CNT samples prepared at 650 ℃ and 750 ℃

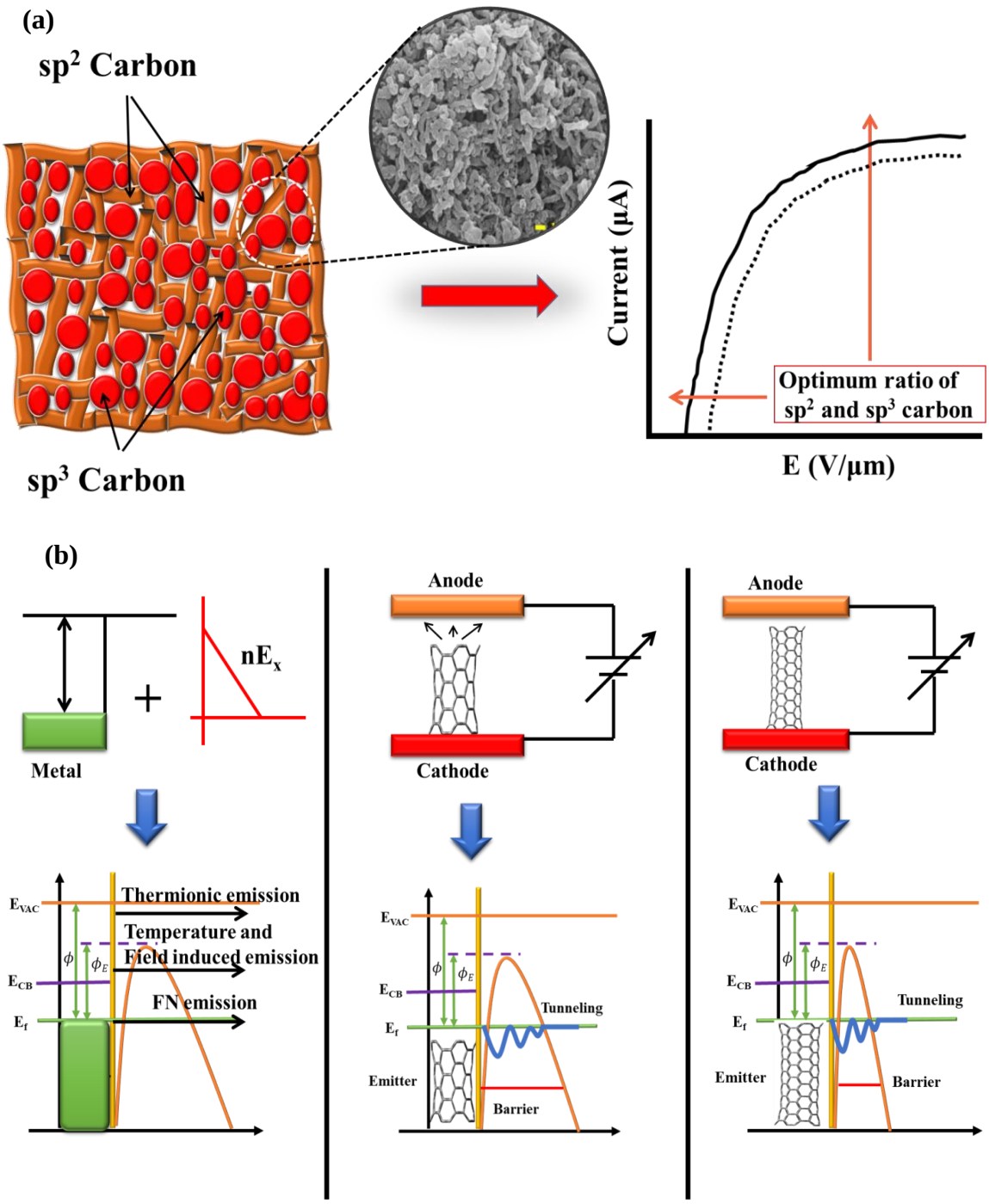

Fig. 2.10 (a) The transport of electrons between sp^2 cluster embedded in sp^3 rich matrix (b) Field emission mechanism in the presence of electric field and FE enhanced on increasing tube length

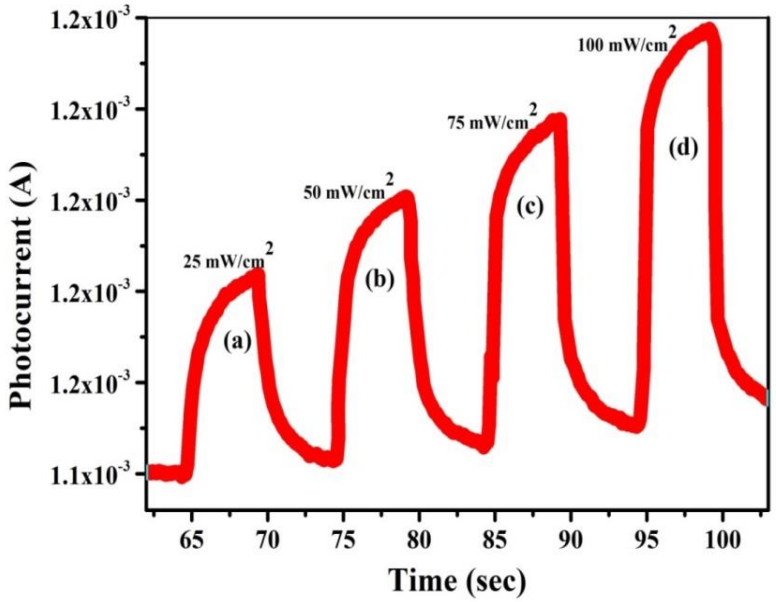

Fig. 2.11 Variation of photocurrent at different light intensities

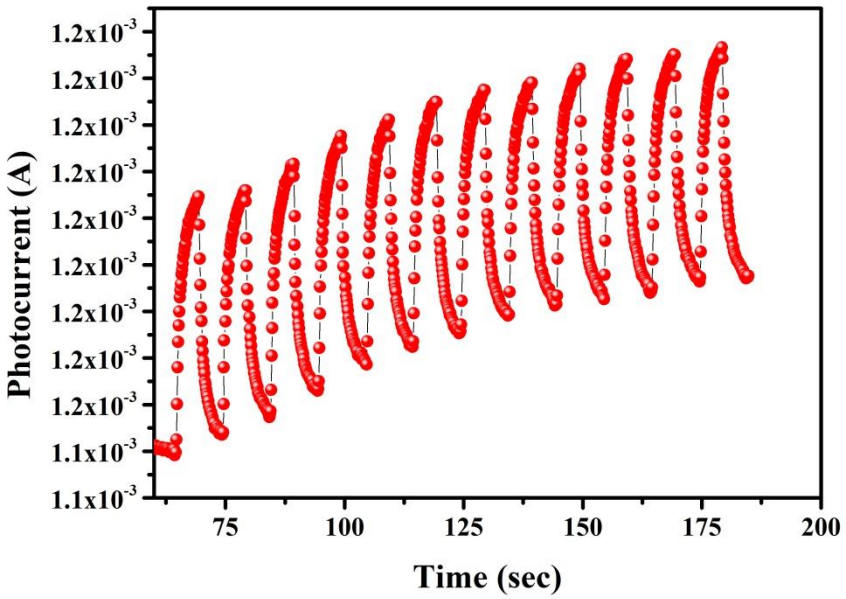

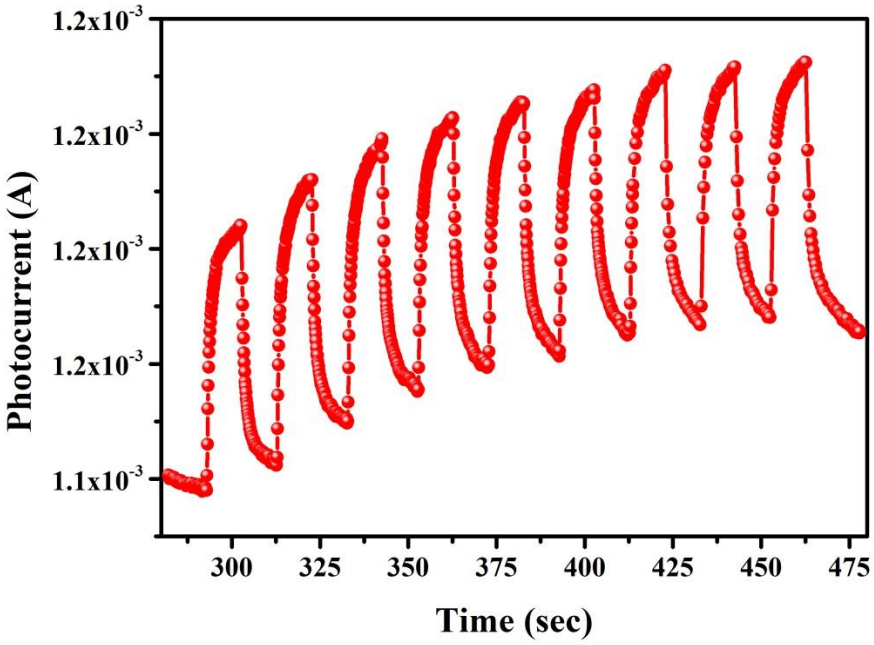

Fig. 2.12 (a) Variation in photocurrent for (a) 5 sec (b) 10 sec.

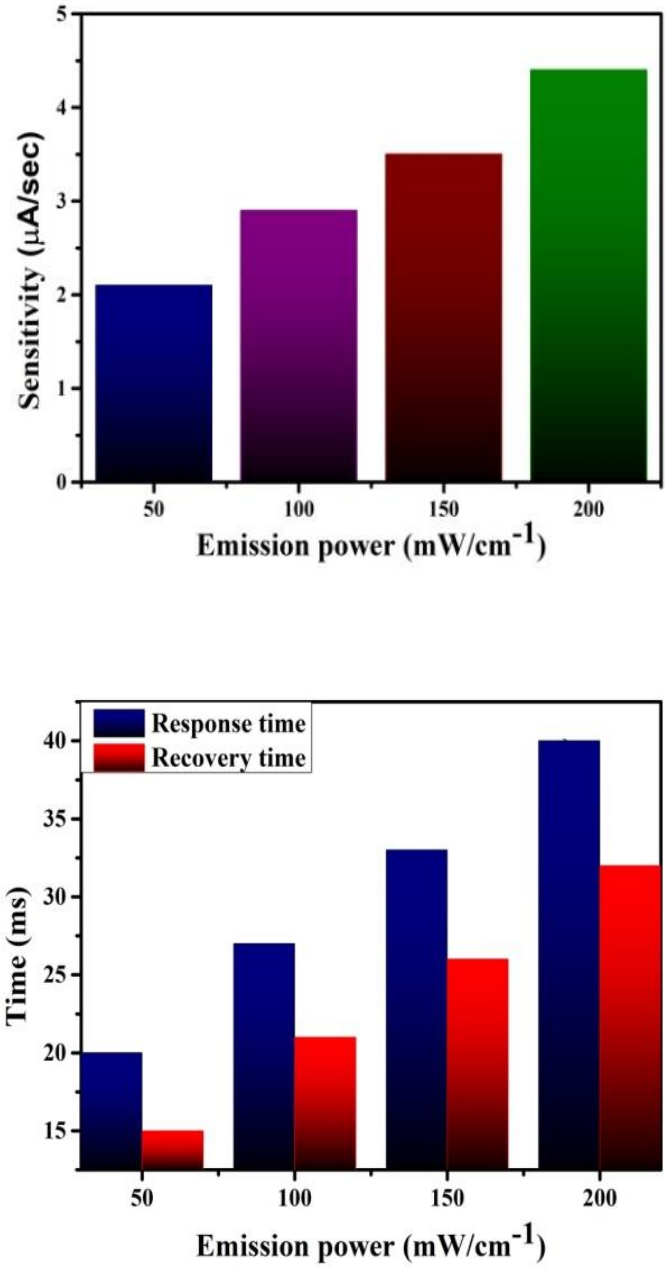

Fig. 2.13 (a) Average sensitivity of the sensor at various light intensity (b) response and recovery time of the sensor at various light intensities

Table 2.1 Field emission parameters of different types of nanomaterials.

S.No.	Nanomaterial	Turn on field (V/μm)	Field enhancement factor, β	References
1	Graphene aggregated films	1.0	5110	34
2	Few layered graphene nanosheets	1.7	7300	35
3	Vertically aligned few layered graphenes	1.0	5000	36
4	CNT-Ni composite emitter	1.1	2860	37
5	Ultrathin BN nanosheets protruded from BN fibres	1.9	1600	38
6	Si NW with $NiSi_2$ tip array	0.82	2440	39
7	Curved CNT synthesized using CVD	0.1	9243	Present paper

Table 2.2 Theoretical study of variation in different parameters by enhancing the tube length

Theoretical Parameters (a.u.)	**CNT (1,1)**	**CNT (2,2)**	**CNT (3,3)**	**CNT (4,4)**
Electron affinity	0.16361	0.16720	0.15270	0.15452
Ionization potential	0.19257	0.19249	0.20790	0.17534
HOMO-LUMO gap	0.02896	0.02529	0.0520	0.02082
Electronegativity	0.17809	0.17985	0.1803	0.1649
Hardness	0.01448	0.01264	0.0276	0.0104
Softness	69.061	79.08	36.23	96.06
Neucleophilicity Index	-1.095	-1.27	-0.588	-1.306

CHAPTER 3

MODIFICATION OF MULTIWALL CARBON NANOTUBE (MWCNT) USING N-METHYL PYRROLIDONE (NMP) AND ITS APPLICATION AS HUMIDITY SENSOR WITH DFT INTERPRETATION

One-dimensional carbon nanostructures e.g. Carbon nanotubes (CNTs) possess outstanding physical properties owing to their unique structure and atomic arrangement. High electrical conductivity, highly exposed surface area and stability of these carbon nanostructures introduce them as the leading choice of nanomaterials for a number of electrical and industrial applications like humidity and gas sensing. The conductance or capacitance of CNTs varies greatly with the adsorption-desorption of molecules such as hydroxyl (OH-) ions. In this paper, we report the preparation of carbon nanotubes based thin film using CVD technique which has been characterized by using Scanning Electron Microscopy (SEM), UV-visible microscopy and X-ray diffraction method. The characterized film was investigated as a humidity sensor. In the experimental part, the variations in the impedance of film were observed by Impedance Analyzer 6440 B on varying the humidity levels. In the theoretical part, we have simulated the CNTs using Ab initio density functional theory (DFT) calculations to investigate the formation of endohedral complexes among CNTs and OH- groups. The binding energy, dipole moment, electronegativity and HOMO-LUMO gaps were monitored by increasing the hydroxyl group levels which results in its better use in developing a robust and cost-effective humidity sensor.

CHAPTER 3

Modification of Multiwall Carbon Nanotube (MWCNT) using N-methyl pyrrolidone (NMP) and its application as humidity sensor with DFT interpretation

3.1. Introduction

Carbon is an exceptional and extraordinary element ever discovered. It has the capability to form different types of bonds with C atoms having varied bond lengths and strengths. This enables its presence in a variety of allotropes corresponding to the various geometries of C atoms. Carbon Nanotubes (CNTs), which consist of single or multiple cylindrical graphene layers, have received much attention due to their novel structural and electronic properties in current years [1–4]. Based on their excellent properties, many stunning applications have been suggested [5, 6]. Large quantities of CNTs are necessary for industrial applications. The electronic structures of carbon nanotubes (CNTs) depend strongly on diameter and chirality, thus CNTs with a narrow distribution of diameters are highly desirable for the investigation of physical properties and future application in nanoelectronics.

Among the various kinds of nanomaterials available for humidity and gas sensing applications, Carbon Nanotubes (CNTs) are interesting alternatives due to their remarkable characteristics such as high surface to volume ratio, outstanding electrical conductivity, high mechanical and chemical stability [7]. Also the nanotube has also such on outstanding property that it can detect the gas at a very low concentration which have already been reported in various journals [8- 10].

SWCNTs [11] are most favourable for device fabrication towards the sensing of different gases due to their purity and high electrical conductivity but experimentally MWCNTs have been more attractive because they can be produced in large industrial scale, reducing the production cost in comparison with SWCNT. Various methods have been developed for the integration or deposition of CNT over the surface of devices but

the direct liquid injection chemical vapour deposition (DLICVD) method is one of cheapest methods and can be employed for synthesizing ~ 100% pure nanotubes.

The content of water vapour present in the atmosphere is known as humidity and it plays a very significant role in day to day life of human beings and animals. Therefore, monitoring and control of humidity are essential for the industrial progress of the world. Electrical humidity sensors [12, 13] play an important role, besides requiring high sensitivity and reproducibility, sensors are also easily fabricated and used for most of the industrial purposes. Therefore, there is an ever-increasing need to develop a cheap and highly sensitive humidity sensor, which can be adapted to meet these requirements. Out of several humidity, sensitive compounds such as inorganic acetates, halides, nitrates, sulfates, carbonates, phosphates and oxides, metal oxides are considered to be the most promising candidate for this study because of their inherent chemical and physical stability [14-17]. Earlier investigations based on the study of the electrical behaviour of thin films have, however, shown that MWCNTs are one of the most promising materials, among carbon nanomaterials, for use in humidity sensors [18, 23, 25]. MWCNTs have a high capacity for adsorption of water molecules and its porosity is easily controlled. A detailed literature survey regarding this sensor has been carried out and the data have been presented as Table 3.1 which establishes the significance of MWCNT based humidity sensor. Sensitivity (pF/%RH) of modified MWCNT (dispersed in NMP) was found enhanced by six times.

3.2 Carbon nanotube-based humidity sensors

Nanostructured carbon materials like carbon nanotube and graphene have great potential for developing a new generation of chemical sensors to detect the gases and vapour species, particularly the humidity. MWCNT-based sensors have the following properties: high sensitivity due to the large surface to volume ratio, fast response, in the case of one-dimensional quantum wire nature, that makes its electronic properties very sensitive to gas adsorption, lower power consumption, which is ideal for persistent surveillance applications, small size and light weight.

Traditionally, nanotube-based humidity sensors are categorized in two ways; resistive type and capacitive type [27]. However, the basic mechanism is essentially the

same for both types, with the difference that, in the former, the physical parameter sensitive to the humidity variation is the electrical conductivity (σ) while, in the latter case, is the electrical permittivity $\in$. These parameters can be easily converted into resistance and capacitance respectively, taking into account the geometry of the sensor device.

3.3 Materials and methods

3.3.1 Synthesis and Characterization of Carbon Nanotubes

Highly oriented MWCNTs were synthesized by using direct liquid injection chemical vapour deposition (DLICVD) technique. In this process, firstly the Co substrate was put inside the programmable furnace and MWCNTs were directly grown on the substrate. Before starting the growth on the substrate, the substrate was cleaned by distilled water and acetone followed by propane-2-ol. Now the cleaned substrate was put inside the sonication chamber for 30 min. Later on, it was placed in a quartz tube inside the furnace and then the growth was initiated by the continuous flow of Argon (Ar) gas at the rate of 100 sccm. When the temperature of the furnace reaches 750 ℃, the catalyst particles create the nucleation points by the dissipation of energy then the ethanol was injected with the rate of 1 ml/min for 15 min. At this temperature, the ethanol was decomposed into acetylene and further into C and H_2 molecules. The H_2 gas emerged out with Ar and the C molecules were attached to the nucleation point which initiated the growth process. After the injection process, the temperature of the furnace was decreased slowly and the growth mechanism of the material was started in such a way that both the SWCNTs and MWCNTs were formed [28].

3.3.2 Device fabrication

An impedance-measuring holder was designed as shown in Fig. 3.1. For preparing sensing element the synthesized MWCNTs were functionalized by exohedral functionalization process. In this case, the MWCNT was put in the complex solution of nitric acid (HNO_3) and sulfuric acid (H_2SO_4) in the 3:1 ratio, then sonicated for 30 min. Later the solution was centrifuged several time at 2000 rpm and washed with distilled water so black precipitate was obtained. Further, this precipitate was dispersed in n-

methyl pyrrolidone (NMP) solution with 2 h of sonication, and then the modified MWCNTs have been formed. The sensing element of modified MWCNT (dispersed in NMP) in the form of a thin film having a thickness ~ 500 nm and a length of 1 cm was placed between the Ag electrodes arrangement. The Ag electrodes were square-shaped of side length 0.25 cm having a gap of 0.5 cm between them. The holder connected with impedance analyzer 6440 B was placed inside a controlled humidity chamber. A saturated solution of potassium hydroxide in deionized water was used as a dehumidifier and a saturated solution of potassium sulfate in deionized water was used as humidifier. Variations in impedance were noted by using the impedance analyzer. Relative humidity was measured using a standard hygrometer associated with a thermometer (Huger, Germany). The temperature of the chamber was maintained at 27 ℃ throughout the experiment and later it was dehumidified up to 10 %RH by using the dehumidifier.

3.4 Morphological and optical characterization

The surface morphological and structural property of thin film were characterized by using Scanning Electron Microscope (SEM) (JOEL JSEM 6490 LB) and Raman spectrometer (A Renishaw using 514.5 nm Ar^+ with power 15 mW) has been used for studying the structural properties. The data obtained by the XRD (Philips X'Pert Pro PAN analytical using laser source CuKα (1.542 Å) in scanning region from 10 to 90° with a scanning step of 0.02° per sec) were used for calculating the average crystallite size. Average dimensions of nanotube were measured by Particle Size Analyzer (NZS90 using a laser of 625 nm). The optical properties of the thin film were analyzed by UV-vis spectrophotometer (Evolution 302) and infrared spectrometer (Shimadzu 8700 1992). The humidity sensing parameters were measured by using Impedance analyzer (6400 B) which gives the variation of impedance and capacitance w.r.t. relative humidity with higher accuracy.

3.4.1 SEM analysis

Scanning electron microscopic (SEM) observations were performed with a JEOL JSM-6031 on the gold-coated surface of samples using secondary electron detector [29]. Fig. 3.2 (a-c) shows the SEM images of CNT at 500, 200 and 100 nm scale respectively.

Surface morphology of CNTs shows the porous structure that gives a higher surface area for the adsorption of water molecules. The EDX spectrum of MWCNT is shown in Fig. 3.2 (d). The X-axis of the spectrum represents the energy (keV) and Y-axis represented the count. We know that the X-rays are the characteristics of elements and hence in the spectrum, carbon (C) has been confirmed.

3.4.2 UV-vis spectroscopy

UV-visible spectroscopy was performed by using Evolution 302 spectrometer on thin film based sensor placed inside the chamber [30-32]. Fig. 3.3 shows the absorption spectra of CNTs ranging from 190 nm to 1100 nm wavelength and the estimated band gap was found as 3.75 eV.

The optical band gap of the film was analyzed by the absorption peak of the CNT towards the ultraviolet and visible region of electromagnetic spectrum. In our case, the higher band gap was found because of the dissolution of nanotubes in the conducting polymer i.e. n-methyl-pyrrolidone (NMP). These NMP molecules react with carbon atoms forming a helical structure around the MWCNTs. As a result, the permittivity of the environment surrounding the MWCNTs increases with raising the energy bandgap. Also, it may be understood in terms of a red-shift in optical transition energies of MWCNTs as “debundling” of MWCNTs was occurred which causes a blue-shift in optical transition energy and higher band gap was observed.

3.4.3 FTIR analysis

The vibration spectra and the different types of bonding found in nanotubes were analyzed by using Fourier transform infrared spectroscopy [33]. The vibration peak at 3100 cm^{-1} shows the sp^2 bonding in the nanotubes and if the band shifts towards the right-hand means near 3300 to 3350 and near 1600 then it causes aromatic ring and if both the behaviour show the IR spectra then it causes the formation of nanotubes as shown in Fig. 3.4.

3.4.4 XRD analysis

The samples were investigated through X-ray diffractometer along with the source CuKα. Fig. 3.5 shows the XRD pattern of MWCNT and the crystallite size of the sample prepared by the DLICVD technique at 750℃ was calculated using Debye-Scherrer formula for the plane 002 at a highest peak 26.232° [34-36]. In this pattern, peak (002) confirms the hexagonal structure of nanotubes [26]. FWHM was found as 1.0576° and corresponding estimated size was found 7.3 nm.

3.4.5 Particle size analysis

The particle size of the nanotubes was analyzed by using nano zeta sizer NZS90 in which the average particle size was measured by dynamic light scattering method which provides the bulk average of particles dispersed in solution as shown in Fig. 3.6. This method assumes a spherical particle with an aspect ratio of 1 while for a tubular structure, the aspect ratio is assumed as 1000 approximately. Dynamic Light Scattering (DLS) technique can measure its hydrodynamic diameter, and can be validated hypothetically using Eqn. 3.2 and 3.3 that describes the diffusion coefficient.

$$D = \frac{kT}{3\pi\eta L}\left[\ln\left(\frac{L}{d}\right) + 0.32\right] \ldots\ldots\ldots (3.1)$$

$$D = \frac{kT}{3\pi\eta D_h} \text{ Stock- Einstein}\ldots\ldots.(3.2)$$

k represents the Boltzmann constant; D represents the diffusion coefficient; T stands for temperature, D_h is the hydrodynamic diameter; η is the viscosity; and L and d represent the length and diameter of the nanotube respectively. Combining Eqns 3.1 and 3.2 which relates D_h to the nanotube's dimension in the form of Eqn. 3.3.

$$D_h = \frac{L}{\ln\left(\frac{L}{d}\right)+0.32}\ldots\ldots\ldots\ldots\ldots\ldots\ldots(3.3)$$

Applying Eqn. 3.3, the theoretical hydrodynamic diameter of nanotubes with length 1000 nm and the radial diameter of 7 nm is 200 nm. This theoretical hydrodynamic diameter correlates well with the hydrodynamic diameter acquired via DLS measurement. Since the high aspect ratio is present in MWCNTs, even the smallest error in the DLS measurement of the hydrodynamic diameter can result in significant

changes in the measured length. Hence, the measured length must be taken as an approximate value.

3.4.6 Raman analysis

Fig. 3.7 shows the Raman spectrum of MWCNT synthesized by using DLICVD method. The Raman spectrum of carbon nanotube (CNT) consists of two main graphitic bands. The band at 1360 cm^{-1} (D band) activated by the presence of the disorders in carbon system and the defective graphitic like materials another band at 1597 cm^{-1} (G band) assigned to the in-plane vibration of the C–C bond (G band). According to the literature, G bands are higher for samples containing large amounts of MWCNTs [37–41]. Due to having a less intensity of D peak, the formation of the nanotube in such case is very high with very fewer defects in the tube and most of the graphitic layers are converted into tubular structures [42–44].

3.5. Experimental investigation

3.5.1 Humidity sensing mechanism

The mechanism to interpret the electrical response of MWCNT based materials to humidity is based on the physically and chemically adsorbed water molecules as well as capillary condensation of water inside the walls of the nanotube and also on the tiny pores found in the film. The nanostructure and the surface reactivity with water are fundamental parameters for the performance of MWCNT based humidity materials [23, 45, 46]. Due to having the tubular structure of sensing element and highly porous film with a large surface to volume ratio is the key elements for humidity sensing. Water was absorbed by nanotubes when they were exposed to humidity leading to an increase in their electrical conductivity [25, 47]. Water adsorption inside the walls and surface functionalization of nanotubes are important for electrical conduction, being dominant for low relative humidity. Adsorbed water condensed on the surface of materials and protons were conducted in the form of aquatic layers. The larger is the surface area, the larger is the content of adsorbed water and, consequently, larger is the density of charge carriers, usually protons.

The operation of the sensor is based on the conductivity of the tubes and highly porous films due to having high surface area preferred for the humidity sensing investigation. The mechanism of the humidity is based on the physisorption and chemisorption of hydroxyl ion on the surface of MWCNTs. When the film interacts with the water molecule then physisorption of the water molecule with MWCNTs occured. Physisorbed water dissociates into H_3O^+ and OH^- because of high electrostatic fields at the interface between the surface and adsorbed layer. Transportation of charge occurs by movement of a proton from H_3O^+ ion to an adjacent water molecule and so on. Now, protonic conduction is set-up on the surface. This mechanism of charge transport is known as Grotthuss chain reaction mechanism as shown in Fig.3.8. Protonic conduction causes the observed drop in impedance in the humid atmosphere. At low humidity, only the surface protonic conduction causes a change in resistance. However, at higher values of humidity, water may condense polarize on the sensing surface; hence, electrolytic conduction also occurs, causing a large change in impedance [48].

3.5.2 Results and discussion

Fig. 3.9 shows the variation of the impedance of MWCNT based thin film for RH 10 % to 90% at room temperature. For lower humidity region from 10-40%, the sensitivity of the film is 13.63 MΩ/%RH. Similarly, for the mid humidity region 40-70%, the sensitivity of the film is 16.63 MΩ/%RH but in the higher humidity region, the sensitivity of the film enhances drastically and reaches to 161.93 MΩ/%RH. The mechanism of humidity sensing is based on the capillary action of the film which adsorbs the hydroxyl molecules from the atmosphere and gets polarized so the impedance of the device changes on changing the humidity level around them. For lower and mid humidity region the capillary action and polarization of molecule are very low but for higher humidity level the water molecule gets absorbed by most of the tubes and polarization increases so the higher change was observed. The average sensitivity of MWCNT based thin film sensor was found as 67.5% which is the best for fabricating MWCNT based humidity sensor. For low humidity region, the change in impedance with changing the humidity level is found very low because of having high binding energy in the MWCNT atoms but when the humidity level increases, the CNT gets polarized and drastic change

in impedance was found in higher humidity region [12, 23, 25, 49]. The response and recovery time indicates no variation along with the cycling measurement. The response and recovery speeds were investigated in dynamic measurement. Response time was defined as 90% of full response change while recovery time was set as the time when the response reaches 10% of the total value. The MWCNT based thin film presented a rapid response (24 sec) when environment changes from dry (30 %RH) to very humid (85 %RH), and a recovery time of 30 sec as displayed in Fig. 3.9 (c).

As in Fig. 3.10, the sensing curve shows the change in capacitance of the film with the variations of humidity levels. At lower humidity level, the MWCNTs were stable and no polarization was found in the tube so the capacitance was nearly same till 70 %RH and the average sensitivity of the film was found as 20.48 pF/%RH. After 70% of RH, the sensitivity of the thin film enhanced drastically and reached to 1882.63 pF/%RH as given in Table 3.2. In such case, the atmosphere contains a large amount of hydroxyl ion which is responsible for the polarization of MWCNT and later the drastic changes in capacitance were found. Response and recovery time were calculated and found as 32 sec and 36 sec respectively.

All the physical properties favour considering the porous nanotube film synthesized at 750 ℃ to be the best hydrophobic material in comparison with other metal oxide based sensors. The hydrophilic character of the surface should be helpful for improving the water molecule adsorption/ desorption process and hence, enhanced the sensitivity of the sensors. To investigate the effect of frequency on sensing a characteristic of MWCNT based sensor, its capacitance value has been calculated under different humidity environment with the variation of frequencies from 10^2 Hz to 10^6 Hz. The result is depicted in Fig. 3.11. It has been observed that the capacitance value decreases with increasing frequency and the rate of decrease is faster at higher %RH. The capacitance value increases significantly below 10^4 Hz and above this, the change is very less with the variation of humidity.

Generally, in the ideal capacitive sensor, the C value is independent of applied frequency. However, in low humidity region, the sensing material adsorbs a small number of water molecules, the sensing material possesses leak conduction (γ). The

capacitance (C) of the material with leak conduction can be expressed by thr relation given in the Eqn. 3.4.

$$C = \varepsilon^* C_0 = (\varepsilon_r - i\frac{\gamma}{\omega\varepsilon_0})C_0 \ldots..(3.4)$$

Where ε^*, C_0 and ε_r are the complex dielectric constant, capacitance and relative dielectric constant of an ideal capacitor, respectively; ω is the angular frequency, γ is the conductance and ε_0 is the permittivity of free space. From the equation, it can be noticed that the capacitance of the sensing material is inversely proportional to the frequency ω and directly proportional to γ. Hence, the value of capacitance decreases with increasing frequency and γ attributed to the physisorption of water molecules on the surface of porous CNT film [50]. The sensitivity of the sensor is defined as the change in output power (Impedance/Capacitance/Inductance) to the change in relative humidity.

3.5.3 Theoretical investigation

To explain the observed result, we have designed a theoretical model of CNT using Gaussian 09 and Gauss view 05 for the humidity sensing, and presented through the schematic of the conduction mechanism of CNTs in Fig. 3.8. On the glass, the current pathway is formed only across CNTs. The overall impedance of glass (Z_{Glass}) is composed of n resistances of k^{th} CNT (Z_{CNTk}) in series

$$Z_{Glass} = z_{(CNT1)} + z_{(CNT2)} + z_{(CNT3)} + \ldots\ldots\ldots\ldots\ldots + z_{(CNTk)}$$

For observing the change in impedance of the overall film, we choose a single CNT which interacts with the hydroxyl group. After analyzing the change in the energy level of CNT we multiply the energies with the number of CNTs present in the thin film. In such molecular model, the calculation was carried out by using armchair (2, 2) nanotube and the calculation method as B3LYP with basis set 6-31 G. In the whole calculation, the spin is taken to be single with C1 point group having a null charge. In this computation method, we analyzed the binding energy and HOMO-LUMO band gap before and after interacting with hydroxyl atom with CNTs. The sensing of carbon nanotubes directly depends on the variation of energy lattice sites because of the OH^- molecules interact only on lower energy sites and giving extra charge by endohedrally non-covalent functionalization method. Therefore, for finding the energy levels and free

energy sites, we firstly optimize the nanotube structure and find its lower energy levels that interact with OH^- molecules as shown in Table 3.3. The binding energy of the carbon atom on the substrate is calculated by using the following convention given in Eqn 3.5:

$$E_{bind} = E_{(nanotube)} - nE_{(C)}\text{.....}(3.5)$$

where $E_{(nanotube)}$, and $E_{(C)}$ stand for the total energies of the relaxed C atom in the nanotube and n is the number of carbon atoms. We also define the adsorption energy of the OH^- molecule on the adsorbent by using Eqn 3.6:

$$E_{ad} = E_{(OH^- + adsorbent)} - E_{(adsorbent)} - E_{(OH^-)}\text{.....}(3.6)$$

where $E_{(OH^- + adsorbent)}$, $E_{(adsorbent)}$, and $E_{(OH^-)}$ stand for the total energies of a system of OH^- molecule and the adsorbent (the adsorbents are CNT), isolated adsorbent, and isolated OH^- molecule [51-54].

In the case of adsorption of several molecules (for instance "N" molecules of OH) the average adsorption energy per molecule would be defined by using Eqn 3.7:

$$E_{ad}^{ave} = \frac{E_{(OH- + adsorbent)} - E_{(adsorbent)} - NE_{(OH-)}}{N}\text{.....}(3.7)$$

In the case of electronegativity, hardness, softness and nucleophilic index, we have first calculated Higher Occupied Molecular Orbit (HOMO) and Lower Unoccupied Molecular Orbit (LUMO) and later calculated these parameters using the following formula given in Eqn 3.8 to 3.10

$$\text{Electronegativity } (\mu) = -\frac{1-A}{2}\text{.....}(3.8)$$

$$\text{Hardness } (\eta) = \frac{I+A}{2}\text{.....}(3.9)$$

$$\text{Softness } (s) = \frac{1}{\eta}\text{.....}(3.10)$$

Where "A" is LUMO and "I" is HOMO.

The nucleophilicity index of the material is calculated by using electronegativity and hardness of the material using the relation given in Eqn. 3.11

$$\text{Nucleophilicity index} = -\frac{\mu^2}{2\eta} \ldots\ldots (3.11)$$

The binding energy and the band gap of the nanotube vary by increasing the hydroxyl level on the CNTs. The binding energy firstly decreases because of gaining free electrons from OH^- atom and when the humidity level becomes very high then rapid changes in the binding energy have been observed which are responsible for the change in impedance for higher humidity region as shown in experimental data.

It can be observed from table 3.3, the electronegativity increases with increasing the hydroxyl level which indicates that the bonding of CNT with hydroxyl ion is very high and due to having strong bonding between the CNT and hydroxyl ion, the electron cloud at the OH^- was formed so the nucleophilicity index (NI) of the material was also increased. Thus the theoretical model indicates that this material is more appropriate for the detection of humidity present in the atmosphere. On the analysis of data presented in the table, we found that the band gap of the CNTs was wider at lower humidity levels but after the rise of humidity level, the band gap of CNTs started decreasing and more electrons were transferred from valence band to conduction band. Consequently, the conduction band enriched with the free electrons and the impedance of the thin film starts decreasing and becomes constant at 90% which may be seen through Fig. 3.9.

3.6. Conclusion

Multiwall Carbon nanotubes (MWCNTs) were successfully synthesized via direct liquid injection chemical vapour deposition method and the minimum crystallite size or diameter of the nanotubes was found to be 7 nm. Surface morphology of thin film shows that most of the particles are cylindrical in shape leaving spaces as pores, and hence the film was found more sensitive. Maximum average sensitivities in terms of capacitance, impedance and inductance respectively were found as 18.8, 1.67 and 2.21 at 10^2 Hz. The results were found 82% reproducible after two months. Thus this material carries a good scope for the development of sensitive moisture sensors in the range of relative humidity from 10 to 90 %RH for the indoor and outdoor applications. Also, the derived theory confirms the experimental results.

References

[1] S. Lijima, Helical microtubules of graphitic carbon, Nature 354 6348 (1991) 56.

[2] M. S. Dresselhaus, Electronic, thermal and mechanical property of carbon nanotubes, Philo. Trans. R Soc. Lond. Ser. A Math. Phys. Eng. Sci. 362 1823 (2004) 2065.

[3] C. G. Lu, J. Liu, Controlling the diameter of carbon nanotubes in chemical vapor deposition method by carbon feeding, J. Phys. Chem. B 110 41 (2006) 20254-20257.

[4] S. Ming, B. Zheng, J. Liu, A scalable CVD method for the synthesis of single-walled carbon nanotubes with high catalyst productivity, Chem. Phys. Lett. 322 (2000) 321.

[5] S. Maruyma, R. Kojima, Y. Miyaunchi, S. Chiashi, M. Kohno, Low-temperature synthesis of high-purity single-walled carbon nanotubes from alcohol, Chem. Phys. Lett. 360 (2002) 229.

[6] L. M. Huang, Cobalt ultrathin film catalyzed ethanol chemical vapor deposition of single-walled carbon nanotubes, J. Phys. Chem. B 110 23 (2006) 11103.

[7] B. C. Yadav, R. Kumar, R. Srivastava, T. Shukla, Flame Synthesis of Carbon Nanotubes using Camphor and its Characterization, Int. J Green Nanotech. 3 (2011) 170.

[8] U. Kumar, S. Sikarwar, R. K. Sonkar, B. C. Yadav, Carbon nanotube: synthesis and application in the solar cell, J Inorg. Organomet. Poly. 26 6 (2016) 1231.

[9] R. K. Sonker, M. Singh, U. Kumar, B. C. Yadav, MWCNT Doped ZnO Nanocomposite Thin Film as LPG Sensing, J Inorg. Organomet. Poly. 26 6 (2016) 1434.

[10] U. Kumar, B. C. Yadav, Synthesis of carbon nanotube by direct liquid injection chemical vapor deposition method and its relevance for developing an ultra-sensitive room temperature based CO_2 sensor, Journal of Taiwan Institute of Chemical Engineering 96 (2019) 652.

[11] U. Kumar, B. C. Yadav, State of Art: An Approach to the Synthesis of Pure and Doped Graphene, Adv. Sc. Eng. Med. 10 (2018) 638.

[12] S. Arunachalam, A. A. Gupta, R. Izquierdo, F. Nabki, Suspended Carbon Nanotubes for Humidity Sensing, Sensors 18 (2018) 1655.

[13] E. Singh, U. Kumar, R. Srivastava, B. C. Yadav, Carbon Nanotubes Based Thin Films as Opto-Electronic Moisture Sensor, Adv. Sc. Eng. Med. 10 (2018) 790.

[14] H. J. Dai, Nanotube growth and characterization, Topics in App. Phys. 80 (2001) 29.

[15] X. Guo, J. P. Small, J. E. Klare, Y. Wang, M. S. Purewal, I. W. Tam, B. H. Hong, R. Caldwell, L. Huang, S. O'Brien, J. Yan, R. Breslow, S. J. Wind, J. Hone, P. Kim, C. Nuckolls, Covalently bridging gaps in single-walled carbon nanotubes with conducting molecules, Science 311 (2006) 356.

[16] Y. Y. Wang, S. Gupta, M. Liang, R. J. Nemanchin, Increased field-emission site density from regrown carbon nanotube, J. App. Phys. 97 (2005) 104309.

[17] M. Sveningsson, R. E. Morjan, O. Nerushev, E. E. B. Campbell, Field emission of electrons by carbon nanotube twist-yarns, Carbon 42 (2004) 1165

[18] S. Sikarwar, B. C. Yadav, Opto-electronic humidity sensor: A review, Sens. Actuators A: Phys. 233 (2016) 54.

[19] D. Z. Zhang, J. Tong, B. K. Xia, Humidity-sensing properties of chemically reduced graphene oxide/polymer nanocomposite film sensor based on layer-by-layer nano self-assembly, Sens. Actuators B: Chem.197 (2014) 66.

[20] M. S. Park, T. H. Lim, Y. M. Jeon, J. G. Kim, S. W. Joo, M. S. Gong, Humidity sensitive properties of copoly (TEAMPS/VP)/silver nanocomposite films, Sens. Actuators B: Chem. 133 (2008) 166.

[21] Q. Qi, Y. Feng, T. Zhang, X. Zheng, G. Lu, Influence of crystallographic structure on the humidity sensing properties of KCl-doped TiO_2 nanofibers, Sens. Actuators B: Chem. 139 (2009) 611.

[22] Q. Q. Lin, Y. Li, M. J. Yang, Polyaniline nanofiber humidity sensor prepared by electrospinning, Sens. Actuators B: Chem. 61 (2012) 967.

[23] P. G. Ramos, J. M. Noé, G. Silvia, J. C. Roberto, R. Juan, Moisture-sensitive properties of multi-walled carbon nanotubes/polyvinyl alcohol nanofibers prepared by electrospinning electrostatically modified method, Mater. Lett. 185 (2016) 278.

[24] Y. Li, M. Jiao, H. Zhao, M. Yang, Humidity sensing properties of the composite of electro spun crosslinked polyelectrolyte nanofibers decorated with Ag nanoparticles, Sens. Actuators B: Chem. 273 (2018) 133.

[25] Y. Li, M. J. Yang, Y. Chen, Nanocomposites of carbon nanotubes and silicone-containing polyelectrolyte as a candidate for construction of humidity sensor, J. Mater. Sc. Elec. 40 (2005) 245.

[26] M. V. Nikolic, Z. Z. Vasiljevic, M. D. Lukovic, V. P. Pavlovic, J. Vujancevic, M. Radovanovic, J. B. Krstic, B. Vlahovic, V. B. Pavlovic, Humidity sensing properties of nanocrystalline pseudo brookite (Fe_2TiO_5) based thick films, https://doi.org/10.1016/j.snb.2018.09.063.

[27] L. Liu, X. Ye, K. Wu, R. Han, Z. Zhou, T. Cui, Humidity Sensitivity of Multi-Walled Carbon Nanotube Networks Deposited by Dielectrophoresis, Sensors 9 (2009) 1714.

[28] E. G. Ordoñez-Casanova, M. Román-Aguirre, A. Aguilar-Elguezabal, F. Espinosa-Magaña, Synthesis of Carbon Nanotubes of Few Walls Using Aliphatic Alcohols as a Carbon Source, Materials 6 (2013) 2534.

[29] T. Wortmann, S. Fatikow, Carbon Nanotube Detection by Scanning Electron Microscopy MVA2009 IAPR Conference on Machine Vision Applications. May 20-22, (2009) Yokohama, Japan.

[30] G. A. Rancea, D. H. Marsha, R. J. Nicholasb, N. Khlobystova Andrei, UV–vis absorption spectroscopy of carbon nanotubes: Relationship between the π-electron plasmon and nanotube diameter, Chem. Phys. Lett. 493 1–3 (2010) 19.

[31] N. Božović, J. Misewich, I. Božović, Nano-crystallography of individual carbon nanotubes, Nano Lett. 8 (2008) 4477.

[32] N. Nair, W. Kim, R. Braatz, M. Strano, Dynamics of Surfactant-Suspended Single-Walled Carbon Nanotubes in a Centrifugal Field, Langmuir 24 (2008) 1790.

[33] H. Shang, C. Liu, F. Wei, FT-IR Study of Carbon Nanotube Supported Co-Mo Catalysts, J. Nat. G. Chem. 13 (2004) 95.

[34] B. C. Yadav, S. Singh, A. Yadav, T. Shukla, Experimental investigations on nanosized ferric oxide and its LPG sensing, Int. J of Nanosci. 10 (2011) 135.

[35] M. Perez-Cabero, I. Rodriguez-Ramos, A. Guerrero-Ruiz, Characterization of carbon nanotubes and carbon nanofibers prepared by catalytic decomposition of acetylene in a fluidized bed reactor, J. Catal. 215 (2003) 305.

[36] J. W. Snoeck, G. F. Froment, M. Fowles, Preparation of nickel nanoparticles and their catalytic activity in the cracking of methane, J. Catal. 169 (1997) 240.

[37] M. H. Pócsik, M. Koós, L. Ley, Origin of the D peak in the Raman spectrum of microcrystalline graphite, J. Non-Cryst. Solids 227 (1998) 1083.

[38] M. J. Matthews, M. A. Pimenta, G. Dresselhaus, M. S. Dresselhaus, M. Endo Origin of dispersive effects of the Raman D band in carbon materials, Phys. Rev. B 59 (1999) R6585.

[39] C. Thomsen, S. Reich, Double resonant Raman scattering in graphite, Phys. Rev. Lett. 85 (2000) 5214.

[40] S. D. M. Brown, A. Jorio, M. S. Dresselhaus, G. Dresselhaus, Observations of the D-band feature in the Raman spectra of carbon nanotubes, Phys. Rev. B 64 (2001) 073403 1.

[41] L. Bokobza, J. Zhang, Raman spectroscopic characterization of multiwall carbon nanotubes and of composites, Express Polym. Lett. 6 (2012) 601.

[42] Y. Ouyang, L. M. Conga, L. Chena, Q. X. Liu, Y. Fang, Raman study on single-walled carbon nanotubes and multi-walled carbon nanotubes with different laser excitation energies, Physica E 40 (2008) 2386.

[43] A. Jorio, M. A. Pimienta, A. G. Souza Filho, R. Saito, G. Dresselhaus, M. S. Dresselhaus, Characterizing carbon nanotubes samples with resonance Raman scattering, New J. Phys. 5 139 (2003) 1.

[44] M. S. Dresselhaus, G. Dresselhaus, M. Hofmann, The big picture of Raman scattering in carbon nanotubes, Vib. Spectrosc. 45 (2007) 711.

[45] R. Kumar, B. C. Yadav. Fabrication of Polyaniline (PANI)—Tungsten oxide (WO_3) Composite for Humidity Sensing Application, J Inorg Organomet Poly. 26 6 (2016) 1421.

[46] Q. Y. Tang, Y. C. Chan, K. Zhang, Fast response resistive humidity sensitivity of polyimide/multiwall carbon nanotube composite films, Sens. Actuators B: Chem. 152 (2011) 99.

[47] J. Wang, X. H. Wang, X. D. Wang, Study on dielectric properties of humidity sensing nanometer materials, Sens. Actuators B: Chem. 108 (2005) 445.

[48] N. Agmon, The Grotthuss mechanism, Chem. Phys. Lett. 244 (1995) 456.

[49] W. P. Chen, Z. G. Zhao, X. W. Liu, Z. X. Zhang, C. G. Suo, A capacitive humidity sensor based on multi-wall carbon nanotubes (MWCNTs), Sensors 9 (2009) 7431.

[50] A. Tripathy, S. Pramanik, A. Manna, S. Bhuyan, N. F. A. Shah, Z. Radzi, N. A. A. Osman, Design and Development for Capacitive Humidity Sensor Applications of Lead-Free Ca, Mg, Fe, Ti-Oxides-Based Electro-Ceramics with Improved Sensing Properties via Physisorption, Sensors 16 (2016) 1135.

[51] P. Koskinen, V. Makinen, Density-functional tight-binding for beginners, Comput. Mater. Sci. 47 (2009) 237.

[52] J. C. Slater, G. F. Koster, Simplified LCAO Method for the Periodic Potential Problem, Phys. Rev. 94 (1954) 1498.

[53] M. Elstner, D. Porezag, G. Jungnickel, J. Elsner, M. Haugk, T. Frauenheim, a self-consistent-charge density-functional tight-binding method for simulations of complex materials properties, Phys. Rev. B 58 (1998) 7260.

[54] T. A. Niehaus, M. Elstner, T. Frauenheim, S. Suhai, Application of an approximate density-functional method to sulfur-containing compounds, J. Mol. Struct. Theochem. 541 (2001) 185.

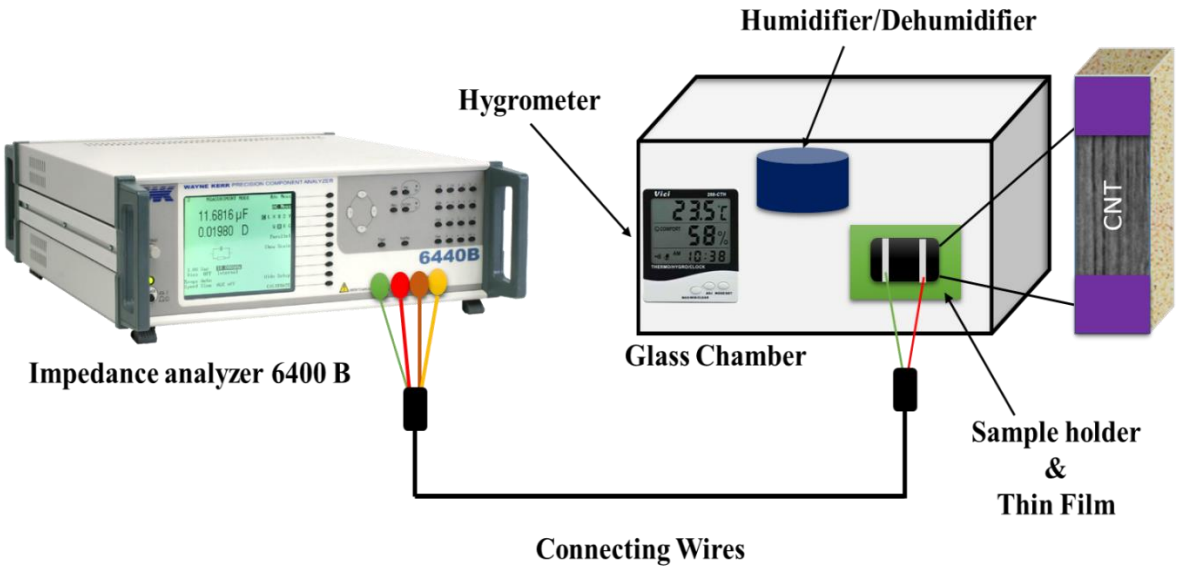

Fig 3.1 Block diagram of CNT based thin film as a humidity sensor.

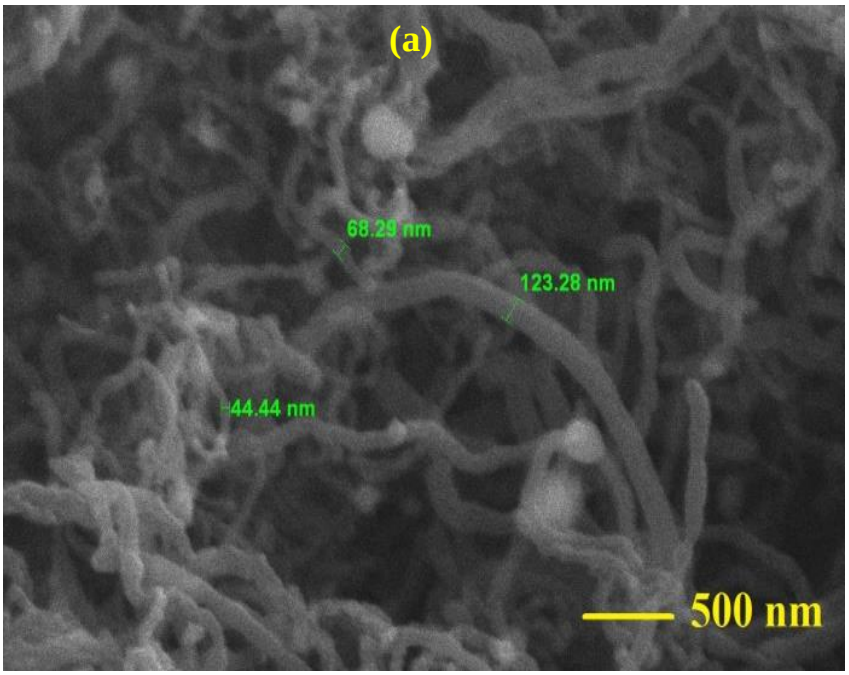

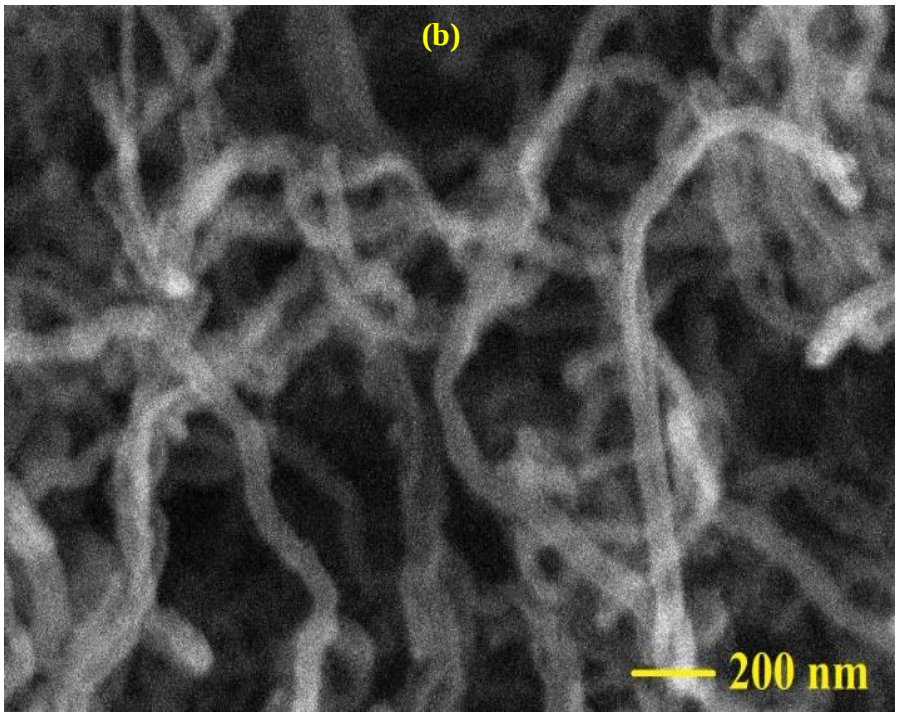
(b)
200 nm

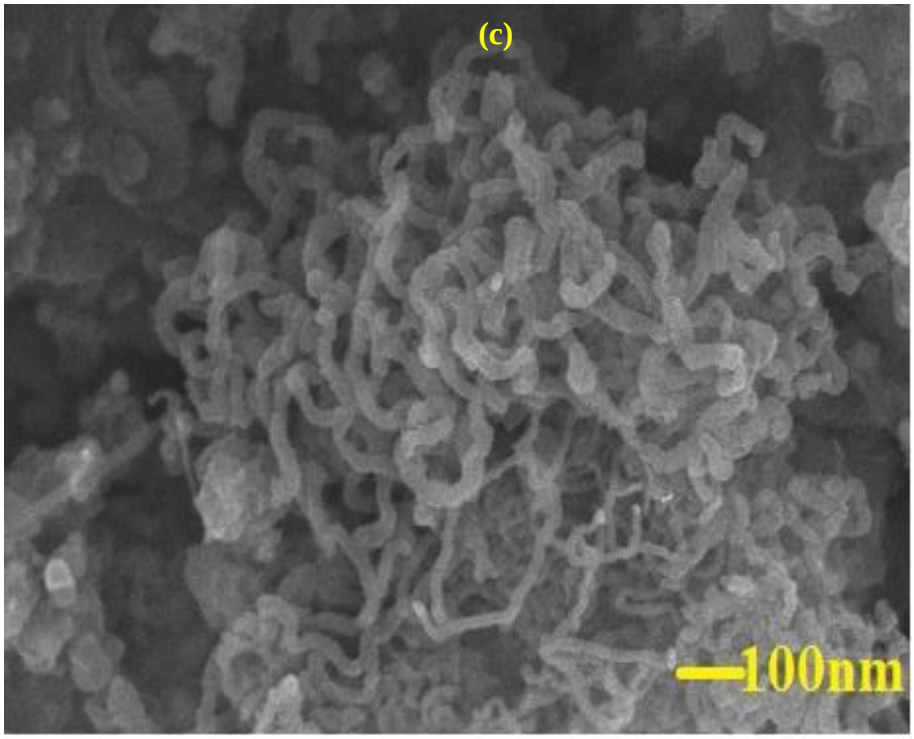
(c)
100nm

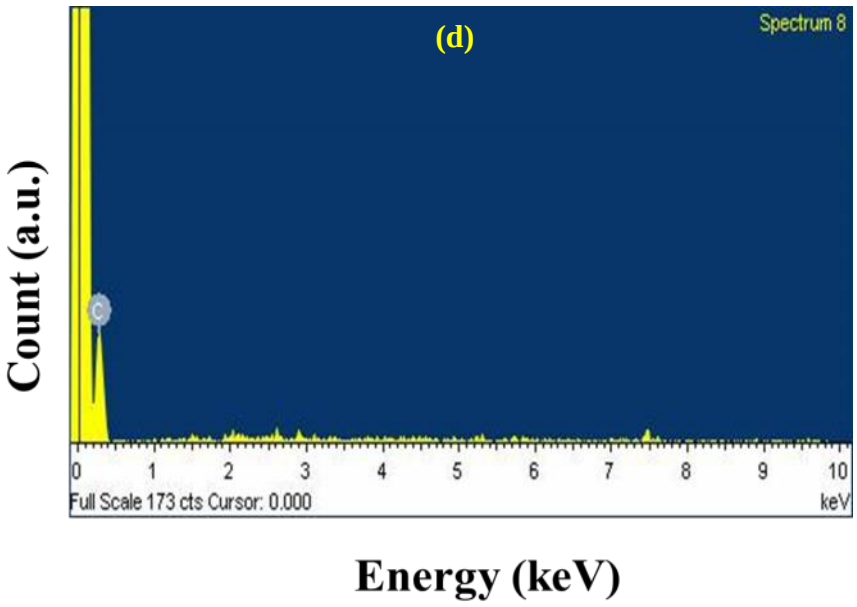

Fig. 3.2 SEM analysis of MWCNT at (a) 500 nm (b) 200 nm (c) 100 nm scale (d) EDX spectrum of MWCNT.

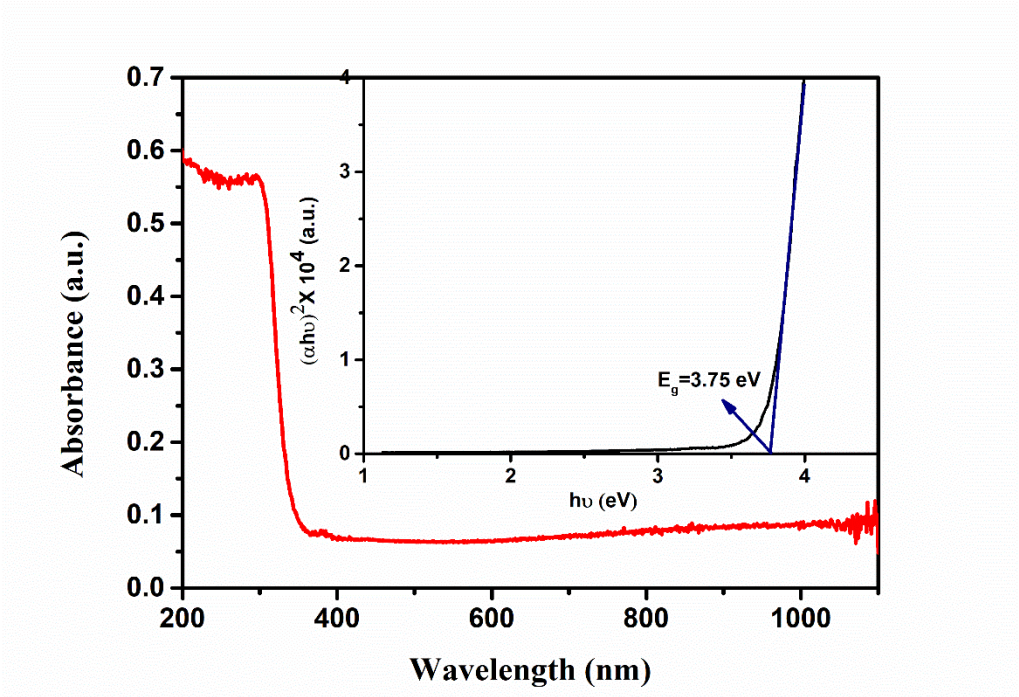

Fig. 3.3 UV analysis and Tauc plot of CNT based thin film.

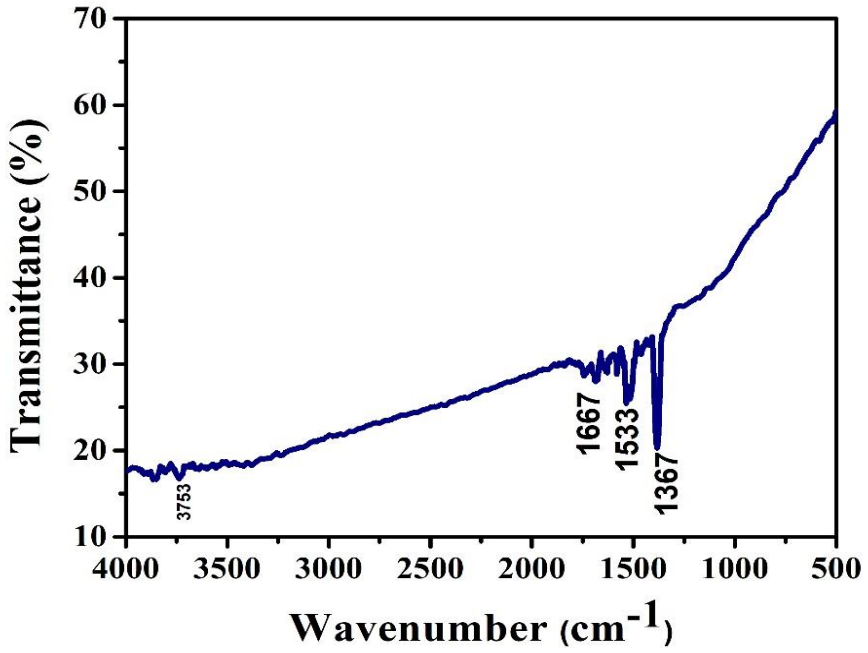

Fig. 3.4 FTIR analysis of MWCNT for the detection of bond formation in MWCNT.

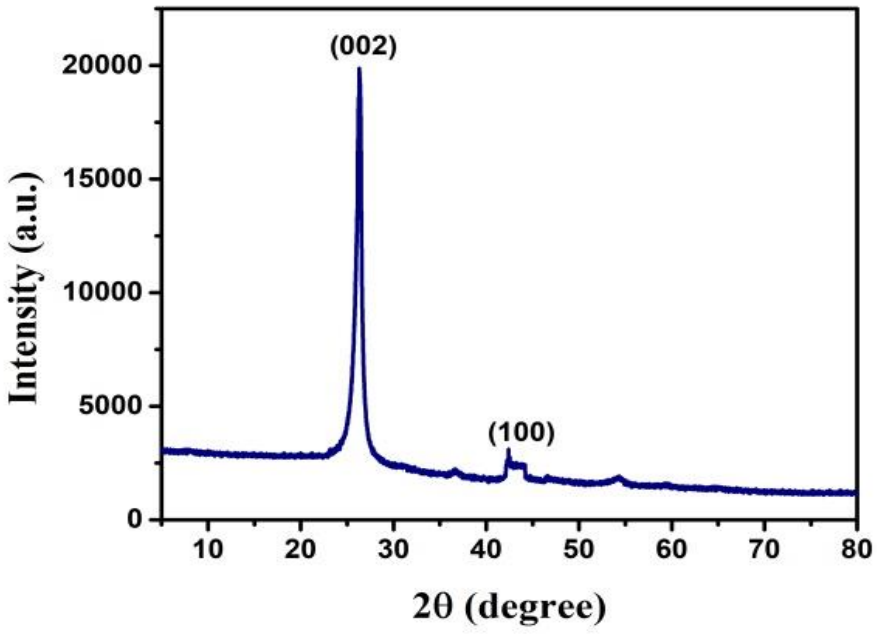

Fig. 3.5 XRD analysis of MWCNT based thin film.

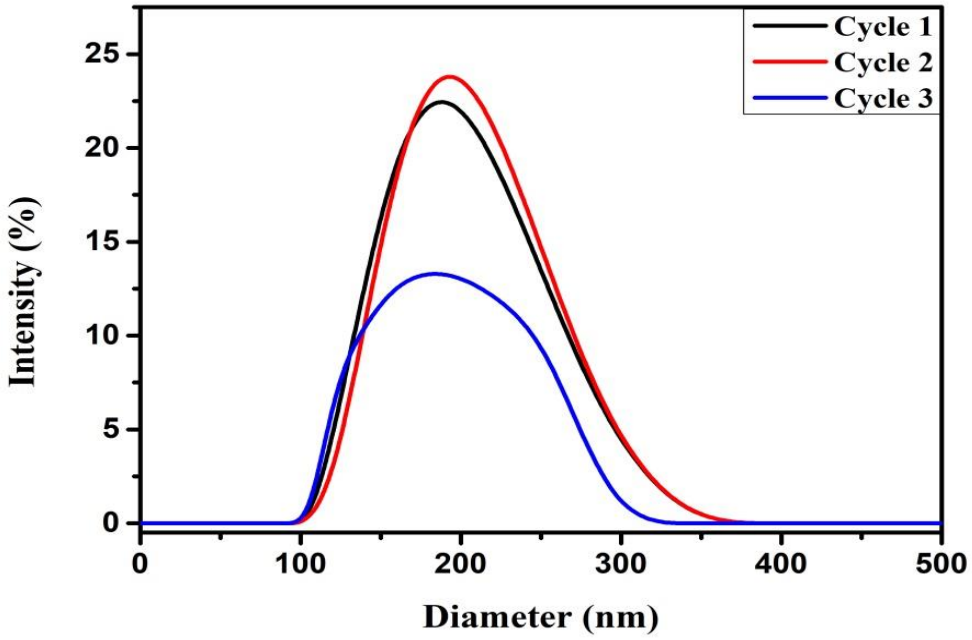

Fig. 3.6 Particle size analysis of MWCNTs dispersed in n-methyl-pyrrolidone.

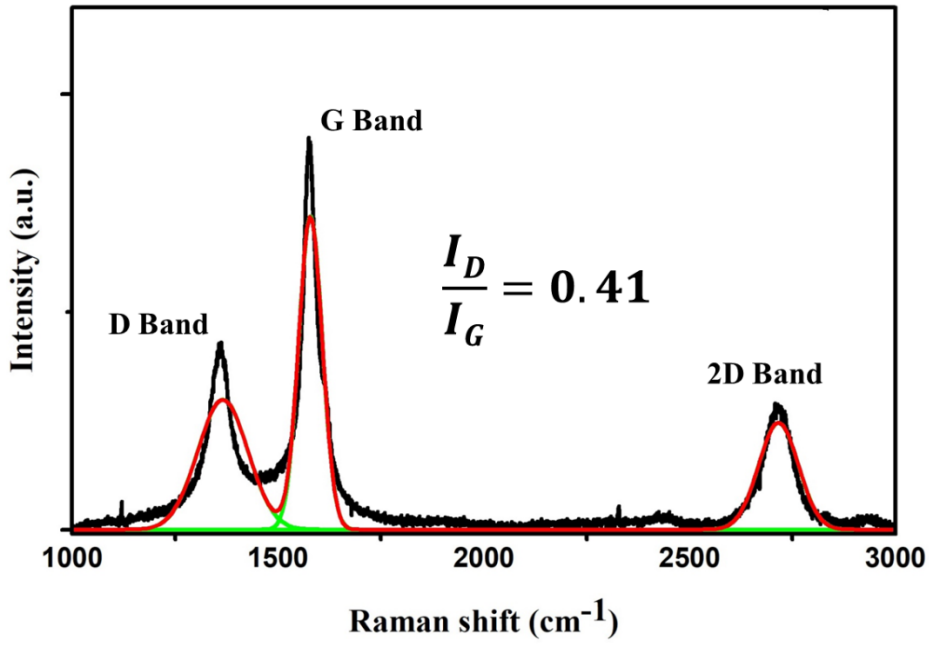

Fig. 3.7 Raman analysis of MWCNTs.

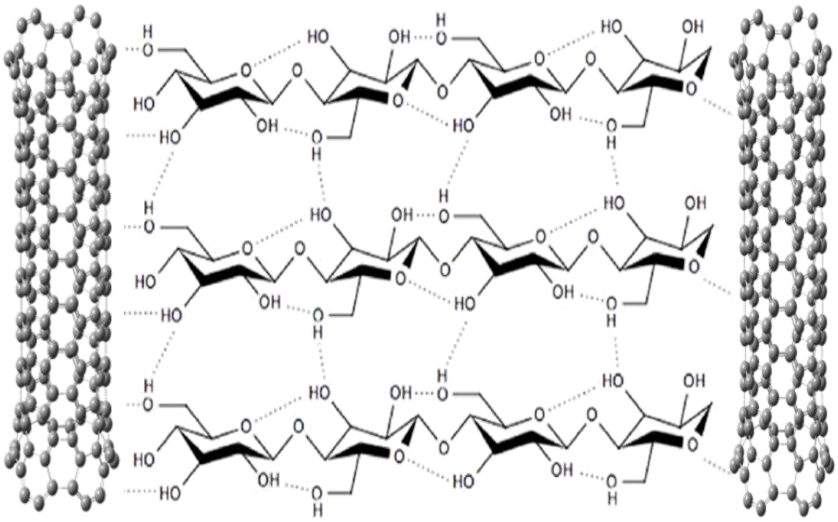

Fig. 3.8 Grotthuss chain reaction in MWCNT based thin film.

(a)

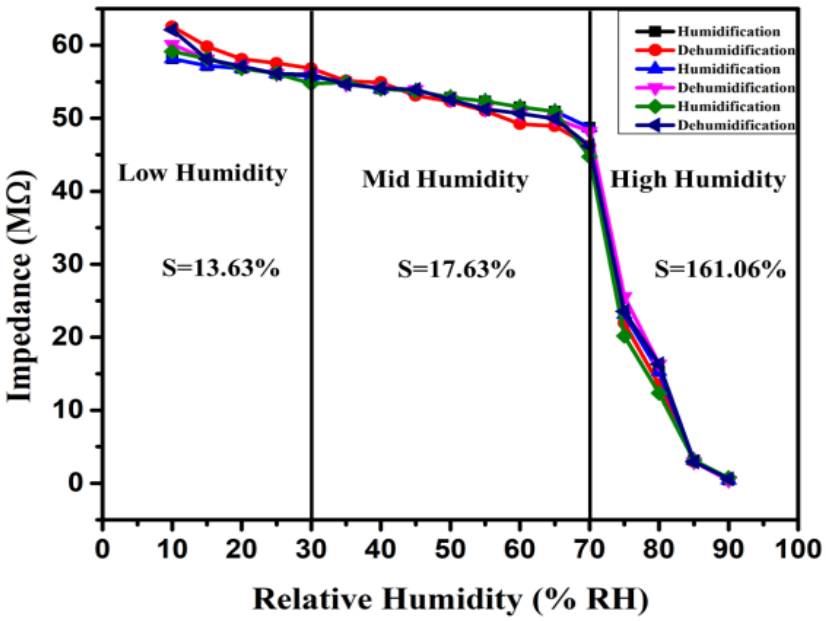

(b)

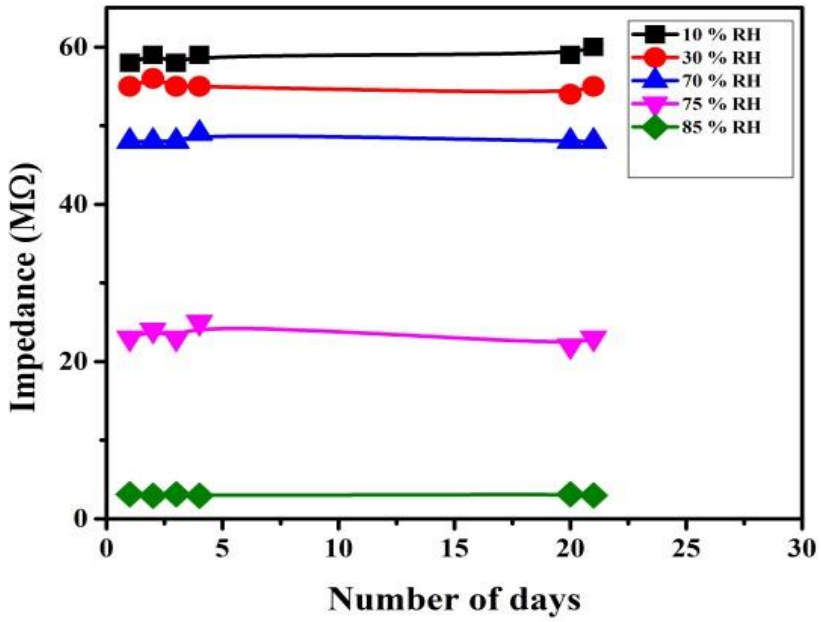
10 % RH
30 % RH
70 % RH
75 % RH
85 % RH
Impedance (MΩ)
Number of days
0
20
40
60
0
5
10
15
20
25
30

(c)

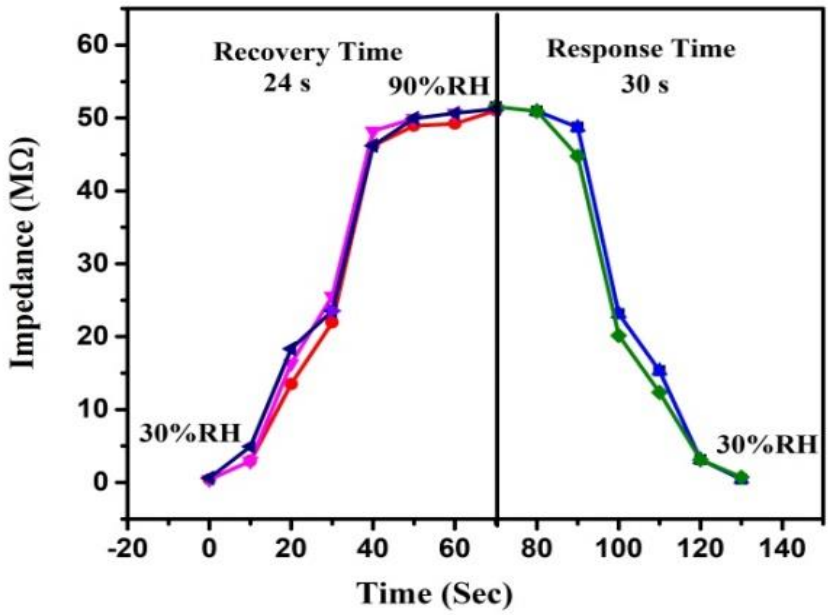
Recovery Time
24 s
90%RH
Response Time
30 s
30%RH
30%RH
Impedance (MΩ)
Time (Sec)
0
10
20
30
40
50
60
-20
0
20
40
60
80
100
120
140

(d)

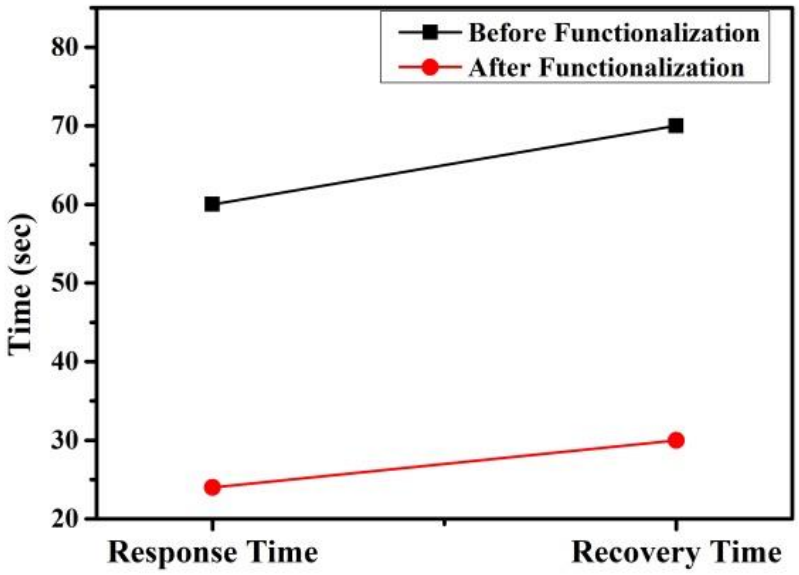

Fig. 3.9 (a) Change in impedance of the film by changing the relative humidity at room temperature (b) reproducibility and ageing effect of result (c) response and recovery time of CNT based thin film (d) change in response and recovery time by functionalization.

(a)

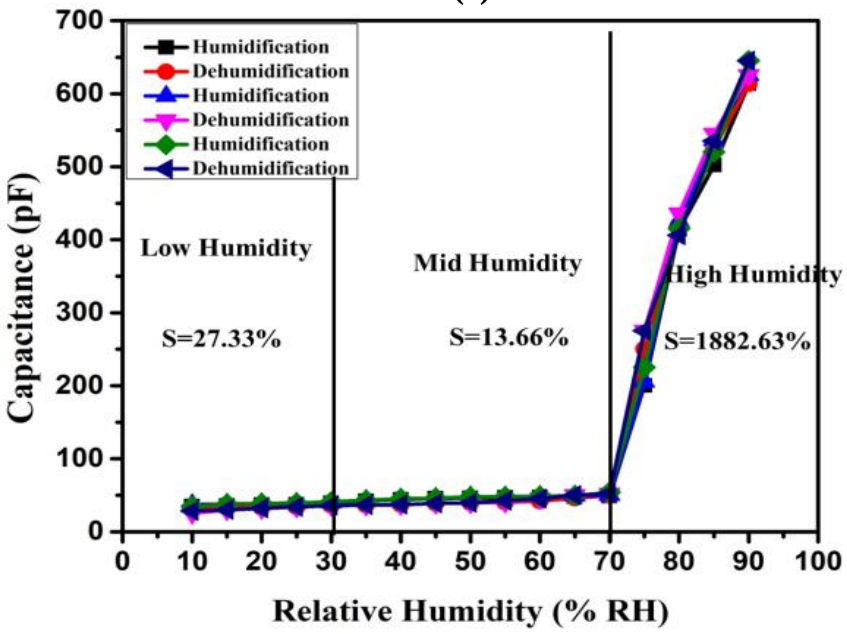

(b)

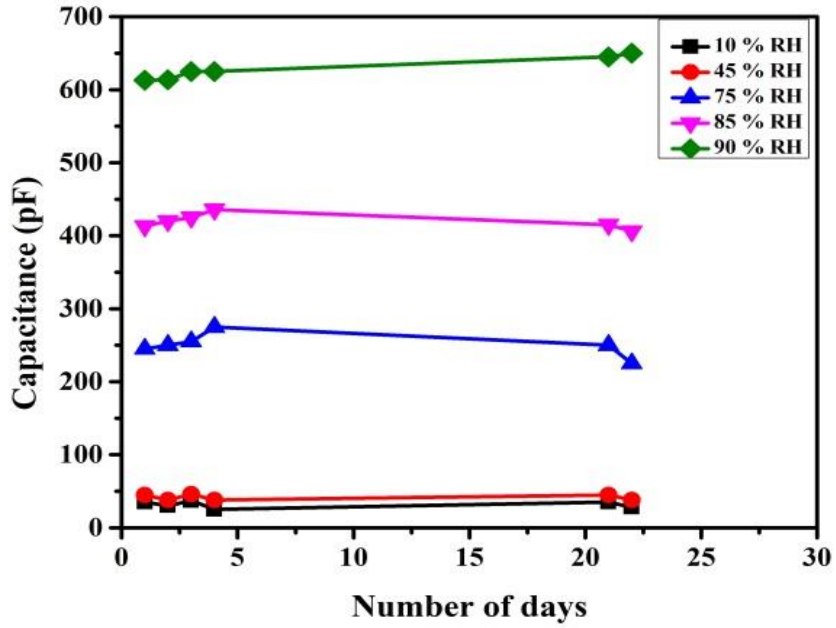
10 % RH
45 % RH
75 % RH
85 % RH
90 % RH
Capacitance (pF)
Number of days
0
100
200
300
400
500
600
700
0
5
10
15
20
25
30

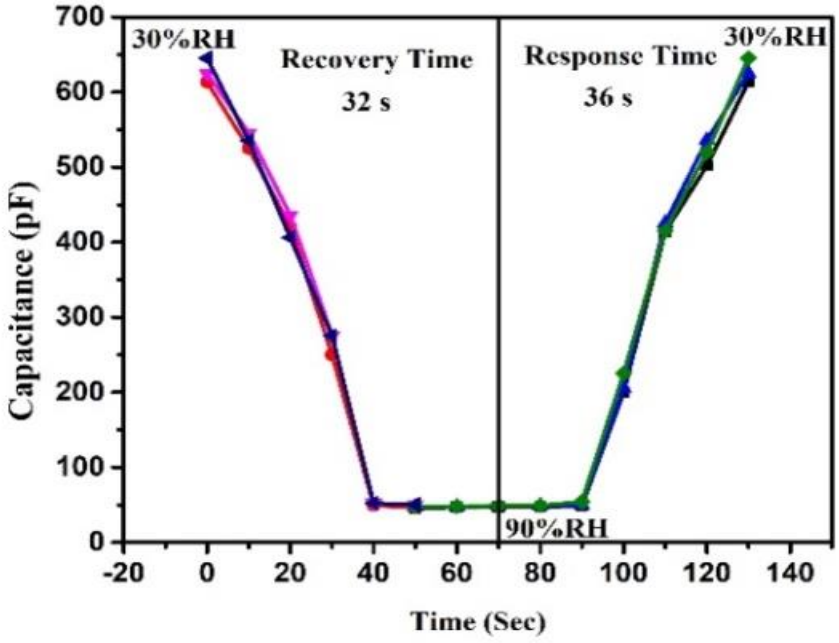
30%RH
Recovery Time
32 s
Response Time
36 s
30%RH
90%RH
Capacitance (pF)
Time (Sec)
0
100
200
300
400
500
600
700
-20
0
20
40
60
80
100
120
140

(d)

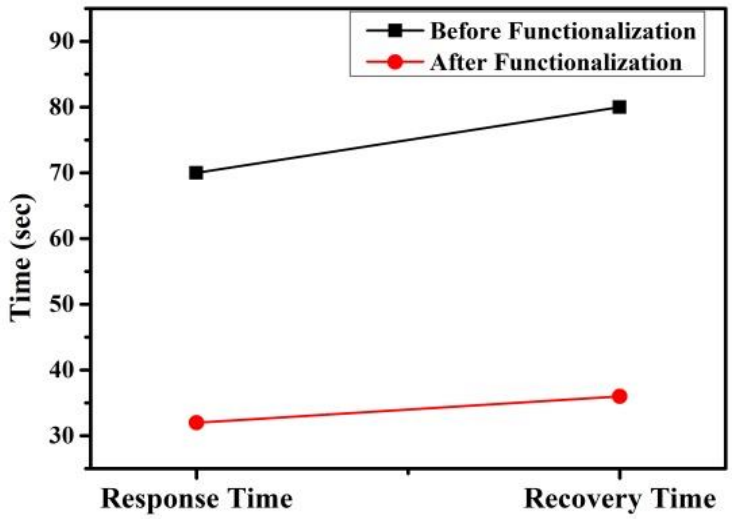

Fig. 3.10 (a) Change in capacitance of the film by changing the relative humidity at room temperature (b) reproducibility and ageing effect of film (c) response and recovery time of MWCNT based thin film (d) change in response and recovery time by functionalization.

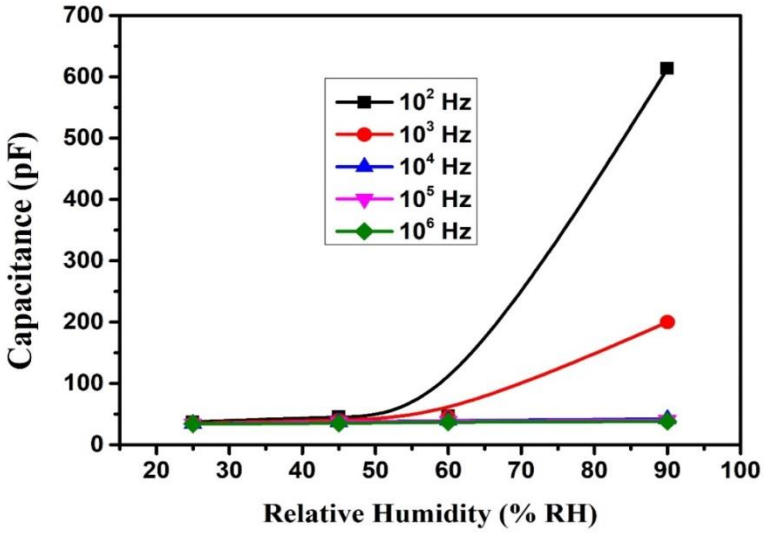

Fig. 3.11 Sensor response of MWCNT based capacitive sensors with %RH at different test frequencies at room temperature.

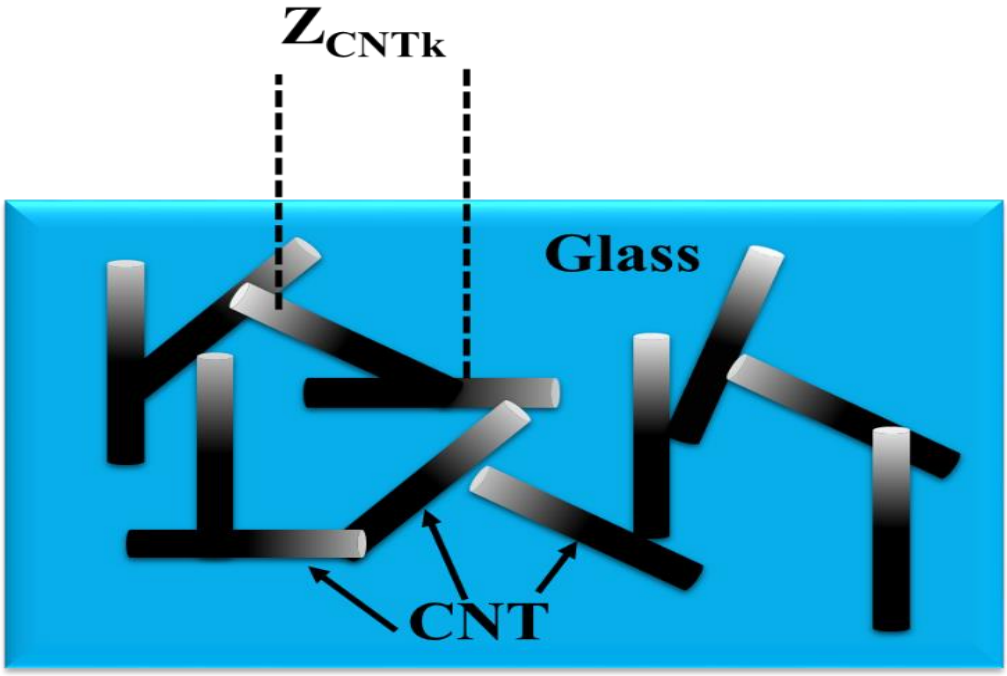

Fig. 3.12 Formation of nanotubes on a glass substrate.

Table 3.1 Literature survey on various types of humidity sensors

S.No.	Sensing material	Measuring Range	Sensitivity	Response time/ Recovery time	Reference
1	MWCNT suspended	15-98	2.46 kΩ/%RH	290/510	12
2	PDDA/RGO	11-97	0.34 Ω/%RH	143/133	19
3	Copoly(TEAMPS/VP)/silver nanocomposite	30-95	0.015 MΩ/%RH	180/195	20
4	KCl-doped TiO_2 nanofiber	11-95	0.11 MΩ/%RH	3/3	21
5	PANI nanofiber	11-98	0.101 MΩ/%RH	8/6	22
6	MWCNT/PVA	40-90	1.4 MΩ/%RH	-	23
7	QC-PVVP nanofiber/Ag nanoparticle	3.6-98	0.104 kΩ/%RH	16/24	24
8	SWNT/DI-PE	33-98	1.7 MΩ/%RH	-	25
9	Fe_2TiO_5	30-90	0.511 MΩ/%RH	-	26
10	Modified MWCNT (Dispersed in NMP)	10-90	0.644 MΩ/%RH/ 6.41 pF/%RH	24/30 32/36	Present work

Table 3.2 The sensitivity of the sensor at different regions of humidity in terms of impedance, capacitance and inductance respectively.

Relative Humidity (%RH)	**% Sensitivity**		
	Impedence (MΩ/%RH)	**Capacitance (pF/%RH)**	**Inductance (kH/%RH)**
10%-40%	13.63%	27.33%	28.73%
40%-70%	17.63%	13.66%	29.66%
70%-90%	161.06%	1882.63%	232.23%

Table 3.3 Theoretical study on variations in different parameters of CNT (1,1) before and after interaction with OH^- molecule.

	Before Interaction	**After Interaction No of OH^- ion interact with CNT (1,1)**				
		2	**4**	**6**	**8**	**10**
Change in binding energy (eV)	7.61	5.53	6.39	8.26	14.23	13.96
HOMO-LUMO band gap (a.u.)	0.1089	0.1698	0.1779	0.1557	0.1579	0.1499
Dipole moment (Debye)	0.0053	6.5523	10.049	9.9743	7.5452	13.96
Electronegativity (a.u.)	0.4181	0.4412	0.4546	0.4509	0.45095	0.45099
Hardness (η)	0.1780	0.17202	0.17568	0.18801	0.1759	0.17699
Softness (s)	5.6151	5.8132	5.6920	5.3188	5.6827	5.6500
Nucleophilicity index	0.4907	0.5659	0.5885	0.5407	0.5781	0.5747

CHAPTER 4

FUNCTIONALIZATION OF MWCNT BY HNO_3 & H_2SO_4 AND ITS RELEVANCE FOR DEVELOPING AN ULTRA-SENSITIVE CO_2 SENSOR WORKING AT ROOM TEMPERATURE

This chapter reports the synthesis and characterization of Multiwall Carbon Nanotube (MWCNT) based thin film and its application as CO_2 gas sensor. The MWCNT was prepared by direct liquid injection chemical vapor deposition method (DLICVD) using ethanol as precursor in the presence of argon gas atmosphere and furnace temperature at 750 ℃. The thin film of MWCNT was prepared by using the spin coating technique and characterized using Scanning electron microscope (SEM), UV-Visible spectrometer, Particle size analyzer and X-ray diffractometer (XRD). The vibrational and rotational spectra were observed through Fourier Transform Infra-Red Spectroscopy (FTIR) and Raman Spectroscopy. The SEM image of the thin film exhibited the tubular structure grown throughout the surface. From XRD, the minimum crystallite size was found to be 14 nm. The optical energy band gap of the nanotube-based thin film was found as 3.6 eV. The synthesized CNT-based thin film was employed for the CO_2 sensing at room temperature. The sensor response was found as 2.1 and the results were found 98% reproducible. The response and recovery times were found to be 30.2 and 49.6 s respectively. Theoretical calculations were also performed in the support of CO_2 sensing through the MWCNT.

CHAPTER 4

Functionalization of MWCNT by HNO_3 & H_2SO_4 and its relevance for developing an ultra-sensitive CO_2 sensor working at room temperature

4.1 Introduction

Nowadays environmental pollution has become a severe problem towards the whole world and its prevention is very challenging for us. Many sensors have been designed and fabricated to detect the levels of various toxic gases in order to avoid disasters. Thin film based sensors operated at room temperature are one of them [1, 2] and such types of gas sensors have been established as an emerging technology in the field of environmental sensing. In the present work, we have focused on carbon nanotube (CNT) based thin film gas sensors because carbon nanotubes (CNTs) [3] have extraordinary physical, chemical, structural and mechanical properties [4, 5]. These are an ideal quantum system for exploring the one-dimensional physical application in nanoscale devices [6]. The growth of CNTs may be done by using a chemical vapour deposition method for having one-dimensional growth with high aspect ratio and unique structural properties [7]. Catalysts such as Au, Ag, Pt, Fe, Mn, Mo and Mg may be used for the growth of CNTs but the best growth was found by using metal catalysts like Co, Ni and Fe. These catalysts may be easily filtrated from the nanotubes by the distillation process [8].

The burning of fossil fuels from the industries, motor vehicle and volcanic eruptions are the sources of major environment pollutant like carbon monoxide and carbon dioxide. The continuous increase in the concentration of CO_2 in the natural environment has raised the temperature of the earth causing global warming which is further liable for the melting of glaciers and rising sea levels. Also, the excessive presence of CO_2 in the ambient environment causes suffocation and creates unconsciousness in human beings. Therefore, precise measurement and control of CO

and CO_2 are necessary but in the current scenario several metal oxides are widely used for sensing purposes, however, these materials have a high operating temperature (200-400℃) [9-14]. This is a great drawback of the devices used. Thus the sensors which may be operated at room temperature with fast recovery and response times are highly desirable.

CNTs behave as p-type semiconductor without having any type of doping. A number of interpretations were made for its p-type behaviour including atmospheric oxygen or metal electrode or due to impurity or defects introduced during the synthesis process. They have very high absorptive property due to very large surface to volume ratio. CNT based sensors also gave very high sensing response to gases e.g. NH_3, NO_2, CO_2 etc. [15]. The sensing mechanism through these nanotubes is based on the chemisorption and physisorption process. Also, the CNT-based thin film may be used for the fabrication of solar cells having high efficiency [16].

The chemical sensors [17, 18] fabricated by using carbon nanotubes (CNTs) have created a great interest in the research community and it was demonstrated that these can be used to detect toxic gases such as CO_2 and CO with low concentration level at room temperature [19, 20]. The gas sensing mechanism of CNTs is based on the gas molecule adsorption on its surface. In this chapter, we have expanded the theoretical calculations to more configurations, with analysis of CO_2 gas adsorption on CNTs as a complement to the existing calculations [21, 22]. In such calculations, we also have analyzed the dipole moment, binding energy and HOMO-LUMO band gap before and after interacting with CO_2 gas.

Despite extensive studies of CO_2 sensing with various complex structures and sensing conditions, we need better performing CO_2 sensor which may easily be designed and fabricated at an industrial scale. For this purpose, we modified chemical vapour deposition technique to direct liquid injection CVD technique. MWCNTs grown by DLICVD technique have better length and diameter compared to conventional CVD which creates more active sites for CO_2. Using this technique we have fabricated an ultrasensitive CO_2 gas sensor operable at room temperature.

4.2 Experimental details

4.2.1 Chemical vapour deposition technique

The chemical vapour deposition (CVD) method is the best method for the fabrication of nanotube-based thin film used in modern technology having a wide range of applications [8, 15, 16]. It is a well-established process by which a gas or liquid get decomposed and deposited on a solid surface via phase transformation chemical reaction. The activation energy is required to proceed the CVD. There are several methods which can be used for providing such activation energy. In thermal CVD, the activation energy is provided by increasing high temperature above 700 ℃ [24]. Apparatus consists of the high vacuum system, gas supply system, exhaust system and deposition chamber. In plasma CVD, plasma is used for activating the reaction as the temperature varies from 350 to 750℃ [25]. In laser CVD, high energy laser emits thermal energy for pyrolysis which occurs on the absorbing substrate [26]. In photo-laser CVD, the ultraviolet radiation having sufficient photon energy for breaking the bond in the reactant molecule in the chemical reaction. Nanocomposite powder may also be prepared by CVD. The main advantage of CVD is the high deposition rate with the production of 100% pure nanomaterials.

4.2.2. Synthesis of carbon nanotubes using DLICVD

For the production of CNTs by using direct liquid injection chemical vapour deposition method (DLICVD), the modified CVD setup is shown schematically in Fig. 4.1. The apparatus consists of a (5×100 cm) cylindrical quartz tube provided one end with a connection for a vacuum system, and for the injection of carrier gas (Ar/N_2) and ethanol vapour at another end. In this process, the catalyst particles were prepared by chemical reduction of cobalt chloride particles by the sol-gel process. The synthesized cobalt nanoparticle was used as a catalyst particle for the growth of CNTs and a thin film of such nanoparticles on quartz substrate were fabricated by using spin coating technique with revolution rate of 1500 per min for 30 s and later the prepared film was placed in a hot air oven for 15 min at 100℃ [27].

As prepared catalyst thin film was placed inside the quartz tube as shown in the diagram (Fig. 4.1) and increases the temperature of the furnace uniformly with a continuous flow of nitrogen gas. When the temperature of the furnace was maintained at 750 ℃ the ethanol was injected at the rate of 2 ml/min for 15 min. After injecting ethanol, the temperature of the furnace was decreased very slowly but uniformly for the growth of CNTs because the decreasing rate of temperature is mostly responsible for the diameter and, length of CNTs. Now, after the filtration process, a thin film was fabricated by using pure CNTs. In this process, the prepared film was dipped into the nitric acid solution so that cobalt nanoparticles were dissolved in it and pure nanotubes (PMWCNT) were obtained.

The synthesized CNTs were functionalized by exohedral functionalization process. In this case, the CNT was put in the complex solution of nitric acid (HNO_3) and sulfuric acid (H_2SO_4) in the 3:1 ratio, then sonicated for ½ h. Later, the solution was centrifuged at 1500 rpm and the black coloured precipitate was obtained. Further, it was washed with distilled water and functionalized nanotubes (FMWCNT) were obtained.

4.3 Characterization

The surface morphological and structural property of thin film were characterized by Scanning electron microscopy (SEM) (JEOL JSM 6490 LB) and Raman spectrometer (A Renishaw using 514.5 nm Ar^+ with power 15 mW) was used for studying the nanostructural properties. The data obtained by the XRD (Philips X'Pert Pro PAN analytical using laser source CuKα (1.542 A) in scanning region from 10 to 90° with a scanning step of 0.02° per sec) were used for calculating average crystallite size. Particular dimensions of nanotube were measured by Particle Size Analyzer (NZS90 using a laser source of wavelength 625 nm). The optical characterization of the thin film was analysed by UV spectrometer (Evolution 302) and infrared spectrometer (Shimadzu 8700 1992). The sensing parameters were measured by using Keithley electrometer (6514 B) which gives the variation of resistance w.r.t. time with higher accuracy.

4.3.1 SEM analysis

A typical SEM image of the CNT-based thin film shows a lot of nanotubular rod-like structures uniformly distributed throughout the surface of the film as shown in Fig. 4.2. This image also shows that the film has a higher porosity with tubular structures of nanotubes. Due to this, the film may exhibit higher sensing property towards the CO_2 gas. The average length and the diameter of nanotubes are found to be 125.36 nm & 18 nm respectively. The zig-zag structure of CNTs gives the higher surface area for the interaction of CO_2 so such structure of nanotube is very useful for the sensing purpose.

4.3.2 EDX analysis

Elemental Dispersive X-ray (EDX) spectrum of Co contained CNT and Pure CNT are shown in Fig. 4.3. In the first spectrum 90% of CNT with 10% of Co but after the filtration process, 100 % of nanotubes are formed as shown in the second spectrum. The higher peak of carbon confirms the presence of pure nanotubes in the sample.

4.3.3 UV-vis spectroscopy

Fig. 4.4 shows the variation of absorption spectra of the CNT-based thin film with the variation of wavelength. The data were further used for calculating the optical band gap of CNT synthesized at 750 ℃ using the formula described in Chapter 2 and the direct band gap was found as 3.6 eV.

The absorbance spectra show the highest absorbance in the near 300 nm ie UV region and after this, a sharp change in the spectra was observed and for the visible and infrared region, the absorption spectra are nearly the same and very fewer changes are observed so the thin film fabricated has a low absorbance in this region [28]. Eventually, it has been observed that due to having a small size the quantum confinement is occured and the blue shift in absorption peak is observed at the edge of bulk CNT (300 nm). The higher absorption spectra of CNT in the range 200-350 nm which reflects the band gap of the material. For determining the optical band gap and nature of nanotubes, we use higher absorption range in which excitation of the electron is found from valence band to the conduction band. The plot of energy (eV) versus $(\alpha h\nu)^2$ gives a curve of electron

excitation and the tangent corresponding to them gives the optical band gap as shown in Fig. 4.4.

4.3.4 XRD analysis

The crystallite size of the sample prepared by the DLICVD technique was calculated using Debye-Sherrer formula [29]. The XRD pattern of the P-MWCNT and f-MWCNT reveal the larger formation of CNT with the minor formation of graphene and the peak intensity and width also varies after functionalization because of the addition of some functional group on the wall of nanotubes [30, 31].

4.3.5 FTIR analysis

In the measured IR absorbance spectrum, the region from 1600-1400 cm^{-1} shows higher vibration, in particular at 1380 & 1540 cm^{-1} for MWCNT. The region at 1540 cm^{-1} is IR active and due to sp^2 hybridized carbon, the graphite-like E_{1u} mode (also known as the G band) is formed.

As in Fig. 4.6 the absorbance peak at 1381 cm^{-1} is observed because of having tetrahedral structure at the corners of nanotubes, same as in the neutron-irradiated diamond and nitrogen impurity rich nanodiamonds also categorized as disordered-induced one phonon absorbance band. The peak near 600 cm^{-1} shows the aromatic ring formation on the surface of the nanotubes [32, 33]. Due to having some translational symmetry of the diamond lattice, the lattice mode arose. The analogy between the nanotubes (CNTs) and density of state (DOS) of the disordered diamond consist of disordered sp^3 bonded carbon and also responsible for nucleation to functionalized nanotubes. In general, the nanotube functionalization activates the bands near 2360 cm^{-1} and 3750 cm^{-1} offered the presence of no conjugate carboxylic group and CH_x group respectively. These bands are also responsible for many sensing applications.

4.3.6 Particle size analysis

Fig. 4.7 shows the average particle size of the CNT dissolved in n-methyl pyrrolidone. In this method, the particle size was analyzed by the dynamic light scattering

technique of the Brownian motion of particles. In such a process, the detector considered nanotube as a virtual diameter of the particle so the peaks having value 195 nm shows the average length of the nanotubes.

4.3.7 Raman analysis of CNTs

Fig. 4.8 shows the Raman spectrum of ethanol-based carbon nanostructured sample. The Raman spectrum of carbon nanotube (CNT) consists of two main graphitic bands. The band at 1303 cm^{-1} (D band) activated by the presence of the disorders in carbon system and the defective graphitic like materials another band at 1597 cm^{-1} (G band) assigned to the in-plane vibration of the C–C bond (G band). These Raman spectra have been obtained on the powder of synthesized MWNT and the relative intensity I_D/I_G of the samples are same so the reaction was not modified by the crystal structure. According to the literature, D bands are higher for the samples containing large amounts of MWCNTs [34–38]. Due to having a higher intensity of D peak, the formation of the nanotube in such case is very high and most of the graphitic layers are converted into tubular structures [39–41].

4.3.8 BET analysis of MWCNTs

The Brunauer-Emmett-Teller and BJT plot of CVD synthesized CNT have been shown in Fig 4.9 (a) & (b). The average pore diameter of CNT is 10.57 nm. The surface area measurement of CNT is most commonly based upon N_2 gas adsorption. The standard BET method is used to calculate the specific surface area of CVD synthesized CNT specimens. The BET adsorption isotherm equation can be described by Eqn. 4.2

$$\frac{n}{n_m} = \frac{CP}{(P-P_0)[1+(C-1)\,(\frac{P}{P_0})} \quad \text{……(4.2)}$$

Where n is the amount of gas absorbed at pressure P, P_0 is the vapour pressure of the adsorbate, n_m is the monolayer coverage and C is the fitting parameter. The slope and the intercept of the continuous equation provide the necessary characteristics employed in calculating surface area. The surface area can be calculated by Eqn. 4.3. based on the

monolayer coverage (n_m), Avogadro's number (N_A) and the molecular cross-sectional area of adsorbate molecule (σ).

$$A = n_m N_A \sigma \text{……...(4.3)}$$

Where the cross-sectional area of N_2 is 0.162 nm^2 and Avogadro's number is 6.02×10^{23} $mole^{-1}$. After completing the calculation of BET for CNTs, the surface area of CNT's synthesized by DLICVD technique was found as 91.223 m^2gm^{-1} at room temperature, which is higher in comparison to other synthesized CNTs [42, 43].

4.4 Principle of operation

The gas sensitivity of the sensing material is the measure of change of chemical or physical property when the sample is exposed to the desired gas atmosphere [44]. This term is also used to detect the smallest increment of the concentration of gas in the sensing environment. In this experiment, we used the résistance of CNT based thin film as a sensing parameter [45]. The electrical resistances of CNT in the air (R_a) and in the presence of CO_2 (R_g) were measured to estimate the sensor response (SR) which is given by Eqn. 4.4 [46].

$$\%SR = \frac{\left|R_a - R_g\right|}{R_a} * 100 \text{ ……. (4.4)}$$

Fig. 4.10 shows that the energy of pristine CNTs decreased on absorbing reducing gas molecules due to having fewer electrons in the conduction band and for absorbing oxidizing gas molecules, the energy of pristine CNT increased due to having a free electron in the conduction band.

4.5 Device fabrication

Fig. 4.11 shows the gas sensing setup of the CNT-based thin film for CO_2 sensing. A holder was designed to measure the resistance of the sensing element made of CNT thin film having a thickness of ~ 500 nm and a length of 1 cm was placed between the Ag electrodes. The gap between the square-shaped Ag electrodes is 0.5 cm having a side length of 0.25 cm. The holder connected with Keithley electrometer 6514 B was

placed inside a closed chamber. The variations of the film resistance with the variations in the concentration of CO_2 were measured by using electrometer. The temperature of the chamber was maintained throughout the experiment and the gas concentrations were varied from 1670 ppm to 6670 ppm using a controlled mass flow meter.

4.6 Results and discussion

Before the exposure of CO_2 gas, the film was placed in the vacuum chamber for 15 min to reduce the surface contamination of the film and after the stabilization of film, R_a was taken as stabilized resistance. The variations in resistance of the film for different concentration of CO_2 were observed. Fig. 4.12 shows the variation of film resistance at room temperature with time before and after exposure for different ppm of CO_2 gas. The first peak of sensing curve for 1670 ppm of CO_2 shows a constant variation of resistance when the gas exposed to it and having low sensing response. The second curve for 3300 ppm shows higher sensing response in comparison to first one and response and recovery time also decreases, on again increasing the quantity of gas exposed in the chamber, highest sensing response (2.1) was found at 5000 ppm but the response and recovery time increases. Then again increasing the quantity of gas inside the chamber the sensing response was decreased because of filling of all free lattice sites on the film surface.

The sensitivity of the CNT based CO_2 sensor was found maximum at 5000 ppm as shown in Fig. 4.13. Response and recovery times were calculated and found as 30 and 49 s respectively. When the gases exposed on the film then the resistance of CNT based thin film decreased from initial value became constant whereas when the outlet of the chamber was opened then the resistance approaches to the initial value of stabilized resistance (R_a). When the CO_2 gas introduces into the chamber then the sensor response changes from R_a to R_g according to changing gas concentration as shown in Fig. 4.13. The CNT based CO_2 sensor has a maximum sensing response of 2.1 for 5000 ppm CO_2.

Fig. 4.14 shows the reproducibility of the film at 5000 ppm for CO_2 and the results were found reproducible within ± 98% accuracy.

For thin film sensor, the maximum average sensitivity is 2.1 for 5000 ppm of CO_2. The CNT based thin film having a large surface area contribute to a higher surface

area for the interaction of reducing gas on the surface of the material which enhanced the sensitivity of the CNT based thin film. This enhancement also increases the replacement of oxygen species (O^-, O^{2-}) during the adsorption and desorption process on the CNT based thin film. It is clear from the above observation that CO_2 sensing behaviour of the CNT-based thin film prepared by CVD technique shows maximum average sensitivity for 5000 ppm CO_2.

The gas sensing mechanism of the gas sensor depends on the oxygen chemisorption centres which are localized donor and acceptor states, oxygen vacancies and defects formed on the nanomaterial surface during the synthesis process. When the film was exposed to air, the O_2 present in the air was adsorbed on the nanotube surface and ionized to oxygen ion by trapping the free electron and building a thick space charge layer, which increases the potential barrier. At lower concentration (<5000 ppm) of gas, the CO_2 molecules interact with oxygen species and form a metastable compound CO_3 and release electrons which attenuate the potential barrier and the resistance starts decreasing. The reaction given in equation 4.5 to 4.7 are involved in this mechanism.

$$O_2 \text{ (ads)} + 3e^- \rightarrow O^{2-} \text{ (ads)} + O^- \text{.....(4.5)}$$

When interacting with CO_2

$$CO_2 + O^{2-} \rightarrow CO_3 + 2e^- \text{……(4.6)}$$

When the concentration of CO_2 increases more than 5000 ppm, a reverse mechanism take place in which the metastable compound CO_3 interactswith itself and releases the oxygen atom causing less change in the resistance at higher level.

$$CO_3 + CO_3 \rightarrow 2CO_2 + O_2 \text{ (gas)……..(4.7)}$$

The response time and recovery time are measured by using exponential fitting of data by th equations 4.8 & 4.9:

$$R_m = R_0 exp(\frac{-\tau}{\tau_{res}}) \text{……..(4.8)}$$

$$R_m = R_0 \left\{1 - exp(\frac{-\tau}{\tau_{rec}})\right\} \text{……..(4.9)}$$

Here, R_0 is the initial state resistance of the film, τ_{res} and τ_{rec} are the response and recovery time respectively. The response time is the time required to acquire the 90% of maximum resistance and recovery time is defined as the time required to achieve the initial value of resistance $R_{0.}$ The response and recovery times at 1650 ppm are 25.84 and 37.84 s, whereas, for 3300 ppm these times are 21.99 and 36.46 s and at 5000 ppm they are 30.21 and 49.62 respectively. The response of the sensor is directed by several types of transition like the band to band transition in which transition from valance band to conduction band was occurred and other transition like valance band to unoccupied state or defect state to conduction band etc. On the other hand, the recovery time of the film depends on the recombination and de-excitation of an electron to the ground state. In the case of $CO_{2,}$ the recombination process depends on the negatively charged oxygen species which creates the hole for recombination of unpaired electrons.

After the repeated experiments, due to the formation of water content during the exposure of CO_2, the film gets wet therefore it is kept for obeying. To examine the effect of direct moisture on the gas sensing mechanism we performed the experiment in the presence of humidifier (saturated solution of K_2SO_4) which increases humidity from 10% to 90%. Firstly, the experiments were formed in the absence of CO_2 and later the whole experiment was repeated in the presence of 3300 ppm CO_2. The observed data have been presented as Fig. 4.16. In figure, we can clearly observe two curves; black dotted curve indicating a change in relative humidity without CO_2 and red dotted curve with CO_2. There is a minute difference in the impedance in both the cases on increasing the humidity from 10% to 90%. It is obvious that the presence of CO_2 contributed uniformly to the impedance of the film and parallel variations were observed. This explains that the variation of impedance is approximately the same at lower humidity levels so the humidity level does not affect the sensor below 60 %RH. Above this, the higher changes were observed so we need to dry the film at a higher humidity level before the exposure of CO_2.

4.6.1 Sensing mechanism

As CO_2 is a chemically stable gas, its sensing mechanism for single phase and composite oxides are still unclear and controversial. The formation of carbonation was

suggested to be responsible for the CO_2 sensing mechanism of some composite p-n system. Some experimental results showed that the oxygen adsorbed on the surface of metal oxides and the adsorbed oxygen atom finally form a metastable compound or complex species which are responsible for sensing [47]. The gas sensing mechanism of CNT based thin film is based on the chemical kinetics. In such a mechanism, the film gets interacted with gas and the reaction kinetics between the physisorbed oxygen species on the surface and targeted gas molecules. A space charge layer is created on the surface of CNT based thin film with air due to the trapping of an electron by the adsorbed oxygen gas molecules on the porous surface of the CNT based thin film. This space charge region hinders the easy flow of free electrons and a high value of initial resistance (R_a) is found. As the dry film contains O^-, therefore, on the exposure of CO_2 gas with the film, it produces CO_3^- with the release of one electron which results in an increased conductivity or less value of R_g.

4.6.2 Computational analysis of CNTs

The adsorption process of the molecule of carbon dioxide on the (1,1) and (2,2) CNTs was studied using the density functional theory (DFT) [48-52] implemented in the Computational Quantum Chemical HF code of basis set 6-31g. In the present work, two different structure of CNT are modelled, Single-walled armchair CNT (ac-CNT) can be obtained by rolling the graphene sheet along the x-axis direction & improve it (i.e., along $\vec{r} = \overrightarrow{a_1} + \overrightarrow{a_2}$) in this case, we have rolled the sheet along the vector $\vec{r} = n\overrightarrow{a_1} + m\overrightarrow{a_2}$ then repeating the ring structure for 2 periods along the tube axis. CNTs have high adsorbing capacity due to the high aspect ratio, so we simulate the nanotubes, interacting with the carbon dioxide molecule.

In this computational method, we have analyzed the binding energy and HOMO-LUMO band gap of CNT before and after interaction with the exposed gas. The sensing potential of carbon nanotubes directly depends on the low energy lattice sites because the CO_2 molecules interact only on lower energy sites by endohedrally non-covalent functionalization method. So for finding the energy levels and free energy sites, we firstly optimize the nanotube structure then find its lower energy levels and made it to interact

with CO_2 molecule as shown in Fig. 4.17. The binding energy of the carbon atom on the substrate is calculated using the following convention given in Eqn. 4.10

$$E_{bind} = E_{(Substrate)} - nE_{(C)} \quad \text{.....(4.10)}$$

where $E_{(substrate)}$, and $E_{(C)}$ stand for the total energies of the relaxed C atom in the substrate (here the substrate is CNT), and n is the number of carbon atoms. We also define the adsorption energy of the CO_2 molecule on the adsorbent by the Eqn 4.11.

$$E_{ad} = E_{(CO2+adsorbent)} - E_{(adsorbent)} - E_{(CO2)} \quad \text{.....(4.11)}$$

where $E_{(CO2+adsorbent)}$, $E_{(adsorbent)}$, and $E_{(CO2)}$ stand for the total energies of a system of CO_2 molecule and the adsorbent (the adsorbents are CNT), isolated adsorbent, and isolated CO_2 molecule [53].

In the case of adsorption of several molecules (for instance "N" molecules of CO_2), the average adsorption energy per molecule would be defined by the Eqn 4.12

$$E_{ad}^{ave} = \frac{E_{(CO2+adsobent)} - E_{(adsorbent)} - NE_{(CO2)}}{N} \quad \text{.....(4.12)}$$

For calculating electronegativity, hardness, softness and nucleophilic index, we will follow the reactions 3.8-3.11 and given in previous chapter.

Table 4.3 (a) & (b) exhibits that the length of the tubes is directly proportional to the sensing sites of nanotubes. Further, we analyzed the change in binding energy on increasing the CO_2 levels to the nanotubes, which shows that the binding energy of CNTs drastically decreased by increasing the concentration of CO_2 because the CO_2 molecules interacted with the surface of CNT and the surface energy of CNT was modified creating the free lattice sites. In the case of CNT (1,1), the binding energy of nanotube varies lesser in comparison to CNT (2,2) which shows that the sensitivity towards as CO_2 is directly proportional to the leghth of CNTs towards CO_2. After analyzing the binding energy of CNTs attached to CO_2 we found that the dipole moment has also been changed by increasing the CO_2 level.

Regarding the electronic behaviour of breaking and forming bonds along with a chemical reaction, organic reactions can be classified as non-polar and polar reactions. While non-polar reactions take place through species with some radical character, polar reaction take place through zwitterion one. Most organic molecules having polarized functional groups present in it are characterized by electrophilic interaction and in the case of CNT (1, 1) & CNT (2, 2) the electrophilic index decreases in CNT (2, 2) and increases in CNT (1, 1) when the CNT interacts with CO_2 molecule so we can observe that the length of tube is a very important parameter in CO_2 sensing mechanism and the experimental data was the same as theoretical data for larger length of nanotubes.

When the CNTs interacted with the CO_2 molecules, the width of the energy band gap and the free electrons increases or decreases according to free electron carriers in the conduction band. The electrons in the conduction band are responsible for the conductivity. The flow of level of the electrons is decreased with the increase in energy bandgap, as a result, the resistance of film increases but in the case of CNTs, the free carriers increase in the conduction band so the band gap decreases as shown in Fig.4.18.

Table 4.3 (a) & (b) shows the shifting of Fermi level towards the HOMO which exhibits the enhancement of the sensitivity of the CNTs towards CO_2. In this case, when the gas interacts with the CNT, the number of free electrons have been increased so the Fermi level is found near the HOMO and the ionization potential is decreased. The band gap decreases and when the free lattice sites are filled then the band gap again starts increasing. We found that theoretical evidence is very analogous to the experimental data and confirmed the result obtained.

4.7 Conclusion

MWCNTs were grown on Co nanoparticle from ethanol by DLICVD method at a temperature of 750 ℃. Co nanoparticles were prepared by using the sol-gel method and the precipitate was annealed at 500 ℃ for stabilization. The prepared Co nanoparticle were stable and had a pure composition which exhibited the effective catalytic activity for CNT synthesis. The grown CNTs had a tubular structure, dense morphology and good crystallinity. After growth, the purification and functionalization were done through acid

treatment. The sensor was fabricated using the spin coating of functionalized nanotubes on borosilicate glass substrates. CNT-based sensor yielded the maximum sensitivity of 2.1 at 5000 ppm with comparatively fast response and recovery time as 30.21 s and 49.62 s respectively at room temperature. Improved sensing response characteristics of CNT-based sensor structure are attributed to the formation of the large surface area to interact and conducting channels to the charge carriers at low temperatures. In the computational part, we found that the binding energy, dipole moment and HOMO-LUMO gap of CNTs are significantly changed on interacting with CO_2 molecules. Thus the CNT based sensor investigated here is ultra-sensitive towards the detection of CO_2 gas at room temperature, robust and cheap for commercialization.

References

[1] J. Zhang, X. Liu, G. Neri, N. Pinna. Nanostructured Materials for Room Temperature Gas Sensors Adv. Mater. 28 (2016) 795.

[2] X. Liu, T. Ma, N. Pinna, J. Zhang. Two Dimensional Nanostructured Materials for Gas Sensing Adv. Funct. Mater. 170 (2017) 2168.

[3] S. Lijima. Helical microtubules of graphitic carbon Nature. 354 6348 (1991) 56-58.

[4] M. S. Dresselhaus. Electronic, thermal and mechanical property of carbon nanotubes. Philosophical Transaction of Royal Society of London Deries A: Mathematical, Phys. and Eng. Sci. 362 1823 (2004) 2065.

[5] C. G. Lu, J. Liu. Controlling the diameter of carbon nanotubes in chemical vapor deposition method by carbon feeding. J. Phys. Chem. B 110 41 (2006) 20254.

[6] E. Pop. Thermal conductance of an individual single-wall carbon nanotube above room temperature. Nano Letters. 6 1 (2006) 96.

[7] S. Ming, B. Zheng, J. A. Liu. A Scalable CVD method for the synthesis of single-walled carbon nanotubes with high catalyst productivity. Chem. Phy. Letter. 322 (2000) 321.

[8] U. Kumar, B. C. Yadav, State of Art: An Approach to the Synthesis of Pure and Doped Graphene Adv. Sci. Eng. Med. 10 (2018) 638.

[9] R. Chapelle, F. Oudrhiri-Hassani, L. Presmanes, A. Barnabe, P. Tailhades. CO_2 sensing property of semiconducting copper oxide and spinal ferrite nanocomposite thin film App. Surf. Science; 256 (2010) 4715.

[10] J. Herra´n, G. G. Mandayo, I. Ayerdi, E. Castan˜o. Influence of silver as an additive on $BaTiO_3$–CuO thin film for CO_2 monitoring. Sens. Actuators B: Chem. 129 (2008) 386.

[11] K. Fan, H. Qin, L. Wang, L. Ju, J. Hu. Sens. Actuators B: Chem.; 177 (2013) 265.

[12] T. Krishnakumar, R. Jayaprakash, T. Prakash, D. Sathyaraj, N. Donato, S. Licoccia, Latino M, Stassi A, G. Neri. CdO-based nanostructures as novel CO_2 gas sensors. Nanotechnology 22 (2011) 325501.

[13] Y. Xiong, Q. Q. Xue, C. Ling, W. Lu, D. Ding, L. Zhu, X. Li. Effective CO_2 detection based on LaOCl-doped SnO_2 nanofibers:Insight into the role of oxygen in carrier gas. Sens. Actuators B: Chem. 241 (2017) 725.

[14] D. Ding, W. Lu, Y. Xiong, X. Pan, J. Zhang, C. Ling, Y. Du, Q. Xu. Facile Synthesis of $La_2O_2CO_3$ Nanoparticle Films and Its CO_2 Sensing Properties and Mechanisms App. Surf. Science. 426 (2017) 725.

[15] M. Mittal, A. Kumar. Carbon nanotube (CNT) gas sensors for emissions from fossil fuel burning. Sens. Actuators B: Chem. 203 (2014) 349.

[16] U. Kumar, S. Sikharwar, R. K. Sonkar, B. C. Yadav. Carbon nanotube: synthesis and application in solar cell. J. Inorg. Organomet. P. 26 6 (2016) 1231.

[17] R. K. Sonker, M. Singh, U. Kumar, B. C. Yadav. MWCNT Doped ZnO Nanocomposite Thin Film as LPG Sensing. J. Inorg. Organomet. P. 26 6 (2016) 1434.

[18] P. Tyagi, A. Sharma, M. Tomar, V. Gupta. A comparative study of RGO-SnO_2 and MWCNT-SnO_2 nanocompositesbased SO_2 gas sensors. Sens. Actuators B: Chem. 248 (2017) 980.

[19] B. C. Yadav, K. Agrahari, S. Singh, T. P. Yadav. J of Mater. Sci: Mater. in Elect., 27 5 (2016) 4172.

[20] R. K. Sonker, S. R. Sabhajeet, B. C. Yadav. TiO_2–PANI nanocomposite thin film prepared by spin coating technique working as room temperature CO_2 gas sensing. J Mater Sci: Mater Electron. 27 11 (2016) 11726.

[21] E. Singh, R Srivastava, U Kumar, A. Katheria. Carbon Nanotube: A Review on Introduction, Fabrication Techniques and Optical Applications. Nanosci. and Nanotech. Research. 4 (4) (2017) 120.

[22] E. Singh, U. Kumar, R. Srivastava, B. C. Yadav Carbon Nanotubes Based Thin Films as Opto-Electronic Moisture Sensor. Adv. Sci. Eng. Med. 10 (2018) 785.

[23] Y. J. Jeong, C. Balamurugan, D. W. Lee Enhanced CO_2 gas-sensing performance of ZnO nanopowder by La loaded during the simple hydrothermal method. Sens. Actuators B: Chem. 229 (2016) 288.

[24] C. J. Lee, D. W. Kim, T. J. Lee, Y. C. Choi, Y. S. Park, Y. H. Lee, W. B. Choi, N. S. Lee, G. S. Park, J. M. Kim. Synthesis of aligned carbon nanotubes using thermal chemical vapor deposition. Chem. Phy. Letters. 312 (1999) 461.

[25] Y. H. Wang, J. Lin, C. H. A. Huan, G. S. Chen. Synthesis of large area aligned carbon nanotube arrays from C_2H_2-H_2 mixture by rf plasma-enhanced chemical vapor deposition. Appl. Phys. Lett. 79 (2001) 680.

[26] B. O. Boskovic, V. Stolojan, R. U. Khan, S. Haq, S. R. P. S. Silva. Large-area synthesis of carbon nanofibres at room temperature. Nat. Mater. 1 (2002) 165.

[27] E.G. Ordoñez-Casanova, M. Román-Aguirre, A. Aguilar-Elguezabal, F. Espinosa-Magaña. Synthesis of Carbon Nanotubes of Few Walls Using Aliphatic Alcohols as a Carbon Source. Materials. 6 (2013) 2534.

[28] G. A. Rance, D. H. Marsh, R. J. Nicholas, A. N. Khlobystov. UV–vis absorption spectroscopy of carbon nanotubes: Relationship between the p-electron plasmon and nanotube diameter. Chemical Physics Letters. 493 (2010) 19.

[29] B. C. Yadav, S. Singh, A. Yadav, T. Shukla. Experimental investigations on nanosized ferric oxide and its LPG sensing. Inter. J. of Nanosci. 10 (2011) 135.

[30] M. Perez-Cabero, I. Rodriguez-Ramos, A. Guerrero-Ruiz. Characterization of carbon nanotubes and carbon nanofibers prepared by catalytic decomposition of acetylene in a fluidized bed reactor. J. Catal. 215 (2003) 305.

[31] J. W. Snoeck, G. F. Froment, M. Fowles. Preparation of nickel nanoparticles and their catalytic activity in the cracking of methane. J. Catal. 169 (1997) 240.

[32] N. Kouklin, M. Tzolov, D. Straus, A. Yin, J. M. Xu. Infrared absorption properties of carbon nanotubes synthesized by chemical vapor deposition. Appl. Phys. Lett. 85 (2004) 513.

[33] H. Shang, C. Liu, F. Wei. FT-IR Study of Carbon Nanotube Supported Co-Mo Catalysts, J Nat. Gas Chem. 13 (2004) 95.

[34] M. H. Pócsik, M. Koós, L. Ley. Origin of the D peak in the Raman spectrum of microcrystalline graphite. J. Non-Cryst. Solids. 227 (1998) 1083.

[35] M. J. Matthews, M. A. Pimenta, G. Dresselhaus, M. S. Dresselhaus, M. Endo Origin of dispersive effects of the Raman D band in carbon materials. Phys. Rev. B. 59 (1999) 6585.

[36] C. Thomsen, S. Reich, Double resonant Raman scattering in graphite. Phys. Rev. Lett. 85 (2000) 5214.

[37] S. D. M. Brown, A. Jorio, M. S. Dresselhaus, G. Dresselhaus. Observations of the D-band feature in the Raman spectra of carbon nanotubes. Phys. Rev. B. 64 073403 (2001) 1.

[38] L. Bokobz, J. Zhang. Raman spectroscopic characterization of multiwall carbon nanotubes and of composites. Express Polym. Lett. 6 (2012) 601.

[39] Y. Ouyang, L. M. Cong, L. Chen, Q. X. Liu, Y. Fang. Raman study on single-walled carbon nanotubes and multi-walled carbon nanotubes with different laser excitation energies. Physica E. 40 (2008) 2386.

[40] A. Jorio, M. A. Pimient, A. G. Souza Filho, R. Saito, G. Dresselhaus, M. S. Dresselhaus, Characterizing carbon nanotubes samples with resonance Raman scattering. New J. Phys. 5 139 (2003) 1.

[41] M. S. Dresselhaus, G. Dresselhaus, M. Hofmann. The big picture of Raman scattering in carbon nanotubes. Vib. Spectrosc. 45 (2007) 711.

[42] S. B. A. Hamid, T. L. Tan, C. W. Lai, E. M. Samsudin. Multiwalled carbon nanotube/TiO_2 nanocomposite as a highly active photocatalyst for photodegradation of Reactive Black 5 dye. Chinese Journal of Catalysis. 35 (2014) 2014.

[43] M. Maryam, A. B. Suriani, M. S. Shamsudin, M. Rusop. BET Analysis on Carbon Nanotubes: Comparison Between Single and Double Stage Thermal CVD Method. Advance material Research. 626 (2013) 289.

[44] A. Kaushik, R. Kumar, S. K. Arya, M. Nair, B. D. Malhotra, S. Bhansali. Organic-Inorganic hybrid nanocomposite based gas sensor for environmental monitoring, Chemical reviews, 115 11 (2015) 4571.

[45] M. Singh, B. C. Yadav, A. Ranjan, R. K. Sonkar, M. Kaur. Detection of liquefied petroleum gas below lower explosion limit (LEL) using nanostructured hexagonal strontium ferrite thin film. Sen. Actuator B: Chem. 249 (2016) 96.

[46] M Singh, B. C. Yadav, A. Ranjan, M. Kaur, S. K. Gupta. synthesis and characterization of perovskite barium titanate thin film and its application as LPG Sensor. Sen. Actuator B: Chem. 233 (2017) 1170.

[47] T. Frauenheim, G. Seifert, M. Elstner, T. A. Niehaus, C. Köhler, M. Amkreutz, M. Sternberg, Z. Hajnal, A. D. Carlo, S. Suhai, Atomistic simulations of complex materials: ground-state and excited-state properties. J. Phys. Condens. Matter. 9 14 (2002) 3015.

[48] X. Wang, H. Qin, L. Sun, J. Hu. CO_2 sensing properties and mechanism of nanocrystalline $LaFeO_3$ sensor. Sens. Actuator B: Chem. 188 (2013) 965.

[49] P. Koskinen, V. Makinen. Density-functional tight-binding for beginners. Comput. Mater. Sci. 47 (2009) 237.

[50] J. C. Slater, G. F. Koster. Simplified LCAO Method for the Periodic Potential Problem Phys. Rev. 94 (1954) 1498.

[51] M. Elstner, D. Porezag, G. Jungnickel, J. Elsner, M. Haugk, T. Frauenheim. A self-consistent-charge density-functional tight-binding method for simulations of complex materials properties. Phys. Rev. B. 58 (1998) 7260.

[52] T. A. Niehaus, M. Elstner, T. Frauenheim, S. Suhai. Application of an approximate density-functional method to sulfur-containing compounds. J. Mol. Struct. Theo. chem. 541 (2001) 185.

[53] N. Tit, M. M. A. H. Ezzi, M. Abdullah, M. Yusupov, S. Kouser, H. Bahlouli, Z. H. Yamani. Detection of CO_2 using CNT-based sensors: Role of Fe catalyst on sensitivity and selectivity. Mat. Chem. and Phys. 186 (2017) 353.

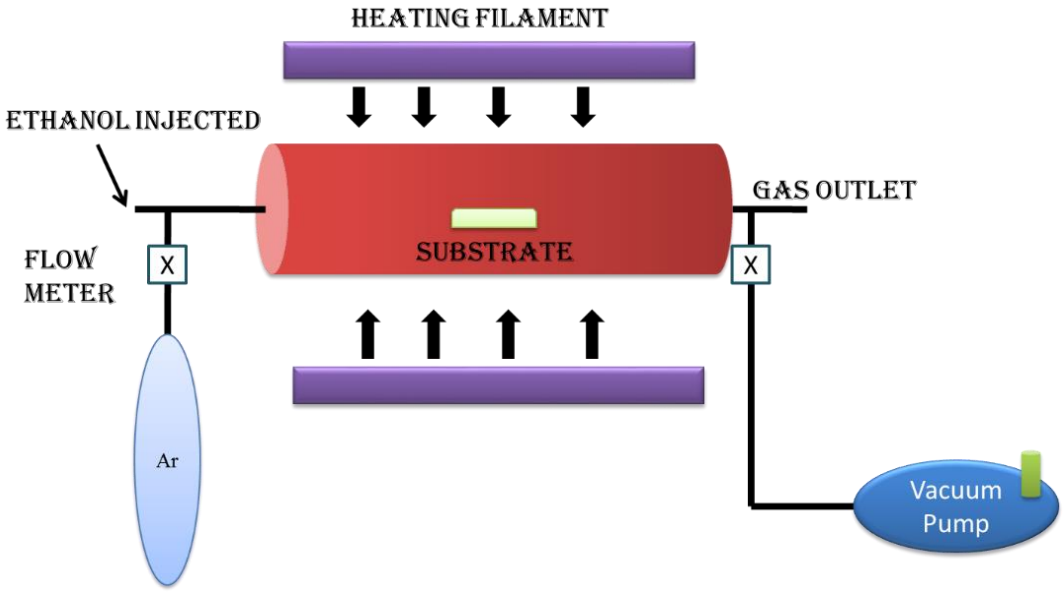

Fig. 4.1 Synthesis of horizontally aligned CNTs using DLICVD method

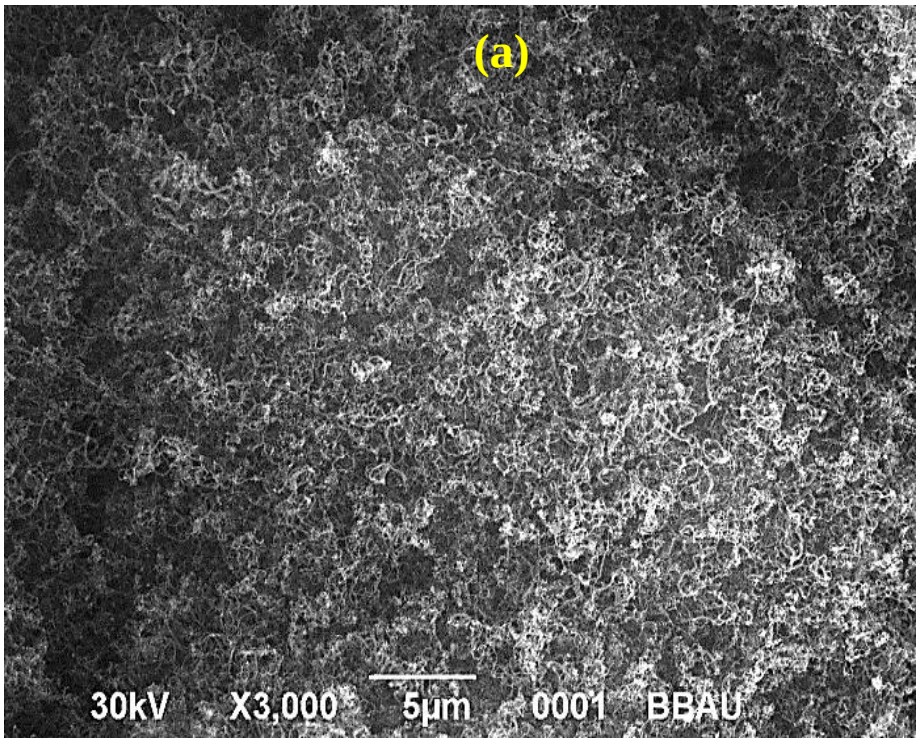

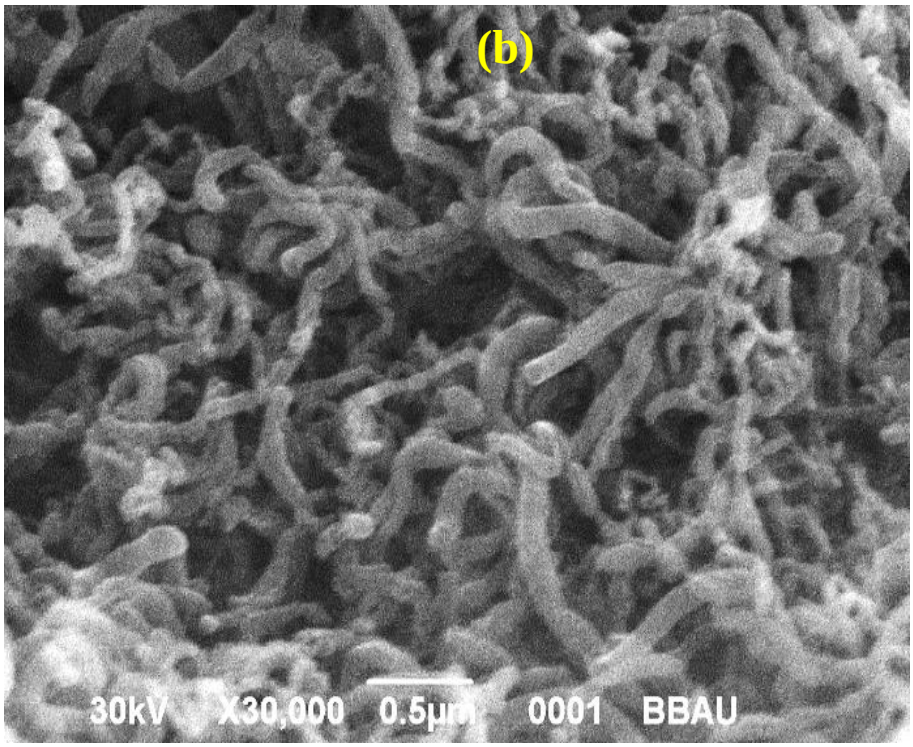
(b)
30kV X30,000 0.5µm 0001 BBAU

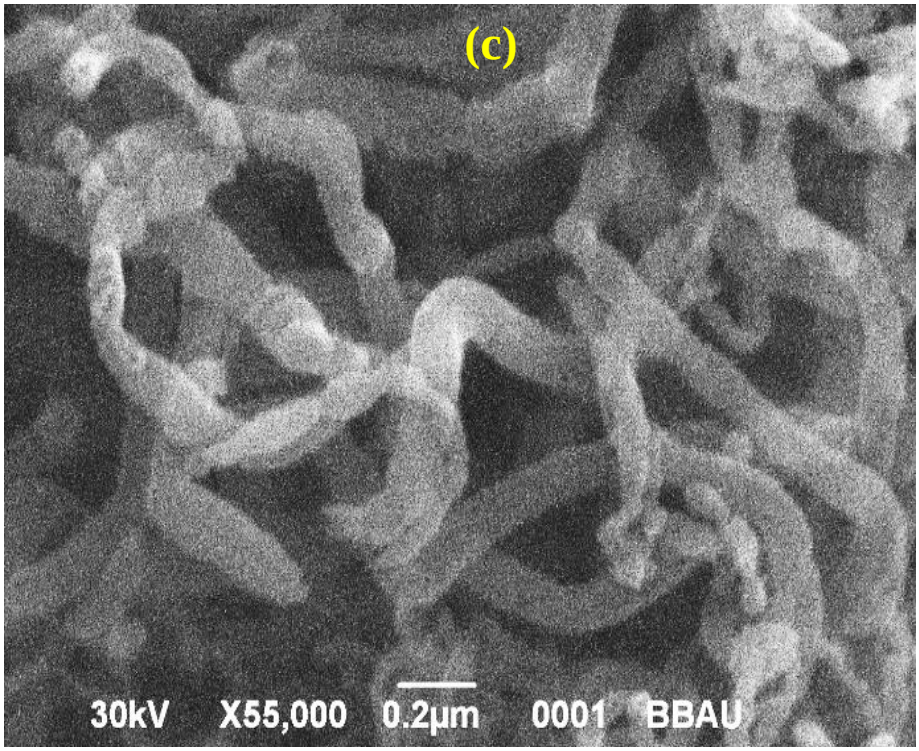
(c)
30kV X55,000 0.2µm 0001 BBAU

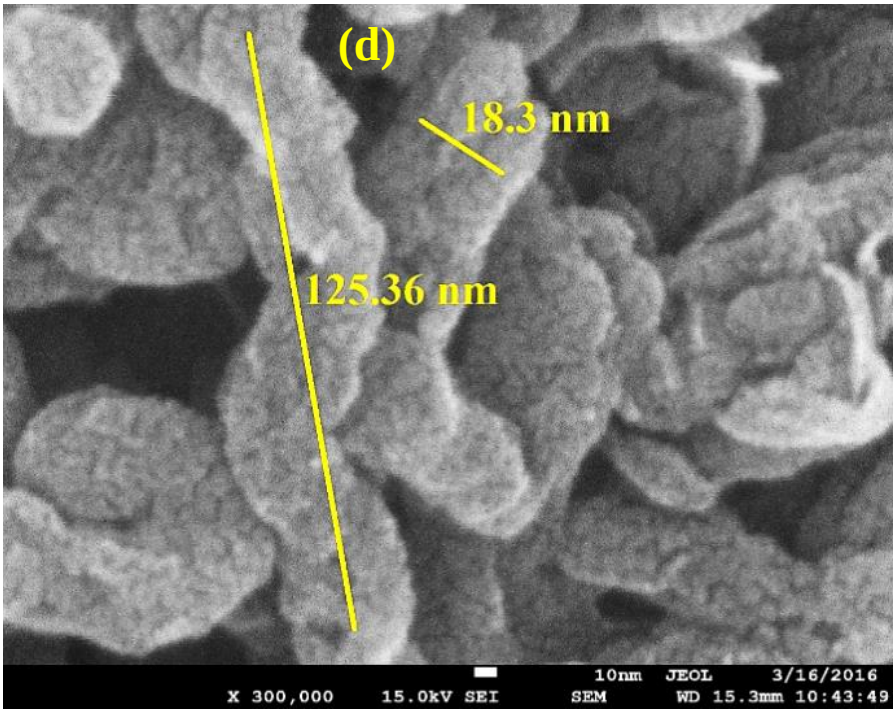

Fig. 4.2 (a) CNT grown on catalyst at 5 µm scale (b) CNT at 500 nm scale (c) CNTs at 200 nm scale (d) CNTs at 10 nm scale

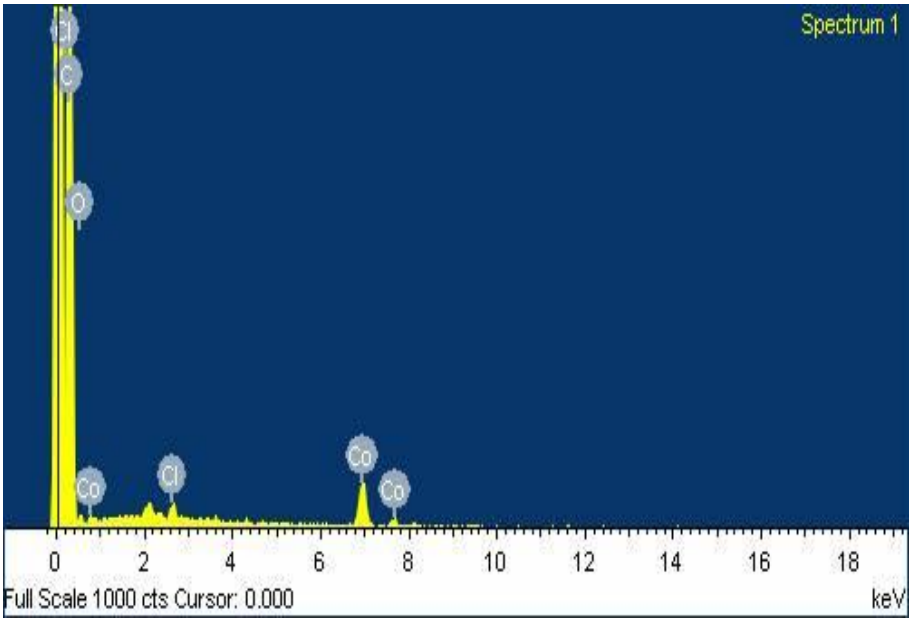

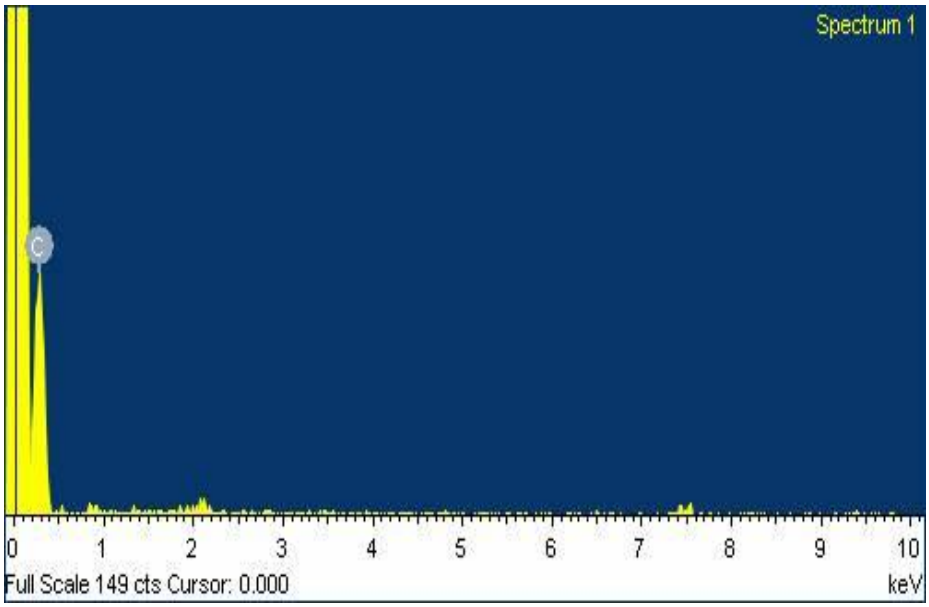

Fig. 4.3 EDX of MWCNT before and after the filtration process

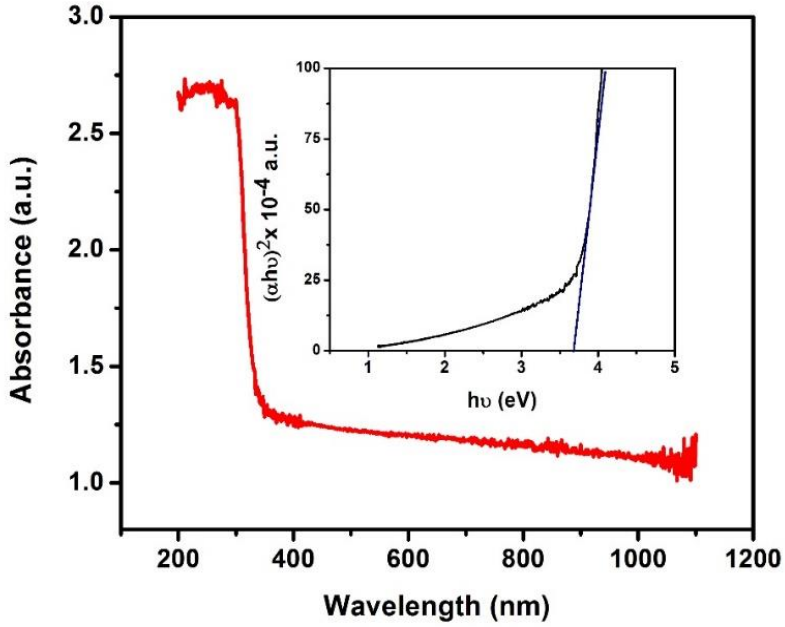

Fig. 4.4 Absorption spectra and Tauc plot of CNTs synthesized at 750 ℃

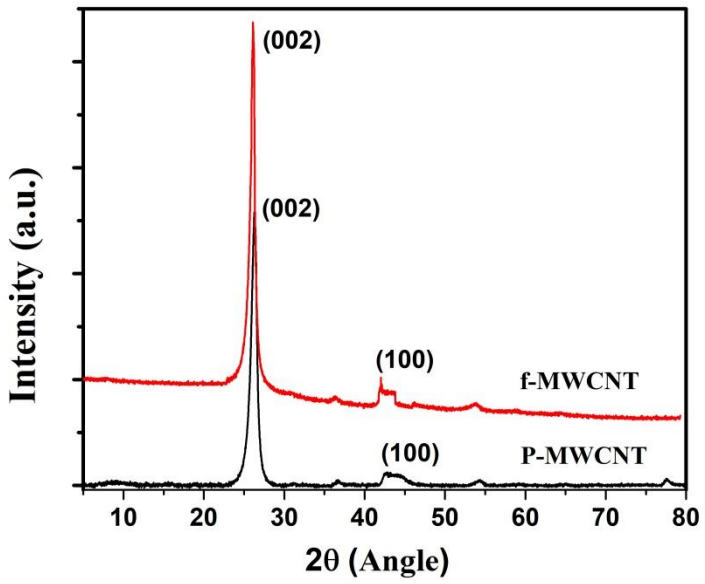

Fig. 4.5 XRD analysis of f-MWCNT and P-MWNT after removing the catalyst particle

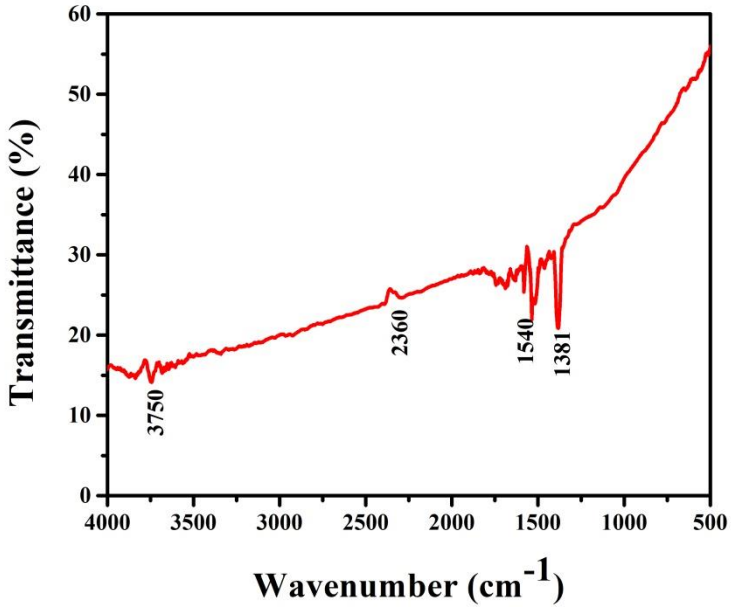

Fig. 4.6 IR analysis of MWCNTs synthesized by DLICVD method

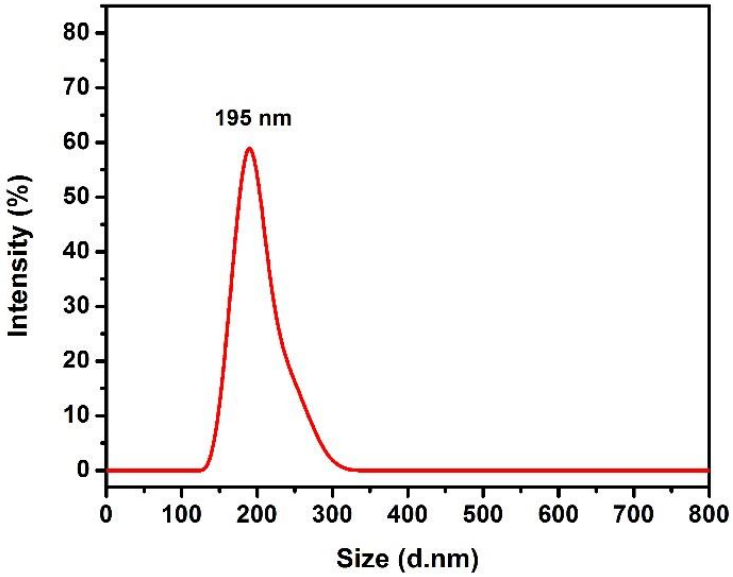

Fig. 4.7 The average length of nanotube using particle size analyzer

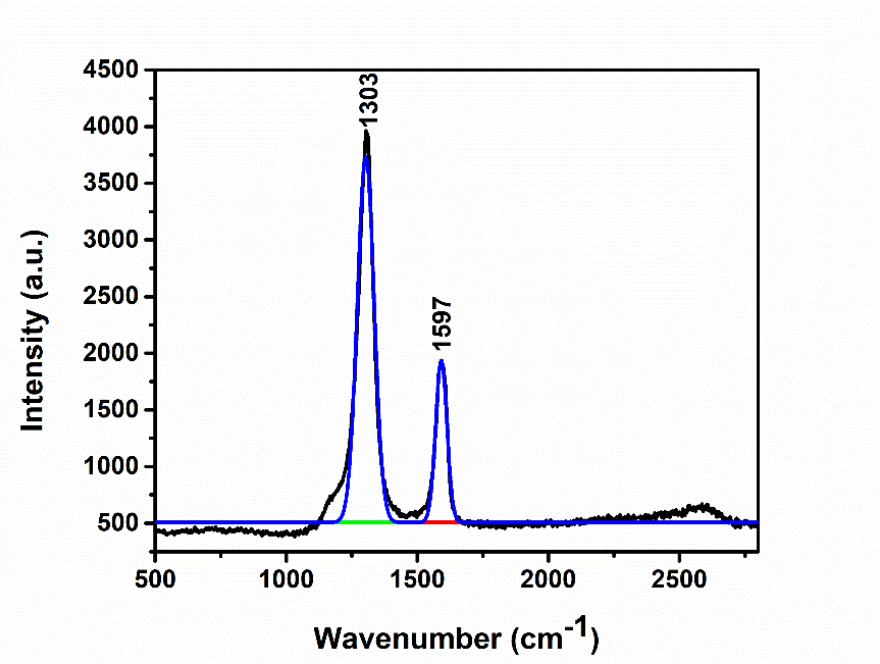

Fig. 4.8 Raman spectra of MWCNTs showing D and G band respectively

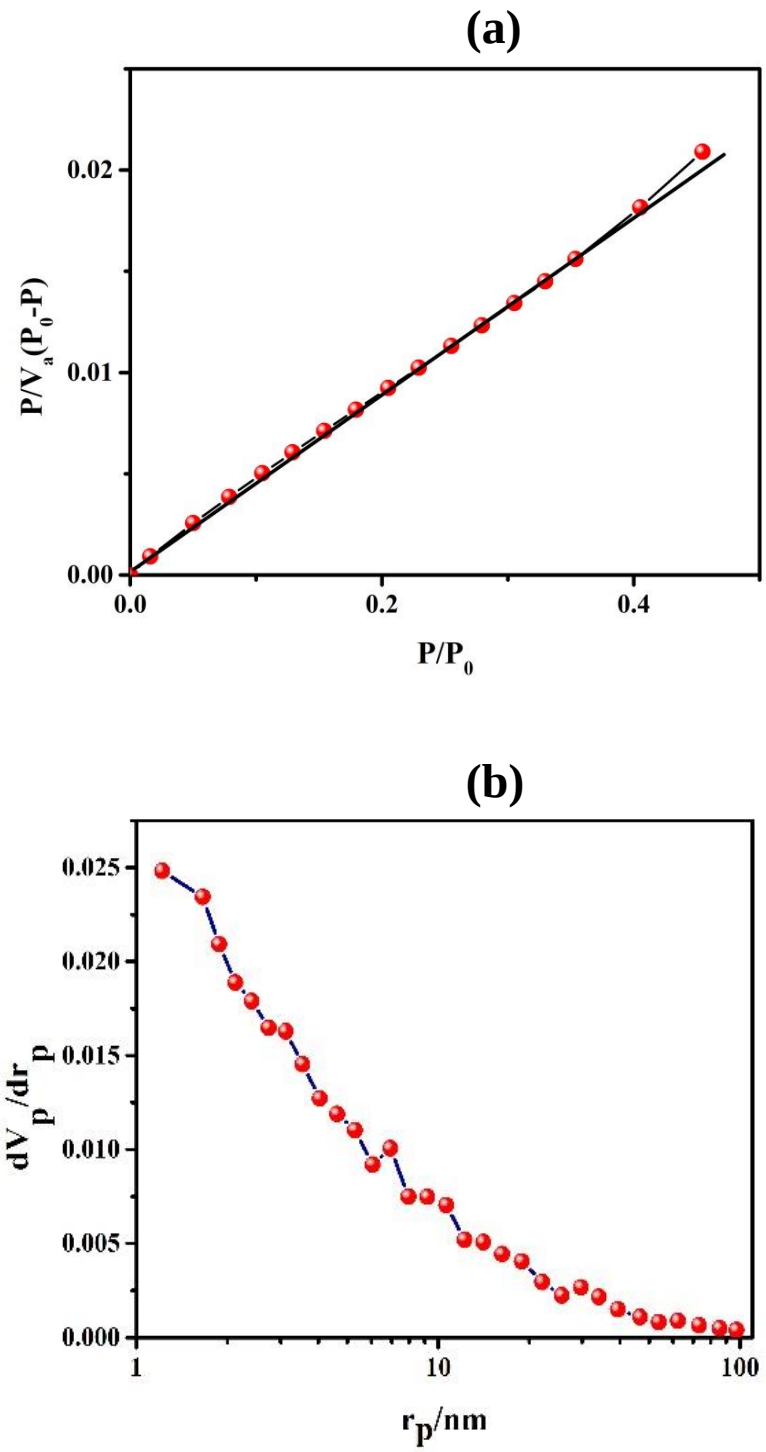

Fig. 4.9 (a) BET plot and (b) BJT plot of MWCNT

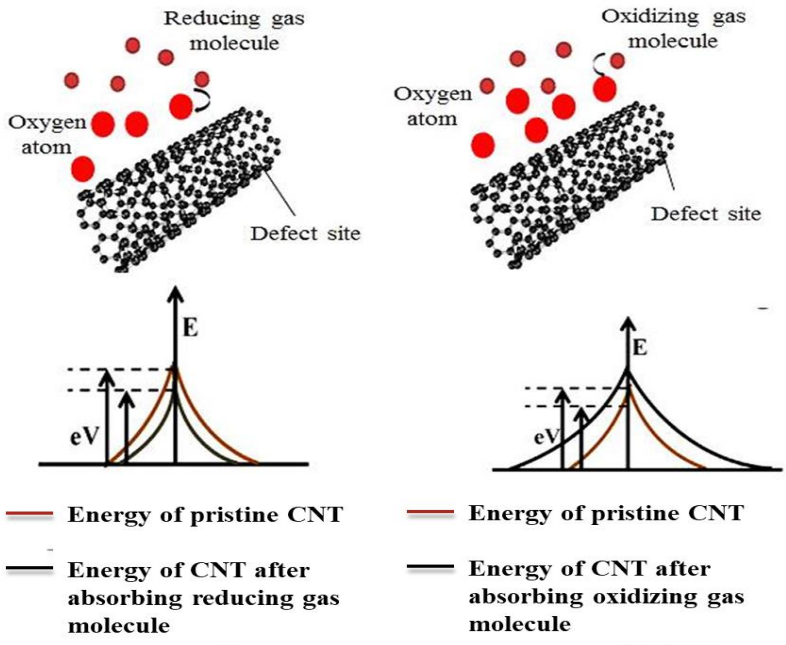

Fig. 4.10 Gas sensing mechanism of CNTs on the exposure of the gas

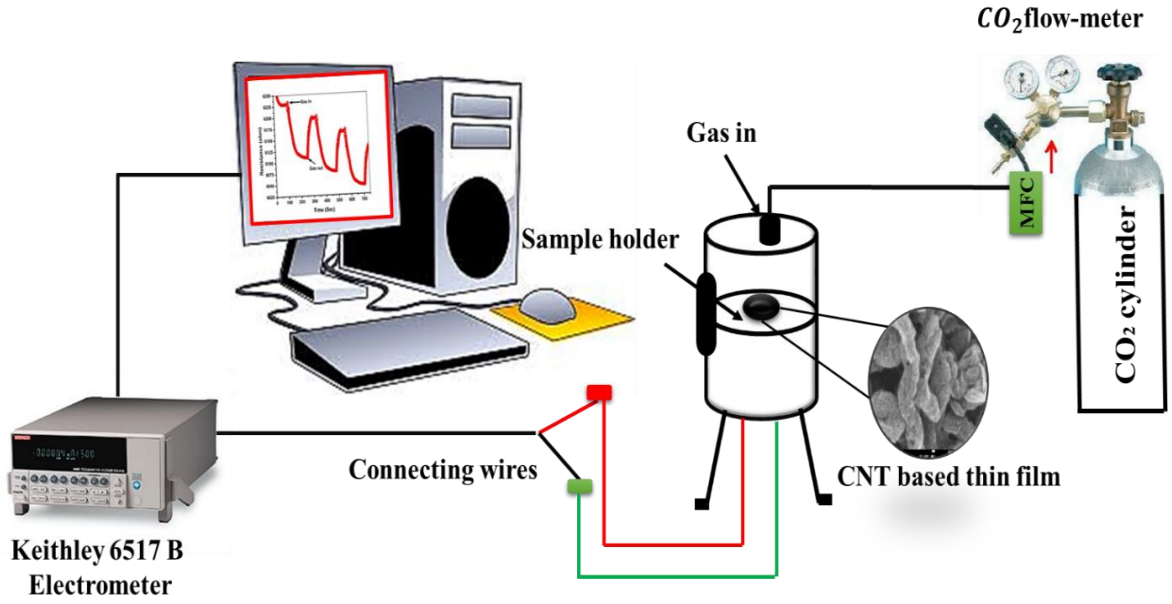

Fig. 4.11 Gas sensing setup of the CNT-based thin film for CO_2 sensing

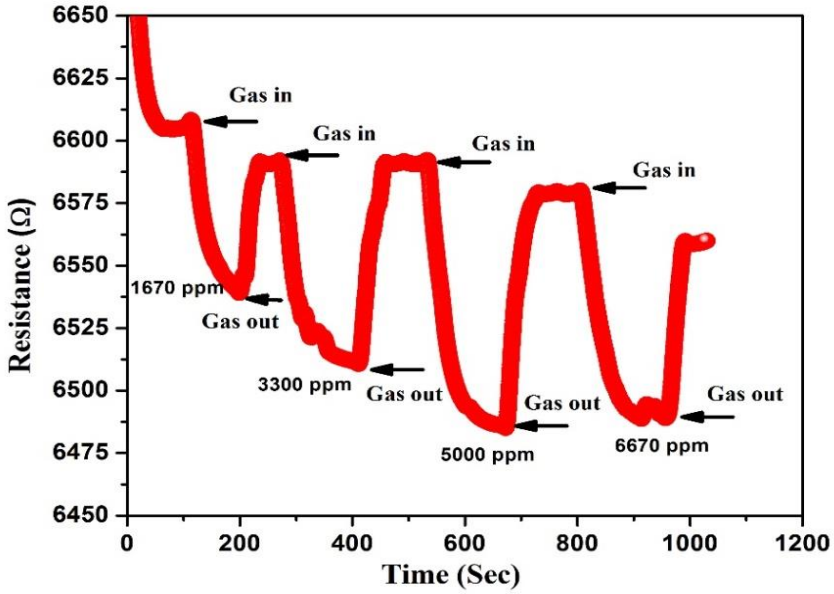

Fig. 4.12 Variation in resistance of CNT-based thin film at various concentrations of CO_2 gas

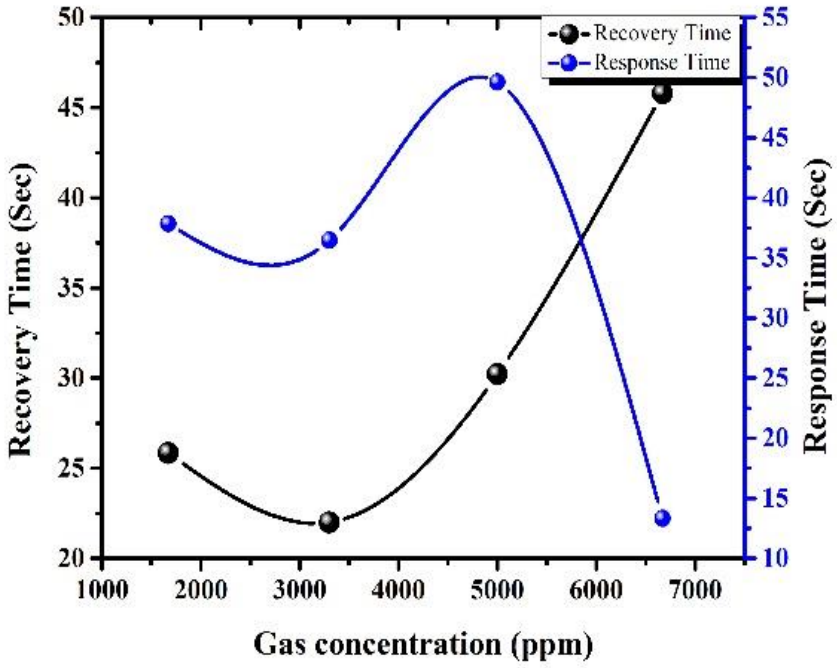

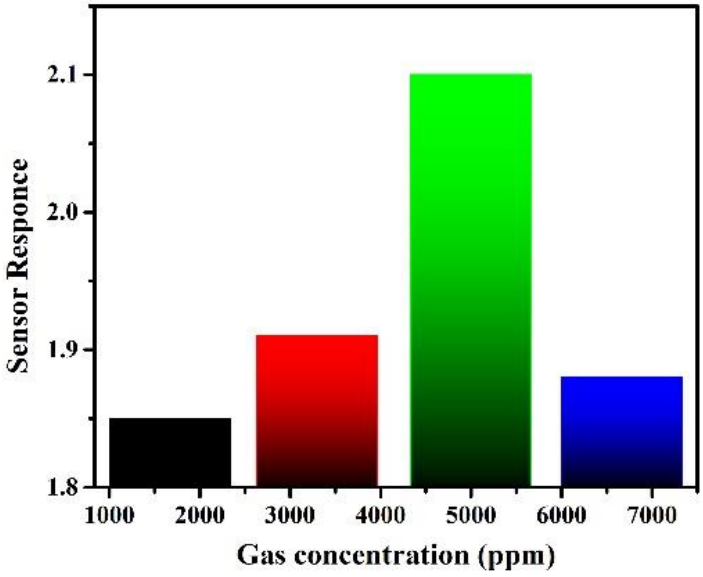

Fig. 4.13 (a) Response time, recovery time (b) sensitivity of the thin film at various concentrations of CO_2

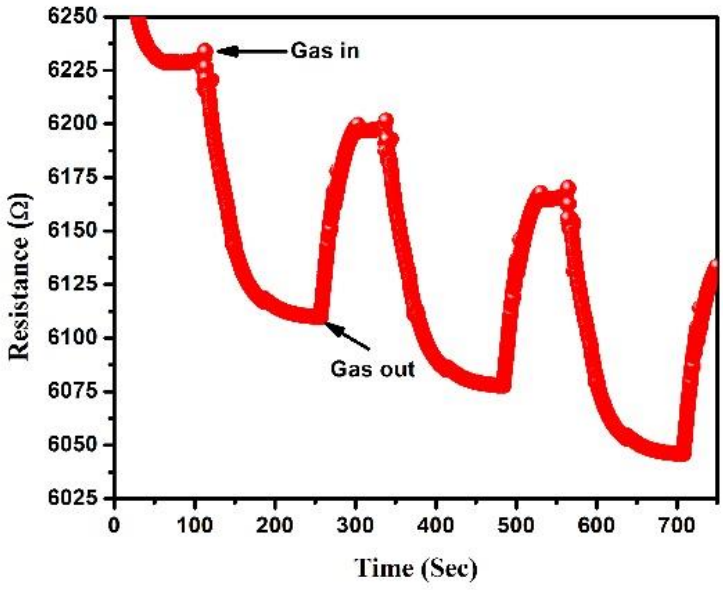

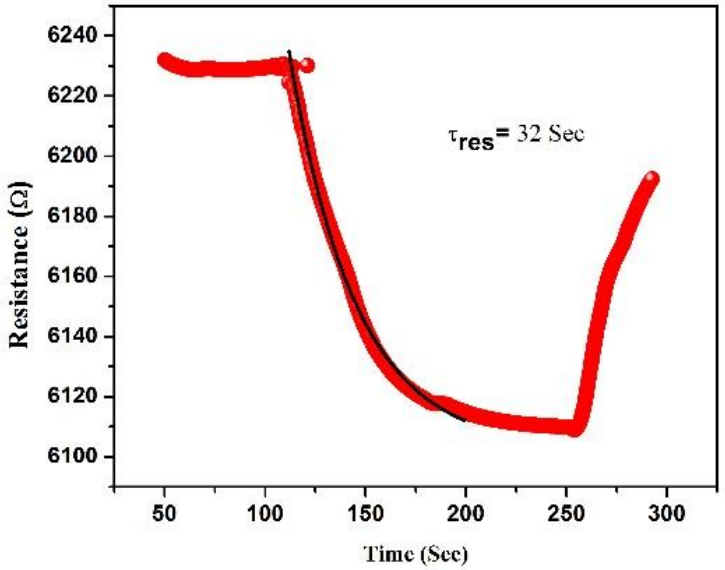

Fig. 4.14 (a) Reproducibility of the CNT-based thin film at 5000 ppm concentration (b) Calculation of response time using exponential fitting

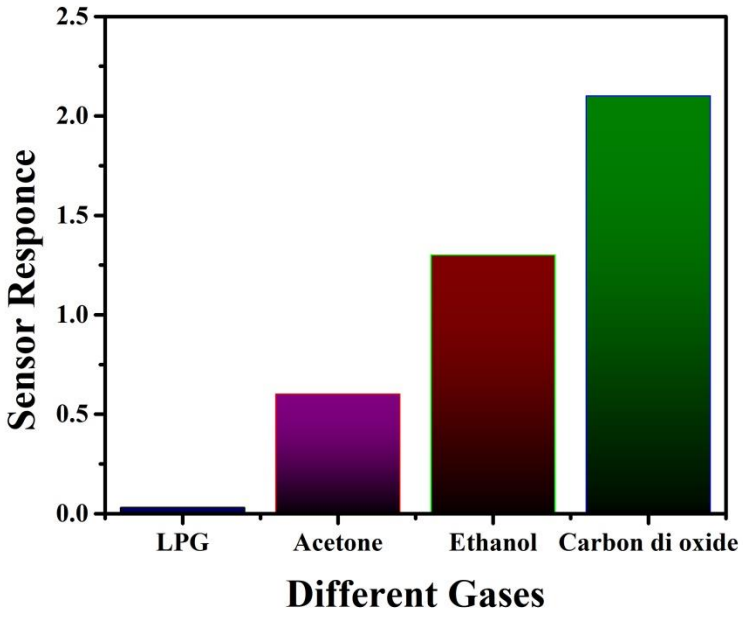

Fig. 4.15 Selectivity of CNT based thin film as a CO_2 sensor

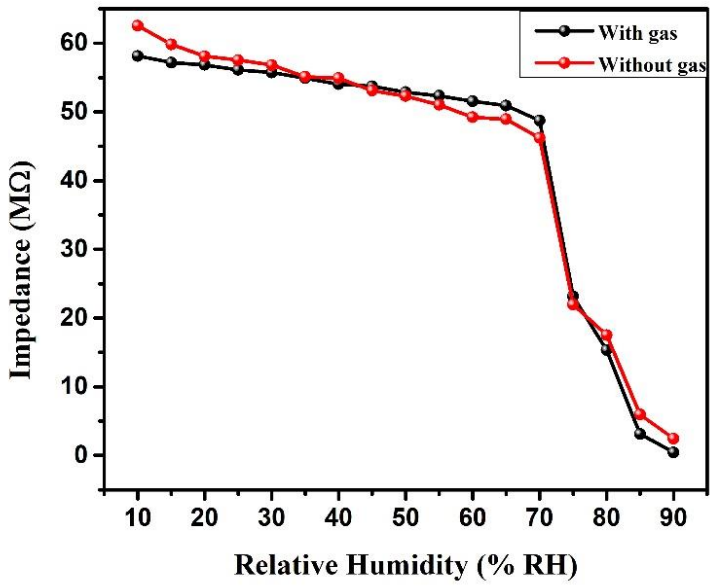

Fig. 4.16 Effect of relative humidity on CO_2 sensing of CNT based thin film.

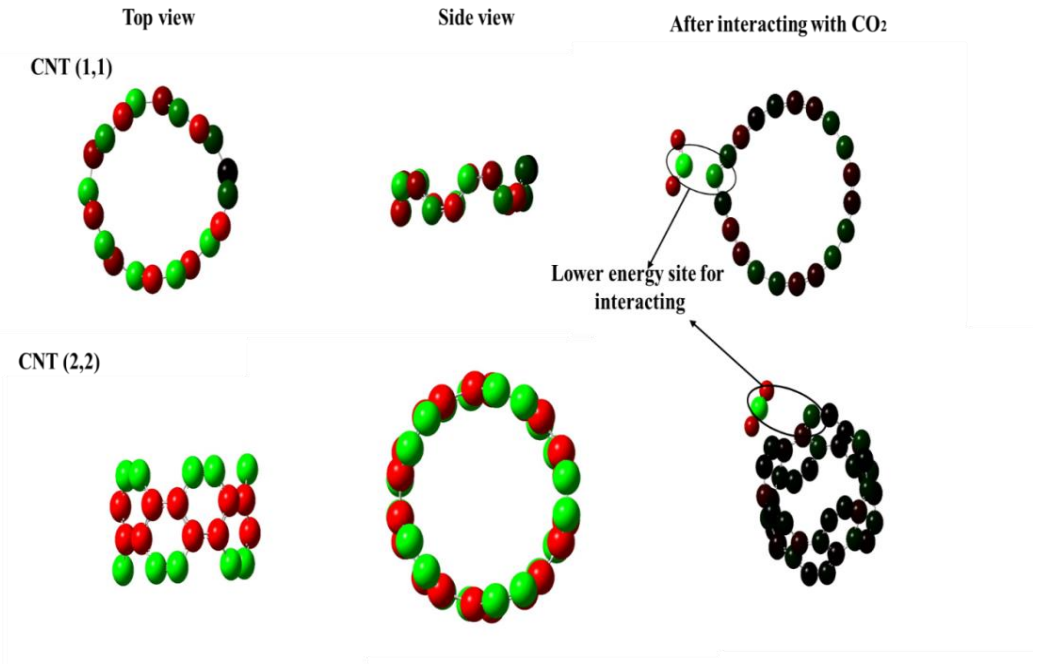

Fig. 4.17 Top and side view of growing CNTs with different interacting sites

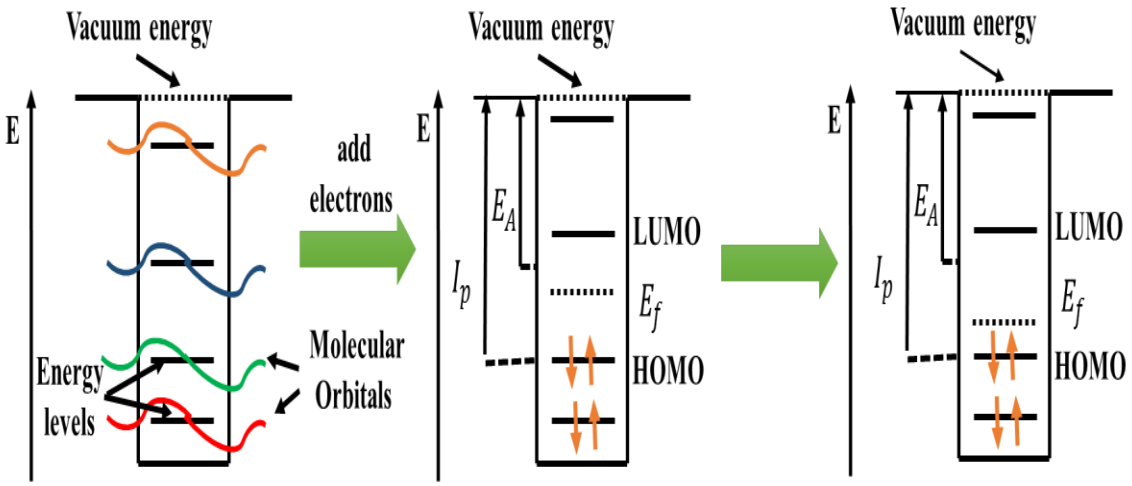

Fig. 4.18 Variation of Fermi level and the energy band of CNTs on interacting with gas

Table 1. Literature survey on various types of CO_2 gas sensors

S.No.	Material	Operating temp. (℃)	Gas (ppm)	Sensor Response	Response Time	Recovery Time	Ref.
1	CuO–$CuxFe_{3-x}O_4$	250	5000	0.50	9.5 h	-	[9]
2	Ag–$BaTiO_3$–CuO	250	5000	0.28	15 min	10 min	[10]
3	$La_{1-x}Sr_xFeO_3$	380	2000	0.25	11 min	15 min	[11]
4	CdO	250	5000	0.01	3.33 min	5 min	[12]
5	LaOCl-SnO_2	300	1000	3.7	110 sec	40 sec	[13]
6	$La_2O_2CO_3$	300	5000	0.62	53	120	[14]
7	TiO_2–PANI (1 %)	30	1000	53	9.2 min	5.7 min	[17]
8	SnO_2–In_2O_3	RT	1000	17	5 min	7 min	[18]
9	ZnO–La (50 %)	400	5000	0.65	90 sec	38 sec	[23]
10	**MWCNT**	**30**	**5000**	**2.1**	**30 sec**	**49 sec**	**Present work**

Table 2. Response time, recovery time and sensitivity of thin film at various concentrations of CO_2

Gas Concentration (ppm)	Response Time (Sec)	Recovery time (Sec)	Sensor response
1670	25.8471	37.8455	1.85
3300	22.00	36.4656	1.91
5000	30.2184	49.6212	2.10
6670	45.8033	13.3221	1.88

Table 4.3 (a) Theoretical study on the variation in different parameters of CNT (1,1) before and after interaction with CO_2 molecule

	Before Interaction	**After Interaction No of CO_2 molecule interact with CNT (1,1)**			
		1	**2**	**3**	**4**
Change in Binding energy (eV)	6.69	6.16	6.03	5.95	5.89
HOMO-LUMO band gap (eV)	0.2267	0.2367	0.2397	0.2404	0.2085
Dipole moment (Debye)	2.7598	11.108	13.4202	14.681	15.710
Electronegativity (eV)	0.4773	0.3462	0.3812	0.4460	0.4239
Hardness (η)	0.3825	0.1892	0.2248	0.2278	0.2564
Softness (s)	2.6146	5.2854	4.9215	4.0885	3.9001
Nucleophilicity index	0.29787	0.331299	0.3942	0.4364	0.3504

Table 4.3 (b) Theoretical study on the variation in different parameters of CNT (2,2) before and after interaction with CO_2 molecule.

	Before Interaction	**After Interaction No of CO_2 molecule interact with CNT (2,2)**			
		1	**2**	**3**	**4**
Change in Binding energy (eV)	7.61	6.293	6.14	5.99	5.48
HOMO-LUMO band gap (eV)	0.28034	0.18435	0.17466	0.15734	0.18435
Dipole moment (Debye)	0.0053	14.9274	17.9861	34.2313	31.4623
Electronegativity (eV)	0.49001	0.4552	0.4441	0.4112	0.4286
Hardness (η)	0.1601	0.1817	0.1989	0.2566	0.2361
Softness (s)	6.1957	5.5028	5.0257	3.8955	4.23
Nucleophilicity index	0.7498	0.5664	0.4963	0.3293	0.3889

CHAPTER 5

SYNTHESIS OF MWCNT/PPY NANOCOMPOSITE USING OXIDATION POLYMERIZATION METHOD AND ITS APPLICATION AS CO_2 AND HUMIDITY SENSOR

This chapter includes the synthesis of multiwall carbon nanotube (MWCNT) and polypyrrol (PPY) nanocomposite and its characterizations along with the applications. The MWCNT was prepared by using direct liquid injection chemical vapor deposition technique (DLICVD) and MWCNT/PPY based nanocomposite was synthesized by the oxidation polymerization method. The thin film of MWCNT/PPY was prepared by spin coating technique and characterized using Scanning electron microscope (SEM), Transmission electron microscope (TEM), Particle size analyzer and X-ray diffractometer (XRD). The vibrational and rotational spectra were observed through Fourier Transform Infrared Spectroscopy (FTIR) and Raman spectroscopy. The optical band gap was found to be 3.2 eV and the minimum crystallite size was found to be 8 nm. The synthesized MWCNT/PPY has been used for CO_2 and humidity sensing. The sensor response of thin film towards CO_2 was found to be 7.2 at 1000 ppm and minimum response and recovery time at 250 ppm were found to be 30 s and 37 s respectively. The sensitivity of thin film towards humidity was found to be 41.3kΩ/%RH. Theoretical calculation was also performed in support of experimental data.

CHAPTER 5

Synthesis of MWCNT/PPY nanocomposite using oxidation polymerization method and its application as CO_2 and humidity sensor

5.1. Introduction

Nowadays the detection of toxic gas such as CO_2, CH_4, NO_2, SO_2, etc has become an important area of research. The leakage of such gases causes a lot of disasters so we need to design such sensors which can be used for the detection these toxic gases. There are so many metal oxide-based gas sensors available for the detection of these toxic gases, but these sensors have one major drawback that they are operating at high temperature. So it's our first priority to design and fabricate such gas sensor which can be operated at room temperature. CO_2 is one of the toxic gases which are very hazardous to the environment. The increment in the level of carbon dioxide causes greenhouse effect which increases the earth's temperature so we can say that this gas is also responsible for global warming which is one of the major issues of present scenario [1].

The control of climate change has become a big issue and leads to an expansion in gas sensor research. Mostly CO_2 is responsible for such climate change so the detection and control of CO_2 releasing from motor vehicles, industries and other sources of pollutants in the environment become necessary and urgent. In order to reduce the quantity release, sensors are needed to monitor the gas concentration to capture the storage of CO_2 gas. For humans, in enclosed spaces such as mine, wells and sewers, a gas mixture containing 5-20% CO_2 is required for safety regulations. Metal oxides are used for fabricating such type of gas sensor but the sensitivity of such sensors is very low so for improving the sensitivity of the sensor we need a different type of nanostructure which has very high aspect ratio [2, 3].

In order to prepare different carbon nano-structured sample, MWCNT was synthesized by chemical vapour deposition technique [4,6] and further it was polymerized with pyrrole in which the MWCNT were covered with PPY to form a

nanocomposite. The chemical sensors fabricated by using carbon nanotube have created a great interest in research community and such type of sensors can also be used for detecting toxic gases at room temperature [7, 8]. In this chapter, we firstly analyzed the effect of CO_2 and humidity on the MWCNT/PPY nanocomposite, after that analysis, we created a theoretical model in which the changes in electron affinity, ionization potential, HOMO-LUMO gap and electronegativity before and after interacting with CO_2 and hydroxyl molecule have been investigated.

5.2 Experimental detail

5.2.1 Synthesis of multiwalled carbon nanotube

The multiwalled carbon nanotube has been synthesized by using direct liquid injection chemical vapour deposition technique. In such a technique, we take ethanol (C_2H_5OH) as precursor and argon (Ar) as a carrier gas. The growth was obtained at 750 ℃ in the presence of Co catalyst as reported in Chapter 2 [14, 15]. After synthesis and purification of MWCNT, the nanotube has been functionalized by the exohedral functionalization method. In this case, the MWCNT was put in the complex solution of nitric acid (HNO_3) and sulfuric acid (H_2SO_4) in the 3:1 ratio, then sonicated for 30 min. Later, the solution was centrifuged several times at 2000 rpm and washed with distilled water so black precipitate was obtained.

5.2.2 Synthesis of MWCNT/PPY nanocomposites

The MWCNT/PPY nanocomposite has been synthesized by using the oxidation polymerization method [16]. In this method, firstly 0.5 M aqueous solution of pyrrole was mixed with a 0.5 M aqueous solution of ammonium persulphate in the ratio of 1:1 then we added 20 mg of f-MWCNT in the solution with continuous stirring for 45 min. Then polymerization was carried out for 5 hrs. After execution of polymerization, the precipitate was obtained. Then PPY sample was filtered out and washed consecutively with methanol followed by water to remove impurities and reacting monomers. A thin film of PPY was prepared on the glass substrate using spin coater.

5.3 Characterization details

The surface morphological and structural property of thin film were characterized by using Scanning electron microscopy (SEM) (JOEL JSEM 6490 LB) and Transmission electron microscopy (TEM). The data obtained by the XRD (Philips X'Pert Pro PAN analytical using laser source CuKα (1.542 Å) in scanning region from 10 to 90° with a scanning step of 0.02° per sec) was used for calculating the average crystallite size. Average dimension of nanotubes was measured by Particle size analyzer (NZS90 using a LASER of wavelength 625 nm). The optical characterizations of the thin film were investigated by UV-vis spectrometer (Evolution 302) and infrared spectrometer (Shimadzu 8700 1992). The humidity sensing parameters were measured by using impedance analyzer (6400 B) which gave the variation of impedance and capacitance w.r.t. relative humidity with higher accuracy. The gas sensing parameter has been measured by Keithley electrometer (6517B).

5.3.1 XRD analysis

The prepared thin film was investigated through X-ray diffractometer along with the source CuK_{α}. Fig. 5.1 shows the XRD spectra of MWCNT/PPY nanocomposite prepared by oxidation polymerization method. The crystallite size of the sample was calculated by using the Debye Scherrer formula for the highest peak found at 26.25° [17]. The highest peak at 26.25° confirms the hexagonal structure of nanotubes and the vibration near 24.12° confirms the presence of PPY in the sample [18,19]. FWHM was calculated as 2.74° and the corresponding crystallite size was found 8 nm.

5.3.2 Scanning Electron Microscopy (SEM)

The surface morphology of synthesized MWCNT/PPY thin film was analyzed by using scanning electron microscopy [20]. Fig. 5.2 (a) shows the tubular structure of MWCNT at 500 nm scale. The average diameter and length calculated by using such data were found to be 15 nm and 250 nm respectively. Fig. 5.2 (b, c) shows the MWCNT and PPY combining with each other by exohedral functionalization method and leaving some spaces as pores. The tubular structure of nanotube gives higher surface area for

interaction of CO_2 and humidity. The porous surface provide number of active sites for interaction of gas and humidity with the synthesized nanomaterial.

5.3.3 Transmission Electron Microscopy (TEM)

Fig. 5.3 shows the TEM analysis of MWCNT/PPY at different scales. The TEM images confirm the tubular structure with hollow space and the PPY polymer covers the nanotube by the exohedral functionalization method. The thickness of the polymer was found to be 2.6 nm and the diameter of the nanotube was found to be 18.5 nm.

5.3.4 UV analysis

The optical characterization of the thin film was done by using UV-visible spectrometer (Evolution 302) [21]. Fig. 5.4 represents the variation of optical absorption with respect to wavelength ranging from 190 to 1100 nm. The small absorption peak near 430-460 nm confirms the polymerization of the material. The optical bandgap of the thin film was calculated by using the Tauc plot and the estimated band gap was found as 3.92 eV.

5.3.5 FTIR analysis

Fig. 5.5 shows the FTIR spectrum of MWCNT/PPY nanocomposite. The vibrational peak at 3100 cm^{-1} shows the sp^2 bonding in the nanotubes. The strong bands in the region 500- 1700 cm^{-1} shows the characteristic peak of the PPY and the strong band at 1560, 1505 and 1465 cm^{-1} correspond to the C-C, C=C and C-N respectively. The band near 1600 correspond to aromatic ring formation whereas the bands at 1600 and 3100 cm^{-1} confirms the formation of nanotubes in the nanocomposite.

5.3.6 Particle size analysis

The particle size of the MWCNT/PPY was analyzed by using nano zeta sizer NZS90. In this method, the average particle size has been calculated by using dynamic light scattering (DLS) method which provides the average of particle size dispersed in the solution. This method assumes the spherical geometry of particles having aspect ratio 1 while in the tubular structure the aspect ratio is assumed as approximately 1000. For

tubular structure, the length and diameter of the tube were calculated by using Eqns 5.1 and 5.2 which describes the diffusion coefficient.

$$D = \frac{kT}{3\pi\eta L}\left[\ln\left(\frac{L}{d}\right) + 0.32\right] \ldots\ldots\ldots (5.1)$$

$$D = \frac{kT}{3\pi\eta D_h} \text{ Stock- Einstein}\ldots\ldots.(5.2)$$

k represents the Boltzmann constant; D represents the diffusion coefficient; T stands for temperature, D_h is the hydrodynamic diameter; η is the viscosity; and L and d represent the length and diameter of the nanotube respectively. Combining Eqns 5.1 and 5.2 which relates D_h to the nanotube's dimension in the form of Eqn. 5.3.

$$D_h = \frac{L}{\ln\left(\frac{L}{d}\right)+0.32}\ldots\ldots\ldots\ldots\ldots\ldots\ldots(5.3)$$

From Eqn. 5.2, the peaks at 82 and 230 nm show the tube having length 1000 nm and diameter 8 nm. Due to the high aspect ratio, there are some probabilities of finding an error so the measured length must be taken as an approximate value.

5.4 Application of MWCNT/PPY nanocomposite

5.4.1 Gas sensing characteristics

The gas sensing characteristics of the MWCNT/PPY based thin film has been measured in the terms of sensor response and sensitivity. These parameters are measured by the change in resistance of the film before and after exposure of CO_2 gas w.r.t time at various concentrations [14, 22].

5.4.2 Humidity sensing characteristics

Experimental set-up for humidity sensing has been described in Chapter 3. The thin film of MWCNT/PPY prepared by spin coating technique is inserted between the electrodes of an Impedance analyzer having Ag-film-Ag electrode arrangement. Variation in impedance/capacitance have been observed by varying the humidity of the chamber from 10-90%. A saturated solution of potassium sulphate with de-ionized water was used as humidifier and saturated solution of potassium hydroxide was used as dehumidifier.

The sensitivity of the sensor has been defined as the change in output power of the sensor per unit change in %RH and written as below:

$$S=\frac{\Delta output\ Impedance}{\Delta\ \%\ RH}\ k\Omega/\%RH \quad \text{.....(5.4)}$$

5.4.3 Result and discussion

Before the exposure of CO_2, the MWCNT/PPY based thin film was placed in a chamber for 20-30 min, in which the film interact with the air and get stabilized and the stabilized resistance was taken as R_a. The stabilization of the film in ambient air is important because it ensures a stable zero level for gas sensing application. Variation of the resistance of the film for different concentration of CO_2 was observed. Fig. 5.8 shows the variation in the resistance of the thin film with exposure time of different ppm of CO_2.

From the figure, it is clear that as time increases the resistance of the film increases drastically in the beginning; after that the resistance of the film become saturated. Finally, when the outlet of the chamber is opened, the resistance of the film approaches to their initial value of stabilized resistance in the air (R_a). Curve 'a' shows the variation of resistance with time for 250 ppm exposure of CO_2 having low sensor response. Curve 'b' and 'c' shows the variable resistance with time for 500 ppm and 750 ppm exposure of CO_2 respectively. These curves exhibit improvement over the previous and the sensing element has better sensing response. The maximum sensing response of the film was found at 1000 ppm exposure of CO_2 as shown by curve 'd'. Fig. 5.7 (a) shows the variation of average sensing response of thin-film for different concentrations of CO_2 and it is found that as the concentration of CO_2 increases inside the chamber, the average sensing response also increases linearly. Fig. 5.7 (b) shows the variation of sensitivity at various concentration of CO_2 and the maximum sensitivity was found as 80 Ω/sec at 1000 ppm of CO_2.

Response and recovery time is also an important parameter for gas sensing. The response time is defined as the time required to acquire the 90% of maximum resistance and recovery time is defined as the time required to achieve the initial value of resistance

after removing the gas. The minimum response and recovery time of the thin film has been observed at 250 ppm and found to be 30 s and 37 s respectively.

The polymers are generally insulator, but in conducting polymer, the polymer backbone structure is conjugate with the existence of ionic delocalization of double bond electrons. Doping of MWCNTs in polymer can increase in the conductivity of the material. The conducting or semiconducting polymers have the conjugated double bonds. These double bond consist of a "σ" bond and a "π" bond. The electrons in "σ" bond form the backbone of the chain, dominating the mechanical properties of the polymer. Due to the "π" orbital overlap of the neighboring molecules of the conjugated structure, the "π" electron delocalize along the entire chain, which provided the semiconducting and conducting properties of polymer. In MWCNT/PPY nanocomposite, a positive charge of unpaired electron associated with a quoinoid structure are formed as a result of removal electron from the polymer chain, since CO_2 has two lone pair of electron with "π" type C=O bindings. It may be possible that CO_2 molecules form weak bond with "π" electron of the MWCNT/PPY surface which results in a decrease of conductivity or an increase in the sensor resistance.

When CO_2 is exposed on the film the increase in resistance has been observed. This is because the chemisorbed oxygen captures free electron from the conduction band so the concentration of electron inside the film starts decreasing. The decrease in the concentration increases the width of the depletion layer so the higher resistance has been observed [14].

Fig. 5.10 (a) shows the variation in impedance with the change in %RH of MWCNT/PPY thin film. The impedance of the thin film decreases on increasing the humidity so the sensitivity of the film has been analyzed for three different regions; first is lower humidity region (10-30 %RH), second is mid humidity region (30-60 %RH) and third is high humidity region (60-90 %RH). For low humidity region, the sensitivity of the thin film has been found as 44 kΩ/%RH and the sensitivity of the film in mid humidity region was 50 kΩ/%RH. For higher humidity region the sensitivity is 30 kΩ/%RH which is very low. The reason for the decreased sensitivity in the higher humid region is that the larger of the film has been already covered by the hydroxyl molecules.

In mid humidity region, most of the hydroxyl molecules interact with the oxide surface of the film and get adsorbed [23,24].

Fig. 5.10(b) shows the variation of capacitance with a change in %RH of MWCNT/PPY thin film. The capacitance of the thin film increases on increasing the humidity as shown in Fig. 5.10 (b) and the sensitivity of thin-film in lower humidity region was found to be 4.65 pF/%RH, for mid humidity region 5.33 pF/%RH and for higher humidity region 4.06 pF/%RH. The average sensitivity of the thin film was found as 4.68 pF/%RH. Fig 11 (a) and (b) shows the reproducibility of the thin film and results were found reproducible within $\pm$ 94% accuracy.

Generally the ideal capacitive sensor, the C value is independent on applied frequency but experimentally we found that at lower humidity region, the water molecule possesses small leak conduction in the sensing material. So the capacitance offered by the leak conduction is expressed by the Eqn. 5.8

$$C = (\varepsilon_r - i\frac{\gamma}{\omega\varepsilon_0})C_0 \ldots\ldots\ldots\ldots (5.8)$$

From Eqn. 5.8 we found that the capacitance is dependent on the testing frequency which is also another important factor for determining the response of MWCNT/PPY nanocomposite based thin-film [26]. Fig. 5.12 shows the variation of capacitance with %RH of MWCNT/PPY based humidity sensor at the different testing frequency at ambient temperature. The sensor response of the thin film was found to be maximum for the lower frequency because the capacitance offered by the leak conduction is inversely proportional to the frequency.

The change in impedance/capacitance of the thin film is directly related to the water adsorption mechanism of oxide surface of the thin film. The negatively charged hydroxyl ion is electrostatically attached to the positive cationic site of MWCNT/PPY surface. Physisorbed water dissociates into H_3O^+ and OH^- because of high electrostatic fields at the interface between the surface and adsorbed layer. Transportation of charge occurs by the movement of a proton from H_3O^+ ion to an adjacent water molecule and so on. Now on the surface of the film protonic conduction takes place. This mechanism of

charge transport is known as Grotthus chain reaction mechanism [27]. The impedance of the film decreases in the humid region because of protonic conduction. At low humidity region, only surface protonic conduction takes place so less change in impedance was found but in the high humidity region, the water molecules fill inside the porous area of the film so both protonic conduction and electrostatic conduction takes place so higher change was observed. The dependence of impedance on relative humidity can be quantified by this mechanism.

5.5 Theoretical investigations

A theoretical model has been designed using Gauss view 05 and Gaussian 09 to explain the experimental result of CO_2 and humidity sensing. For observing the sensing mechanism of the sensor we have designed a single armchair (2,2) CNT then PPY has been attached to CNT by exohedral non-covalent bonding. After optimizing the CNT/PPY structure, interaction of nanocomposite with CO_2 and hydroxyl group has been studied. The intraction effect was observed on individual CNT/PPY. For thin film, the interaction energy was multiplied by the number of CNT/PPY present in the film. The whole calculation was carried out by using armchair (2,2) CNT/PPY and the computational method as B3LYP. In this computational method, the sensing mechanism has been analyzed by and for the change in the energy level, HOMO-LUMO gap, electron affinity, ionization potential, the dipole moment of molecules before and after interaction with the CO_2 and hydroxyl group [28-31].

Table 5.2 shows the changes found in the energy and different theoretical parameters before and after interaction with CO_2 and humidity. Higher Occupied Molecular Orbit (HOMO) and Lower Unoccupied Molecular Orbit (LUMO) were calculated and these parameters e.g. electronegativity, hardness, softness and nucleophilicity index were calculated using the Eqns 3.8-3.11 given in Chapter 3.

5.6 Conclusion

Nanostructured MWCNT/PPY was successfully synthesized by chemical oxidation route. The morphological evolution and structural studies proved the nanocrystalline nature of the material. The crystallite size was found as 8.1 nm. The optical bandgap of the nanocomposite was found as 3.92 eV. The surface morphology of the MWCNT/PPY shows that most of the nanotube gets enveloped with polymer hence the sensitivity towards CO_2 and humidity enhanced. MWCNT/PPY composite sensor structure exhibited the maximum sensing response as 7.1 and sensitivity as 81.2 for 1000 ppm of CO_2 concentration towards at room temperature (30°C). This film was also successfully used for the detection of humidity and maximum sensitivity was found as 41.33 kΩ/%RH. The sensor is quite sensitive and can be used for the commercial production.

References

[1] M. Mittal, A. Kumar, Carbon nanotube (CNT) gas sensors for emissions from fossil fuel burning. Sens. Actuators B: Chem. 203 (2014) 349.

[2] R. Chapelle, F. Oudrhiri-Hassani, L. Presmanes, A. Barnabe, P. Tailhades. CO_2 sensing property of semiconducting copper oxide and spinal ferrite nanocomposite thin film App. Surf. Science 256 (2010) 4715.

[3] J. Herra´n, G. G. Mandayo, I. Ayerdi, E. Castan˜o Influence of silver as an additive on $BaTiO_3$–CuO thin film for CO_2 monitoring. Sens. Actuators B: Chem. 129 (2008) 386.

[4] U. Kumar, S. Sikarwar, R. K. Sonker, B. C. Yadav Carbon nanotube: synthesis and application in solar cell. J. Inorg. Organomet. P. 26 6 (2016) 1231.

[5] S. Ming, B. Zheng, J. A. Liu, A Scalable CVD method for the synthesis of single-walled carbon nanotubes with high catalyst productivity. Chem. Phy. Letter 322 (2000) 321.

[6] E. Singh, U. Kumar, R. Srivastava, B. C. Yadav, Carbon Nanotubes Based Thin Films as Opto-Electronic Moisture Sensor. Adv. Sci. Eng. Med. 10 (2018) 785.

[7] P. Tyagi, A. Sharma, M. Tomar, V. Gupta, A comparative study of RGO-SnO_2 and MWCNT-SnO_2 nanocomposites based SO_2 gas sensors. Sens. Actuators B: Chem. 248 (2017) 980.

[8] R. K. Sonker, M. Singh, U. Kumar, B. C. Yadav, MWCNT Doped ZnO Nanocomposite Thin Film as LPG Sensing. J. Inorg. Organomet. P. 26 6 (2016) 1434.

[9] K. Fan, H. Qin, L. Wang, L. Ju, J. Hu, Sens. Actuators B: Chem. 177 (2013) 265.

[10] T. K. Kumar, R. Jayaprakash, T. Prakash, D. Sathyaraj, N. Donato, S. Licoccia, M. Latino, A. Stassi, G. Neri, CdO-based nanostructures as novel CO_2 gas sensors. Nanotechnology 22 (2011) 325501.

[11] Y. Xiong, Q. Q Xue, C. Ling, W. Lu, D. Ding, L. Zhu, X. Li, Effective CO_2 detection based on LaOCl-doped SnO_2 nanofibers:Insight into the role of oxygen in carrier gas. Sens. Actuators B: Chem. 241 (2017) 725.

[12] D. Ding, W. Lu, Y. Xiong, X. Pan, J. Zhang, C. Ling, Y. Du, Q. Xu. Facile Synthesis of $La_2O_2CO_3$ Nanoparticle Films and Its CO_2 Sensing Properties and Mechanisms App. Surf. Science 426 (2017) 725.

[13] Y. J. Jeong, C. Balamurugan, D. W. Lee, Enhanced CO_2 gas-sensing performance of ZnO nanopowder by La loaded during the simple hydrothermal method. Sens. Actuators B: Chem. 229 (2016**)** 288.

[14] U. Kumar, B. C. Yadav Synthesis of carbon nanotube by direct liquid injection chemical vapor deposition method and its relevance for developing an ultra-sensitive room temperature based CO_2 sensor, J. Taiwan Inst. Chem. Eng. 96 (2019) 652.

[15] U. Kumar, B. C. Yadav, Development of humidity sensor using modified curved MWCNT based thin film with DFT calculations, Sens. Actuators B Chemical, 288 (2019) 399.

[16] R. Kumar, B. C Yadav, Fabrication of Polyaniline (PANI)—Tungsten oxide (WO3) Composite for Humidity Sensing Application. Journal of Inorganic and Organometallic Polymers and Materials 26 (6) 2016 1421-27.

[17] B. C. Yadav, S. Singh, A. Yadav, T. Shukla, Experimental investigations on nanosized ferric oxide and its LPG sensing. Inter. J. of Nanosci. 10 (2011**)** 135.

[18] M. Perez-Cabero, I. Rodriguez-Ramos, A. Guerrero-Ruiz, Characterization of carbon nanotubes and carbon nanofibers prepared by catalytic decomposition of acetylene in a fluidized bed reactor. J. Catal. 215 (2003**)** 305.

[19] J. W. Snoeck, G. F. Froment, M. Fowles, Preparation of nickel nanoparticles and their catalytic activity in the cracking of methane. J. Catal. 169 (1997**)** 240.

[20] T. Wortmann, S. Fatikow, Carbon Nanotube Detection by Scanning Electron Microscopy MVA2009 IAPR Conference on Machine Vision Applications. May 20-22, (2009) Yokohama, JAPAN

[21] G. A. Rance, D. H. Marsh, R. J. Nicholas, N. Khlobystova Andrei, UV–vis absorption spectroscopy of carbon nanotubes: Relationship between the π-electron plasmon and nanotube diameter, Chem. Phy. Lett. 493 1–3 (2010) 19.

[22] A. Kaushik, R. Kumar, S. K. Arya, M. Nair, B. D. Malhotra, S. Bhansali. Organic-Inor- ganic hybrid nanocomposite based gas sensor for environmental monitoring. Chem Rev 115(11) (2015) 4571.

[23] K. Kumar, U. Kumar, M. Singh, B.C. Yadav, Synthesis and characterizations of exohedral functionalized graphene oxide with iron nanoparticles for humidity detection. J. Mater. Sci. 30 (14) (2019) 13013.

[24] Q. Y. Tang, Y. C. Chan, K. Zhang, Fast response resistive humidity sensitivity polyimide/multiwall carbon nanotube composite films, Sens. Actuators B Chem 152 (2011) 99.

[25] J. Wang, X. H. Wang, X. D. Wang, Study on dielectric properties of humidity sensing nanometer materials, Sens. Actuators B Chem. 108 (2005) 445.

[26] A. Tripathy, S. Pramanik, A. Manna, S. Bhuyan, N. F. A. Shah, Z. Radzi, N. A. A. Osman, Design and development for capacitive humidity sensor applications of lead-free Ca,Mg,Fe,Ti-oxides-based electro-ceramics with improved sensing properties via physisorption, Sensors 16 (2016) 1135.

[27] N. Agmon, The Grotthuss mechanism, Chem. Phys. Lett. 244 (1995) 456.

[28] P. Koskinen, V. Makinen, Density-functional tight-binding for beginners, Comput. Mater. Sci. 47 (2009) 237.

[29] J. C. Slater, G. F. Koster, Simplified LCAO method for the periodic potential problem, Phys. Rev. 94 (1954) 1498.

[30] M. Elstner, D. Porezag, G. Jungnickel, J. Elsner, M. Haugk, T. Frauenheim, A selfconsistent-charge density-functional tight-binding method for simulations of complex materials properties, Phys. Rev. B 58 (1998) 7260.

[31] T. A. Niehaus, M. Elstner, T. Frauenheim, S. Suhai, Application of an approximate density-functional method to sulfur-containing compounds, J. Mol. Struct. Theochem. 541 (2001) 185.

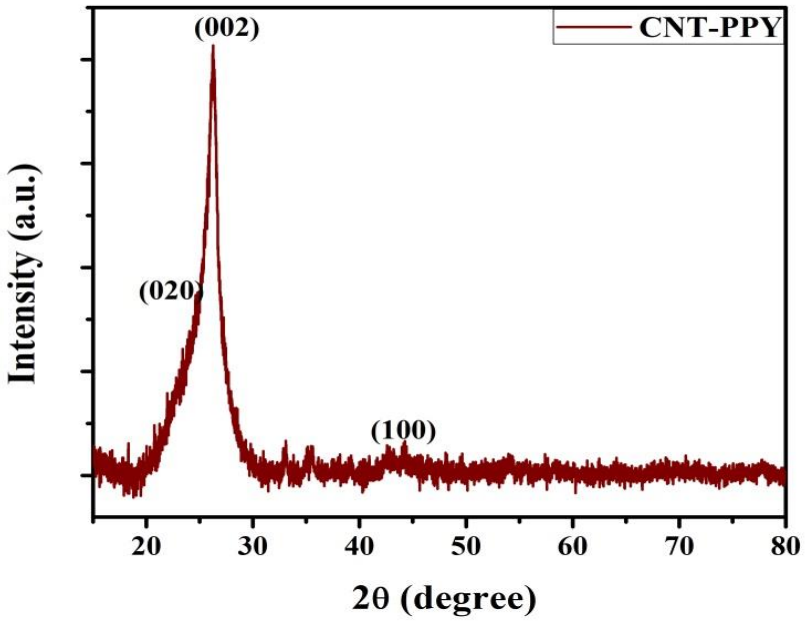

Fig. 5.1 XRD analysis of MWCNT/PPY nanocomposite

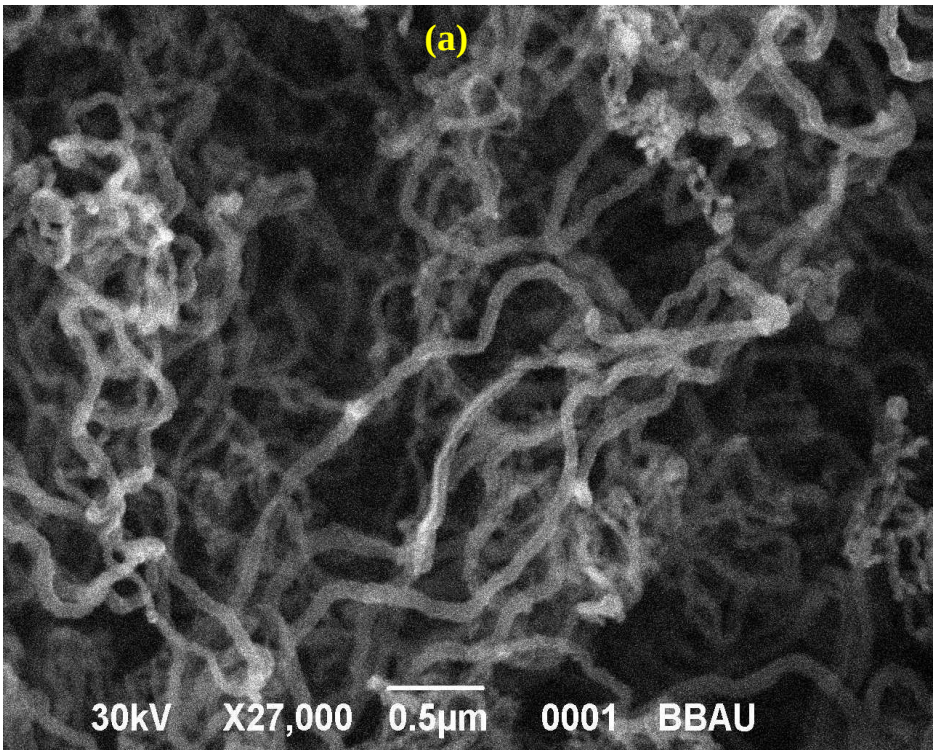

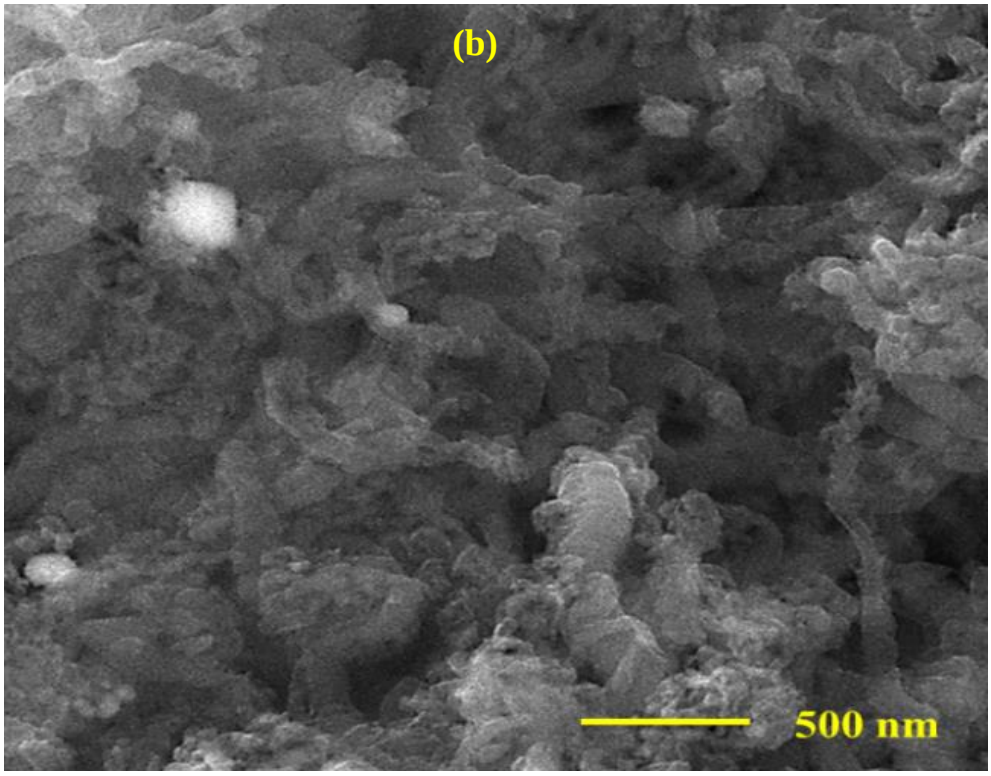
(b)
500 nm

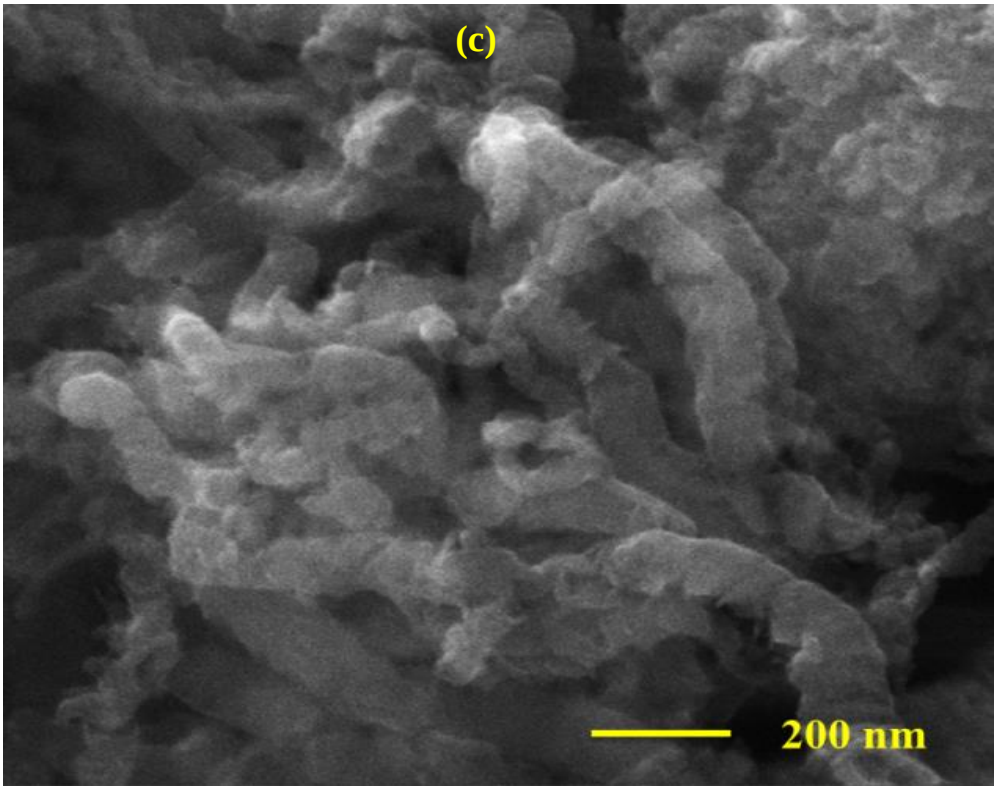
(c)
200 nm

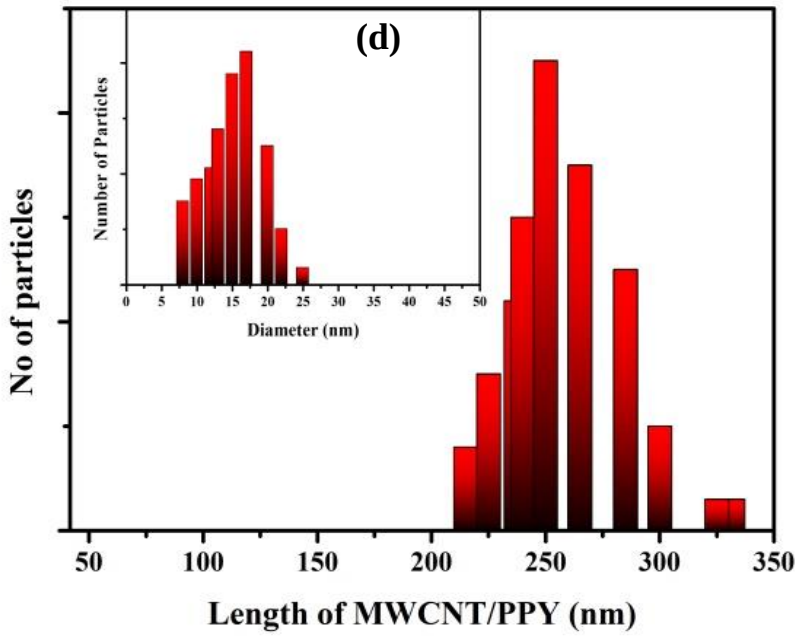

Fig. 5.2 (a) SEM image of pure MWCNT (b,c) SEM analysis of MWCNT/PPY at different scale (d) Length and diameter of MWCNT/PPY

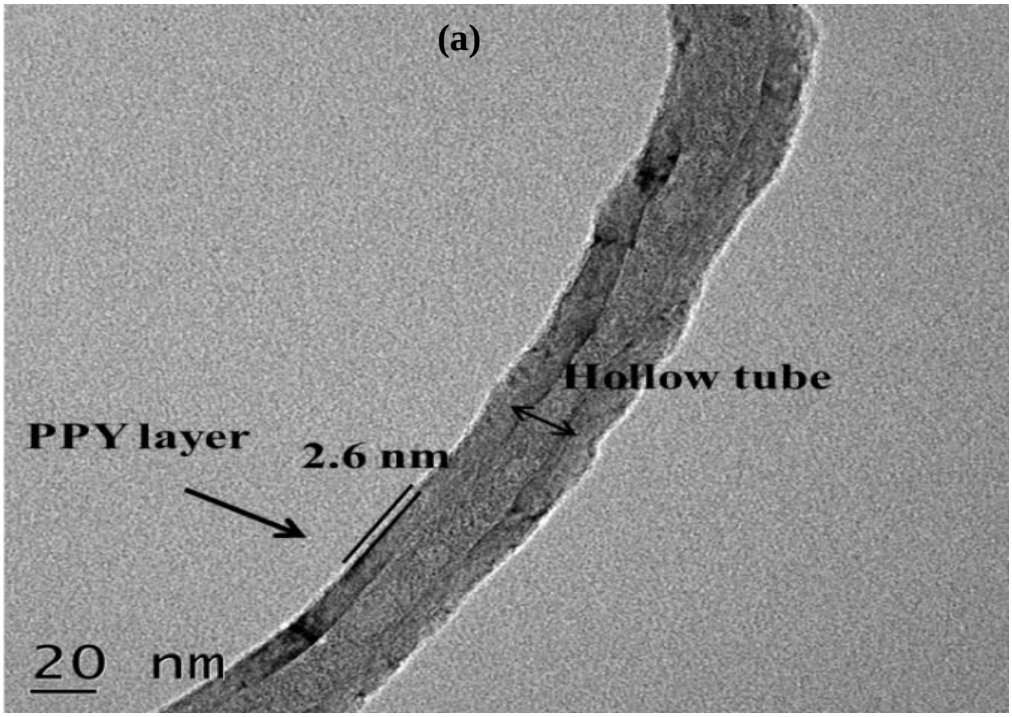

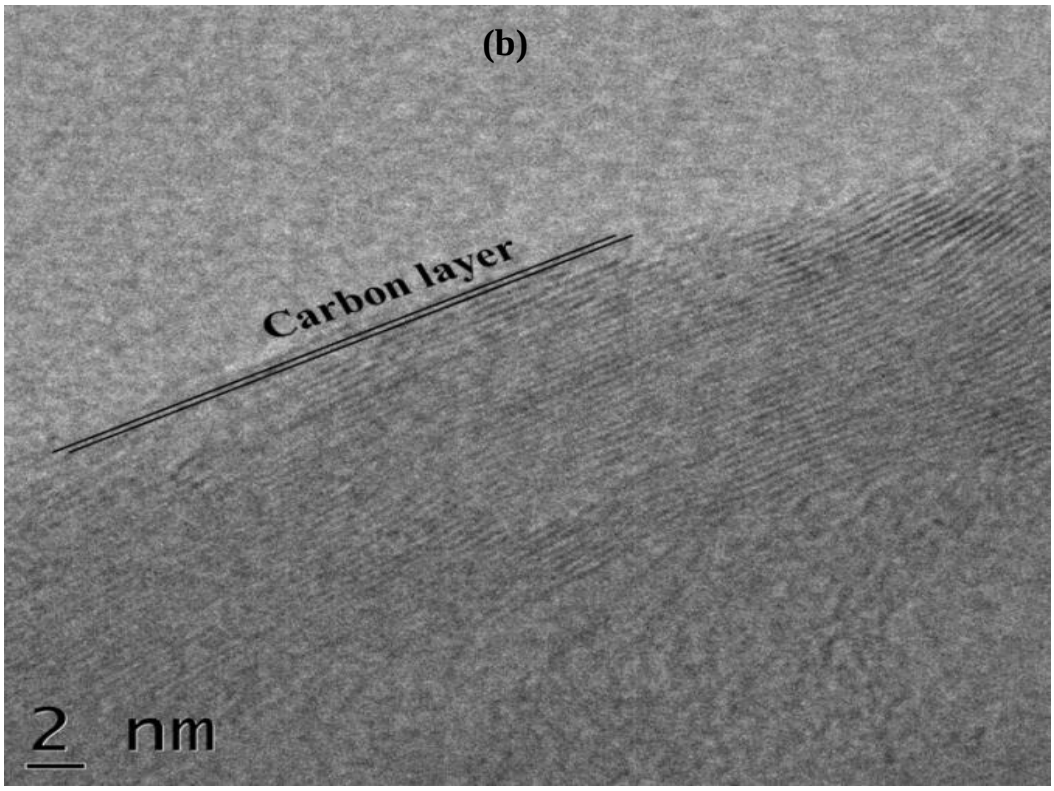

Fig. 5.3 The TEM analysis of MWCNT/PPY nanocomposites

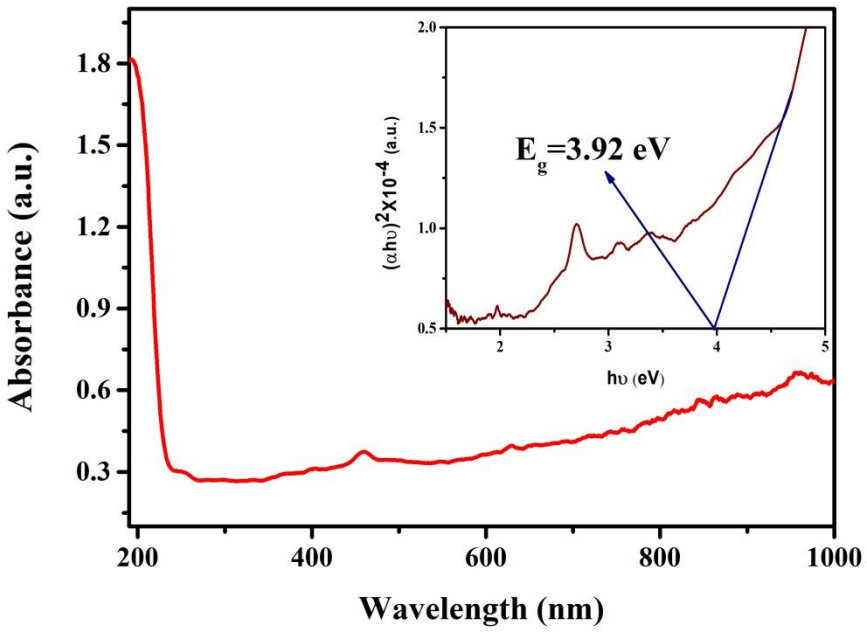

Fig. 5.4 UV-vis absorption analysis and Tauc plot of MWCNT/PPY nanocomposite

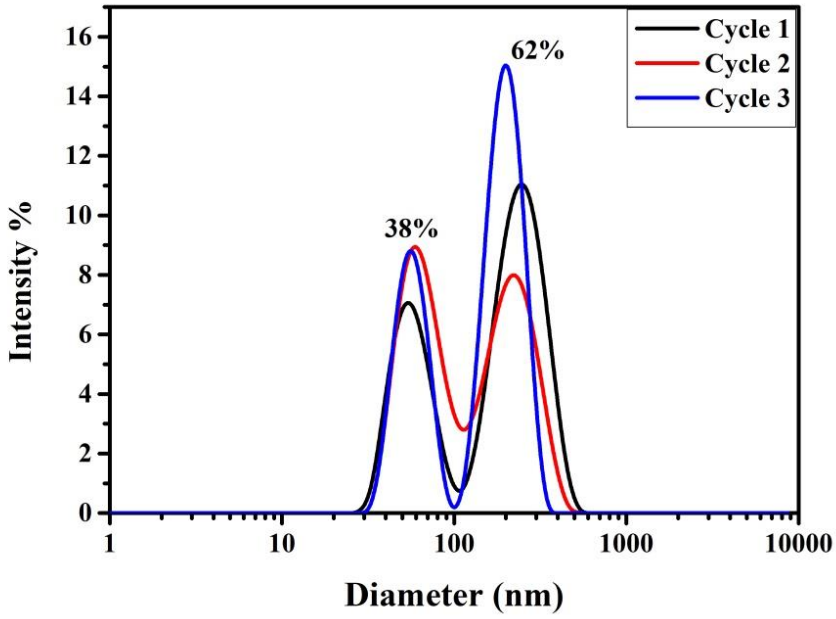

Fig. 5.6 Particle size analysis of MWCNT/PPY

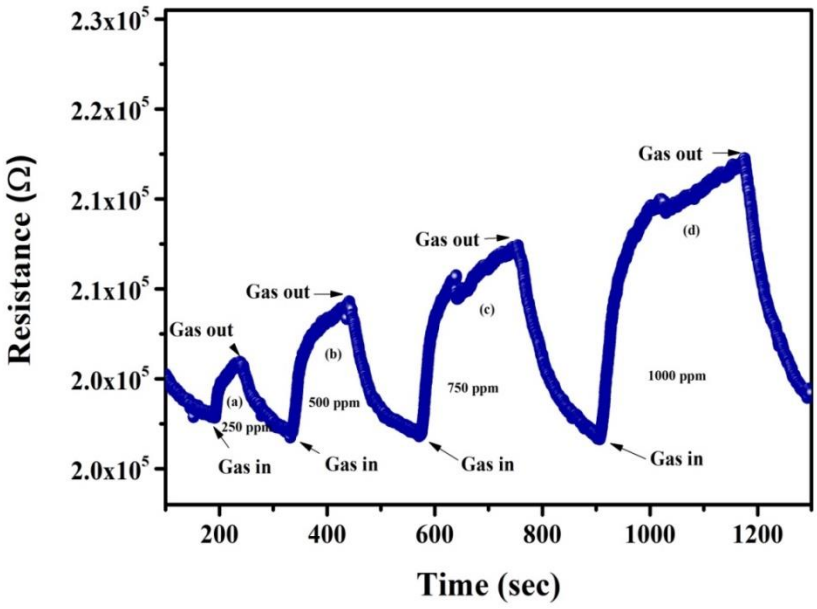

Fig. 5.7 Variation in resistance of CNT/PPY based thin film at various concentrations of CO_2 gas

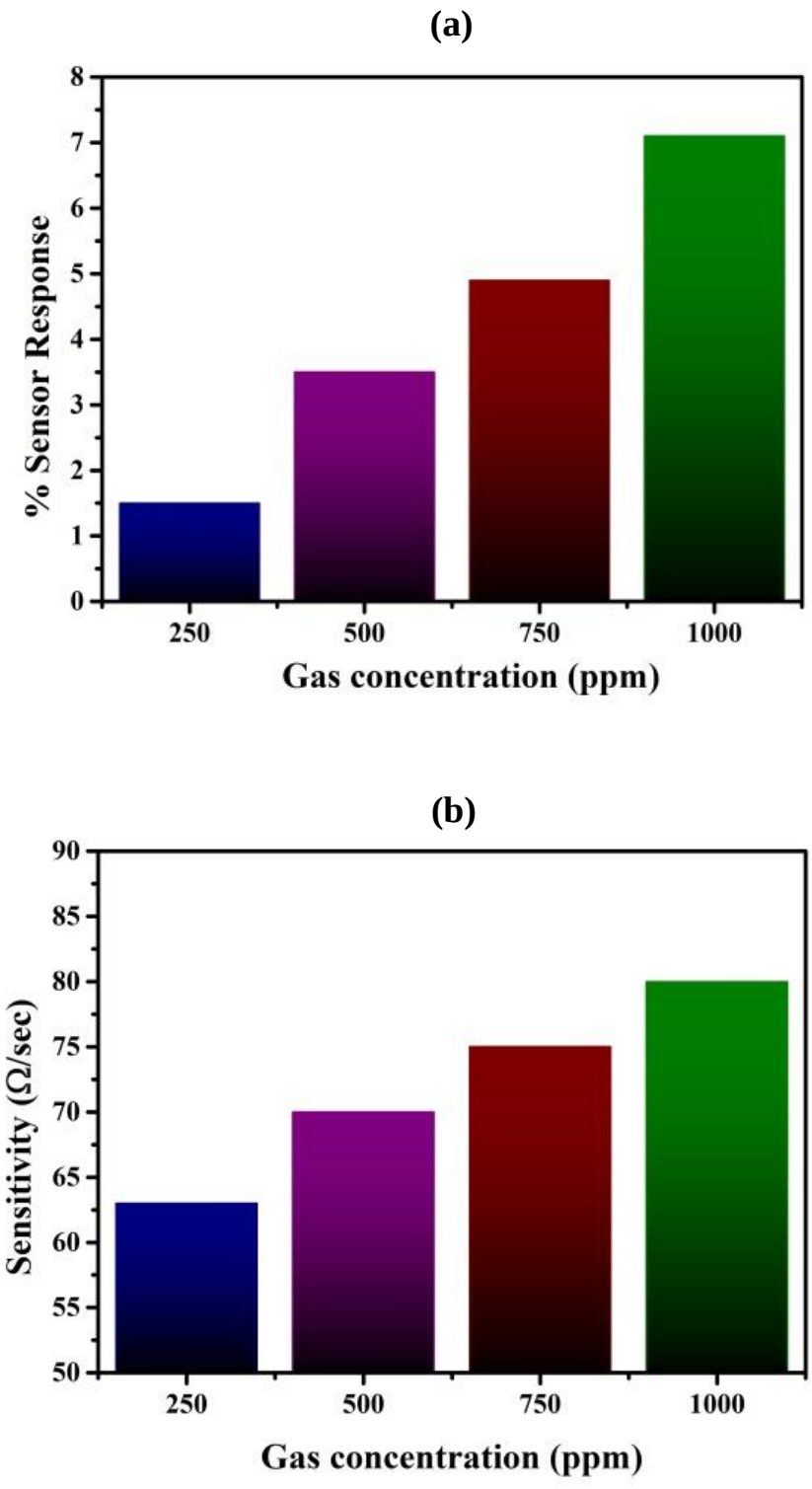

Fig. 5.8 (a) Sensitivity vs CO_2 gas concentration (b) % Sensor response vs CO_2 concentration

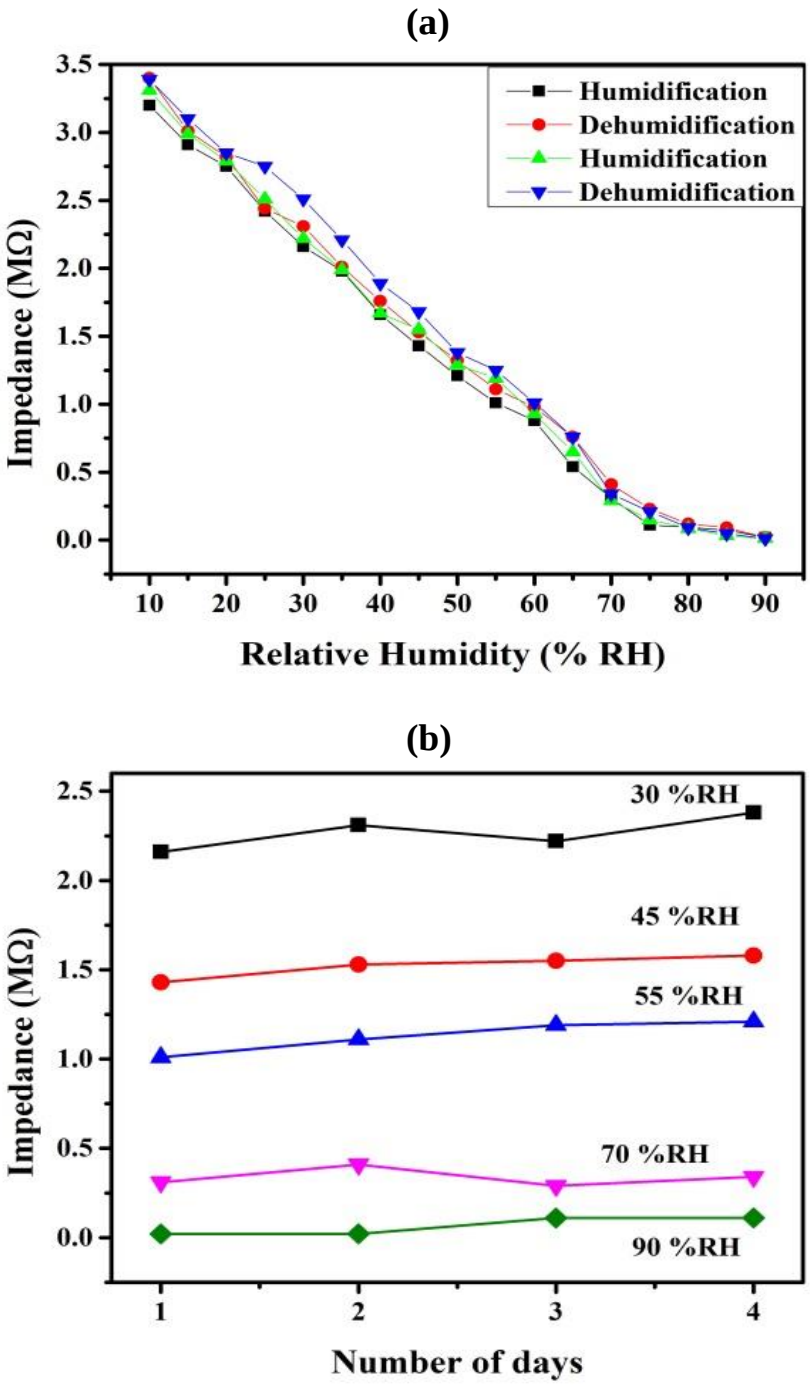

Fig. 5.9 (a) Change in impedance of the film by changing the relative humidity at room temperature (b) Reproducibility of the film after a fixed interval of time

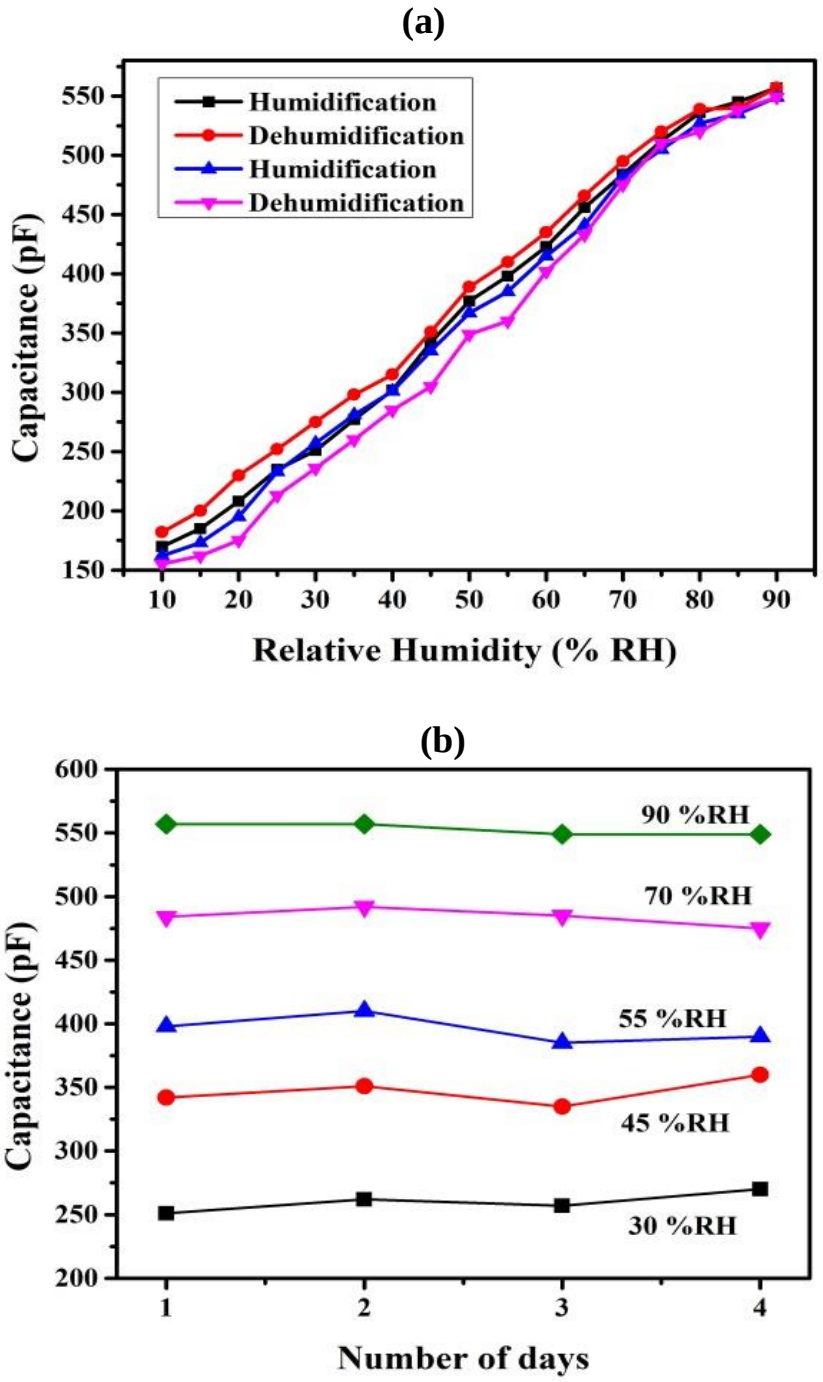

Fig. 5.10 (a) Change in the capacitance of the film by changing the relative humidity at room temperature (b) Reproducibility of the film after a fixed interval of time

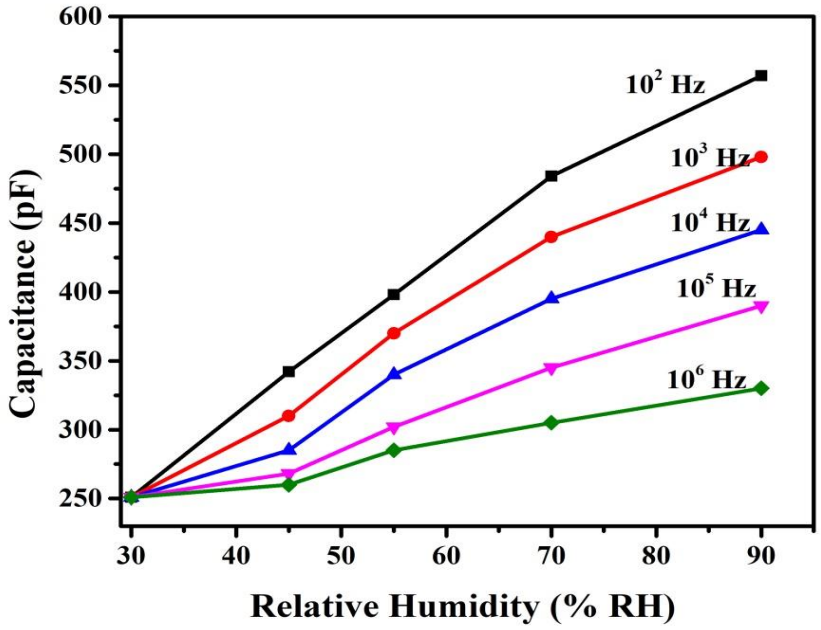

Fig. 5.11 Variations of capacitance (pF) of the sensing film with %RH at different test frequencies at room temperature.

Table 5.1. Literature survey on various types of CO_2 gas sensors

S.No.	Material	Operating temp. (℃)	Gas (ppm)	Sensor Response	Response Time	Recovery Time	Ref.
1	CuO–CuxFe$_{3-x}$O$_4$	250	5000	0.50	9.5 h	-	[2]
2	Ag–BaTiO$_3$–CuO	250	5000	0.28	15 min	10 min	[3]
3	La$_{1-x}$Sr$_x$FeO$_3$	380	2000	0.25	11 min	15 min	[9]
4	CdO	250	5000	0.01	3.33 min	5 min	[10]
5	LaOCl-SnO$_2$	300	1000	3.7	110 sec	40 sec	[11]
6	La$_2$O$_2$CO$_3$	300	5000	0.62	53 sec	120 sec	[12]
8	SnO$_2$–In$_2$O$_3$	RT	1000	17	5 min	7 min	[7]
9	ZnO–La (50 %)	400	5000	0.65	90 sec	38 sec	[13]
10	MWCNT	30	5000	2.1	30 sec	49 sec	[14]
11	**MWCNT/PPY**	**30**	**1000**	**7.2**	**30 sec**	**37 sec**	**Present work**

Table 5.2 Theoretical study on the variation of the different parameter of CNT/PPY before and after interaction with CO_2 and humidity

Theoretical parameters (a.u.)	**Before Interaction**	**After Interaction with CO_2**	**After interaction with humidity (OH^-)**
Ionization Potential (IP)	0.20206	0.2026	0.2021
Electron Affinity (EA)	0.12131	0.1226	0.1522
HOMO-LUMO band gap	0.0808	0.0799	0.0499
Dipole moment (Debye)	0.5053	0.5758	0.9137
Electronegativity	0.1617	0.1626	0.1772
Hardness (η)	0.0404	0.0399	0.02496
Softness (s)	24.767	25.06	40.072
Nucleophllicity index	-0.3237	-0.3312	-0.6290

CHAPTER 6

DEVOLOPMENT OF MWCNT/ZnO AND MWCNT/TiO_2 NANOCOMPOSITE THIN FILMS FOR THE DETECTION OF LPG AND HUMIDITY AT ROOM TEMPERATURE

In this chapter, the synthesis of MWCNT based nanocomposite was carried out. Further their thin film used as was room temperature LPG & humidity sensor. The first part precepts preparation of MWCNT/ZnO based thin film at room temperature. The film was then investigated using SEM, TEM, FTIR and UV-visible spectroscopy. The average Particle size of the material was calculated by using particle size analyzer. Variations in resistance of film with the exposure of LPG and humidity have been investgated. The highest sensor response was found as 60 at 2 vol%. In the second part, we enhanced the sensitivity and sensor response of the sensor by doping MWCNT with TiO_2. This film was further analyzed by using SEM, TEM, XRD, FTIR and Raman spectroscopy. The average pore size and surface area were calculated by using BET. These films were employed as room temperature LPG sensor to observe the LPG sensing potential of the film. Sensor response along with response and recovery time was calculated. Experimental data were verified by theoretical data using DFT calculations

CHAPTER 6

Development of MWCNT/ZnO and MWCNT/TiO_2 nanocomposite thin films for the detection of LPG and humidity at room temperature

6.1 Introduction

Liquefied petroleum gas (LPG) is a complex mixture of hydrocarbon compounds, which contains butane (C_4H_{10}) and propane (C_3H_8) in the ratio of 4:3. LPG is widely used in cooking, heating and in automotive vehicles. It is one of the most dangerous gas due to its flammable and explosive nature which affects the human being as well as the environment. To avoid damage caused by leakage and gas explosion, there is a fundamental need to sense the LPG at lower exposure limit (~2 %Vol of LPG) [1]. In the past few decades, metal oxide semiconducting material has been used for investigations; however, their optimal sensing properties were studied at high temperature (200-600℃). In such a case, a heater needs to be installed for the sensor functioning, which causes high power consumption, complexity and high budget. To overcome these drawbacks we need to fabricate a sensor which can be operated at room temperature [2].

In the recent years, few reports are available on fabrication of the LPG sensor operated at room temperature [3, 4]. They have used many different strategies such as reduction in size, doping with other metal oxide nanoparticle and making heterojunction hybrid materials. In the advancing process, variety of different nanomaterials were added to the sensing material which increases the contact potential, porous sites and also increases surface reaction sites which enhanced the gas sensing performance of the nanomaterial-based sensor. Therefore, more studies have been carried out in fabricating the devices based on the heterojunction system of nanomaterials [5].

In recent studies, we have observed that ZnO/MWCNT composite is highly suitable for sensing LPG at room temperature and has the ability to arrest the effect of moisture, by which the stability of the sensor is enhanced markedly, in spite of the lower

operating temperature. Our experimental results confirmed that ZnO-MWCNT nanocomposite sensors exhibit less with the shorter response and recovery times.

6.2 Experimental details

6.2.1 Fabrication of ZnO-CNTs Nanocomposite Thin Film Sensor

Quartz plates (1 × 1 cm^2) were used as substrates for thin films then Fe was deposited by spin coating as catalyst for promoting the nanoparticle growth. The catalyst (Fe) film thickness (Veeco Dektak 150 surface profiler) was ~50 nm. Carbon nanotubes were synthesized by high thermal chemical vapour deposition method in which Fe catalyst was placed inside the quartz tube and ethanol was decomposed inside the same. Such process consists of three steps; firstly the formation of a precursor consisting of some metal nanoparticles that provide the nucleation point at high temperatures where dissociation of gas takes place. Later the carbon atoms are deposited on the nucleation point and the growth will start in two ways: in root growth (the catalyst will be placed at the bottom of the tubes) and in tip growth (the catalyst will be at the top of the tubes). Therefore, carbon atom was deposited on Fe catalyst by growth mechanism and MWCNTs were formed. The nanotube synthesized using Fe was filtered by DMF treatment in which the prepared film was dipped inside the DMF so that Fe nanocatalyst may be dissolved and pure nanotubes were found on the film. A quartz tube was placed in a single zone furnace providing a temperature plateau of about 1 m length at temperatures between 700 and 850 °C. The annealing of the catalyst films was made in situ in the quartz tube, followed by the growth of the MWCNTs by ethanol decomposition. The reactor tube was heated at about 20 °C/min in the air or N_2 flow until the desired temperature was obtained. The deposition was done by bubbling N_2 through an ethanol reservoir at room temperature. The flow rate of N_2 could be varied between 10 and 100 sccm/min. All treatments in the quartz tube were made at atmospheric pressure. To investigate the influence of the different parameters, the time for ethanol decomposition and thus the deposition time was set at 20 min for every experiment.

Nanostructured ZnO was prepared using the chemical route as prescribed in our published paper [21]. The prepared MWCNTs were added to ZnO nanoparticles (NPs)

solution. The MWCNTs incorporated in ZnO nanoparticles suspension was sintered at 100 °C in air for 2 h to obtained powder. MWCNTs and ZnO were dissolved in the ratio of 1:100 in DMF with vigorous stirring for one day. During this process, CNT interacts with ZnO and form covalent bonds. Thin films of pure MWCNT, ZnO NPs and ZnO/MWCNT composites were prepared on corning glass substrates by spin coating technique at 2200 rpm for 30 s and dried on a hot plate at 100 °C for 10 min [22, 23]. The sensing response characteristics of ZnO/MWCNT nanocomposite thin film deposited on IDE/ glass substrates has been studied and shown in Fig. 6.1. The Pt IDEs were patterned over the corning glass substrates using conventional photolithography technique, prior to deposition of sensing layer (ZnO/MWCNT nanocomposite thin film). The platinum thin film of 90 nm thickness was deposited by RF sputtering using a platinum metal target in 100 %Ar. In order to improve the adhesion of Pt on corning glass substrate an ultrathin (10 nm) buffer layer of titanium was sputtered prior to Pt deposition.

For studying the gas sensing properties, gas dilution system developed by our group was utilized [22]. Two platinum electrodes were grown on ZnO thin film and LPG was injected by syringe into the test chamber. The change in sensor resistance was recorded for different concentrations of LPG with the help of Keithley electrometer (6517B) interfaced with a computer. The sensing response [24] of prepared sensor structure towards reducing (LPG) gas is given by Eqn. 6.1

$$S= R_a/R_g \ldots\ldots\ldots\ldots (6.1)$$

where R_a and R_g are the values of resistance of the sensor in the presence of atmospheric air and target gas, respectively. Once the maximum resistance value was accomplished, the target gas was flushed out from the test chamber and sensor was allowed to regain its initial resistance value in atmospheric air while keeping the sensor at the same temperature.

6.2.1.1 Result and Discussion

6.2.1.2 Structural Studies

Figure 6.2 represents the X-ray diffraction (XRD) pattern of the ZnO-MWCNT composite thin film. The reflection peaks occur at $2\theta = 24.98°$ which corresponds to (002) plane of MWCNT [25]. Also, (100), (002), (101), (102), (110), (103), (112) and (201) reflection planes correspond to the wurtzite polycrystalline structure of ZnO [26]. The lattice constants calculated from the XRD data for (101) phase (strong reflection) are a = 3.263 Å and c = 5.211 Å, respectively. The average crystallite size was calculated as 28.43 nm.

6.2.1.3 Optical Properties

The optical transmission spectra of the as-grown, ZnO and ZnO-MWCNT composite thin films deposited on corning glass substrates were obtained in the wavelength range of 190–800 nm, and are shown in Fig. 6.3. MWCNT, ZnO and ZnO-MWCNT composite thin films exhibit a high transmission (80–50 %) in the visible region and show a sharp fundamental absorption edge at ~280 nm.

The optical band gap of MWCNT, ZnO and ZnO-MWCNT composite thin films deposited on corning glass substrate, was calculated from the intercept on energy axis obtained by extrapolating the linear portion of the Tauc plot of $(\alpha h\nu)^2$ versus photon energy (hv) as shown in the inset of Fig. 6.3. The estimated value of bandgap for pure MWCNT and ZnO film were found to be 3.87 and 3.95 eV. The value of bandgap was found to increase slightly to 4.05 eV with the incorporation of MWCNT (1 mg) into ZnO thin film. The increase in the bandgap with the incorporation of MWCNT into ZnO thin film may be due to electronic transition between dopant and ZnO thin film.

6.2.1.4 TEM analysis

The surface structure, morphology and distribution of pure ZnO, MWCNT and ZnO-MWCNT composite material were characterized by Transmission electron microscope (TEM) and these images are presented in Fig. 6.4. Fig. 6.4 a and b represents

the structure and size of the pure ZnO nanoparticles and MWCNT prepared by the ultra-sonication assisted method. The surface structure and morphology of the ZnO-MWCNT composite materials are shown in Fig. 6.4c. The figure shows that the MWCNTs are naturally grown on the substrate with precise configurations. From the figure, it is clear that ZnO grains and carbon nanotubes co-exist in the same frame. It can be seen that the MWCNT chains are closely surrounded by the mesh-like structure built by ZnO nanoparticles. The obtained rough and porous morphology of prepared thin film is shown in Fig. 6.4c provided the high surface to volume ratio which enhanced the sensing response.

6.2.1.5 Surface Morphological Studies

The morphology of samples was observed using SEM. SEM images of the prepared ZnO-MWCNT nanocomposite thin film is shown in Fig. 6.5a–c. These micrographs show the presence of metal oxide grains. At low magnification, the carbon nanotubes were not visible in Fig. 6.5a. However, carbon nanotubes can be observed in few regions (Fig. 6.5b, c). Therefore, the morphology confirms the presence of multiwall nanotubes on the film surface.

6.2.1.6 LPG Sensing

Before the exposure of LPG to the sensing material, the gas chamber was allowed to stabilize at room temperature for 30 min and the resistance was taken as R_a (stabilized resistance in presence of air). The data of the variations of resistance with time for different concentration of LPG for ZnO-MWCNT (1 mg) have been plotted and shown in Fig. 6.6. Curves exhibit that the resistance increases gradually at the initial stage, then becomes constant. Sensor response of ZnO-MWCNT (1 mg) sensing material is shown in Fig. 6.6b. At 200 ppm of LPG sensor shows small variation in resistance with time after exposure with slow sensor response. For 500 ppm of LPG, the sensor exhibits improvement over the previous and has shown better sensor response. The curve for 1000 ppm of LPG shows that there is a drastic increase in sensor response up to 276 s. Further for 1500 ppm of LPG, the sensor shows increased sensor response. Here, the response increases with time after exposure up to 475 s, then become constant. Response and

recovery times were 475 and 491 s respectively. Average sensitivity was plotted as a function of the concentration of LPG (ppm) as shown in Fig. 6.6c. It has a maximum average sensitivity of 41.95 MΩ/sec for 1500 ppm of LPG.

We observed that as the concentration of LPG increases, the average sensitivity increases linearly in the beginning and later it becomes saturated. The linear relationship between sensitivity and gas concentration may be attributed to the availability of a sufficient number of sensing sites on the film surface to act upon the LPG. The low concentration implies a lower surface coverage of gas molecules, resulting in a lower surface reaction between the surface adsorbed oxygen species and the gas molecules.

The gas sensing mechanism of LPG sensor is a surface controlled phenomenon i.e., it is based on the surface area of the film. Initially, oxygen from the atmosphere gets adsorbed on the surface of the film and pick up electrons from its conduction band.

The adsorption of O_2^- ions on the nanostructured ZnO/MWCNT surface is vital to enhance the receptor function of the sensor, and, hence, its sensing response. The electron transfer from the conduction band to the chemisorbed oxygen results in the decrease in electron concentration at the film surface. As a consequence, an increase in the resistance of the film was observed before exposure to LPG. The resistance gets stabilized through above-mentioned chemisorption reactions and the stabilized value of the resistance is known as resistance in the presence of air (Ra). When the film is exposed to LPG, it reacts with the chemisorbed oxygen and a surface charge layer would be formed. When the LPG reacts with the surface oxygen ions then the combustion products such as water depart and a potential barrier to charge transport would be developed i.e., this mechanism involves the displacement of adsorbed oxygen species by the formation of water. The overall reaction of LPG with the chemisorbed oxygen may take place as described by Eqn. 6.2 [27]:

$$C_nH_{2n+2} + O_2^- \rightarrow C_nH_{2n}O + H_2O + e- \text{.....(6.2)}$$

where C_nH_{2n+2} represents the various hydrocarbons. Due to the liberation of the electrons, the resistance of the sensing film decreases drastically in the beginning due to rapid adsorption, afterwards, it decreases slowly and finally becomes saturated. When the

flow of LPG is stopped for the study of recovery characteristics, the oxygen molecules in the air will be adsorbed on the surface of the film, and the capture of electrons through the process indicated in the equation will increase the sensor resistance. As the sensing mechanism is based on the chemisorption reaction that takes place at the surface of the film, so increasing specific surface area of the sensitive material leads to more sites for the adsorption of the target gas. The receptor function is an ability of sensing surface to receive the target gas which is directly related to surface capability of adsorbed O_2^- ions. Larger the ability of the surface to receive the target gas, larger may be the change in resistance of the sensor, and hence, improvement in the sensing response of the device.

Titanium dioxide is a widely occurring transition metal oxide semiconductor used in the modern world. It occurs naturally in several kinds of rocks and mineral sands. It is most preferred semiconductor photocatalytic material due to its favourable properties like low cost, chemical inertness, non-toxicity, accessible bandgap and stability over a wide pH range under irradiation condition [33-35]. The important characteristic of TiO_2 is that it has high melting and boiling point with temperature dependant paramagnetic susceptibility. Pure TiO_2 does not occur naturally but it can be extracted by the ores of ilmenite and leucoxene. TiO_2 occurs naturally in different forms such as Anatase, Rutile and Brookite. Rutile is the most stable form and the metastable Brookite and Anatase phases converted into Rutile phase by heating it above the temperature the range from 600-800℃.

Fig. 6.7 shows the chemical structure of MWCNT and TiO_2. TiO_2 has attracted much attention as an effective material for various gases because of high surface activities and high surface to volume ratio. Due to having a larger bandgap, the conductivity of TiO_2 nanoparticles is limited so it requires a higher temperature to work so for enhancing the conductivity when MWCNT were mixed with TiO_2 nanoparticle. MWCNTs are the hollow cylindrical structure of carbon and highly conductive material at room temperature [36-39]. There are so many strategies for mixing the nanotubes with TiO_2 nanoparticles but all the processes have some limitations such as functionalization as it requires high acid treatment which affects the property of nanotube therefore, we have developed a new technique in which the nanotube and TiO_2 nanoparticles were simultaneously synthesized by chemical vapour deposition process.

6.2.2 Synthesis of MWCNT/TiO_2 using CVD

MWCNT/TiO_2 based thin film sensor was fabricated by using direct liquid injection chemical vapour deposition (DLICVD) process. In this method, pure titanium powder was dissolved in deionized water and dropped on the Ni substrate then put in the horizontally aligned thermal CVD chamber. In the CVD chamber oxidation of titanium was carried out. Pure argon was first introduced into the chamber at a flow rate of 99 sccm for about 4 h to flush out the air inside the chamber. The temperature of the target was increased up to 850 ℃, and then 15 ml acetone was introduced inside the chamber using argon as a carrier gas [40].

The acetone was decomposed into carbon monoxide, which acts as reducing gas so the decomposition and reduction happened at the same time. Oxygen was partially removed from the TiO_2 surface to create TiO_{2-x}. The resultant interstitials of Ti were quickly diffused on the surface, as shown in Fig. 6.8 (a). The diffusion in grain boundary controls the diffusion process over the lattice diffusion, making the Ti cations assemble in the grain boundaries as shown in Fig. 6.8 (b). After collection of the Ti cation on grain boundary, the Ti cations are re-oxidized as shown in Fig. 6.8 (c). With the diffusion, reduction and re-oxidation leads to formation of nano-wall structures at the grain boundaries with the conjunction of three boundaries as shown in Fig. 6.8 (d). At 850 ℃, the motion of Ti cations decreases. Similarly, at the same time due to the presence of Ni substrate, the MWCNTs were grown on the Ni and attached with the TiO_2 nanoparticles due to having grain boundary diffusion in Ti cation [41-43].

6.2.2.1 Characterization Results

6.2.2.2 XRD analysis

The crystal structure and the phase of MWCNT/TiO_2 synthesized by using CVD were analyzed by XRD with CuK_α radiation as a source having wavelength of 1.54 Å. The results clearly indicate that the prominent peak in the patterns corresponds to the rutile structure of TiO_2 with cross-linked MWCNT.

Fig. 6.9 shows the analysis of XRD for CVD synthesized MWCNT/TiO_2. The lattice plane at (002) confirms the presence of MWCNT and the planes (110), (101), (111), (211), (112) and (311) confirms the presence of rutile TiO_2 [44-47]. The crystallite size of the CVD synthesized MWCNT/TiO_2 was found to be 40 nm using the Gauss method.

6.2.2.3 SEM analysis

The surface morphology of the sensing element was investigated by using Scanning Electron Microscope operated at 15 kV [48]. Fig. 6.10 (a-d) shows the microstructure and surface morphology of MWCNT/TiO_2 synthesized by using DLICVD technique. Fig. 10 (a) reveals that the agglomerated TiO_2 nanoparticles cross-linked with the nanotube, leaving some spaces as pores. Usually, the highly porous structure is preferred for gas sensing because of the presence of higher active sites. Fig. 6.10 (b-c) shows the cross-linked structure of grown MWCNTs on the TiO_2 nanoparticle. The particle size of TiO_2 nanoparticles varies from 100-140 nm and the tube length varies from 300-450 nm.

The synthesis process at high temperature mainly reduces the residual stress on the surface of the material. At lower temperature, the grains are randomly oriented, leaving some spaces as pores, but at a higher temperature, the grains get ordered in a specific manner, leaving some more spaces between them. It was found that the nanomaterial synthesized at a higher temperature using CVD, the sample shrank and became more porous as it may easily be observed through the SEM images. This is an advantage of the CVD process in which the pore sizes on the surface of the sample were found increased with high purity.

6.2.2.4 EDX Analysis

Fig. 6.11 shows the Energy-dispersive X-ray analysis of the synthesized sample. The presence of both carbon (C) and Titanium (Ti) elements in the MWCNT/TiO_2 sample is confirmed by the EDX spectrum reported in Fig. 6.5. The EDX data clearly reports, that the space MWCNT/TiO_2 nanostructure contain 7.58 wt%, 16.51 atomic%

carbon element, 30.33 wt%, 49.59 atomic% oxygen element and 62.09 wt%, 33.90 atomic% titanium element.

6.2.2.5 TEM analysis

Fig. 6.12 (a) and (b) shows the HR-TEM image of MWCNT/TiO_2 at different scales. The sample was prepared by making a dispersed solution of the MWCNT/TiO_2 powder in ethanol. After dispersion, the solution was sonicated by ultrasonic machine and a few drops of the floating solution was dropped on the grid. The image at 200 nm scale reveals the crystalline structure of TiO_2 with a cross-linked structure of MWCNT. The image at 10 nm shows the hollow nanotubes with TiO_2 at interconnected sites. The inner and outer diameter of the multiwall nanotube was found as 11 nm and 22 nm respectively.

6.2.2.6 UV analysis

Fig. 6.13 shows the UV-vis absorption spectrum for MWCNT/TiO_2. This absorption spectrum illustrates that the higher absorption was found at lower wavelength i.e., high photon energies. The absorbance spectra of the material have a strong reflective characteristic at 260 nm with a sharp decrease at 260 nm. The reason for the sharp decrease in the absorbance wavelength plot is the fact that the distortion at the edges of the band is not too much and the strong reflective characteristic is due to the high possibility for reflectance for the photons lacking the required energy for interaction with electrons [49].

Insitu figure of Fig. 6.13 shows the Tauc plot for the measurement of bandgap and the optical band gap was found 3.89 eV. It is evident that the blue shift was found in the absorption peak of MWCNT/TiO_2 which is very useful for the gas sensing application. This blue shift arises due to the very small size of the particle and its quantum confinment effect.

6.2.2.7 Particle size analysis

The particle size of the MWCNT/TiO_2 was analyzed by using Nanozetasizer NZS90 in which the average particle size was measured by dynamic light scattering method that provides the bulk average of particles diffusing in solution. The particle size of the MWCNT/TiO_2 has been measured by making a dispersed solution of MWCNT/TiO_2 in ethanol and average tubular particle size was found 100 nm as shown in Fig. 6.14.

6.2.2.8 FTIR Analysis

The CVD synthesized MWCNT/TiO_2 nanoparticle has been characterized by Thermo Scientific Nicolet^{TM} 6700 Fourier Transform Infrared Spectrometer (FTIR). The FTIR spectrum of the prepared sample of MWCNT/TiO_2 nanoparticle is shown in Fig. 6.15. The peak at 3405.1 cm^{-1} correspond to the OH stretch which confirms the presence of hydrogen-bonded alcohol presence. The peak at 2250 cm^{-1} shows the $C \equiv C$ stretching and the vibrational peak at 810 cm^{-1} confirms the metallic bonding between C-Ti [50].

6.2.2.9 Raman analysis of MWCNT/TiO_2 nanocomposite

Fig. 6.16 shows the Raman spectrum of MWCNT/TiO_2 nanocomposite and this spectrum is really faithful to the standard spectra of the TiO_2 and MWCNT. The Raman frequencies of MWCNT/TiO_2 nanocomposites along with their vibration are shown in Fig. 6.16. The observed peaks are the characteristic peaks of MWCNT/TiO_2, which confirm that the MWCNT/TiO_2 has been synthesized successfully using the CVD technique. The lower peaks below 800 cm^{-1} are ascribed to the optical transition of the TiO_2 nanoparticle in the MWCNT/TiO_2 nanocomposites. Two characteristic peaks located about 1310 cm^{-1} and 1512 cm^{-1} correspond to disordered carbon (D band) and graphitic carbon (G band) in nanocomposites respectively [51, 52]. The peak intensity ratio of D-band and G-band (I_D/I_G) is found to be 1.53 which shows that most of the graphitic layers are converted into carbon nanotubes. The lower peaks correspond to the first and second ordered longitudinal optical phonon mode (LO) mode of TiO_2 and these

peaks are shifted to lower side in comparison to pure TiO_2 which indicates that the size of TiO_2 nanoparticle reduces during the MWCNT/TiO_2 nanocomposites formation [53].

6.2.2.10 BET analysis of MWCNT/TiO_2 nanocomposites

The Brunauer-Emmett-Tailor (BET) and BJT analysis of MWCNT/TiO_2 nanocomposite have been shown in Fig. 6.17. The standard BET method is used for calculating the specific surface area and pore size of the sample.

After making out the calculation of BET for MWCNT/TiO_2, the mean pore diameter of MWCNT/TiO_2 was found as 27.075 nm and the specific surface area as 6.65 m^2g^{-1} at room temperature. The formula used for the calculate are given in Eqns. 4.2 and 4.3 of Chapter 4.

6.2.3 Gas and humidity sensing characteristics

The MWCNT/TiO_2 based thin film was used as LPG sensing element. Variations of electrical resistance w.r.t. time were recorded by varying the LPG concentration around them. The sensitivity [54] and sensor response [55] of the film were studied.

The thin film was also used for the detection of the humidity level. The impedance and capacitance of the thin film vary with the amount of water adsorbed through its surface. This principle is used for the measurement of moisture in all capacitive/impedance type humidity sensors.

6.2.3.1 Result and discussion

The fluctuation in electrical resistance of MWCNT/TiO_2 for various concentrations of gas with time is shown in Fig. 6.18. The variation in the resistance increases with increasing the LPG concentration and exposure time [56-58]. The sensitivities of MWCNT/TiO_2 based sensors for different concentration of LPG are depicted in Fig. 6.19 (a) which shows that the sensitivity of the sensor increases linearly with the LPG concentrations. At lower concentrations, the gas molecules cover a minimum surface area, resulting in less surface interaction between oxygen species and the gas molecules. The increasing concentration of the LPG increases the gas quantity in

the chamber so higher surface interaction takes place which gives higher change in the resistance. The maximum sensitivity of the sensor was obtained for 2 vol% of LPG and the variations in the sensor response w.r.t. time is shown in Fig. 6.19 (b). The curve shows that the sensor response was low at lower concentrations and increased linearly on increasing the LPG concentration. The maximum sensor response was 4.29 for MWCNT/TiO_2 based sensor.

The sensing behaviour of the MWCNT/TiO_2 based thin film was observed after 15 days of fabrication, only $\pm$ 4% change was observed showing the reliability and stability of the sensor. The $\pm$ 4% error in the result is due to the effect of moisture on the film, which deteriorates the power of absorption on the surface [60-62].

The repeatability of the sensor is defined as the ability to reproduce the same product over an interval of time for the same measurement. Fig. 6.19 (b) shows the repeatability characteristics of the sensor for 0.5 vol% for LPGand the repeatibility of the sensor has been found as 98.2%.

The gas sensing mechanism is based on the surface controlled phenomenon of MWCNT/TiO_2 based thin film sensor. Such a phenomenon depends on the open surface area of the thin film at which the gas reacts and adsorbs with pre-adsorbed oxygen molecules. The centres of oxygen chemisorption are localized donor and acceptor states, oxygen vacancies and defects formed on the surface of nanomaterial which is formed during synthesis. These pores are filled with oxygen when exposed in the air. For achieving the equilibrium state between atmospheric oxygen and oxygen of the sensing element the gas sensing film has been put inside the sensing setup. So the equilibrium has been formed due to chemisorption process occured at room temperature. The stabilized resistance at this stage is known as the resistance in the presence of air (R_a).

The chemisorption kinematics at room temperature may be explained by the reaction given in Eqn 6.3 and 6.4:

$$O_2\,(gas) \leftrightarrow O_2\,(ads) \text{……..(6.3)}$$

$$O_2\,(ads) + e^- \rightarrow O_2^- \text{…….(6.4)}$$

When the LPG was exposed to the thin film, the increase in resistance was observed. This is because the chemisorbed oxygen captures the free electrons from the conduction band so the electron concentration at the film surface starts decreasing and higher resistance has been observed. Thus, the sensor resistance was used for determining the surface reaction occurred by the charge transfer mechanism at the surface of the sensing element. When the thin film is exposed to the reducing gas molecules such as LPG, it reacts with the chemisorbed oxygen. The adsorbed oxygen is removed and gaseous species are formed on interaction with the hydrocarbons (C_nH_{2n+2}) of LPG. Then the resistance of the film has been changed, which is imputable to the alteration in the width of the depletion layer after exposure of LPG. The reaction of hydrocarbons with oxygen species by given as Eqn. 6.5:

$$C_nH_{2n+2} + O_2^- \rightarrow C_nH_{2n}O + H_2O + e- \text{……..(6.5)}$$

Where C_nH_{2n+2} represents the hydrocarbons present in LPG. When the LPG reacts with the sensing element, then the surface ions interact with LPG and formed water and developed a potential barrier. Initially, the film surface was dry and when the gas is let out along the film then the condensation of the water vapour takes place in the pores so the resistance of the film becomes constant [60, 61].

Response and recovery times are the other significant parameters of any gas sensor. Fig. 6.18 shows the sensing response of the film which is time-dependent and as time increases the response of the sensing film increases drastically. Later it increases slowly. Eventually, when the gas chamber is opened then the response reaches back to its initial value of sensor response in the air for a further range of time. The fast decrease in the resistance when the LPG was turned-off indicating the sensor has good recovery time. The minimum sensing response and recovery time of the film were 36 sec and 20 sec respectively.

The sensing film's selectivity was carried out with the other target gases like CO_2, ethanol and acetone inside the chamber. The sensitivity of the film was found maximum towards LPG and least for other gases. The film also responses for ethanol, but not

recover back after removing the gas. Fig. 6.21 shows that the MWCNT/TiO_2 is a good sensor for the detection of LPG in comparison to other gases at room temperature.

Variations in impedance/capacitance with a change in %RH for sensing element of MWCNT/TiO_2 based thin film synthesized by CVD technique are shown in Fig. 6.16. It was observed that as humidity inside the chamber increases from 10 to 90% RH, the impedance of the film decreases from 85 MΩ to 0.8 MΩ and the capacitance of the film increases from 15.12 pF to 54 pF.

Fig. 6.22 (a) and (b) shows the humidity sensing curve of as-fabricated MWCNT/TiO_2 based thin film. In Fig. 6.22 (a), it is evident that in lower humidity range (till 40 %RH), decrease in impedance is small and then decreases gradually up to 70 %RH. After 70 %RH, the sensor becomes insensitive & a small change was observed. The hysteresis behaviour of the sensor was studied and found as 1.2%. The sensing experiment was repeated and the results were found reproducible up to 98% with the maximum sensitivity of 1.05 MΩ/%RH for this sensor. In Fig. 6.22 (b), the capacitance of the thin film increases slowly in lower humidity range (till 40 %RH), for mid humidity range (from 40 to 70 %RH) the change in the capacitance of the film is very high and the sensitivity was found to be 0.525 pF/%RH, after 70 %RH the film has become insensitive and only small changes in the capacitance were observed. The hysteresis behaviour of the thin film was found to be 0.8% with reproducibility up to 99%.

The reproducibility is also an important parameter for the sensor and here, in this case, it was found to be more than 97% as shown in Fig. 6.23.

The testing frequency is another important factor for determining the response of MWCNT/TiO_2 nanocomposite based thin film. As shown in Fig. 6.24 (a) and (b), lower testing frequency leads to a sharp change in impedance/capacitance of MWCNT/TiO_2 at all the humidity levels. At higher testing frequency, the change in impedance/capacitance is too low. So the sensor fabricated by MWCNT/TiO_2 nanocomposite is best for lower frequency.

Fig. 6.24 (a) and (b) shows the variation of impedance (MΩ)/ capacitance (pF) with %RH for MWCNT/TiO_2 based humidity sensor at different testing frequencies on

the ambient temperature. The alteration in the impedance/capacitance of porous MWCNT/TiO_2 thin film at different humidity is directly linked to the water adsorption mechanism on the metal oxide nanocomposite suface. The negatively charged hydroxyl ion is electrostatically attracted to the positively charged cationic surface of the nanocomposite. If the charge density on the cationic side is low, then hydroxyl ions of water molecules are physically adsorbed at the surface of film by a weak electrostatic field. If the surface charge density is high, then water remains chemisorbed at the surface due to a strong electrostatic field. The irreversible reaction at the foremost layer of a chemisorbed water molecule on the MWCNT/TiO_2 surface can be given by Eqn.6.6

$$C_nH_nTiO_x^+ + H_2O \rightarrow C_nH_nTiO_x\text{-}OH + H^+ \ldots\ldots(6.6)$$

The softening action of the surface electrostatic field stimulates the dissociation of the physisorbed water molecule as shown in Eqn. 6.7

$$2H_2O \leftrightarrow H_3O^+ + OH^- \ldots\ldots\ldots(6.7)$$

The transfer of the charge carriers in pure water happens by the attachment of a proton to a water molecule forming hydronium ion. The hydronium ion gives another proton to a second water molecule, which accepts this proton, while a third proton becomes attached to the water molecule and so on throughout the liquid. The hydronium ion is mostly responsible for electrical conduction [35].

6.2.3.3 Theoretical investigations

To explain the experimental result, we have designed a theoretical model for CNT/TiO_2 using Gauss view 05 and Gaussian 09 for the LPG and humidity sensing. The CNT/TiO_2 was randomly distributed in the film so the overall resistance and impedance of the film were the sum of the resistances offered by the individuals (2, 2) CNT/TiO_2.

For observing the change in resistance and impedance of the overall film, we choose a single armchair (2, 2) CNT/TiO_2, which interacts with LPG and a hydroxyl group. After analyzing the change observed by individual CNT/TiO_2 we multiply the energy with a certain number of CNT/TiO_2 present in the film. The whole calculation was carried out by using armchair (2,2) CNT/TiO_2 and the computational method as

B3LYP. In this computational method, the sensing mechanism is based on the change in the energy level, HOMO-LUMO gap, electron affinity, ionization potential and the dipole moment of molecules before and after interaction with the LPG and hydroxyl group [60,61].

Table 6.1 shows the change found in the energy and different theoretical parameter before and after interaction with LPG and humidity. In case of electronegativity, hardness, softness and nucleophilicity index, we first calculate Higher Occupied Molecular Orbit (HOMO) and Lower Unoccupied Molecular Orbit (LUMO) and later calculated these parameters using the following formula given in Eqn 3.8-3.11.

Fig. 6.25 (a) shows that Ionization potential, HOMO-LUMO gap and dipole moment of the CNT/TiO_2 increases when LPG (C_nH_{2n+2}) interacted with the molecule. The increments in the bandgap and ionization potential were found because the LPG molecule captured free electrons from the conduction band and Fermi level shifts downwards so the bandgap (HOMO-LUMO gap) increases. The bandgap of the material is directly dependent on the resistance of the material, so in such case, the resistance of the film was increased when the molecule interacted with LPG and the same type of changes have been observed in the experimental data as shown in Fig. 6.18.

Fig. 6.25 (b) shows the humidity sensing of MWCNT/TiO_2 thin film. The HOMO-LUMO gap, ionization potential and dipole moment decreases on interaction with humidity (OH^-). The OH^- ions have free electrons and when they interact with CNT/TiO_2, they donate free electrons to the molecule. When the molecule gets free electrons from the OH- ions, the conductivity of the molecule increases and the impedance offered by the molecule decreases which may be seen through Fig. 6.22.

6.4 Conclusion

MWCNT/ZnO nanocomposite was synthesized successfully and confirmed by EDX and XRD. ZnO/MWCNT composite sensor structure exhibited the maximum sensing response as 61.57 and sensitivity as 41.95 MΩ/sec for 1500 ppm of LPG concentration towards at room temperature (30 °C). Nanostructured MWCNT/TiO_2 based thin film was successfully deposited using chemical vapor deposition technique. The

process used for the preparation of thin film is cheap and eco-friendly. XRD revealed that both the MWCNT and TiO_2 were grown simultaneously and minimum crystallite size was found as 40 nm. The SEM micrographs showed that the film is highly porous with cross linked nanotubes. In FTIR spectra, the peaks between 600-1000 cm^{-1} showed the characteristic peak of MWCNT/TiO_2. The maximum sensitivity of the sensor was found as 17.65 MΩ/Sec and % sensor response as 429 for 2 vol% of LPG. The thin film was also used for humidity sensing and the maximum sensitivity was found as 1.05 MΩ/%RH at 10^2 Hz. The linear characteristic of MWCNT/TiO_2 based LPG sensor is rather appropriate for emerging a commercial LPG and humidity sensor operable at room temperature. The experimental data were found analogous to the predicted theory which is unique.

References

[1] S. Singh, B.C. Yadav, M. Singh, R. Kothari, A review report on nanostructured ferrites as liquefied petroleum gas sensor. Int. J. Sci. Technol. Soc. 1, (2015) 5.

[2] S. Sikarwar, B.C. Yadav, S. Singh, G.I. Dzhardimalieva, S.I. Pomogailo, N.D. Golubeva et al., Fabrication of nanostructured yttria-stabilized zirconia multilayered films and their optical humidity sensing capabilities based on transmission. Sens. Actuators B 232, (2016) 283.

[3] R. K. Sonker, B. C. Yadav, Low-temperature study of nanostructured Fe_2O_3 thin films as NO_2 sensor Mater. Today 3 (2016) 2315.

[4] K. K. Dey, D. Bhatnagar, A. K. Srivastava, M. Wan, S. Singh, R. R. Yadav, B. C. Yadav, M. Deepa, VO_2 nanorods for efficient performance in thermal fluids and sensors Nanoscale 7, (2015) 6159.

[5] R. K. Sonker, A. Sharma, M. Tomar, V. Gupta, B.C. Yadav, Low temperature operated NO_2 gas sensor based on SnO_2–ZnO nanocomposite thin film Adv. Sci. Lett. 20, (2014) 911.

[6] S. B. Kondawar, P. T. Patil, S. P. Agrawal, Chemical vapour sensing properties of electrospun nanofibers of polyaniline/ZnO nanocomposites. Adv. Mater. Lett. 5, (2014) 389.

[7] R. K. Sonker, S. R. Sabhajeet, B. C. Yadav, TiO_2–PANI nanocomposite thin film prepared by spin coating technique working as room temperature CO_2 gas sensing. J Mater Sci. 27 (2016). DOI:10.1007/s10854-016-5310-y.

[8] B. Wei, M. Hsu, P. Su, H. Lin, R. Wu, H. Lai, A novel SnO_2 gas sensor doped with carbon nanotubes operating at room temperature. Sens. Actuators B 101, (2004) 81.

[9] C. Marichy, M. Bechelany, N. Pinna, Atomic layer deposition of nanostructured materials for energy and environmental applications. Adv. Mater. 24, (2012) 1017.

[10] C. Marichy, N. Donato, M. G. Willinger, M. Latino, D. Karpinsky, S. H. Yu, G. Neri, N. Pinna, Tin dioxide sensing layer grown on tubular nanostructures by a non-aqueous atomic layer deposition process. Adv. Funct. Mater. 21, (2011) 658.

[11] R. K. Sonker, B. C. Yadav, Growth mechanism of hexagonal ZnO nanocrystals and their sensing application. Mater. Lett. 160, (2015) 581–584.

[12] R. K. Sonker, B. C. Yadav, Chemical route deposited SnO_2, SnO_2-Pt and SnO_2-Pd thin films for LPG detection Adv. Sci. Lett. 20, (2014) 1023.

[13] Y. X. Gao, J. W. Xin, Z. Y. Shen, W. Pan, X. Li, A. G. Wu, A new rapid colorimetric detection method of Mn^{2+} based on tripolyphosphate modified silver nanoparticles. Sens. Actuators B 181, (2013) 288.

[14] C. Wongchoosuk, A. Wisitsoraat, A. Tuantranont, T. Kerdcharoen, Portable electronic nose based on carbon nanotube-SnO_2 gas sensors and its application for detection of methanol contamination in whiskeys. Sens. Actuators B 147, (2010) 392.

[15] U. Kumar, S. Sikarwar, R.K. Sonker, B.C. Yadav, Carbon nanotube: synthesis and application in solar cell. J. Inorg. Organomet. Polym. 26 6 (2016) 1231.

[16] H. F. Dai, P. Xiao, Q. Lou, Application of SnO_2/MWCNTs nanocomposite for SF6 decomposition gas sensor. Phys. Stat. Sol. A 208, (2011) 1714.

[17] P. T. Patil, R. S. Anwane, S. B. Kondawar, Development of electrospun polyaniline/ZnO composite nanofibers for LPG sensing. Mater. Sci. 10, (2015) 195.

[18] D. S. Dhawale, R. R. Salunkhe, U. M. Patil, K. V. Gurav, A. M. More, C.D. Lokhande, Room temperature liquefied petroleum gas (LPG) sensor based on p-polyaniline/n-TiO_2 heterojunction Procedia Sens. Actuators B 134, (2008) 988.

[19] L. A. Patil, D. N. Suryawanshi, I. G. Pathan, D. M. Patil, Nickel doped spray pyrolyzed nanostructured TiO_2 thin films for LPG gas sensing Sens. Actuators B 176 (2013) 514.

[20] R. D. Ladhe, K. V. Gurav, S. M. Pawar, J. H. Kim, B. R. Sankapal, p-PEDOT: PSS as a heterojunction partner with n-ZnO for detection of LPG at room temperature J. Alloys Compd. 515, (2012) 80.

[21] R. K. Sonker, A. Sharma, Md.. Shahabuddin, M. Tomar, V. Gupta, Low-temperature sensing of NO_2 gas using SnO_2-ZnO nanocomposite sensor Adv. Mat. Lett. 4, (2013) 196.

[22] R. K. Sonker, S. R. Sabhajeet, S. Singh, B. C. Yadav, Synthesis of ZnO nanopetals and its application as NO_2 gas sensor Mater. Lett. 152, (2015) 189–191

[23] G. Sarala Devi, V. B. Subrahmanyam, S. C. Gadkari, S. K. Gupta, Anal. Chim. Acta 30, (2006) 102.

[24] R. K. Sonker, A. Sharma, M. Tomar, V. Gupta, B. C. Yadav, Nanocatalyst (Pt, Ag and CuO) doped SnO_2 thin film based sensors for low-temperature detection of NO_2 gas. Adv. Sci. Lett. 20, (2014) 1374.

[25] Y. L. Liu, H. F. Yang, Y. Yang, Z. M. Liu, G. L. Shen, R. Q. Yu, Gas sensing properties of tin dioxide-coated onto multi-walled carbon nanotubes. Thin Solid Films 497, (2006) 355.

[26] H. Xu, X. Chen, J. Zhang, J. Wang, B. Cao, D. Cui, NO_2 gas sensing with SnO_2–ZnO/PANI composite thick film fabricated from porous nano solid, Sens. Actuators B 176, (2013) 166.

[27] B. C. Yadav, R. Srivastava, A. Yadav, V. Srivastava, LPG sensing of nanostructured zinc oxide and zinc niobate Sens. Lett. 6 (2008) 1.

[28] B. C. Yadav, R. Srivastava, A. Yadav, Nanostructured zinc oxide synthesized via hydroxide route as liquid petroleum gas sensor, Sens. Mater. 21 (2009) 87.

[29] X. J. Huang, Y. K. Choi, K.S. Yun, E. Yoon, Oscillating behaviour of hazardous gas on tin oxide gas sensor: Fourier and wavelet transform analysis, Sens. Actuators B 115 (2006) 357.

[30] B. C. Yadav, A. Yadav, T. Shukla, S. Singh, Solid-state titania-based gas sensor for liquefied petroleum gas detection at room temperature, Bull. Mater. Sci. 34 (2011) 1.

[31] R. K. Sonker, M. Singh, U. Kumar, B. C. Yadav, MWCNT Doped ZnO Nanocomposite Thin Film as LPG Sensing. Journal of Inorganic Organometallic Polymers 26 6 (2016) 1434.

[32] V. Guidi, M.A. Butturi, M.C. Carotta, B. Cavicchi, M. Ferroni, C. Malag, G. Martinelli, D. Vincenzi, M. Sacerdoti, M. Zen, Gas sensing through thick film technology, Sens. Actuators B 84 (2002) 72.

[33] T. Shukla, B.C. Yadav, P. Tandon, Synthesis of nanostructured cobalt titanate and its application as liquefied petroleum gas sensor at room temperature, Sens. Lett. 9 (2011) 533.

[34] B. Wang, Mesoporous CNT@TiO_2-C Nanocable with Extremely Durable High Rate Capability for Lithium-Ion Battery Anodes. Sci. Rep. 4, (2014) 3729.

[35] P. N. Zhu, Long term cycling studies of electrospun TiO_2 nanostructures and their composites with MWCNTs for rechargeable Li-ion batteries. RSC Adv. 2, (2012) 531.

[36] U. Kumar, S. Sikharwar, R. K. Sonkar, B. C. Yadav Carbon nanotube: synthesis and application in solar cell. Journal of Inorganic Organometallic Polymers 26 6 (2016) 1231

[37] U. Kumar, B. C. Yadav. State of Art: An Approach to the Synthesis of Pure and Doped Graphene Advanced Science, Engineering and Medicine, 10 (2018) 638.

[38] E. Singh, R. Srivastava, U. Kumar, A. D. Katheria. Carbon Nanotube: A Review on Introduction, Fabrication Techniques and Optical Applications, Nanoscience and Nanotechnology 4 (4), (2017) 120.

[39] E. Singh, U. Kumar, R. Srivastava, B. C. Yadav. Carbon Nanotubes Based Thin Films as Opto-Electronic Moisture Sensor Advanced Science, Engineering and Medicine, 10 (2018) 790.

[40] E. G. Ordoñez-Casanova, M. Román-Aguirre, A. Aguilar-Elguezabal, F. Espinosa-Magaña, Synthesis of Carbon Nanotubes of Few Walls Using Aliphatic Alcohols as a Carbon Source. Materials 6 (2013) 2534.

[41] Hugh O. Pierson "Handbook of chemical vapour deposition" second edition, Noyes Publication.

[42] C. S. Kim, K. Okuyama, K. Nakaso, M.Shimada, Direct measurement of nucleation and growth modes in titania nanoparticles generation by a CVD method, J Chem Eng Jpn, 37 11 (2004) 1379.

[43] K. K. Chattopadhyay, A. N. Banerjee, "Introduction to Nanoscience and Nanotechnology", PHI Learning Private Ltd., 2012.

[44] B. C. Yadav, S. Singh, A. Yadav, T. Shukla, Experimental investigations on nanosized ferric oxide and its LPG sensing. International Journal of Nanoscience 10 (2011) 135.

[45] M. Perez-Cabero, I. Rodriguez-Ramos, A. Guerrero-Ruiz, Characterization of carbon nanotubes and carbon nanofibers prepared by catalytic decomposition of acetylene in a fluidized bed reactor. J. Catal. 215 (2003) 305.

[46] J. W. Snoeck, G. F. Froment, M. Fowles, Preparation of nickel nanoparticles and their catalytic activity in the cracking of methane. J. Catal. 169 (1997) 240.

[47] T. Wortmann, S. Fatikow, Carbon Nanotube Detection by Scanning Electron Microscopy MVA2009 IAPR Conference on Machine Vision Applications. May 20-22, (2009) Yokohama, JAPAN

[48] G. A. Rance, D. H. Marsha, R. J. Nicholas, N. Khlobystova Andrei, UV–vis absorption spectroscopy of carbon nanotubes: Relationship between the π-electron plasmon and nanotube diameter, Chemical Physics Letters 493 1–3 (2010) 19.

[49] S. Battiston, M. Minella, R. Gerbasi, F. Visentin, P. Guerriero, A. Leto, Growth of titanium dioxide nanopetals induced by single wall carbon nanohorns, Carbon 48 (2010) 2470.

[50] L.W. Zhang, H.B. Fu, Y.F. Zhu, Efficient TiO_2 Photocatalysts from Surface Hybridization of TiO2 Particles with Graphite-like Carbon, Adv. Funct. Materials 18 (2008) 2180.

[51] S. K. Yadav, S. R. Madeshwaran, J. W. Cho, Synthesis of a hybrid assembly composed of titanium dioxide nanoparticles and thin multi-walled carbon nanotubes using "click chemistry", J. of Coll. and Interface Science 358 (2011) 471.

[52] H. M. Heise, R. Kuckuk, A. K. Ojha, A. Srivastava, V. Srivastava, B. P. Asthana, Characterisation of carbonaceous materials using Raman spectroscopy: a comparison of carbon nanotube filters, single- and multi-walled nanotubes, graphitised porous carbon and graphite, Journal of Raman Spectroscopy 40 (2009) 344.

[53] D. S. Dhawale, R. R. Salunkhe, U. M. Patil, K. V. Gurav, A. M. More, C. D. Lokhande, . Room temperature liquefied petroleum gas (LPG) sensor based on p-polyaniline/n-TiO_2 heterojunction, Sens. Actuators B 134 (2008) 988.

[54] L. A. Patil, D. N. Suryawanshi, I. G. Pathan, D. M. Patil, Nickel doped spray pyrolyzed nanostructured TiO_2 thin films for LPG gas sensing, Sens. Actuators B 176 (2013) 514.

[55] R. D. Ladhe, K. V. Gurav, S. M. Pawar, J. H. Kim, B. R. Sankapal, p-PEDOT:PSS as a heterojunction partner with n-ZnO for detection of LPG at room temperature. J. Alloys Compd. 515, (2012) 80.

[56] R. K. Sonker, A. Sharma, Md.. Shahabuddin, M. Tomar, V. Gupta, Low Temperature Sensing Of NO_2 Gas Using SnO_2-ZnO Nanocomposite Sensor, Adv. Mat. Lett. 4, (2013) 196.

[57] R. K. Sonker, S. R. Sabhajeet, S. Singh, B. C. Yadav, . Low temperature sensing of NO_2 gas using SnO_2-ZnO nanocomposite sensor. Mater. Lett. 152, (2015) 189.

[58] Y. L. Liu, H. F. Yang, Y. Yang, Z. M. Liu, G. L. Shen, R. Q. Yu, Thin Solid Films 497, (2006) 355.

[59] H. Xu, X. Chen, J. Zhang, J. Wang, B. Cao, D. Cui, NO_2 gas sensing with SnO2–ZnO/PANI composite thick film fabricated from porous nanosolid. Sens. Actuators B 176, (2013) 166.

[60] U. Kumar, B. C. Yadav. Development of humidity sensor using modified curved MWCNT based thin film with DFT calculations, Sens. Actuators B Chemical, 288 (2019) 399-407.

[61] U. Kumar, B. C. Yadav. Synthesis of carbon nanotubes by direct liquid injection chemical vapor deposition method and its relevance for developing an ultra-sensitive room temperature based CO_2 sensor, J. of Taiw. Institute of Chem. Engineering 96 (2019) 652.

[62] W. P. Chen, Z. G. Zhao, X. W. Liu, Z. X. Zhang, C.G. Suo, A capacitive humidity sensor based on multi-wall carbon nanotubes (MWCNTs), Sensors 9 (2009) 7431.

[63] A. Tripathy, S. Pramanik, A. Manna, S. Bhuyan, N. F. A. Shah, Z. Radzi, N. A. A. Osman, Design and development for capacitive humidity sensor applications of lead-free Ca,Mg,Fe,Ti-oxides-based electro-ceramics with improved sensing properties via physisorption, Sensors 16 (2016) 1135.

[64] P. Koskinen, V. Makinen, Density-functional tight-binding for beginners Comput. Mater. Sci. 47 (2009) 237.

[65] J. C. Slater, G. F. Koster, Simplified LCAO method for the periodic potential problem, Phys. Rev. 94 (1954) 1498.

[66] M. Elstner, D. Porezag, G. Jungnickel, J. Elsner, M. Haugk, T. Frauenheim, A selfconsistent- charge density-functional tight-binding method for simulations of complex materials properties, Phys. Rev. B 58 (1998) 7260.

[67] T.A. Niehaus, M. Elstner, T. Frauenheim, S. Suhai, Application of an approximate density-functional method to sulfur-containing compounds, J. Mol. Struct. Theochem. 541 (2001) 185–202.

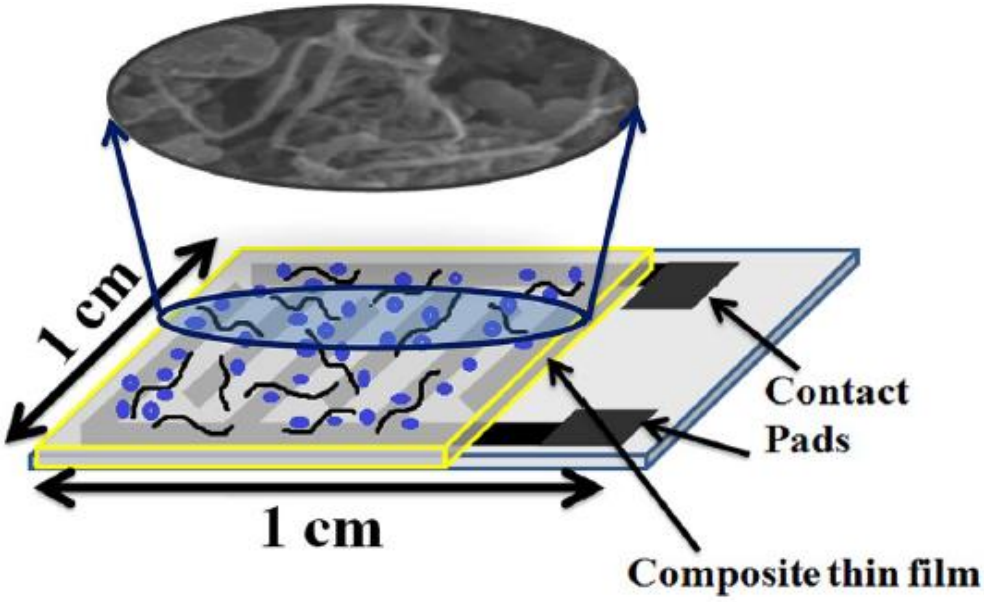

Fig. 6.1 Pt IDEs for sensor structure

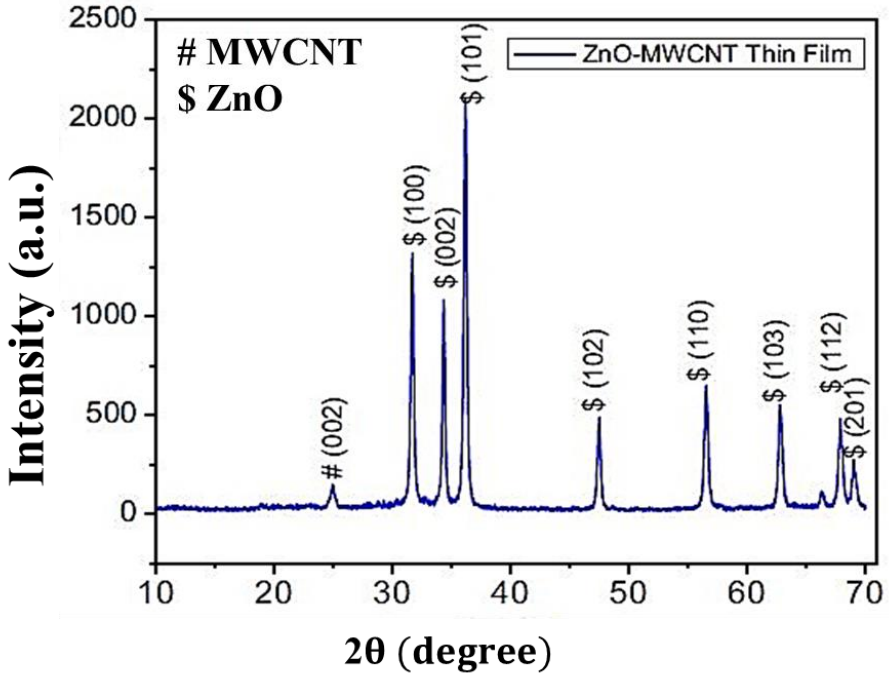

Fig. 6.2 XRD pattern of ZnO-MWCNT composite thin film

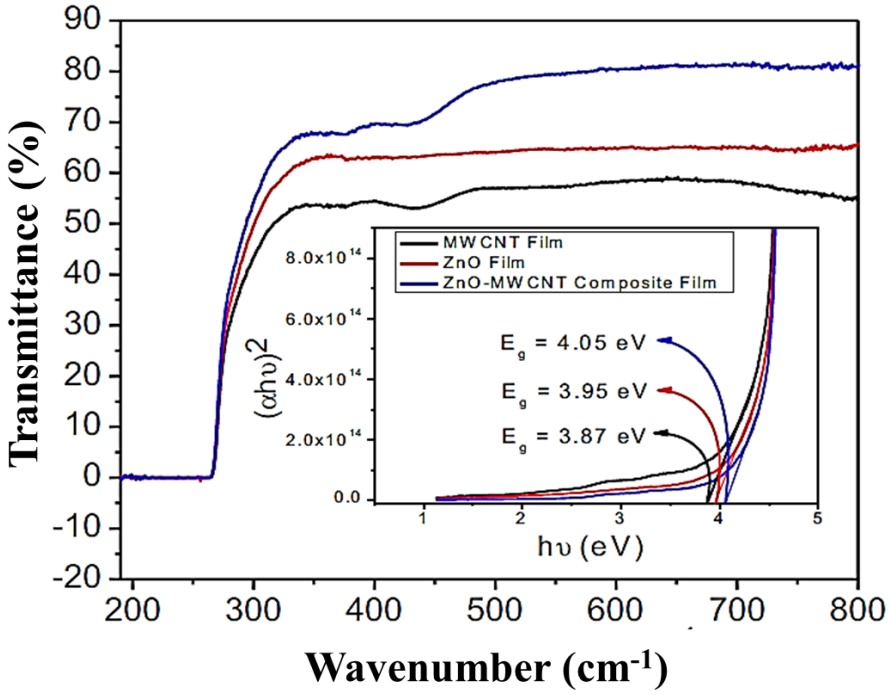

Fig. 6.3 UV–Visible transmittance spectra of MWCNT, ZnO and ZnOMWCNT composite thin films and the inset shows the Tauc plot of $(\alpha h\nu)^2$ versus photon energy ($h\nu$) in eV

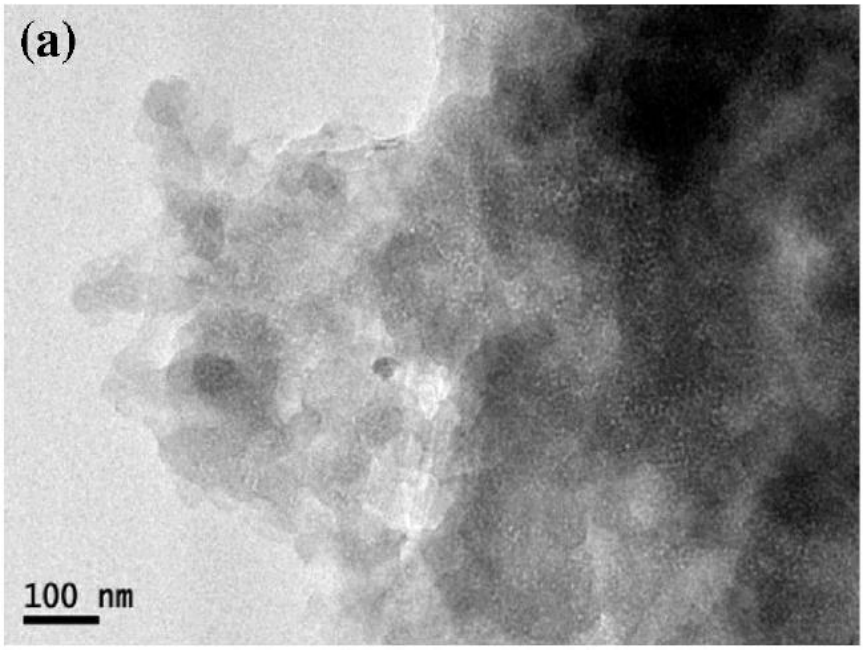

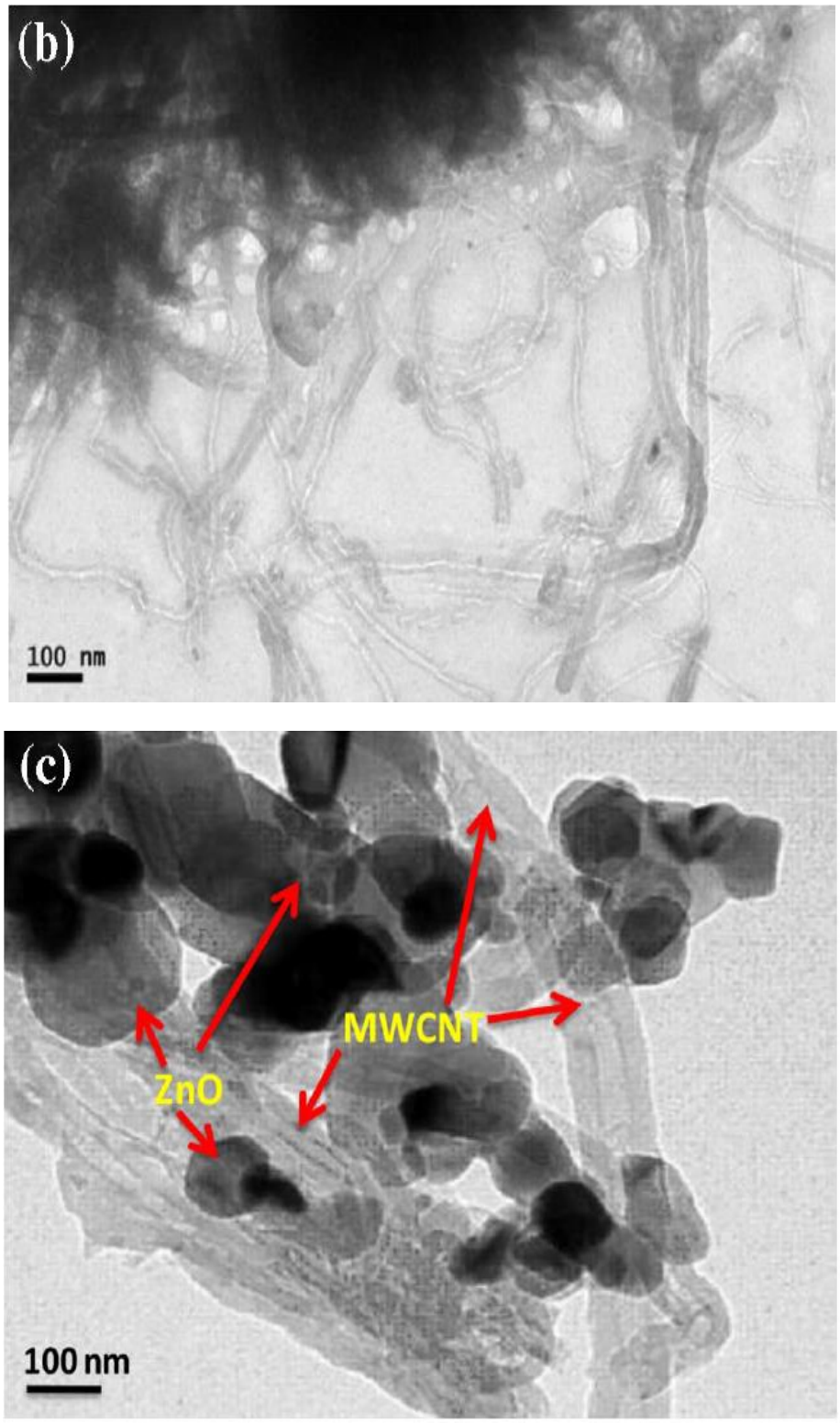

Fig. 6.4 TEM image of a) pure ZnO, b) pure MWCNT and c) ZnO-MWCNT composite

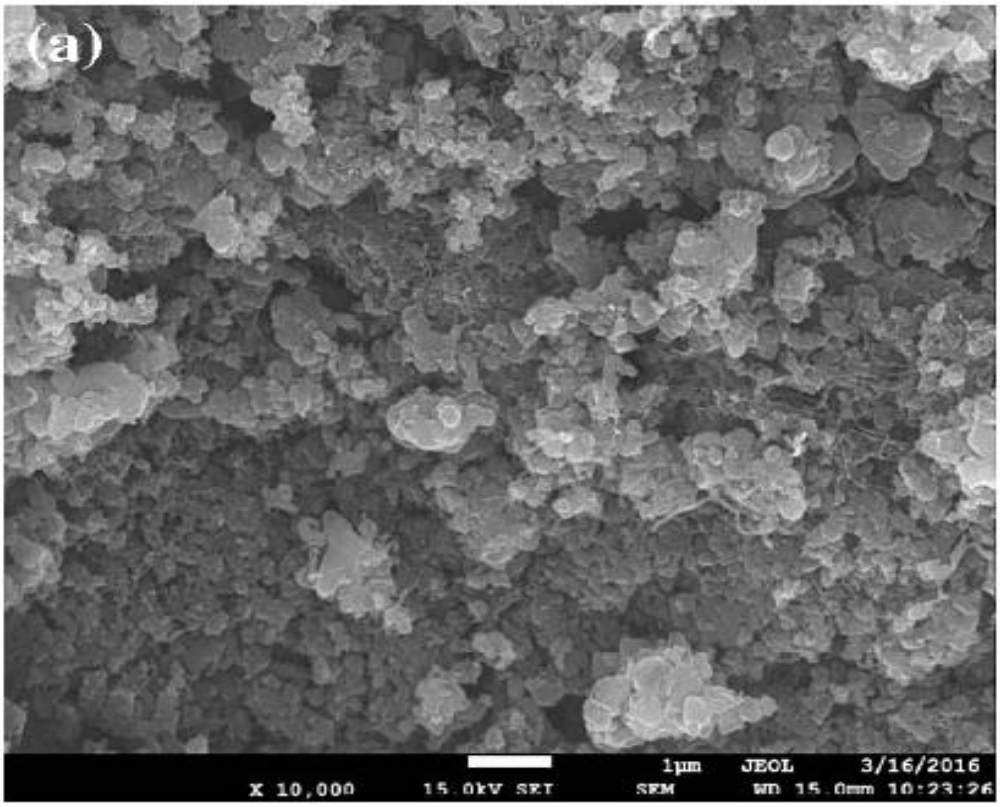
(a)
1μm JEOL 3/16/2016
X 10,000 15.0kV SEI SEM WD 15.0mm 10:23:26

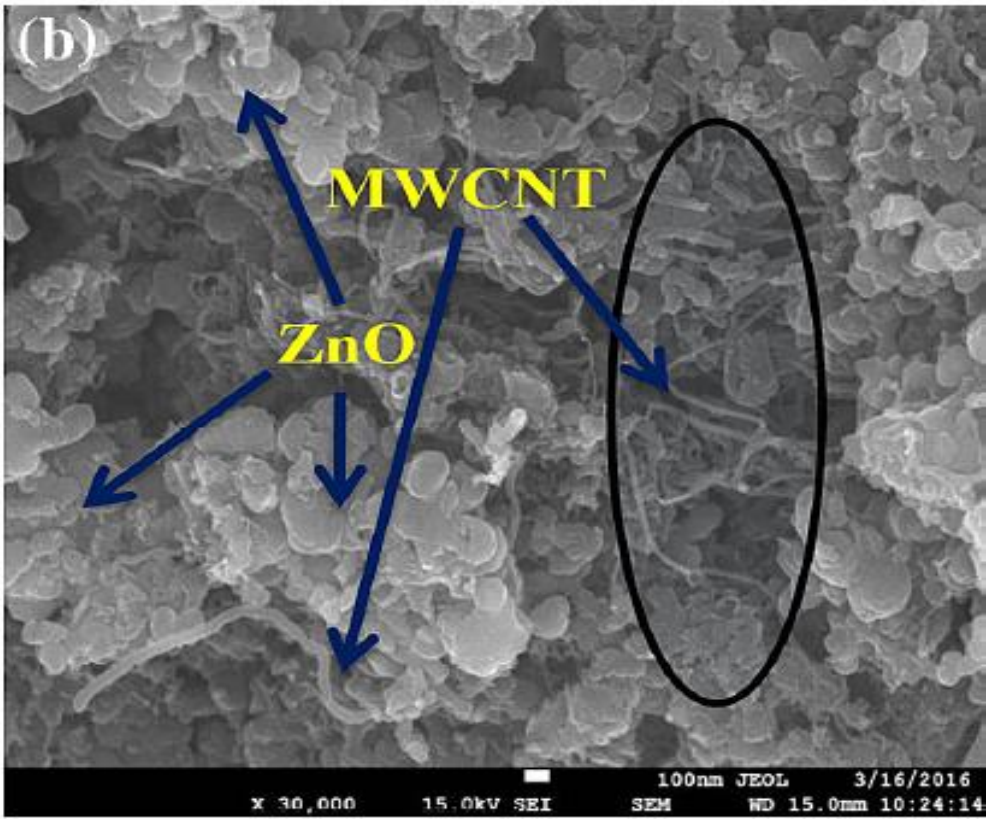
(b)
MWCNT
ZnO
100nm JEOL 3/16/2016
X 30,000 15.0kV SEI SEM WD 15.0mm 10:24:14

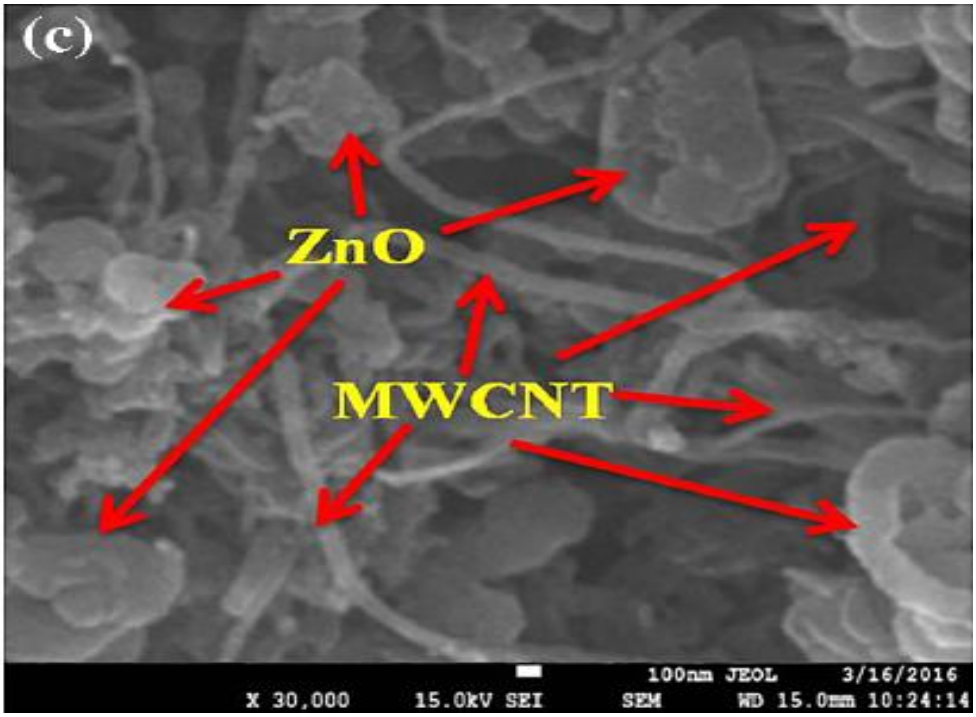

Fig. 6.5 SEM image of ZnOMWCNT nanocomposite thin film (a) 1 µm (b,c) 100 nm scale

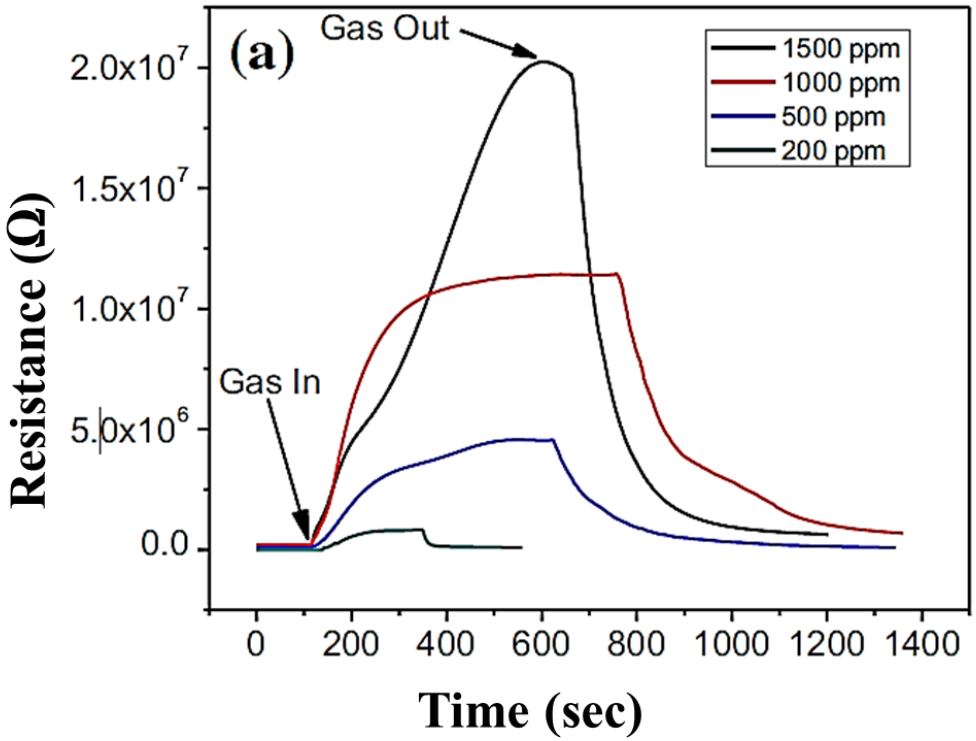

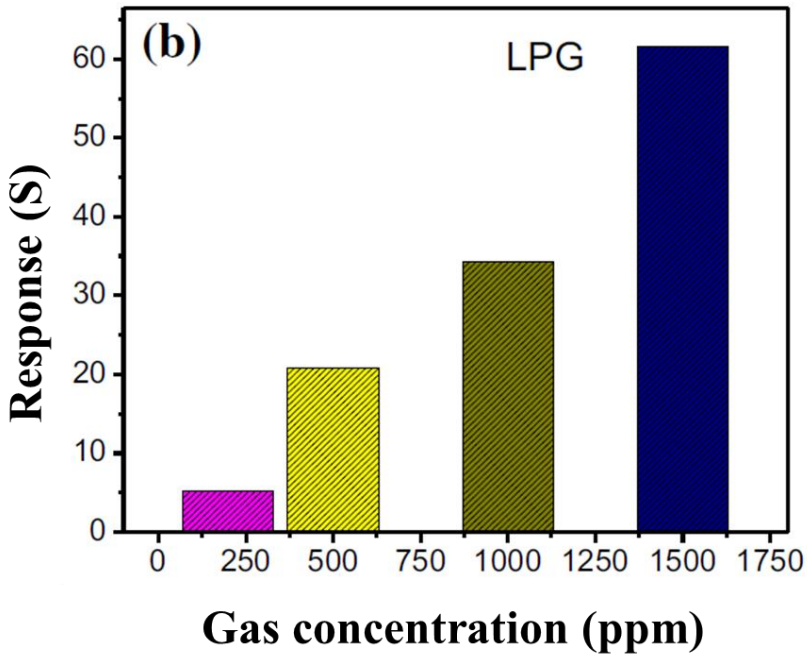

Fig. 6.6 (a) Variation of resistance w.r.t. gas concentration (b) Response vs gas concentration

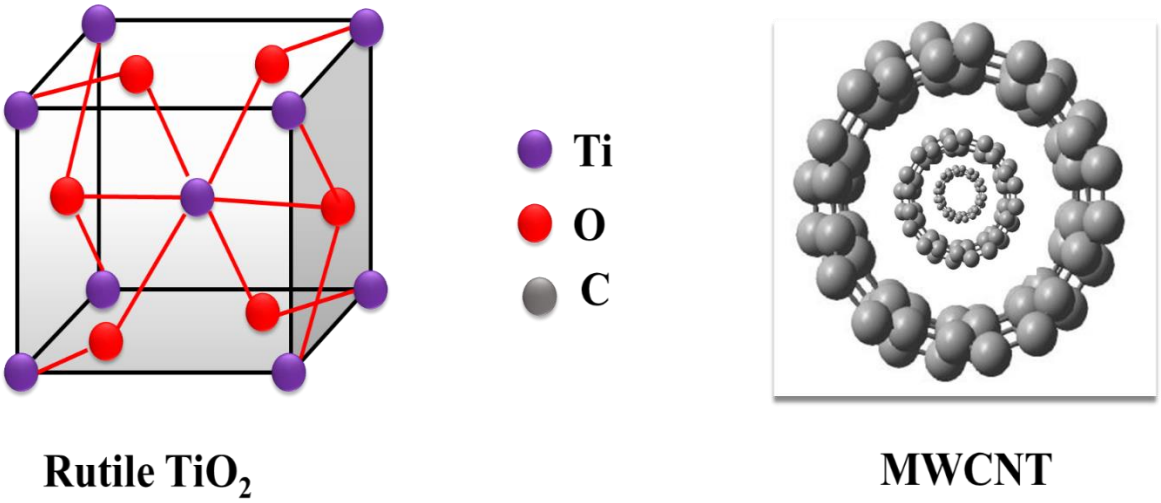

Fig. 6.7 Chemical structure of rutile TiO_2 and MWCNT

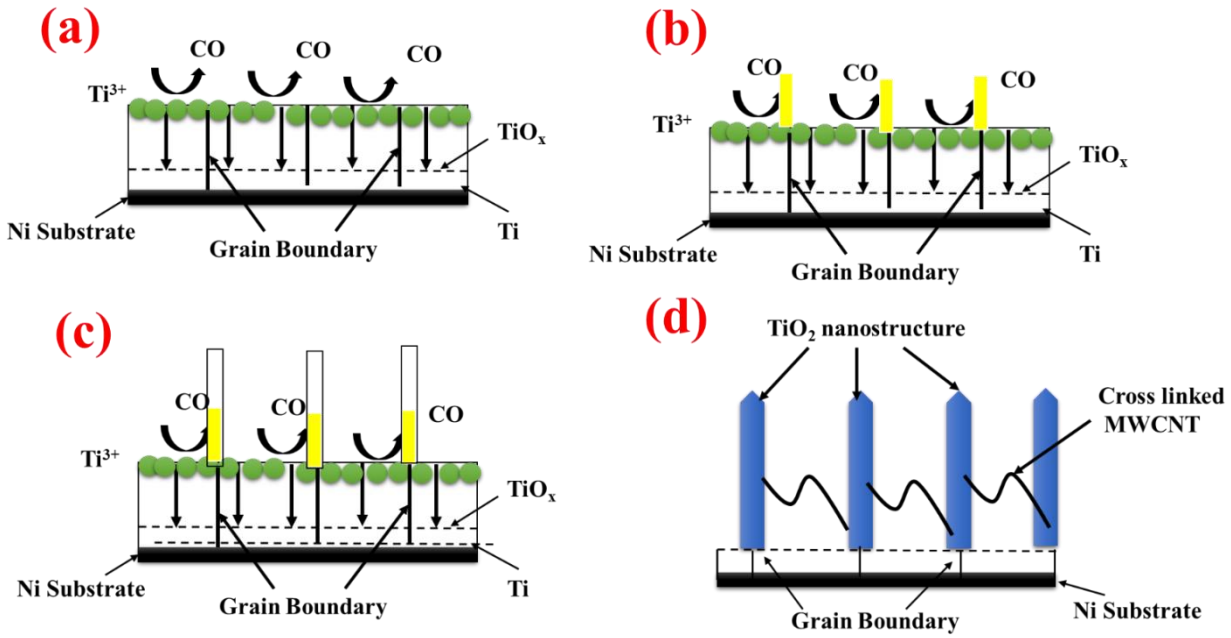

Fig. 6.8 Growth of MWCNT/TiO_2 inside the CVD chamber (a) formation of grain boundry (b) deposition of precursor (c) growth of nanotube (d) TiO_2 nanostructure with crosslinked MWCNT

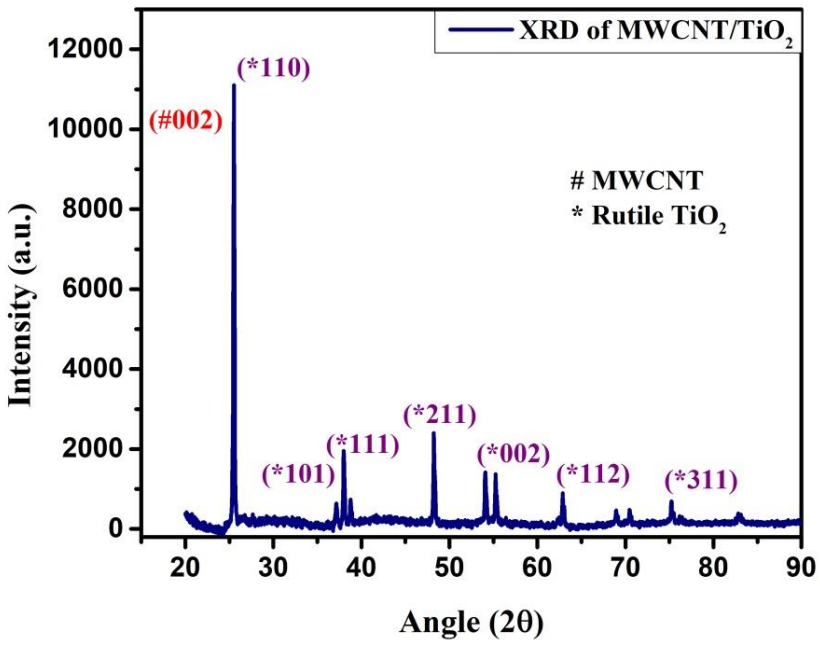

Fig. 6.9 XRD pattern of MWCNT/TiO_2 based thin film

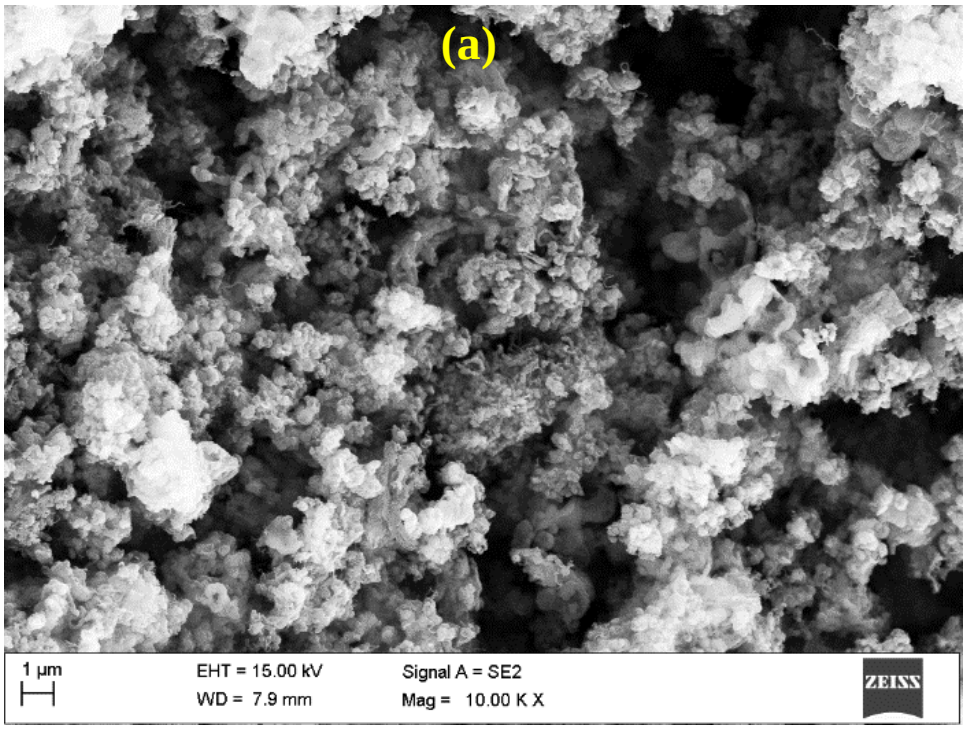
(a)
1 µm
EHT = 15.00 kV
WD = 7.9 mm
Signal A = SE2
Mag = 10.00 K X
ZEISS

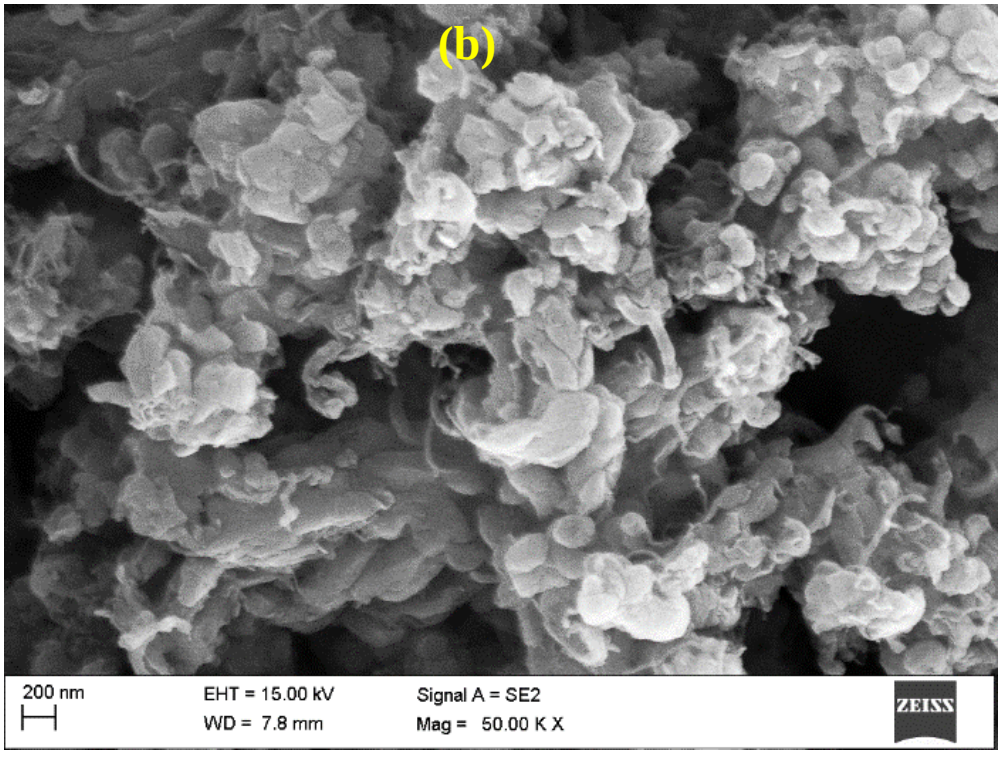
(b)
200 nm
EHT = 15.00 kV
WD = 7.8 mm
Signal A = SE2
Mag = 50.00 K X
ZEISS

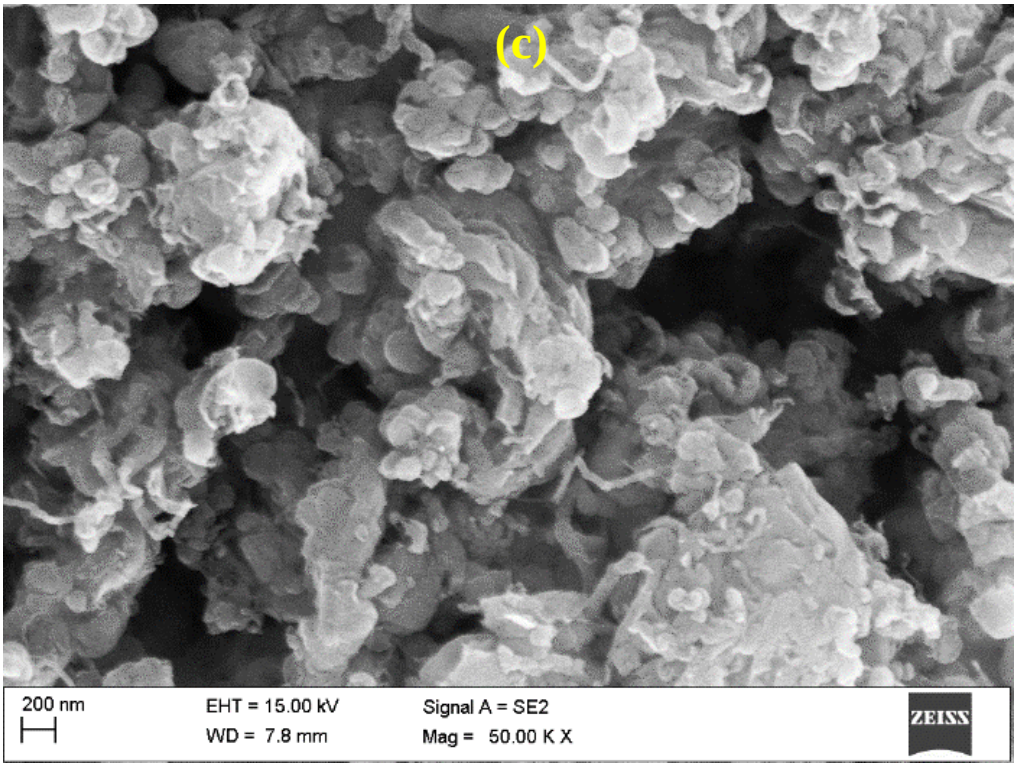

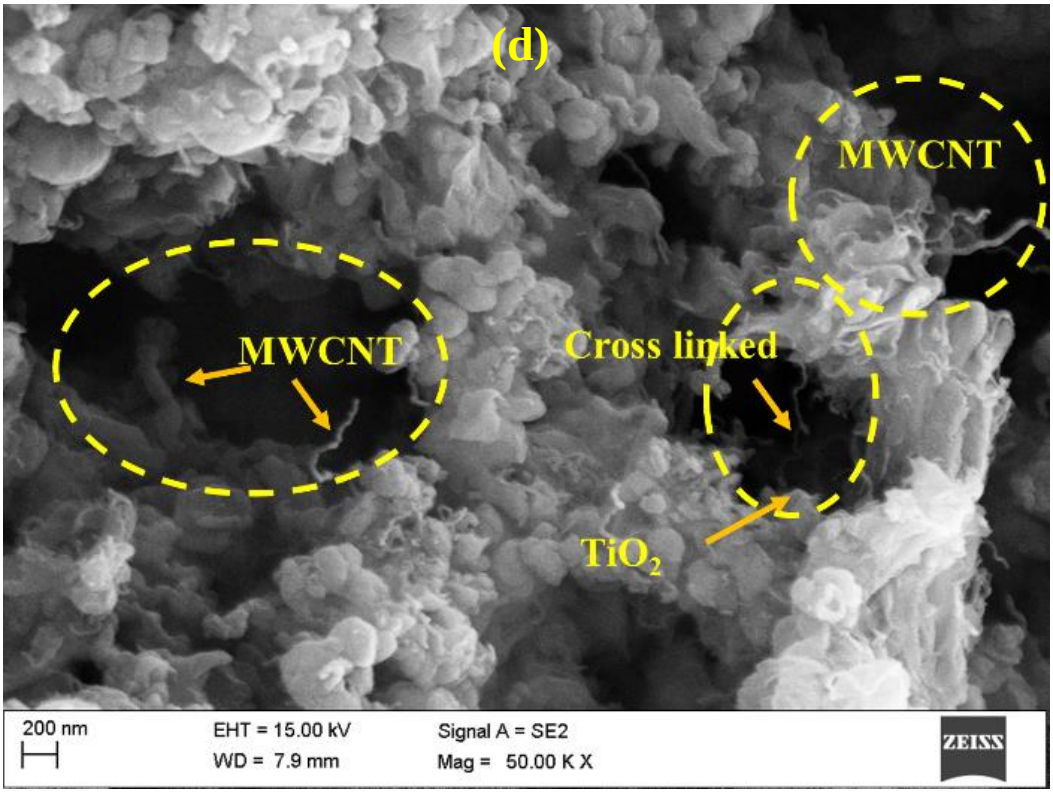

Fig. 6.10 SEM micrograph of MWCNT/TiO_2 at (a) 1 µm (b-d) 200 nm scale

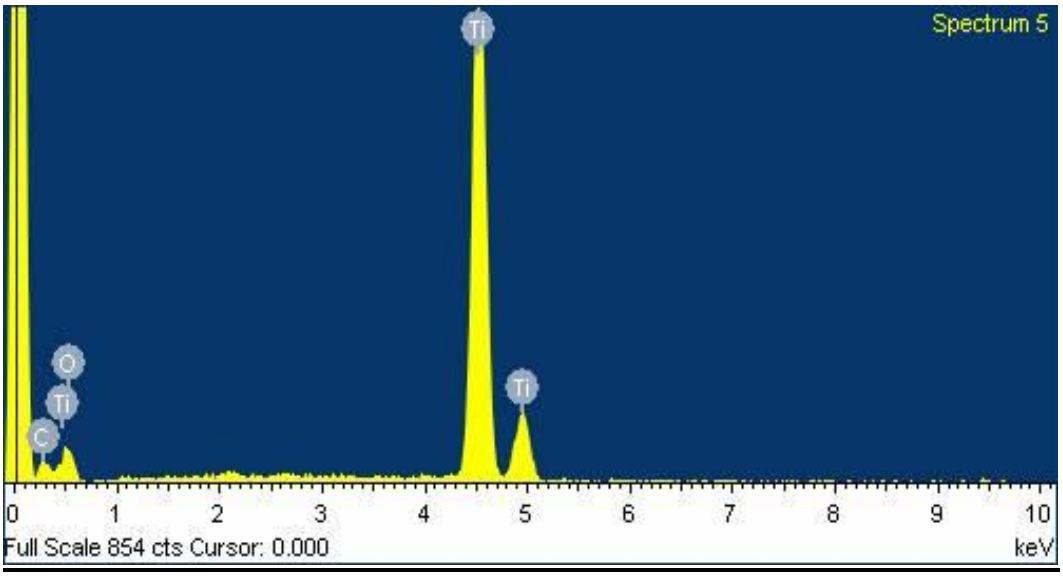

Fig. 6.11 EDX analysis of MWCNT/TiO_2 sample

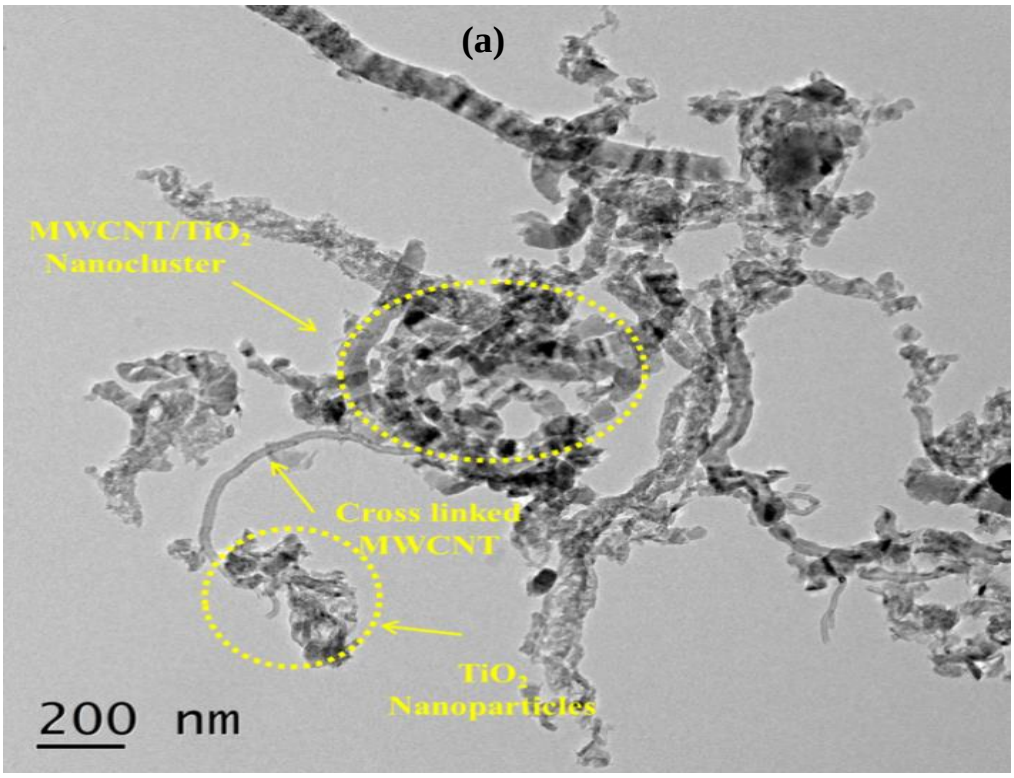

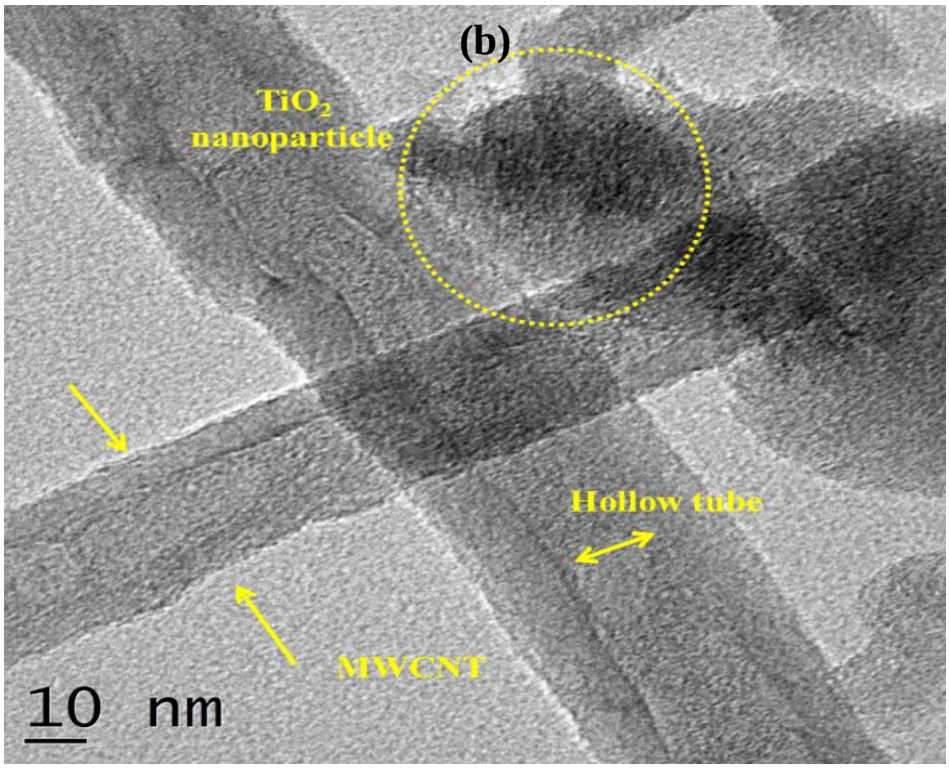

Fig. 6.12 TEM image of MWCNT/TiO_2 nanocomposite (a) 200 nm (b) 10 nm scale

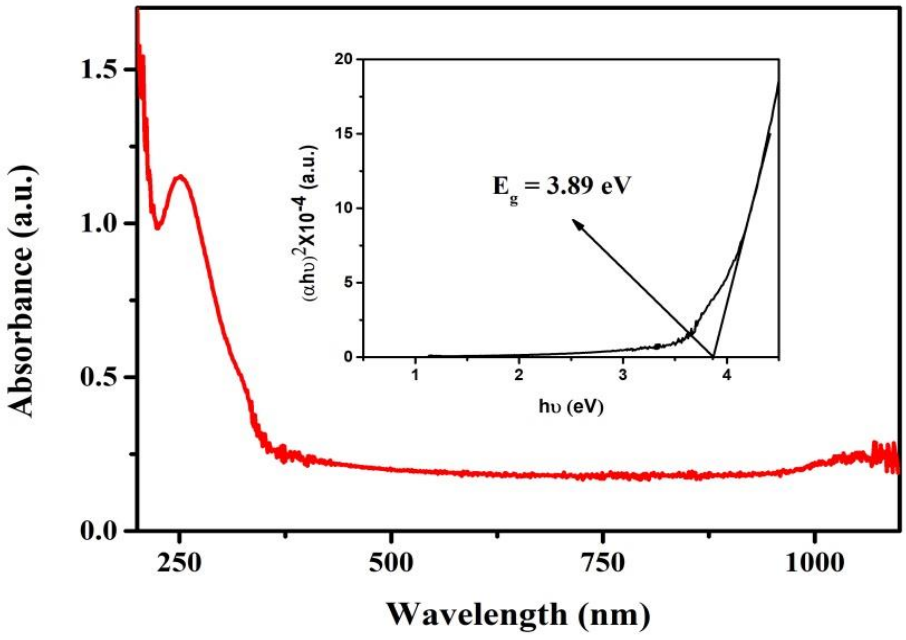

Fig. 6.13 UV-vis analysis of MWCNT/TiO_2 nanocomposite

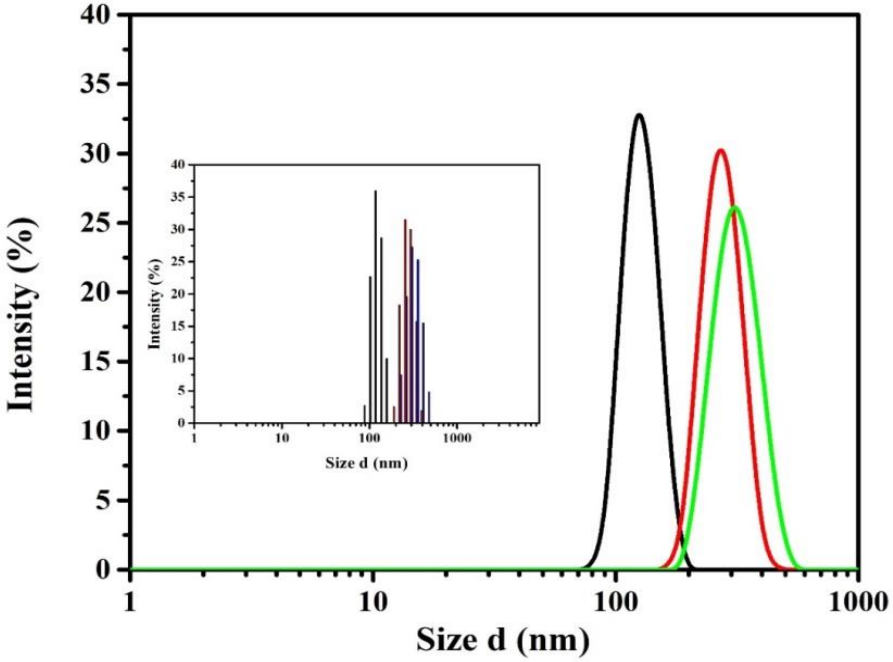

Fig. 6.14 Intensity Vs Size for Particle Size Analysis

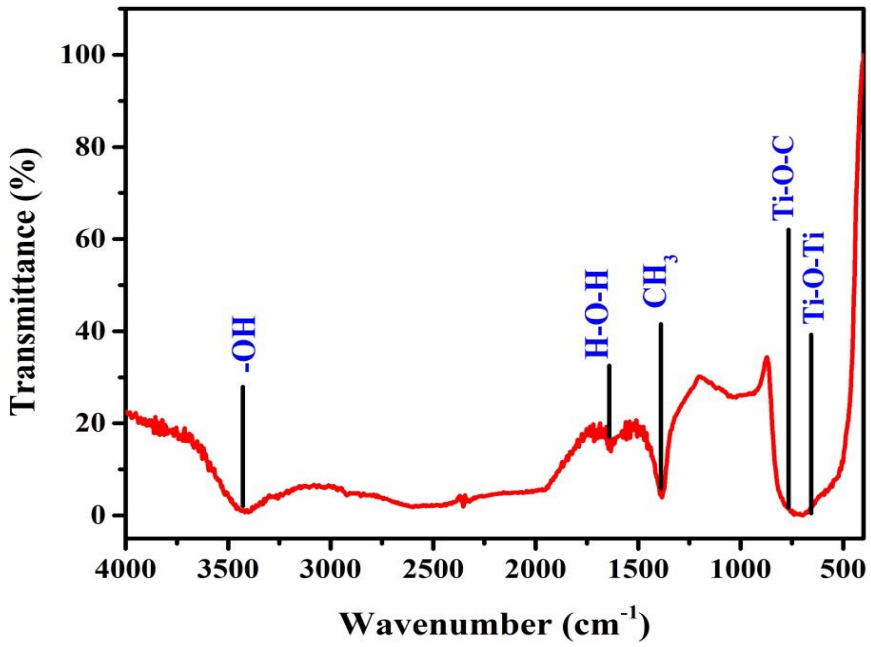

Fig. 6.15 FTIR analysis of MWCNT/TiO_2

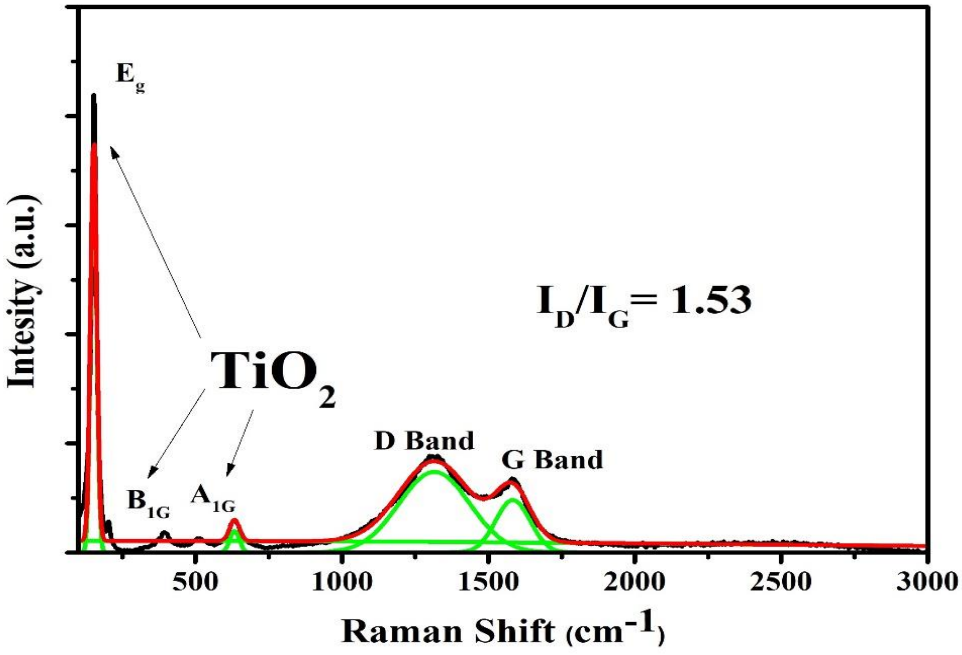

Fig. 6.16 Raman analysis of MWCNT/TiO_2 nanocomposite

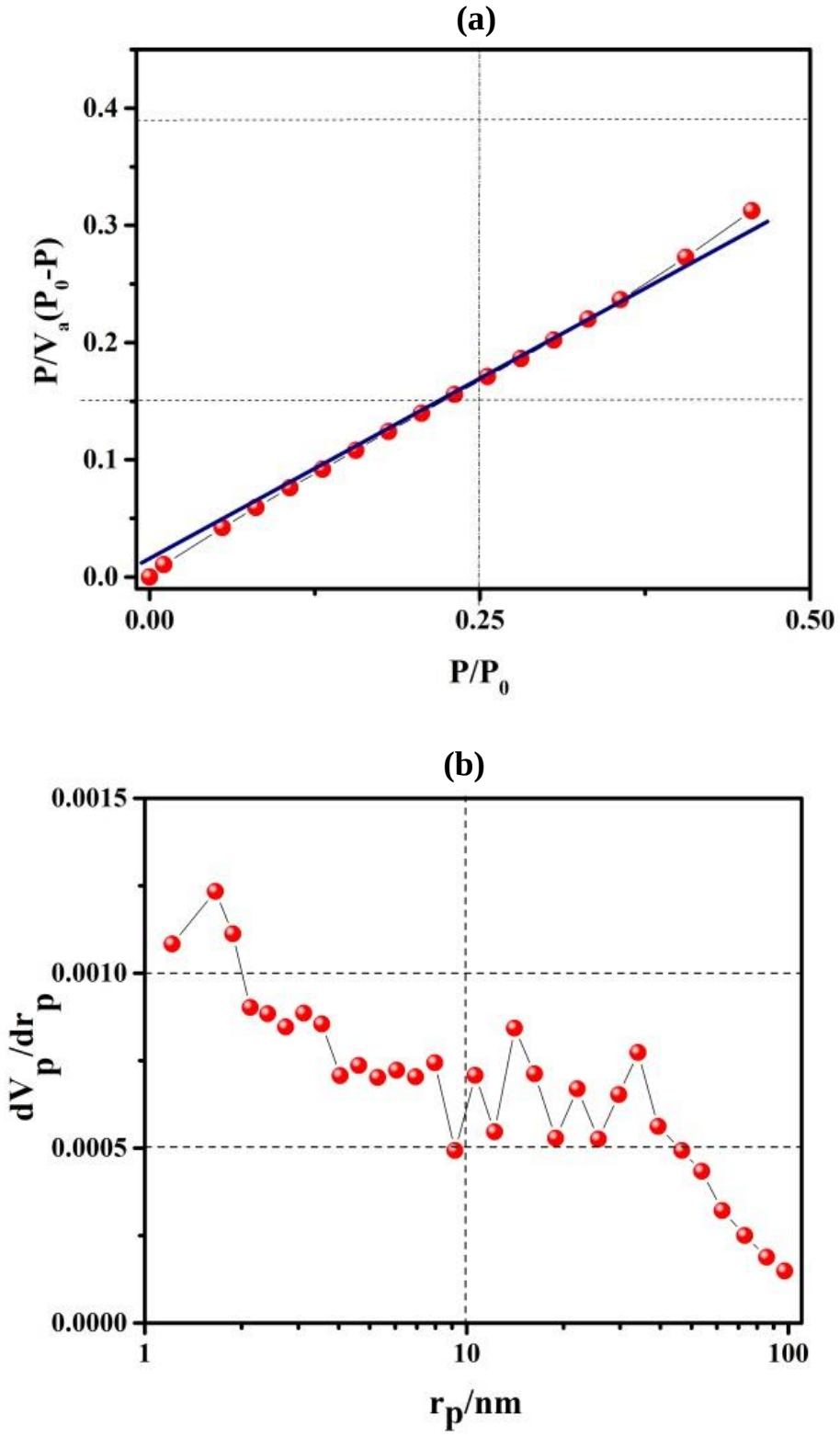

Fig. 6.17 BET and BJT analysis of MWCNT/TiO_2

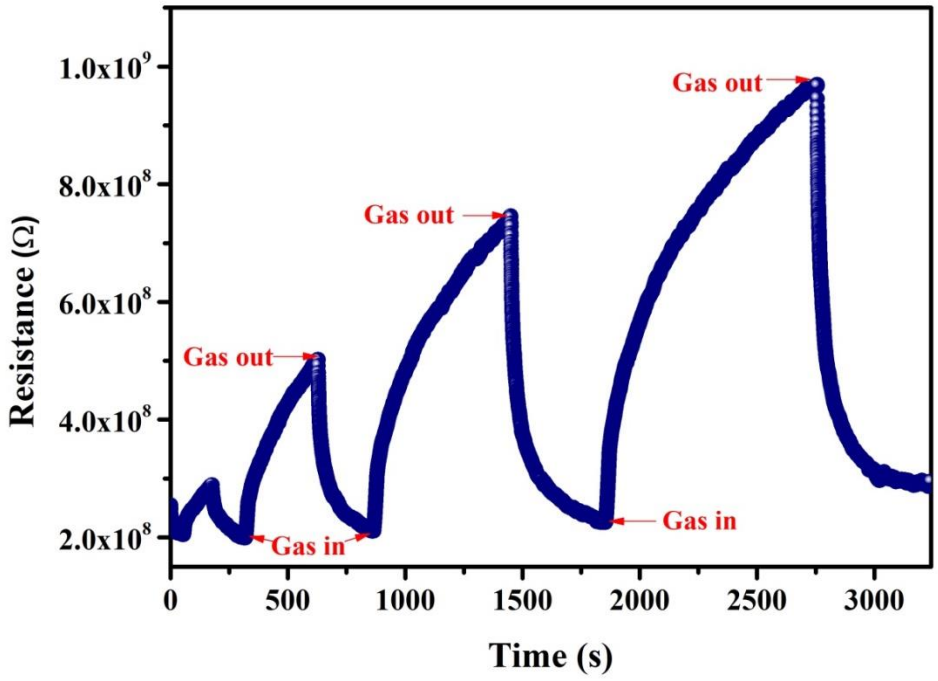

Fig. 6.18 Variations in the resistance of MWCNT/TiO_2 based thin film with exposure time for different vol% of LPG

(a)

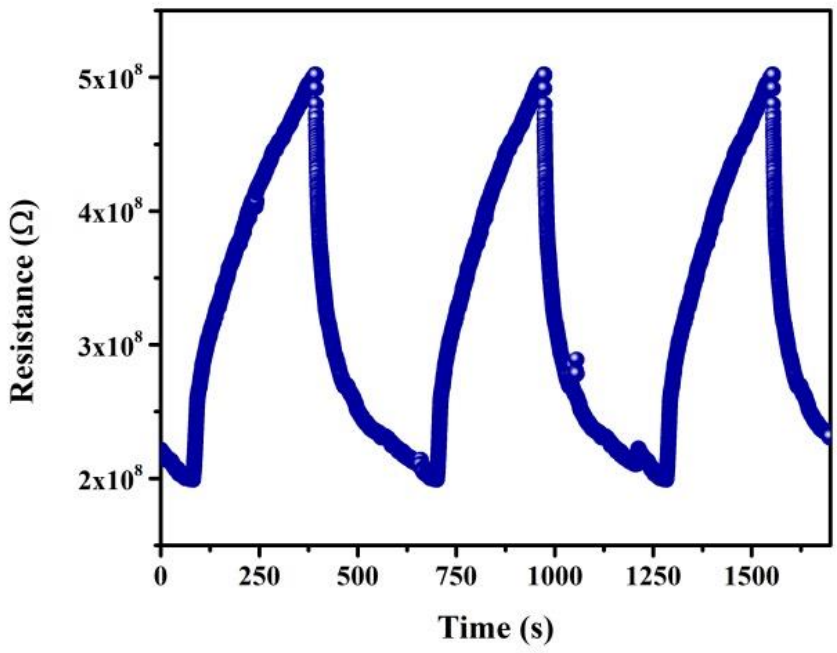

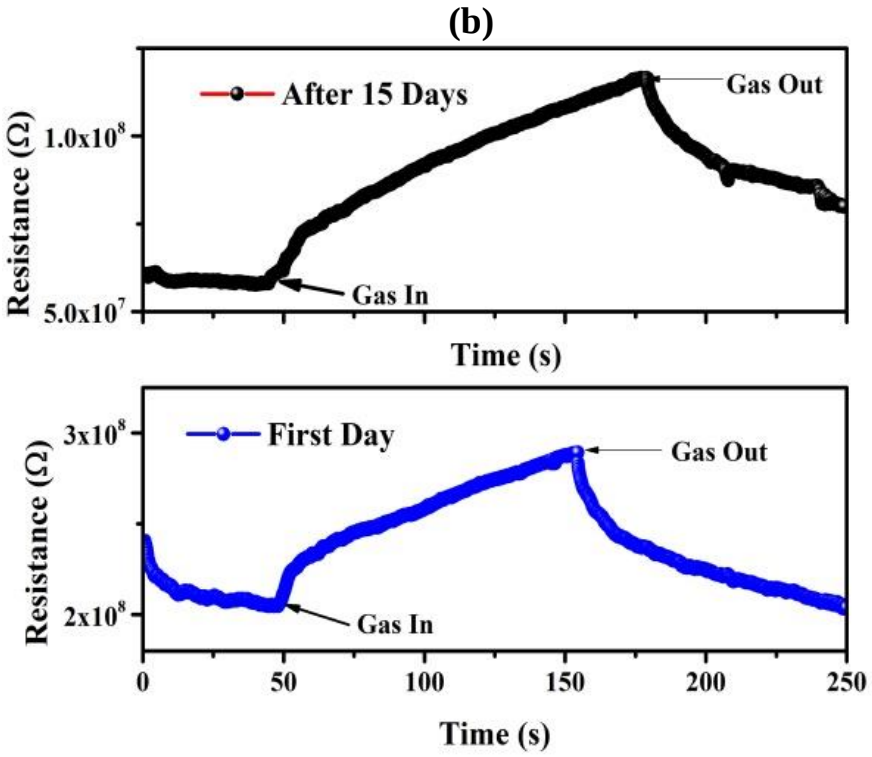

Fig. 6.19 (a) Reproducibility of the sensor at 0.5 vol.% of LPG (b) Repeatability of the curve after 15 days at 0.5 vol.% of LPG

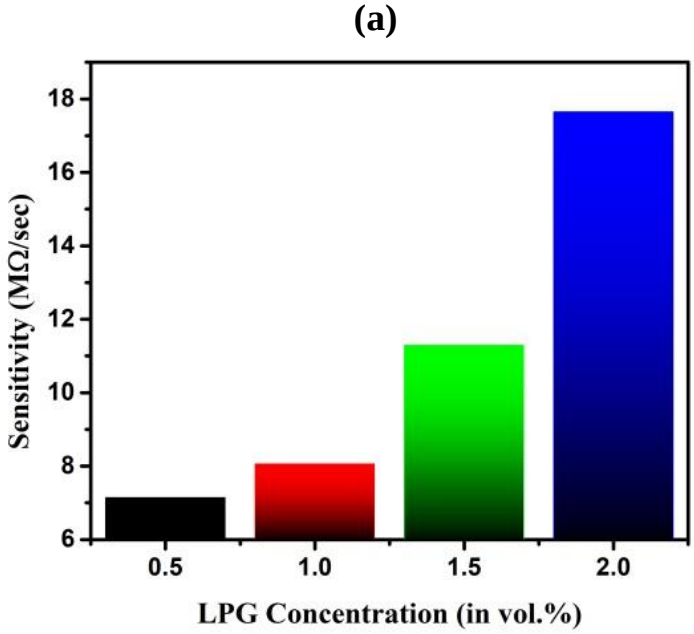

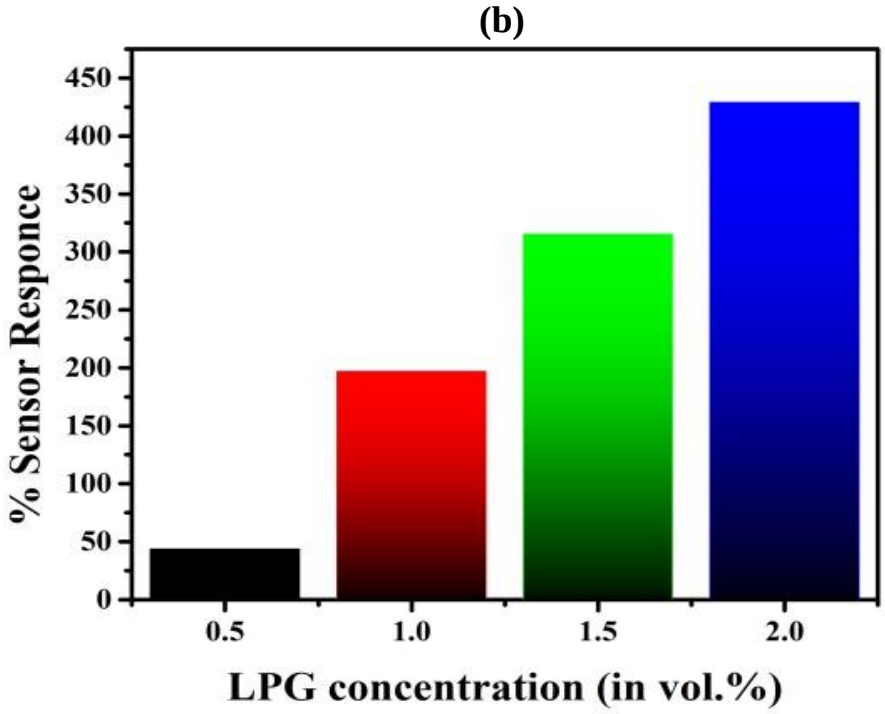

Fig. 6.20 (a) Sensitivity vs LPG concentration (b) % Sensor response vs LPG concentration

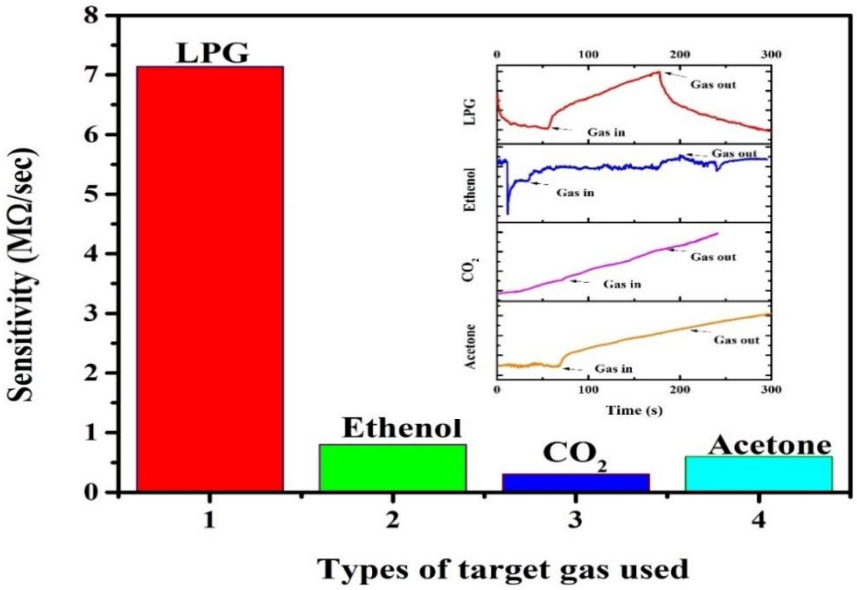

Fig. 6.21 Selectivity of MWCNT/TiO_2 based thin film as LPG sensor

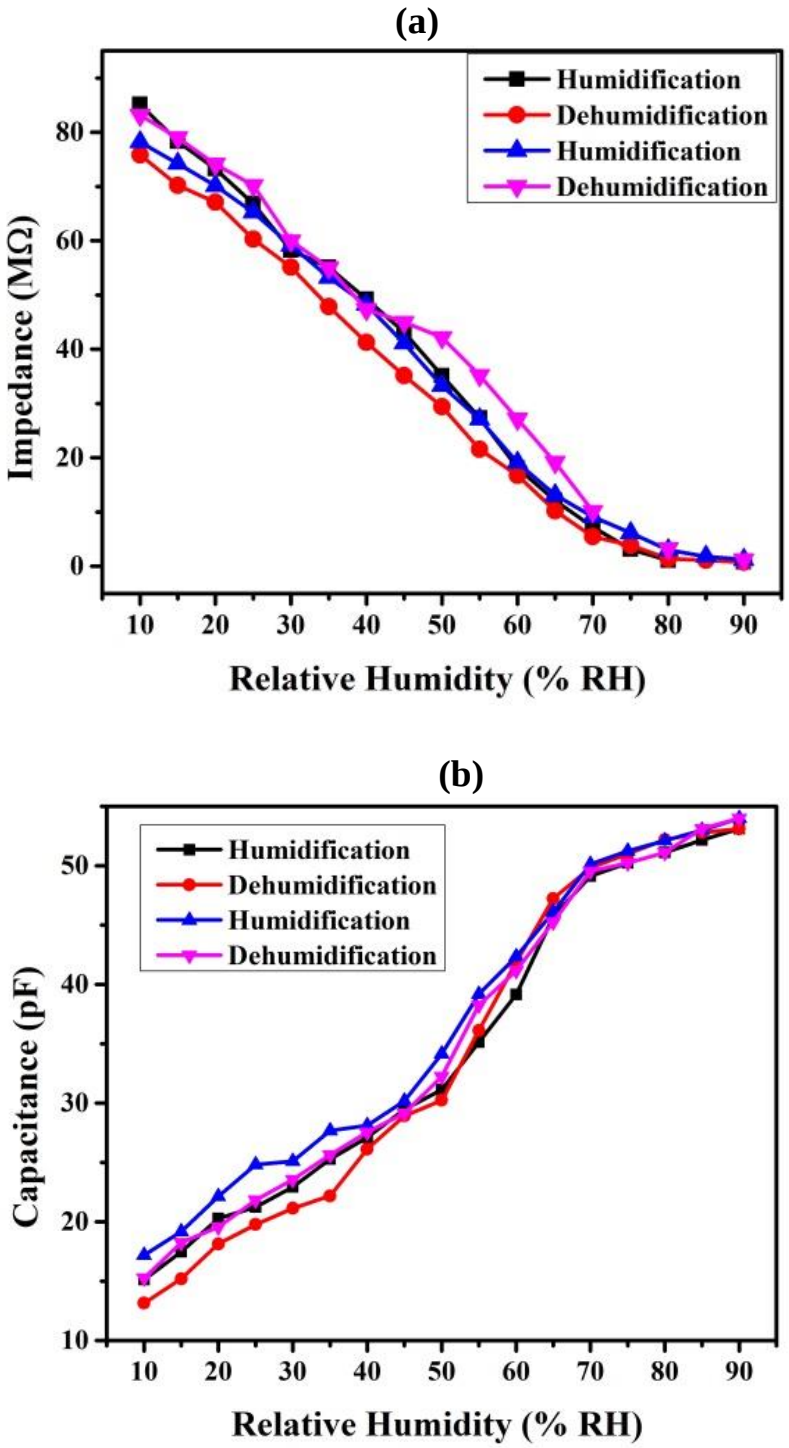

Fig. 6.22 Humidity sensing curve of CVD synthesized MWCNT/TiO_2 nanocomposite

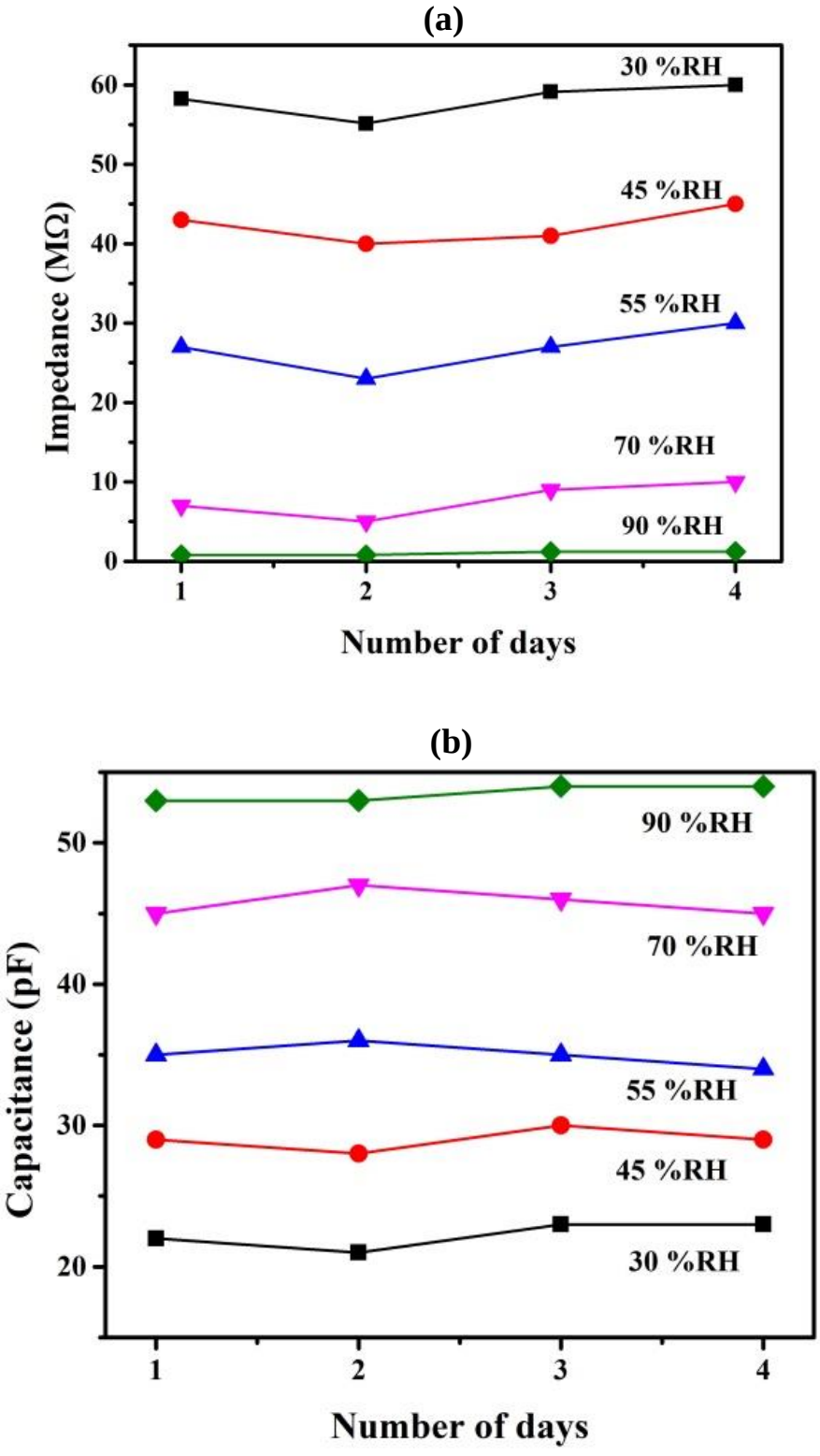

Fig. 6.23 Reproducibility of the film after a fixed interval of time

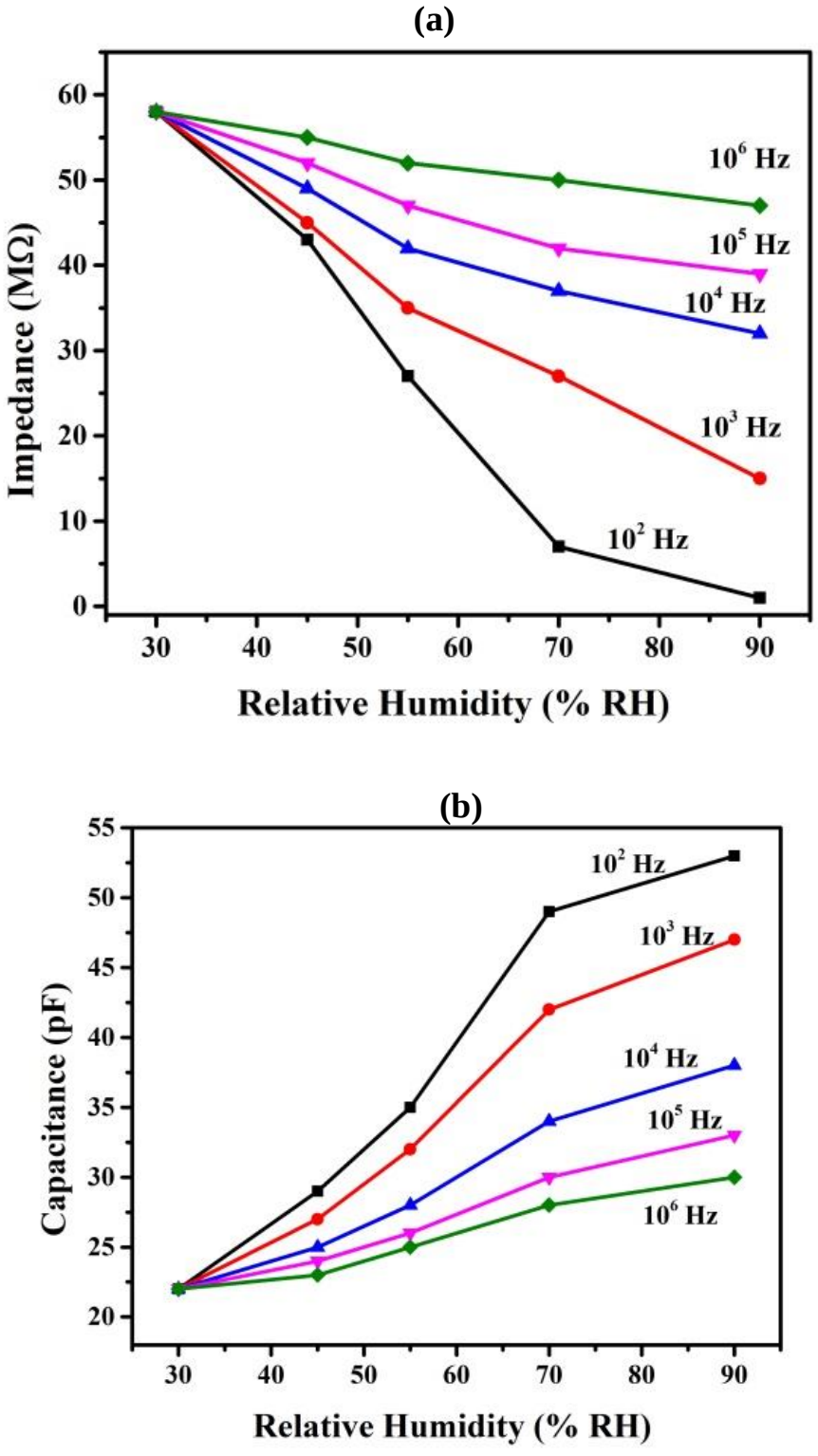

Fig. 6.24 (a) Variation of impedance (MΩ) with %RH at different testing frequencies (b) variation of capacitance (pF) with %RH at different testing frequencies

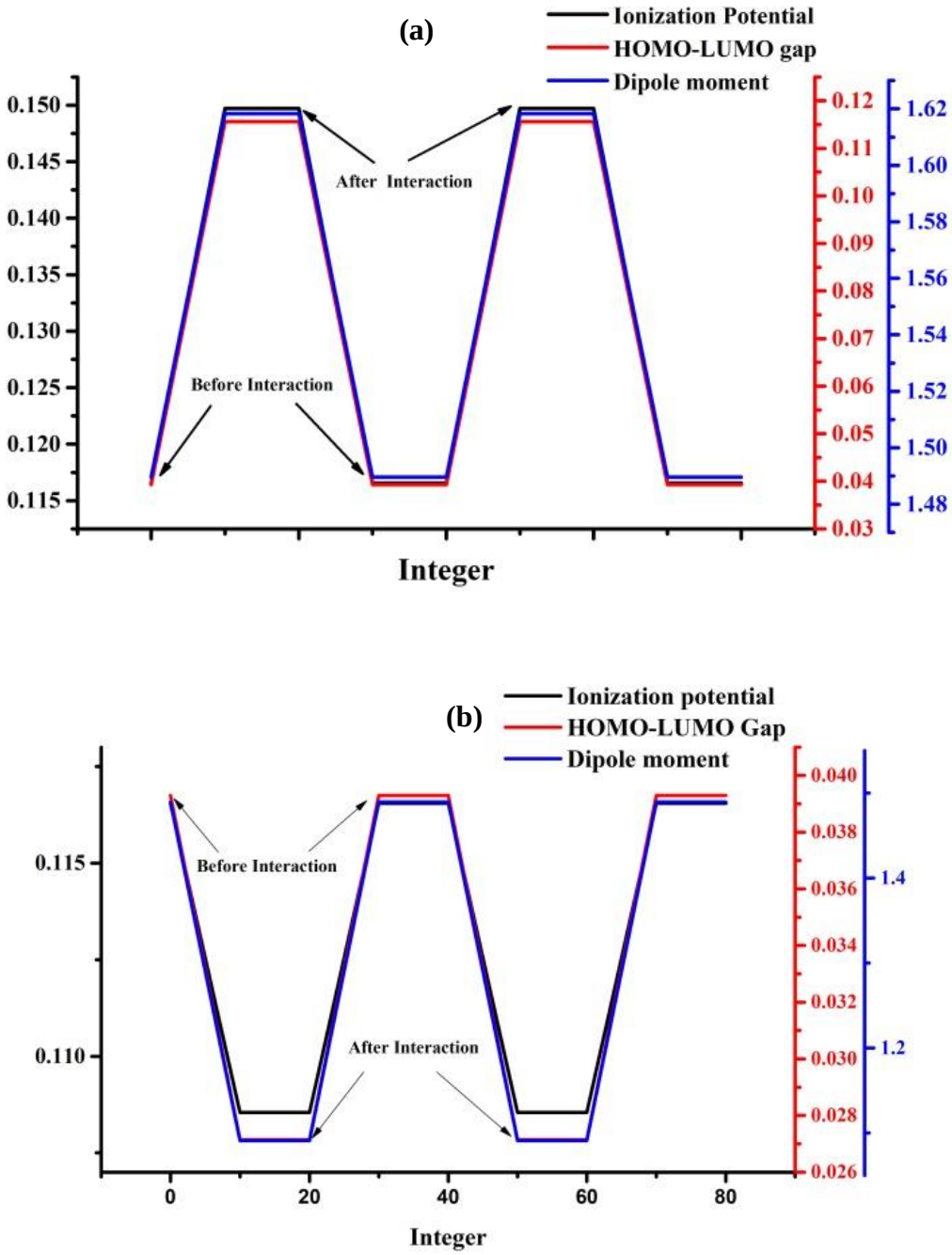

Fig. 6.25 (a) Increment in the IP, HOMO-LUMO gap and dipole moment of CNT/TiO_2 after interaction with C_nH_{2n+2} (b) Decrement in IP, HOMO-LUMO gap and dipole moment of CNT/TiO_2 after interaction with OH^-

Table 6.1 Theoretical study on the variation of the different parameter of CNT/TiO_2 before and after interaction with LPG and humidity

Theoretical parameters	**Before Interaction**	**After Interaction with LPG (C_nH_{2n+2})**	**After interaction with humidity (OH^-)**
Ionization Potential (IP)	0.11655	0.14972	0.10855
Electron Affinity (EA)	0.07718	0.03656	0.08141
HOMO-LUMO band gap (eV)	0.03930	0.1156	0.02714
Dipole moment (Debye)	1.4896	1.6183	1.0913
Electronegativity (eV)	0.09687	0.09011	0.09498
Hardness (η)	0.01968	0.05781	0.01357
Softness (s)	50.813	17.298	73.69
Nucleophillicity index	-0.02367	-0.07021	-0.3323

CHAPTER 7

CONCLUDING REMARKS AND SCOPE OF FURTHER RESEARCH

A study of synthesis, characterization and sensing properties of carbon nanostructure and its nanocomposites is summarized in the present chapter. This chapter also gives the guidelines for further research work in the field of carbon nanostructure and its nanocomposite films as efficient humidity, gas and photosensor.

7.1 Conclusion

Nanoscale materials are the materials having nanometer dimension and the scientific study of these materials, therefore, refers to the materials with sub-nanometer dimension and the scientific study of these objects are known as Nanoscience. It deals with the novel phenomenon of preparing, measuring its property and manipulating the dimension of an object up to the order of nanometer scale. Nanotechnology deals with using nanomaterials to develop products for practical application and for miniaturization of electronic devices. The maximum number of atoms lies on the surface of the nanoparticle which possesses huge surface energy and causes unstable or metastable stage. So there is a change in its chemical, mechanical, and optical properties resulting in the increase in the surface area per unit mass. This increased surface area made the nanomaterial for versatile application in the electronic and technical industry

Carbon nanomaterials like carbon nanotube are one of the most important nanomaterials in the field of nanotechnology which have very extraordinary properties. In the field of sensors, they have played a much efficient role by providing an enhanced surface area or high aspect ratio. Carbon nanomaterials are among the most broadly discussed, researched and applied materials for synthetic nanomaterial. The structural diversity of these materials provides an array of unique electronic, magnetic and optical properties, which when combined with their robust chemistry and ease of manipulation, makes them an attractive candidate for sensor application. Furthermore, the gas sensing capability exhibited by many carbon nanomaterials has seen them used as in vivo gas sensors. Carbon nanotubes, Graphene and Carbon dots have come under intense scrutiny, as either discrete molecular like sensors, or as components which can be integrated into devices. Generally, the metal oxide-based sensors are used in sensing application but when these nanomaterials are doped with carbon nanomaterials then their sensing capability, response and recovery time is improved many times.

In view of above, Chapter 1 includes the introduction of different synthesis techniques used for the synthesis of carbon nanostructure and their sensing applications. The drawback of other synthesis technique over chemical vapour deposition also been discussed. The sensing principle and extensive survey of literature on the development of

carbon-based gas, humidity and photosensor and its present status have been discussed. The orientation of work, aims and objectives of the present research investigation are well described at the end of the Chapter. It also deals with the description of synthesis and characterization techniques used in the present research work. Chapter 2 describes the synthesis of carbon nanotubes using direct liquid injection chemical vapour deposition technique and their application in field emission devices and in photosensors also been discussed. The photosensor fabricated by using MWCNT has response and recovery times of the order of millisecond which is very useful for the fabrication of photosensor. In Chapter 3, we have developed a humidity sensor using modified carbon nanotubes and the sensitivity of such sensors is very high in comparison with other metal oxide-based sensor. Further, the nanotubes synthesized by using DLICVD technique are functionalized and used for the detection of CO_2 level is summarized in Chapter 4. Chapter 5 describes the synthesis, characterization and CO_2 sensing properties of MWCNT/PPY nanocomposite. In this chapter, we enhanced the detection limit and sensitivity of the sensor. Chapter 6 reports the study of liquefied petroleum gas sensing properties of MWCNT/ZnO and MWCNT/TiO_2 prepared by the chemical vapour deposition method. Chapter 7 deals with the summary of the work done and the concluding remarks drawn from the present research work. Future scope for further research work in the field of carbon nanostructure and its nanocomposite films as efficient humidity, gas and photosensor have been depicted at the end of this Thesis. A study of synthesis, characterization and sensing properties of carbon nanostructure and its nanocomposites is summarized as below:

7.2 Synthesis of Multiwalled Carbon Nanotubes (MWCNT) by Direct Liquid Injection Chemical Vapor Deposition method and their applications as ultra-low turn on Field Emitter and Photosensor

The MWCNT was grown at different temperatures at 650 ℃ and 750 ℃. The monitoring of the evaporation temperature during the nanotube growth was used to explore the capacity of CNTs as field emitters, which results in the improved field enhancement factor (β) by 971. It was found that heat treatment affected the surface morphology of CNTs and its device structure may be used as a parameter for FE application. Also, it is concluded that improved FE properties are responsible for the

increased generation of electron emission sites. Such type of nanotubes is also used in photosensors and the highest sensitivity of the sensor has been found as 4.4μA/sec at 100 mW/cm^{-1}. The minimum response and recovery time has been found as 20 msec and 12 msec respectively at 25 mW/cm^{-1}.

7.3 Modification of Multiwall Carbon Nanotube using N-methyl pyrrolidone (NMP) and its application as humidity sensor with DFT interpretation

Multiwall Carbon Nanotubes (MWCNTs) were successfully synthesized via direct liquid injection chemical vapour deposition method and the minimum crystallite size or diameter of the nanotubes was found to be 7 nm. Surface morphology of thin film shows that most of the particles are cylindrical in shape leaving spaces as pores, and hence the film was found more sensitive. Maximum average sensitivities in terms of capacitance, impedance and inductance respectively were found as 18.8 pF/%RH, 1.67 MΩ/%RH and 2.21 mH/%RH at 10^2 Hz. The results were found reproducible with the reproducibility as 82% after two months. Thus this material carries a good scope for the development of sensitive moisture sensors in the range of relative humidity from 10 to 90 %RH for the indoor and outdoor applications. The experimental results were found very analogous to a predicted theory which is very unique.

7.4 Functionalization of MWCNT by HNO_3 & H_2SO_4 and its relevance for developing an ultra-sensitive CO_2 sensor working at room temperature

MWCNTs were grown on Co nanoparticles from ethanol by DLICVD method at a temperature of 750 ℃. Co nanoparticles were prepared by using the sol-gel method and the precipitate was annealed at 500 ℃ for stabilization. The prepared Co nanoparticle was stable and had a pure composition which exhibits the effective catalytic activity for CNT synthesis. The grown CNTs have a tubular structure, dense morphology and good crystallinity. After growth, the purification and functionalization were done by acid treatment. The sensor was fabricated using the spin coating of functionalized nanotubes on borosilicate glass substrates. CNT-based sensor yielded the maximum sensor response 2.1 at 5000 ppm with the comparatively fast response and recovery time as 30.21 sec and 49.62 sec respectively at room temperature. Improved sensing response characteristics of CNT-based sensor structure are attributed to the formation of the large surface area to

interact and conducting channels to the charge carriers at low temperatures. In the computational part, we found that the binding energy, dipole moment and HOMO-LUMO gap of CNTs are significantly changed on interacting with CO_2 molecules. Thus the CNT based sensor investigated here is ultra-sensitive towards the detection of CO_2 gas at room temperature, robust and cheap for commercialization.

7.5 Synthesis of MWCNT/PPY nanocomposite using oxidation polymerization method and its application as CO_2 and humidity sensor

Nanostructured MWCNT/PPY was successfully synthesized by chemical oxidation route. The morphological evolution and structural studies proved the nanocrystalline nature of the material. The crystallite size was found as 8.1 nm. The optical bandgap of the nanocomposite has been found as 3.92 eV. The surface morphology of the MWCNT/PPY exfibited the enveloped CNTs with polymer hence the sensitivity towards CO_2 and humidity enhanced. MWCNT/PPY composite sensor structure exhibited the maximum sensing response as 7.1 and sensitivity as 81.2 Ω/sec for 1000 ppm of CO_2 concentration towards at room temperature (30°C). This film was also used for the detection of humidity and maximum sensitivity was found as 41.33 kΩ/%RH. The sensor is quite sensitive and can be used for commercial production.

7.6 Development of MWCNT/ZnO and MWCNT/TiO_2 nanocomposite thin films for the detection of LPG and humidity at room temperature

Nanostructured ZnO/MWCNT was successfully synthesized by chemical route. The morphological evolution and structural studies proved the nanocrystalline nature of the material. The crystallite size was found at 28.43 nm. ZnO/MWCNT composite sensor structure exhibited the maximum sensing response as 61.57 for 1500 ppm of LPG concentration at room temperature (30°C). Nanostructured MWCNT/TiO_2 based thin film was successfully deposited using chemical vapour deposition technique. The process used for the preparation of thin-film is cheap and eco-friendly. XRD revealed that both the MWCNT and TiO_2 were grown simultaneously and minimum crystallite size was found as 40 nm. The SEM micrographs showed that the film is highly porous with cross-linked nanotubes. In FTIR spectra, the peaks between 600-1000 cm^{-1} show the

characteristic peak of MWCNT/TiO_2. The maximum sensitivity of the sensor was found as 17.65 MΩ/sec and % sensor response as 429 at 2 vol% of LPG. The thin film was also used for humidity sensing and the maximum sensitivity was found as 1.05 MΩ/%RH at 10^2 Hz. The linear characteristic of MWCNT/TiO_2 based LPG sensor is rather appropriate for emerging a commercial LPG and humidity sensor operable at room temperature. The experimental data were found analogous to a predicted theory which is unique.

The complete overview of the Thesis including the sensing materials, dopants, bandgap, sensitivity, crystallite size, average grain size, pore size is depicted in Table 7.1. The main target of our research work was to design and fabricate the different type of sensors using carbon nanomaterials which would be robust, cost-effective and more sensitive than previously reported sensors.

Table 7.1 A chapterwise sketch of the Thesis

Chapter	**Material**	**Method**	**Type of sensing**	**Sensitivity/Sensor response**	**Response time**	**Recovery time**
Chapter 1	**Introduction**					
Chapter 2	**MWCNT**	**DLICVD**	**Photosensor**	**4.4 µA/sec**	**34 m sec**	**38 m sec**
Chapter 3	**Modified MWCNT**	**DLICVD**	**Humidity**	**6.41 pF/%RH**	**24 sec**	**30 sec**
Chapter 4	F-MWCNT	DLICVD	CO_2	2.1	30.2 sec	49.6 sec
Chapter 5	**MWCNT/PPY**	**DLICVD/Oxidation polymerization**	**CO_2**	**7.2**	**30 sec**	**36 sec**

Chapter 6	MWCNT/ZnO	DLICVD/Chemical precipitation	LPG	3.8 MΩ/sec	475 sec	491 sec
	MWCNT/TiO_2	**DLICVD**	**LPG**	**4.2 MΩ/sec**	**36 sec**	**20 sec**
Chapter 7	**Conclusions**					

From the Table 7.1 we infer that the pure MWCNT, Modified MWCNT, CNT/PPY and MWCNT/TiO_2 excellent materials for photo-sensing, humidity sensing, CO_2 sensing and LPG sensing applications respectively and using these materials a commercialized model of sensor applicable for both indoor and outdoor detection gas humidity and photon may be designed. Thus various configurations/systems described in the thesis and the detailed specifications given for each of them are expected to prove useful in fabricating a sturdy, robust and cost-effective sensors suitable for operation at room temperature.

7.7 Scope of Further Research

- Future studies that would be fruitful in further understanding the role of carbon nanomaterials for low temperature applications are needed. These include incorporation of the recovery aspects achieved from incorporation of catalyst onto the surface of a carbon nanomaterials being used to detect a reducing gas. Growth simulations and reconstructions of the different surface species under different synthesis conditions would give rise to even more specific engineering of nanomaterials than what is currently known to the world of research within nanotechnology. Spectroscopic evaluation of the sensing mechanism would be very fruitful in the selection of the material to be used for the fabrication of cost effective sensors in future.
- Detailed analysis of the evolution of the surface reactions with respect to temperature needs to be carried out, in order to exactly understand the reaction products from the

surface interaction. Temperature Programmed Desorption (TPD) experiments give valuable information on the formation and desorption of reaction products on the surface. Controlled TPD experiments, at the sensing temperatures need to carry out for understanding the surface chemistry.

- The presence of crystallographic defects affects the sensing mechanism of gas sensors. A quantitative study that links the presence of these defects and the density of states in the energy gap with the sensitivity of the sensors has to be done. A detailed XPS study before and after sensing of all gas analytes would confirm the reaction mechanism with those gases. An in-situ XPS with gas atmosphere control would give better idea as to what happens to the electronic structure of the carbon nanomaterials and its nanocomposite during high temperature gas interaction and also an idea of how the shear planes grow and whether this leads to an increase in the density of states in the gap.

APPENDIX

EXPERIMENTAL METHODS AND CHARACTERIZATION TECHNIQUES

The experimental techniques used throughout the whole work for the preparation and characterization of the carbon nanomaterials and sensor are over-viewed in this part. The synthesis of carbon nanotube and its composition was performed by chemical vapor deposition method. Thin film was prepared by spin coating method. For the identification, the prepared sample was characterized by XRD, SEM, EDX, TEM, UV-Visible spectroscopy, FTIR, Raman, particle size analysis techniques etc.. Further the variation of resistance corresponding to LPG and CO_2 concentration was observed by high resistance Keithley Electrometer and variation of impedance corresponding to humidity was observed by Impedance Analyzer.

Experimental methods and characterization techniques

The methodology and various experimental techniques used in the synthesis and investigation of carbon nanostructures and its nanocomposites have been described. X-ray diffractometer (XRD), Scanning electron microscope (SEM), Particle Size Analyzer, Tunneling Electron Microscopy (TEM), BET and UV-vis spectrophotometer were used to characterize these nanomaterials. A large number of techniques have been employed for getting the overall information about the properties, structure, shape and size, topology etc. of the specimen. Some of the techniques which have been used in this thesis work are described in detail in this chapter.

A.1 Methodology of Present Work

Following steps were carried out for the present investigation;

1. Synthesis of Carbon nanostructure and its composite using the chemical vapor deposition method.

2. Fabrication of the thin film.

3. Investigation of the material using different characterization techniques to know phase, structure, size, morphology, band gap etc. of the film. The techniques used here are as follows:

a. X-ray Diffraction (XRD): XRD is used for the study of phase identification and structural properties. It is also used to find crystallite size.

b. Scanning Electron Microscopy (SEM): SEM technique is used to know the surface morphology of the nanocomposite thin film.

c. Transmission Electron Microscopy (TEM): TEM is used to obtain the topography of the sample which deals with the internal structure of the nanotube, and its grain distribution and grain diameter.

d. Particle Size Analyzer: It is used to find out the particle size distribution.

e. UV-visible Spectroscopy: This spectroscopy will provide information about the absorption spectra and the optical band gap of the sample.

f. Raman Analysis: It is used for identifying the sample along with the nature of molecular vibrational bonds present in the molecules the sample.

g. Keithley Electrometer: It is used for measuring the resistance of the film.

h. Impedance analyzer: It is used for measuring the impedance of the thin film.

A.2 Synthesis

A.2.1 Chemical Vapor Deposition Technique

Chemical vapour deposition (CVD**)** is a chemical process which is used to produce highly pure solid materials. It is the most reliable method for the synthesis of nanomaterials. In this technique nucleation of particles in the vapour state take place rather than deposition of the film. The process is used to make a very thin film and is used in the electronic industry and semiconductor industry. In a typical CVD process, the wafer (substrate) is exposed to one or more volatile precursor, which react and/or decompose on the substrate surface to produce the desired deposit and when the mixture of gas reactant is inserted inside the reacting chamber and chemical reaction among the gas molecule take place. Chemical reaction types basic to CVD include pyrolysis (thermal decomposition), oxidation, reduction, hydrolysis, nitride and carbide formation, synthesis reactions, disproportionation, and chemical transport [26].

A CVD apparatus will consist of several basic components:

Gas delivery system – For the supply of precursors to the reactor chamber

- **Reactor chamber –** Chamber within which deposition takes place
- **Substrate loading mechanism –** A system for introducing and removing substrates, mandrels etc.
- **Energy source –** Provide the energy/heat that is required to get the precursors to react/decompose.

- **Vacuum system –** A system for removal of all other gaseous species other than those required for the reaction/deposition.
- **Exhaust system –** System for removal of volatile by-products from the reaction chamber.
- **Exhaust treatment systems –** In some instances, exhaust gases may not be suitable for release into the atmosphere and may require treatment or conversion to safe/harmless compounds.
- **Process control equipment –** Gauges, controls to monitor process parameters such as pressure, temperature and time. Alarms and safety devices would also be included in this category.

CVD can be classified into other as:

1. Atmospheric Pressure Chemical Vapour Deposition (APCVD)
2. Low-Pressure Chemical Vapour Deposition (LPCVD)
3. Plasma Enhanced CVD (PE-CVD)
4. Metal-Organic CVD (MO-CVD)
5. Photochemical vapour deposition
6. Direct liquid injection CVD (DLICVD)

A.2.1.1. Atmospheric pressure chemical vapor deposition

APCVD reactors operate in mass transport limited region. So they are designed such that equal flow of reactants is delivered. This ensures uniform film deposition. This is done by placing the wafer horizontally and then moving them under the gas stream. They are used for depositing low-temperature oxide films Samples are carried through the reactor on a conveyor belt. Reactant gases flowing through the center of the reactor are containing by gas curtains formed by the fast flow of nitrogen.

Advantages:

- Simple
- High deposition rate
- Low temp

Disadvantages:

- Poor step coverage

- Particle contamination
- Require excess wafer handling

Application:

- Doped & un-doped low-temperature oxides

A.2.1.2. Low-pressure chemical vapor deposition

The reactor consists of a quartz tube heated by a three-zone furnace. Gas introduced from one end & pumped out from the other end. Wafers stand vertically, perpendicular to the gas flow. They are placed in a quartz holder. It operates in a surface reaction rate limited mode. Therefore the supply of equal flux of reactants is not required. Therefore geometry can be such that it can accommodate a large no. of wafers approx 200 wafers at a time

Advantages:

- Excellent purity
- Comfortable step coverage
- Large wafer capacity

Disadvantage

- High temp
- Low deposition rate
- Application
- Doped & un-doped high temp oxides
- Silicon nitride
- Polysilicon

A.2.1.3. Plasma enhanced chemical vapor deposition (PECVD)

PECVD system uses an 'RF induced' glow discharge to transfer energy into reactant gases. This procedure allows the substrate to remain at a low temp than APCVD & LPCVD

Types:

- Parallel plate type
- Hot wall type
- Single wafer type

Parallel plate type: Reaction chamber is cylinder & constructed of Al-coated stainless steel There are Al plates on the top & bottom. Samples lie on the grounded bottom electrode

RF is applied to the top electrode which creates a glow discharge between 2 plates. Gases flow radially through the discharge. Resistance heater heats the bottom, grounded electrode to a temp b/w 100-400°C. Gases are flowing from outer edges to the center

Advantages:

- Low temp deposition

Disadvantages

- The wafer must be loaded & unloaded individually
- Chance of contamination

Application:

- Silicon dioxide
- Deposition on silicon nitride

Hot wall type: The reaction takes place in a quartz tube heated by a furnace Samples are held parallel to the gas flow. The electrode assembly contains long graphite or al slabs to support the wafers. Alternating slabs are connected to the power supply to generate discharge in the space between the electrode (long slabs serve both as electrode & holder)

Advantage:

- Uniformity
- Large no. of wafer deposition

Disadvantage:

- Contamination while loading and unloading

A.2.1.4. Metal oxide chemical vapor deposition

This is a technique for depositing thin layers of atoms onto a semiconductor wafer. Using MOCVD you can build up many layers, each of a precisely controlled thickness, to create a material which has specific optical and electrical properties

Principle: Atoms that you would like to be in your crystal are combined with complex organic gas molecules and passed over a hot semiconductor wafer. The heat breaks up the molecules and deposits the desired atoms on the surface, layer by layer. By varying the composition of the gas, you can change the properties of the crystal at an almost atomic scale. It can grow high-quality semiconductor layers

A.2.1.5. Photochemical vapor deposition

Photo-Chemical CVD Reactor uses ultraviolet light as an energy source for activating process gases for the deposition of dielectric films at low temperatures (<150ºC). Films of silicon dioxide (SiO_2), silicon nitride (Si_3N_4), silicon oxynitride (SiON) and others can be deposited. Minimal stress is observed in these films due to the low deposition temperature. Since the UV photon energy used does not ionize the process gases, no radiation damage from charged particles has been observed.

A.2.1.6. Direct Liquid Injection Chemical Vapour Deposition

In this method, the precursors are directly injected inside the CVD for the growth process.

Advantage

- Large production of nanomaterials
- Low cost
- High Yield

Application of chemical vapor deposition

CVD has applications across a wide range of industries such as:

- **Coatings –** Coatings for a variety of applications such as wear resistance, corrosion resistance, high-temperature protection and erosion protection.
- **Semiconductors and related devices** – Integrated circuits, sensors and optoelectronic devices
- **Dense structural parts –** CVD can be used to produce components that are difficult or uneconomical to produce using conventional fabrication techniques. Dense parts produced via CVD are generally thin walled and may be deposited onto a mandrel or former.
- **Optical Fibers –** For telecommunications
- **Composites –** Preforms can be infiltrated using CVD techniques to produce ceramic matrix composites such as carbon-carbon, carbon-silicon carbide and silicon carbide-silicon carbide composites. This process is sometimes called chemical vapour infiltration or CVI.
- **Powder production –** Production of novel powders and fibers

A.3 Fabrication Techniques for Thin Film

A.3.1 Spin Coating method

Spin coating is the technique used for several decades to prepare a thin film from a sol-gel. It is used to get the homogeneous thin film. In this method, a small amount of fluid (resin) is put onto the center of the substrate and that substrate is put on the arm rotator and for a small time interval approx 30 sec and the rotator is allowed to spin at 3000 Rpm. The value of rpm is set as per our need. Due to spin centripetal acceleration is produced which help the resin to distribute uniformly on the substrate so that it covers the edges of the substrate also. The thickness of the film and other properties depends on the viscosity of the resin, rpm rate, time interval, surface tension, drying rate, single layering multi-layering, substrate, etc.

A.3.2 Type of dispense technique used in the spin coating method

Dispense of the resin plays an important factor in the preparation of the thin film. For this, the substrate must be cleaned by ultrasonic clean. Then after loading the substrate on spin coater, the main task starts. There are two ways to dispense the resin fluid on the substrate these are as follows:

(a) **Static resin**: Static dispense is deposition of a small puddle of resin fluid on the center of the substrate. A highly viscous and larger substrate is needed in this process. The spinning speed is higher in this process. It also requires a large amount of fluid to cover the whole substrate and due to the high spinning rate the fluid is waste.

(b) **Dynamic resin**: In this process speed of the arm rotator is slow around 500 rpm to 1000 rpm. This is more advantageous than static resins chances of void formation is low in this method. In this less amount of fluid is required and due to low speed, the wastage of fluid around the rotator is less.

A.4 Characterization Techniques

The carbon nanomaterials and its nanocomposite films were characterized by various characterization techniques which are described as follows:

A.4.1 X-ray Diffraction (XRD)

A.4.1.1 XRD Features and Basic principle

Max von Laue, in 1912, discovered that crystalline substances act as three-dimensional diffraction gratings for X-ray wavelengths similar to the spacing of planes in a crystal lattice.

X-ray diffraction is now a common technique for the study of crystal structures and atomic spacing. X-ray diffraction is based on constructive interference of monochromatic X-rays and a crystalline sample. These X-rays are generated by a cathode ray tube, filtered to produce monochromatic radiation, collimated to concentrate, and directed toward the sample. The interaction of the incident rays with the sample produces constructive interference satisfying the Bragg's Law ($2d \sin\theta = 2n\lambda$). This law relates the wavelength of electromagnetic radiation to the diffraction angle and the lattice spacing in a crystalline sample. These diffracted X-rays are then detected, processed and counted. By scanning the sample through a range of 2θ angles, all possible diffraction directions of the lattice should be attained due to the random orientation of the powdered material. Conversion of the diffraction peaks to d-spacings allows identification of the mineral because each mineral has a set of unique d-spacings. Typically, this is achieved by comparison of d-spacings with standard reference patterns.

All diffraction methods are based on the generation of X-rays in an X-ray tube. These X-rays are directed at the sample, and the diffracted rays are collected. A key component of all diffraction is the angle between the incident and diffracted rays. Powder and single crystal diffraction vary in instrumentation beyond this.

A.4.1.2 Crystallite size calculation

The XRD spectra have been used to calculate the crystallite size by Scherrer's formula

$$D = \frac{K\lambda}{\beta cos\theta} \qquad (1)$$

Where D is crystallite size, k is polarization factor, λ is the wavelength of CuK_α line and β is the full width half maximum (FWHM) of reflection peak and is the Bragg's angle about the peak. The value of crystallite size is calculated.

A.4.2 Scanning Electron Microscope

A scanning electron microscope (SEM) is a type of electron microscope that produces images of a sample by scanning the surface with a focused beam of electrons. The electrons interact with atoms in the sample, producing various signals that contain information about the surface topography and composition of the sample.

The most common SEM mode is the detection of secondary electrons emitted by atoms excited by the electron beam. By scanning the sample and collecting the secondary electrons that are emitted using a special detector, an image displaying the topography of the surface is created. The photograph of a scanning electron microscope used in the reported research is shown in Fig. A.7(a). SEM consists of an electron gun of some kind such as Tungsten or Lanthanum Hexaborate (LaB6) which acts as the source of an electron beam. The filament inside the electron gun is heated until a stream of the electron is produced. This stream of the electron is then condensed by first condenser lens, this lens serves two purposes at a time. One, it eliminates the high-angled electron from the beam and second, it limits the amount of current in the beam. The second condenser lens makes the beam narrower and focused. Near the bottom of SEM, a set of scanning coils is present that is used to focus the beam in the back and forth direction. When this beam hits the spot on the sample surface, it removes the secondary electrons and these electrons are detected by the detectors. The detectors role is to count the electrons and amplify the current and record it to visualize the image based on the number of electrons removed from the particular spot in pixels by a computerized system. The working of the SEM is shown in Fig. A.7(b).

Specimen interaction with the beam: Specimen interaction is the process that makes electron microscopy possible.

The various interactions that occur at the surface of the specimen are shown in Fig. A.8 and listed in the following sub-heads:

Secondary electron emission: The emission of the secondary electron is caused when the energized electrons strike the surface of the sample. These electrons transfer some energy to the lower energy electrons (usually the K–shell) and this causes the ionization of the atoms present at the surface of the sample. This electron removed from the surface is called “secondary electron”. This is the most common mode used in the imaging with SEM. The brightness of the signals depends upon the number of secondary electrons reaching the detector.

Backscattered electrons: Backscattered electrons are reflected or backscattered out of the specimen interaction volume. This is caused by the collision of an incident electron to an atom which is nearly normal to the incident path. The production of backscattered electrons varies directly with the atomic number of the specimen, that is, higher the atomic number, higher

will the brightness. Backscattered electrons thus can be used to detect different chemical composition, by examining the contrast between the areas.

Cathodoluminescence: When the high energy electrons strike the surface they excite the atoms and when these atoms return to their ground state they emit light. This process is termed as Cathodoluminescence (CL). In SEM, CL detectors can be used to give an image in real colour.

Auger electron: When the electron is removed from the core level of the atom, a vacancy is created which is filled by higher energy electron releasing energy which is transferred to another electron, which is then ejected as Auger electron. Auger electron has a characteristic energy feature which is unique for each element. Thus these auger electrons are collected and provide useful compositional information of the sample surface.

A.4.3 Energy Dispersive Spectroscopy

The SEM is also capable of performing analyses of selected point locations on the sample; this approach is especially useful in qualitatively or semi-quantitatively determining chemical compositions (using EDS), crystalline structure, and crystal orientations. The design and function of the SEM is very similar to the EPMA(Electron micro probe Analyser) and considerable overlap in capabilities exists between the two instruments. EDX is a qualitative tool for the detection of X-ray microanalysis. This means it gives the analysis based on the output signal of the height of the energy counts. EDX gives result in digitalized form. The X-axis represents Energy provided through the channel while Y-axis represents a number of counts. X-ray produces ionization and a solid state detector with better resolution is used to detect the information and further its result in terms of chemical composition which is further analyzed by the analyzer .

It performs the qualitative analysis by line identification and by qualitative ED analysis:

(a) **Line Identification:** line identification method is used to know the unknown specimen present in the sample by comparing the wavelength or energy of the spectrum from X-ray Spectrum.

(b) **Qualitative ED analysis**: In this, identification is done by superposition of the line spectra of the sample with the recorded spectra. The information of the results obtained is in tabular form or graphs or database.

A.4.4 Transmission Electron Microscopy (TEM)

Transmission Electron Microscopy (TEM) has become a mainstay in the repertoire of characterization techniques for materials scientists. Priebus and Hiller in 1938 built the first TEM whose magnification was 400000 times easier than many other objects. TEM's gives high lateral spatial resolution and its capability to provide both image and diffraction information from a single sample. It gives 2-dimensional Image with three-dimensional reconstructions. In addition, the highly energetic beam of electrons used in TEM interacts with sample matter to produce characteristic radiation and particles; these signals often are measured to provide materials characterization using EDS**,** backscattered and secondary electron imaging, to name a few possible techniques.

A.4.4.1 Principle, Construction and Working of TEM

. In TEM, a focused electron beam is an incident on a thin (less than 200 nm) sample. The signal in TEM is obtained from both undeflected and deflected electrons that penetrate the sample thickness. A series of magnetic lenses at and below the sample position are responsible for delivering the signal to a detector, usually a fluorescent screen, a film plate, or a video camera. Accompanying this signal transmission is a magnification of the spatial information in the signal by as little as 50 times to as much as a factor of 10^6. This remarkable magnification range is facilitated by the small wavelength of the incident electrons and is the key to the unique capabilities associated with TEM analysis. TEM offers two methods of specimen observation, diffraction mode and image mode.

In the diffraction mode, an electron diffraction pattern is obtained on the fluorescent screen, originating from the sample area illuminated by the electron beam. The diffraction pattern is entirely equivalent to an X-ray diffraction pattern: a single crystal will produce a spot pattern on the screen, a poly-crystal will produce a powder or ring pattern (assuming the illuminated area includes a sufficient quantity of crystallites), and a glassy or amorphous material will produce a series of diffuse halos.

The image mode produces an image of the illuminated sample area. The image can contain contrast brought about by several mechanisms: mass contrast, due to spatial separations between distinct atomic constituents; thickness contrast, due to non-uniformity in sample thickness; diffraction contrast, which in the case of crystalline materials results from scattering of the incident electron wave by structural defects; and phase contrast (see discussion later in this article). Alternating between image and diffraction mode on a TEM involves nothing more than the flick of a switch. The reasons for this simplicity are buried in the intricate electron optics technology that makes the practice of TEM possible.

There are a number of drawbacks to the TEM technique. Many materials require extensive sample preparation to produce a sample thin enough to be electron transparent, which makes TEM analysis a relatively time-consuming process with a low throughput of samples. The structure of the sample may also be changed during the preparation process. Also, the field of view is relatively small, raising the possibility that the region analyzed may not be characteristic of the whole sample. There is potential that the sample may be damaged by the electron beam, particularly in the case of biological materials.

A.4.4.3 Advantages of TEM

- TEM is used to characterize the specimen with high spatial resolution
- It gives crystallographic and morphology related information
- Very thin slice of the specimen is needed to identify the presence of atomic species.
- It is also used to detect crystalline defects by strain contrast formation.
- Its diffraction pattern is used to study the amorphous and crystallinity of the material.
- It gives higher magnifying resolution result in comparison to SEM.
- The SAED (Selected Area Diffraction) is used to determine the internal crystal structure and bravis lattice and lattice parameter of the specimen.

A.4.5 UV-vis Spectrophotometer

Ultraviolet and visible (UV-vis) absorption spectroscopy is the measurement of the attenuation (weakening of strength) of a beam of light after it passes through a sample or after reflection from a sample surface. Ultraviolet and visible light are energetic enough to promote

outer electrons to higher energy sublevels. The technique is usually applied to molecules or inorganic complexes in solution. Absorption measurements can be at a single wavelength or over an extended spectral range. UVvis spectra have broad features that are of limited use for sample identification but are very useful for quantitative measurements. The concentration of an analyte in solution can be determined by measuring the absorbance at some wavelength and applying the Beer-Lambert Law. Since the UV-vis range spans the range of human visual acuity of ~400-750 nm, UV-vis spectroscopy is useful to characterize the absorption, transmission, and reflectivity of a variety of technologically important materials, such as pigments, coatings, windows, and filters. This more qualitative application usually requires recording at least a portion of the UV-vis spectrum for characterization of the optical or electronic properties of materials. Electronic orbital of atoms and molecules have characteristic energies, giving rise to a set of discrete energy levels. An electron is able to change from an occupied orbital to another orbital, gaining or losing energy only in amounts exactly corresponding to the difference between two levels. The spectrophotometer used here for the determination of optical properties is shown in Fig. A.10(a). The promotion of an electron from the ground state (lowest possible energy) at energy E1 to higher energy state at E2 is possible if the molecule absorbs electromagnetic radiation of the corresponding wavelength $\lambda = hc/(E2-E1)$ (where, c = speed of light, h = Planck‟s constant). The electron at a higher energy is then said to be in an excited state. Excited states usually exist only for very short periods of time (femto seconds to microseconds), because the higher energy state is unstable and the extra energy is lost through relaxation processes such as emission of light. The typical energy difference between the ground and the first excited levels of many molecules corresponds to electromagnetic waves of the ultra-violet (UV) and visible regions of the electromagnetic spectrum.

The UV-visible range is only a small part of the total electromagnetic spectrum, and is generally defined from wavelengths of 190 nm at the high energy UV end to about 800 nm at the low energy red end of the spectrum. Light of other regions of the spectrum gives rise to different types of transitions and hence different types of spectroscopy. For example, IR radiation is usually not energetic enough to cause electronic transitions but can excite vibrations of molecules.

UV-visible spectrophotometers usually measure absorbance, which is the logratio of transmitted (sample in beam) over incident (no sample in beam) intensities.

The UV-vis photo spectrum of solution is recorded with respect to water placed in the reference beam using single beam spectrophotometer. The spectrum is analyzed by plotting $(\alpha h\nu)^2$ vs $h\nu$, based on eqn A.3:

$$\alpha h\nu = A(h\nu - E_g)^n \quad \ldots. (A.3)$$

Where, α is absorption coefficient, A is a constant and n is the exponent that depends upon the quantum selection rules for the particular material. The value of n characterizes the nature of band transition (n = 1/2 and 3/2 corresponds to direct allowed and direct forbidden transitions while n = 2 and 3 corresponds to indirect allowed and indirect forbidden transitions, respectively). A straight line is obtained when $(\alpha h\nu)^2$ is plotted against photon energy ($h\nu$), which indicates that the absorption edge is due to direct allowed transition. The intercept of the straight line on $h\nu$ axis corresponds to the optical energy band-gap (E_g).

In a standard UV-vis spectrophotometer, a beam of light is split; one-half of the beam (the sample beam) is directed through a transparent cell containing a solution of the compound being analyzed, and one-half (the reference beam) is directed through an identical cell that does not contain the compound but contains the solvent. The instrument is designed so that it can make a comparison of the intensities of the two beams as it scans over the desired region of the wavelengths. If the compound absorbs light at a particular wavelength, the intensity of the sample beam will be less than that of the reference beam. Absorption of radiation by a sample is measured at various wavelengths and plotted by a recorder to give the spectrum which is a plot of the wavelength of the entire region versus the absorption of light at each wavelength. And the band gap of the sample can be obtained by plotting the graph between ($\alpha h\nu$ vs $h\nu$) and extrapolating it along the x-axis. Ultraviolet and visible spectrometry are almost entirely used for quantitative analysis; that is, the estimation of the amount of a compound known to be present in the sample. The sample is usually examined in solution form. The working is shown in Fig. A. 10(b).

A.4.6 Particle Size Analyzer

Particle size influences many properties of particulate materials and is a valuable indicator of quality and performance. This is true for powders, suspensions, emulsions, and aerosols. The size and shape of powders influence flow and compaction properties. Larger, more spherical particles will typically flow more easily than smaller or high aspect ratio particles. Smaller particles dissolve more quickly and lead to higher suspension viscosities than larger ones. Smaller droplet sizes and higher surface charge (zeta potential) will typically improve suspension and emulsion stability. Powder or droplets in the range of 2-5μm aerosolize better and will penetrate into lungs deeper than larger sizes. For these and many other reasons it is important to measure and control the particle size distribution of many products.

A spherical particle can be described using a single number the diameter because every dimension is identical. As seen in Fig. 2.8, non-spherical particles can be described using multiple length and width measures (horizontal and vertical projections are shown here). These descriptions provide greater accuracy, but also greater complexity. Thus, many techniques make the useful and the convenient assumption that every particle is a sphere. The reported value is typically an equivalent spherical diameter. This is essentially taking the physical measured value

(i.e. scattered light, settling rate) and determining the size of the sphere that could produce the data. Although this approach is simplistic and not perfectly accurate, the shapes of particles generated by most industrial processes are such that the spherical assumption does not cause serious problems. Problems can arise, however, if the individual particles have a very large aspect ratio, such as fibers or needles.

A.4.7 Raman Analysis

A.4.7.1 Features and basic principle of Raman Spectroscopy

Raman spectroscopy provides information about molecular vibrations that can be used for sample identification. The technique involves shining a monochromatic light source (i.e. laser) on a sample and detecting the scattered light. The majority of the scattered light is of the same frequency as the excitation source; this is known as Rayleigh or elastic scattering. A very small amount of the scattered light (10^{-5}% of the incident light intensity) is shifted in

energy from the laser frequency due to interactions between the incident electromagnetic waves and the vibrational energy levels of the molecules in the sample. Plotting the intensity of this "shifted" light versus frequency results in a Raman spectrum of the sample. Generally, Raman spectra are plotted with respect to the laser frequency such that the Rayleigh band lies at 0 cm^{-1}. On this scale, the band positions will lie at frequencies that correspond to the energy levels of different functional group vibrations. The Raman spectrum can thus be interpreted similarly to the infrared absorption spectrum.

- When radiation passes through a transparent medium, the species present scatter a fraction of the beam in all directions.
- In 1928, the Indian physicist C. V. Raman discovered that the visible wavelength of a small fraction of the radiation scattered by certain molecules differs from that of the incident beam and furthermore that the shifts in wavelength depend upon the chemical structure of the molecules responsible for the scattering.
- The theory of Raman scattering shows that the phenomenon results from the same type of quantized vibrational changes that are associated with infrared absorption. Thus, the difference in wavelength between the incident and scattered visible radiation corresponds to wavelengths in the mid-infrared region.
- The Raman scattering spectrum and an infrared absorption spectrum of a given species often resemble one another quite closely.

A.4.7.2 Terminologies and basic component needed in instrumentation

When a monochromatic laser light with frequency υ_0 excites molecules and transforms them into oscillating dipoles. Such oscillating dipoles emit light of three different frequencies.A photon with frequency υ_0 is absorbed by a Raman-active molecule which at the time of interaction is in the basic vibrational state. Part of the photon's energy is transferred to the Raman-active mode with frequency υ_m and the resulting frequency of scattered light is reduced to $\upsilon_0 - \upsilon_m$. This Raman frequency is called Stokes frequency, or just "**Stokes**".

- A photon with frequency υ_0 is absorbed by a Raman-active molecule, which, at the time of interaction, is already in the excited vibrational state. The excessive energy of

excited Raman active mode is released, molecule returns to the basic vibrational state and the resulting frequency of scattered light goes up to $\upsilon_o + \upsilon_m$. This Raman frequency is called Anti-Stokes frequency, or just "**Anti-Stokes**".

- A molecule with no Raman-active modes absorbs a photon with the frequency υ_0. The excited molecule returns back to the same basic vibrational state and emits light with the same frequency υ_0 as an excitation source. This type of interaction is called an elastic **Rayleigh scattering**.

A Raman system typically consists of four major components:

1. Excitation source (Laser).
2. Sample illumination system and light collection optics.
3. Wavelength selector (Filter or Spectrophotometer).
4. Detector (Photodiode array, CCD).

A.4.7.3 Advantages of Raman Spectroscopy

Raman scattering is a spectroscopic technique that is complementary to infrared absorption spectroscopy. Raman offers several advantages over mid-IR and near-IR spectroscopy, including:

- Little or no sample preparation is required
- Water is a weak scatterer - no special accessories are needed for measuring aqueous solutions
- Water and CO_2 vapors are very weak scatterers - purging is unnecessary
- Inexpensive glass sample holders are ideal in most cases
- Fiber optics (up to 100's of meters in length) can be used for remote analyses
- Since fundamental modes are measured, Raman bands can be easily related to chemical structure
- Raman spectra are "cleaner" than mid-IR spectra - Raman bands are narrower, and overtone and combination bands are generally weak
- The standard spectral range reaches well below 400 cm^{-1}, making the technique ideal for both organic and inorganic species

- Raman spectroscopy can be used to measure bands of symmetric linkages which are weak in an infrared spectrum (e.g. -S-S-, -C-S-, -C=C-).

Figures

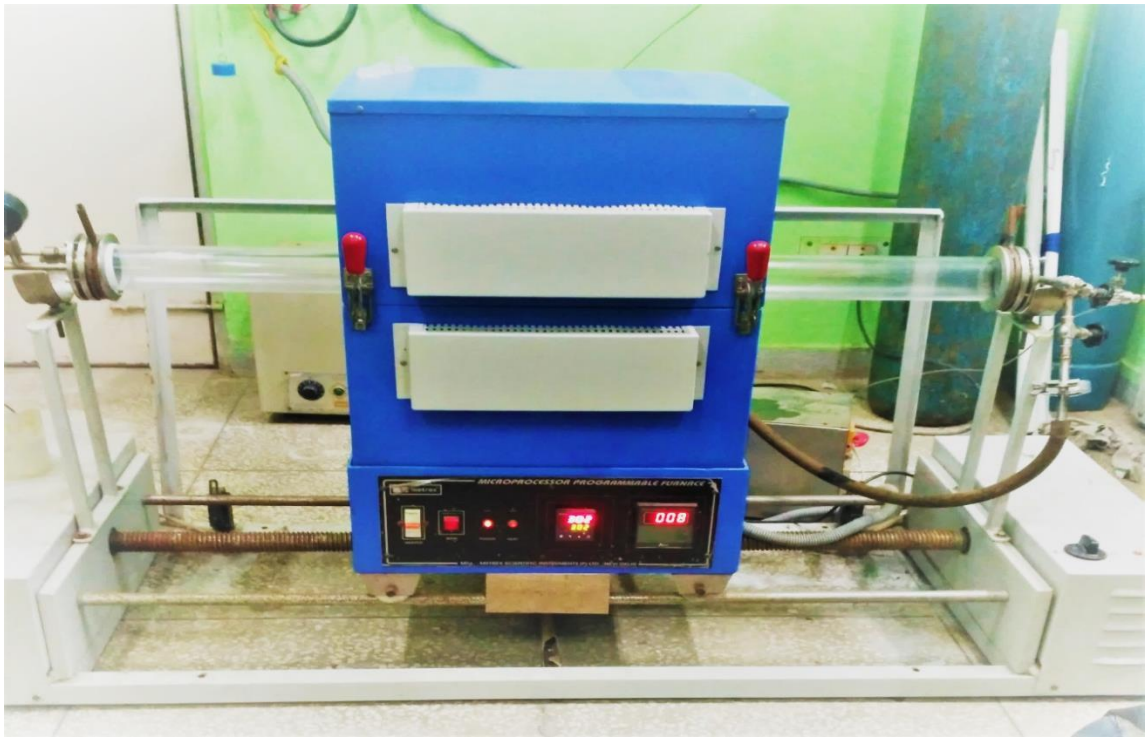

Figure A1 Experimental setup of CVD apparatus for synthesis of carbon nanomaterials (NMSL BBAU Lucknow)

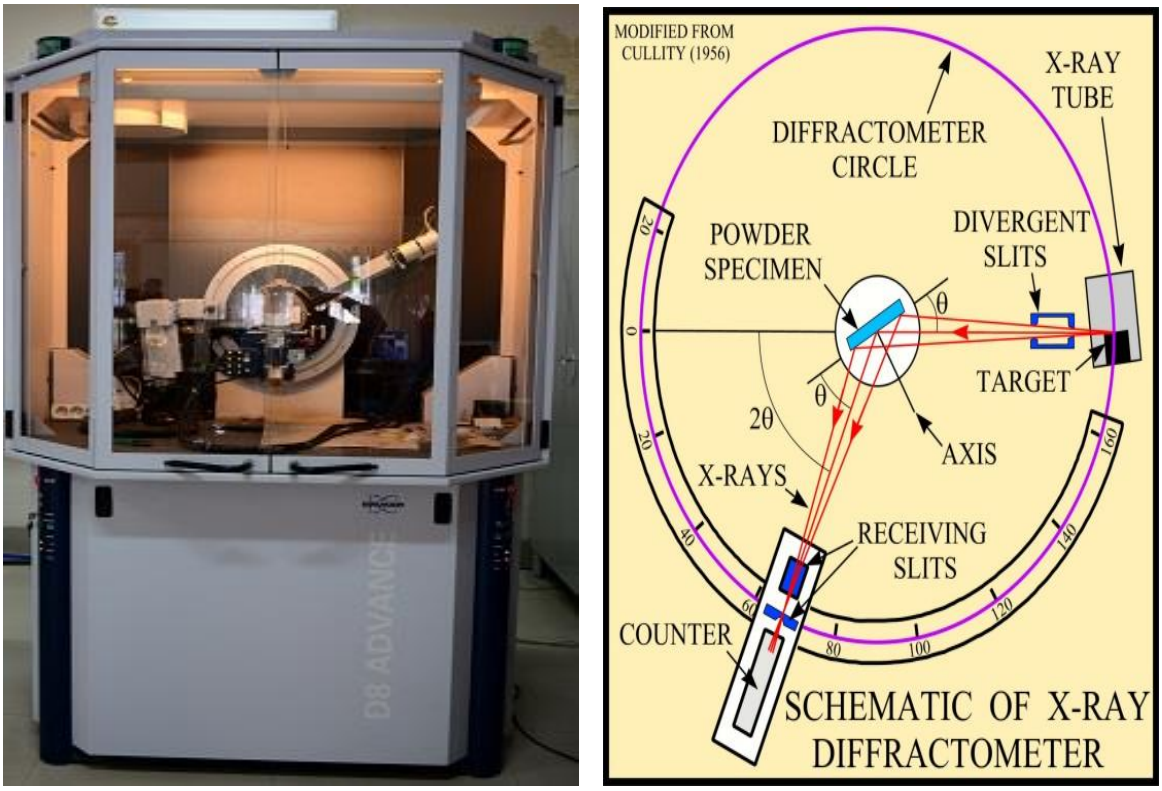

Fig. A3 Experimatal setup and block diagram of XRD

Figure A4 Experimental setup of Scanning Electron Microscope JEOL JSM-6490LV (USIC BBAU Lucknow)

Figure A5 Experimental setup of UV visble spectrometer Evolution 202 (NMSL BBAU Lucknow)

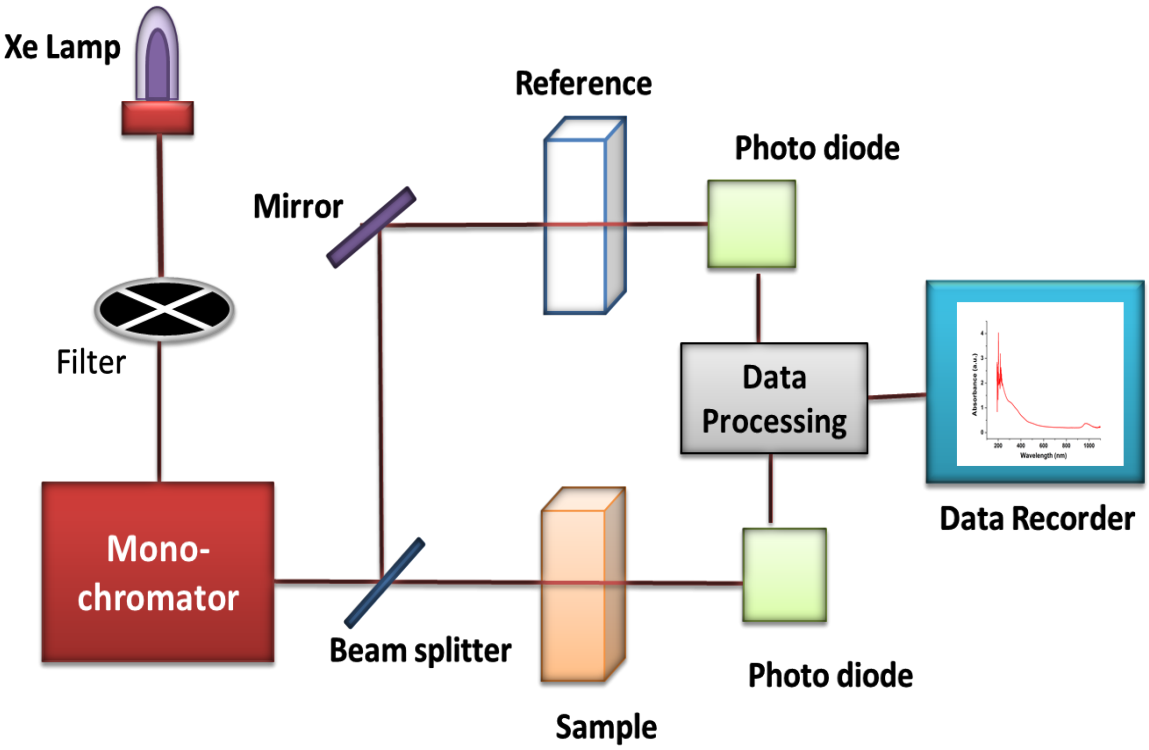

Figure A6 Block diagram of working model of UV visible spectrometer

Figure A7 Experimental setup of particle size analyzer NZS90 (NMSL BBAU Lucknow)

Figure A8 Experimental setup of FTIR spectrophotometer (USIC BBAU Lucknow)